The 1.9 Ga Winnipegosis Komatiite: Implications for Earth Accretion, Mantle Dynamics, and Komatiite Formation

by

Pedro Waterton

A thesis submitted in partial fulfilment of the requirements for the degree of

Doctor of Philosophy

Department of Earth and Atmospheric Sciences
University of Alberta

Abstract

Komatiites are high temperature, high MgO lavas that have the potential to provide geochemical and thermal insights into the evolution of the Earth's mantle. However, komatiite studies are frequently hampered by the altered nature of all komatiites and the presence of large gaps in the komatiite record, most notably during the Proterozoic. This thesis characterises the Palaeoproterozoic Winnipegosis komatiites with a comprehensive study of their petrography, bulk rock and mineral geochemistry, isotope systematics, geochronology, and in-depth thermodynamic and geochemical modelling. These data and modelling are used to explore komatiite formation, the geochemical and thermal history of the mantle, and the relationship between komatiites and basalts.

The komatiites occur in the Winnipegosis Komatiite Belt (WKB), a greenstone belt dominated by basalt and komatiite with no surface exposure. New U-Pb SHRIMP dating of mafic zircons from the WKB yields an age of 1870.3 ± 7.1 Ma. Combined with an abundance of mafic and ultramafic magmatism and depleted geochemical signatures, this age confirms that the WKB is part of the ∼1.88 Ga Circum-Superior Belt, a Proterozoic large igneous province. The komatiites are very well preserved and dominated by massive olivine porphyritic flows with a median thickness of 6 m. Differentiated flows containing layers of olivine spinifex are present, but rare.

Trace element data indicate the komatiites were derived from depleted mantle, and contaminated by interaction with continental crust. Al-in-olivine thermometry combined with olivine-melt Fe-Mg partitioning indicates that the parental melts to Win-

nipegosis komatiites were nominally dry, with an MgO content of 23.6 ± 1.6 wt%. The presence of olivine spinifex textures and derivation from liquids with > 18 wt% MgO demonstrates the Winnipegosis samples are komatiites *sensu stricto*. However, liquidus temperatures of 1501 ± 32 °C are approximately 100 °C cooler than their hottest Archaean counterparts, and are also significantly cooler than the hottest Phanerozoic picrites. The geochemical and geological evidence requires that Winnipegosis Komatiites were erupted onto continental crust, and high liquidus temperatures require anomalously hot mantle. A tectonic model is proposed in which Winnipegosis komatiites were generated in a mantle plume deflected towards the margins of the Superior craton by strong gradients in lithospheric thickness. This interpretation of komatiitic magmatism in the Circum-Superior Belt casts doubt on previous suggestions that ambient mantle potential temperatures were as high as 1600 °C during the Palaeoproterozoic.

Olivine was the liquidus phase during crystallisation of Winnipegosis komatiites, followed by chromite which saturated at ∼1424 °C. Bulk rock geochemical relationships do not represent liquid lines of descent, and are instead controlled by mixing of these phenocryst phases with residual melt shortly before or during eruption. In the massive flows crystallisation continued primarily through the growth of skeletal olivine and clinopyroxene in the groundmass, but some differentiated flows also crystallised clinopyroxene phenocrysts. Plagioclase is a rare groundmass phase though, in general, glass (now devitrified) formed before plagioclase crystallisation. Thermodynamic modelling using MELTS software reproduces this crystallisation sequence and, with minor caveats, can reproduce the liquid line of descent of Winnipegosis komatiites.

The relationship between komatiites and associated tholeiitic basalts has long been a subject of debate. The link between these rock types in the WKB is investigated by extending the MELTS modelling to crystallisation at higher pressures. This modelling demonstrates that tholeiitic basalts in the WKB likely formed through ∼60% crystalli-

sation of Winnipegosis komatiite parental melt in an upper crustal magma chamber. The presence of a large dunite body, representing a komatiitic olivine-chromite adcumulate, provides clear evidence of such upper crustal fractionation in the WKB.

Re-Os isotopic data for Winnipegosis komatiites define an isochron with age 1865 $\pm$ 40 Ma, and chondritic γOs. This age agrees with the U-Pb age of the WKB, and combined with demonstrable PGE control by igneous phases, confirms that the PGE systematics of Winnipegosis komatiites were undisturbed during metamorphism. Winnipegosis komatiites parental melts contained 7.0 $\pm$ 0.8 ppb Pt and 7.2 $\pm$ 0.7 ppb Pd. These concentrations are $>$ 60% lower than predicted by geochemical modelling under any reasonable assumptions of melting conditions, melt fraction and source composition. This discrepancy cannot be explained by melting of a source depleted in PGEs. Instead, comparison with parental melt compositions of other well-preserved komatiites and picrites indicates that both Pd and Pt may exhibit some compatibility during high degree melting, and may not be exhausted from mantle residues until extreme melt fractions are reached. It is suggested that low PGE concentrations in komatiites reflect partial retention of PGEs in their mantle sources, and differences in melting conditions, rather than evidence of low-PGE mantle generated by uneven late accretion and/or magma ocean differentiation.

Preface

Chapter 2 of this thesis, along with parts of Chapter 1 (Geological Setting and Petrography sections), have been published in *Lithos* as Pedro Waterton, D. Graham Pearson, Bruce Kjarsgaard, Larry Hulbert, Andrew Locock, Stephen Parman, and Bill Davis (2017) "Age, origin, and thermal evolution of the ultra-fresh ∼1.9 Ga Winnipegosis Komatiites, Manitoba, Canada". I was responsible for the majority of the data collection and analysis, as well as writing the manuscript. D. Graham Pearson was the supervisory author and aided with data interpretation and manuscript composition. Bruce Kjarsgaard sourced the samples for the paper (and this thesis) and aided with data interpretation. Larry Hulbert was responsible for the initial characterisation of the Winnipegosis Komatiites, and provided the 'GSC database' referred to at many points throughout this thesis. Andrew Locock aided with the development and implementation of high-precision EPMA methods. Stephen Parman provided help with data interpretation and manuscript writing. Bill Davis provided new U-Pb zircon SIMS analyses used to date the Winnipegosis Komatiite Belt.

Chapter 3 of this thesis was submitted to *Earth and Planetary Science Letters* as Pedro Waterton, D. Graham Pearson, and James Mungall "PGE systematics of the ∼1.9 Ga Winnipegosis Komatiites: Implications for PPGE behaviour during high degree melting and mixing of the late veneer". I was responsible for the data collection and analysis. D. Graham Pearson was the supervisory author and was involved with concept formation and manuscript composition. James Mungall provided the PGE model and helped with its implementation.

The remainder of Chapter 1, and all of Chapter 4 are my own work, written for this thesis, under the supervision of D. Graham Pearson.

Acknowledgements

Research presented in this thesis was performed under the tenure of an NSERC Vanier Scholarship awarded to Pedro Waterton at the University of Alberta. Analytical work was funded by a Canada Excellence Research Chairs Program award to D. Graham Pearson, and the Geological Survey of Canada. Larry Hulbert is particularly thanked for providing an extensive body of unpublished data (the 'GSC database'), samples, and interpretations that laid the groundwork for this thesis. Stan Mertzman and Karen Mertzman are thanked for the new XRF analyses presented throughout this thesis, and Thomas Stachel and Gerhard Brey are thanked for supplying and discussing olivine standards. Constructive discussions with Yannick Bussweiler, Richard Stern, Tom Chacko, Mark Hamilton, Richard Ernst and Larry Heaman were a great help during the preparation of Chapter 2. Philippe Pagé and Laurence Coogan are thanked for providing constructive reviews of the published work in Chapter 2, B. M. Saumur is thanked for internal GSC review, and Andrew Kerr for editorial handling. Discussions with Bruce Kjarsgaard greatly benefited the work presented in Chapter 3.

I am grateful to members of my candidacy and defence examination committees: Thomas Stachel, Long Li, and Matthew Steele-MacInnis, at the University of Alberta, and the external examiner, Richard Walker, from the University of Maryland. Robert Luth and Larry Heaman provided excellent advice as members of my supervisory committee, and Sarah Woodland, Chiranjeeb Sarkar, Jingao Liu, and Yan Luo are thanked for teaching me how to do geochemistry. I would like to particularly thank Graham Pearson for being an excellent supervisor throughout this PhD, providing invaluable suggestions, advice, and reading material, and always encouraging me to pursue offshoot ideas.

Finally, to my partner and wife Léanne, thank you for everything.

Contents

List of Tables

List of Figures

Chapter 1
Introduction to the Winnipegosis Komatiite Belt

1.1 Introduction

1.1.1 Komatiites

Komatiites represent the hottest lavas known to have erupted at the Earth's surface (e.g., Green *et al.*, 1975; Puchtel *et al.*, 2013), and have attracted a great deal of scientific interest as an extreme end-member of mantle melting. Their high eruption temperatures and MgO contents give rise to the formation of spectacular spinifex textures (Nesbitt, 1971; Donaldson, 1982; Arndt & Nesbitt, 1982), absent from most lower temperature volcanic rocks, and has led to their use as tracers of changes in mantle potential temperature through time (e.g., Nisbet *et al.*, 1993; de Wit, 1998; Campbell & Griffiths, 2014). Associated high degrees of mantle melting have prompted the study of komatiites as representative chemical samples of the Earth's mantle through time (e.g., Bickle *et al.*, 1976; Maier *et al.*, 2009). Perhaps due to the high temperatures required for their formation, komatiites are also one of a number of rock types with a strong temporal distribution throughout Earth history (Arndt *et al.*, 2008; Condie & O'Neill, 2010); despite their abundance during their Archaean, only a handful of Phanerozoic (Echeverria, 1980; Hanski *et al.*, 2004) and Proterozoic (Arndt *et al.*, 1987; Barnes & Often, 1990; Puchtel *et al.*, 1997) have been described. Aside from their scientific importance, komatiites are also of great economic importance; komatiite hosted nickel-copper-platinum group element (Ni-Cu-PGE) deposits account for about 10% of the world's nickel production (Hronsky & Schodde, 2006).

1.1.2 Review of komatiite literature

Existence and temperature of ultramafic magmas

Field reports of banded ultramafic lava flows and textures recognisable as spinifex date back to the early 20th Century (e.g., Bruce, 1926). However, the existence of ultramafic magmas was for many years widely doubted on the basis of experiments which showed these magmas would have high liquidus temperatures of 1500 – 1600 °C (Bowen, 1927; Bailey & McCalien, 1953). Even at this early stage, evidence of a long standing tension in komatiite research can be seen; Alfred Harker may have been the first to suggest that the liquidus temperature of ultramafic melts might be moderated by the presence of volatiles (personal communication reported in Bowen, 1927).

Widespread acceptance of the existence of ultramafic lavas and the recognition of komatiites as a rock type came with the discovery of the Barberton komatiites (Viljoen & Viljoen, 1969b,a). Komatiites were soon identified in almost all Archaean terranes (Arndt *et al.*, 2008). Early definitions highlighted elevated CaO/Al_2O_3 (Al-depletion) and MgO as defining features (Viljoen & Viljoen, 1969b; Brooks & Hart, 1974), but it was quickly recognised that not all komatiites shared the exceptionally high CaO/Al_2O_3 of some Barberton komatiites (Nesbitt & Sun, 1976; Arndt *et al.*, 1977). Further work led to the subdivision of komatiites into Al-depleted and Al-undepleted classes on the basis of Al_2O_3/TiO_2 or CaO/Al_2O_3 (Nesbitt *et al.*, 1979), and the subsequent definition of komatiites simply as volcanic rocks with $>$ 18 wt% MgO (Arndt & Brooks, 1980; Arndt & Nisbet, 1982). This definition remains little changed (Le Bas, 2000), though arguments remain as to whether the presence of spinifex texture is a prerequisite for a rock to be defined as komatiite (Kerr & Arndt, 2001).

Early experimental work by Green *et al.* (1975) demonstrated that komatiites have extremely high anhydrous liquidus temperatures (∼1650 °C). These authors argued against hydrous melting on the basis that wet komatiites would have crystallised large quantities of olivine *en-route* to the surface, leading to the suggestion that komatiites formed in upwelling mantle plumes (Green, 1975). Following these early works, the vast majority of komatiite studies invoked extremely high temperature melting in a mantle plume (e.g., Nesbitt & Sun, 1976; Nisbet, 1982; Campbell *et al.*, 1989; McDonough & Ireland, 1993; Nisbet *et al.*, 1993). However, the possibility that komatiite liquidus temperatures were depressed by the presence of water remained under consideration, and wet melting was invoked as a means to explain spinifex textures and the interleav-

ing of komatiites with felsic rocks (Brooks & Hart, 1974), and to avoid 'unreasonably' hot geotherms required for dry melting (Allegre, 1982). The 'hydrous komatiite hypothesis' (Arndt *et al.*, 2008) gained popularity in the 1990s, with a number of studies arguing that komatiites were produced in subduction zones with liquidus temperatures of ∼1400 °C, due to clinopyroxene compositions inconsistent with forming from dry melts (Parman *et al.*, 1997) and compositional similarities between basaltic komatiites and boninites (Cameron *et al.*, 1979; Parman *et al.*, 2001). These subduction zone interpretations were fiercely disputed (Arndt *et al.*, 1998; Arndt, 2003), and largely fell out of favour following melt inclusion water content and oxidation state analyses (Berry *et al.*, 2008). However, the almost century-old dispute over the temperature and water content of ultramafic magmas was reignited by Sobolev *et al.* (2016), who identified moderately high H_2O contents in komatiites of the Abitibi greenstone belt, capable of lowering the liquidus temperature by ∼60 °C. Subsequent studies have also highlighted the role of water in lowering the liquidus temperatures of komatiites, though the magnitude of this effect remains unclear and may vary between komatiites (Stone *et al.*, 1997; Gurenko *et al.*, 2016; Asafov *et al.*, 2017).

Mode of formation and tectonic setting

Unsurprisingly, given the long running disputes over komatiite liquidus temperatures and water contents, a wide range of formation models have been proposed for komatiites. These can be broadly divided into dry, high temperature plume models, and wet, low temperature subduction zone models (see above). However, a number of variations exist, including the recent revival of wet plume models (Kawamoto *et al.*, 1996; Sobolev *et al.*, 2016), interactions between subduction zones and plumes (Kerrich *et al.*, 1998; Wyman, 1999; Angerer *et al.*, 2013), and various models invoking qualitatively different tectonic processes during the Archaean, such as giant meteorite impacts (Green, 1972) or mantle overturn beneath a stagnant lid (Bedard, 2017).

Even within these broad categories of formation models, considerable debate remains as to the tectonic setting in which komatiites formed. Early work, summarised by Nisbet (1982), tended to favour the extrusion of komatiites onto rifting continental crust, due to the recognition of unconformities over continental crust (Bickle *et al.*, 1975), widespread correlations between greenstone belts in the same craton (Wilson *et al.*, 1978), and the presence of terrigenous sediments in komatiite-bearing greenstone belts. However, studies of the Barberton greenstone belt generally favoured an oceanic

setting, culminating in the description of the greenstone belt as an obducted ophiolite complex (de Wit *et al.*, 1987). These contrasting ideas of tectonic setting still persist, with proponents of continental crustal settings highlighting basal unconformities, presence of xenocrystic zircons, and evidence of crustal contamination (e.g., Bickle *et al.*, 1994; Pearce, 2008), whereas proponents of oceanic settings highlight the presence of tectonic contacts between units (e.g., Furnes *et al.*, 2013) and geochemical and isotopic similarities to oceanic plateau basalts (e.g., McDonough & Ireland, 1993; Puchtel *et al.*, 1998). Interpretations of whether komatiites formed in oceanic or continental tectonic settings are not necessarily tied to particular melting models; proponents of plume models have invoked both continental (e.g., Nesbitt & Sun, 1976; Mole *et al.*, 2014; Sossi *et al.*, 2016) and oceanic (e.g., Puchtel *et al.*, 1998; Kerr, 2005) settings, and models requiring subduction zones have included island arc (Parman *et al.*, 2004) and continental arc (Hollings *et al.*, 1999) associations.

Basalts and komatiites

The wide variety of rocks found in association with komatiites likely contributes to disagreements over their tectonic setting. Komatiite-bearing greenstone belts may lack terrigenous sediments, as in the Barberton greenstone belt (de Wit *et al.*, 1987; Dann, 2000), or contain abundant detrital sediments, as commonly observed in the Superior Province (Donaldson & De Kemp, 1998; Wyman & Hollings, 1998). Komatiites are also found interlayered with a large variety of volcanic rocks, ranging from boninites (Kerrich *et al.*, 1998; Smithies *et al.*, 2004; Saha *et al.*, 2015) to intermediate and felsic volcanics (Jensen, 1982; Barnes *et al.*, 1988; Hollings *et al.*, 1999). However, the most common rock type associated with komatiites are tholeiitic basalts, which typically dominate komatiite-bearing volcanic sequences (Storey *et al.*, 1991; Bickle *et al.*, 1994; Arndt *et al.*, 2008; Campbell & Davies, 2017). Understanding the link between komatiites and tholeiites, therefore, appears critical to understanding the settings of komatiite formation.

Two main possibilities exist: that basalts associated with komatiites are the product of extensive fractional crystallisation of a komatiitic parental melt, or that compositional differences between basalts and komatiites are due to derivation from parental melts formed by different degrees of mantle melting (Arndt & Nesbitt, 1982). In localities where a continuous compositional spectrum between komatiites and basalts exists, both fractional crystallisation (Arndt *et al.*, 1977) and differences in parental melt (Nesbitt

& Sun, 1976; Sun & Nesbitt, 1978; Stamatelopoulou-Seymour *et al.*, 1983) have been invoked, and it is possible that both mechanisms are in operation. However, in many localities, distinguishing these possibilities has been hampered by the presence of a compositional gap between komatiites and less mafic rocks at ∼18 wt% MgO (Arndt & Nisbet, 1982). Perhaps in part due to this compositional gap, and in part due to the influential work of Campbell *et al.* (1989), later studies have tended to favour basalts and komatiites forming from different degrees of mantle melting in zoned mantle plumes, even for suites with very similar trace element characteristics (Rollinson, 1999; Kerr, 2005; Manikyamba *et al.*, 2008). Nonetheless, this central question of earlier komatiite research has received little recent attention in the literature, and is yet to be convincingly resolved.

Komatiites through time – mantle chemistry and temperature

Much of the recent study of komatiites has focussed on understanding how mantle chemistry and dynamics have changed through the course of Earth's history. The utility of komatiites for these purposes was recognised soon after their discovery; as high degree melts they have the potential to provide estimates of their mantle source composition (Bickle *et al.*, 1976), and as the hottest terrestrial magmas they can place upper bounds on mantle geotherms (Green, 1975). Until the discovery of the Gorgona komatiites (Gansser *et al.*, 1979), komatiites were believed to be restricted to the Archaean, thus limiting the span of Earth mantle history accessible to komatiite studies. Since then, a number of komatiites and komatiite-derived rocks have been discovered in the Phanerozoic (Hanski *et al.*, 2004; Thompson & Gibson, 2000; Trela *et al.*, 2017) and Proterozoic (e.g., Arndt, 1982; Arndt *et al.*, 1987; Hynes & Francis, 1982; Barnes & Often, 1990; Puchtel *et al.*, 1997; Hanski *et al.*, 2001; Minifie *et al.*, 2013). However, large gaps remain in the komatiite record (Condie & O'Neill, 2010), and even in recent years prominent authors have argued that the Proterozoic aeon is entirely devoid of komatiites (Arndt *et al.*, 2008).

In spite of these temporal gaps, komatiites have been used to trace the variation of many aspects of their mantle sources through time, including bulk compositions (Sun, 1982), lithophile isotope systematics (Blichert-Toft & Puchtel, 2010), and oxygen fugacity (Nicklas *et al.*, 2018). However, the aspects of mantle evolution that have received most attention in the recent komatiite literature are the temporal evolution of mantle potential temperatures and platinum group element (PGE) systematics.

Discussions of mantle potential temperatures (T_p) in the komatiite literature have frequently been related to the debate around the water contents and liquidus temperatures of komatiites (see above). In general, proponents of subduction zone models for komatiite formation favour more moderate Archaean T_p, ~100 °C hotter than modern mantle (Parman *et al.*, 1997; Grove & Parman, 2004), whereas proponents of dry plume melting argue for Archaean T_p up to ~300 °C hotter than modern mantle (Nisbet *et al.*, 1993; Herzberg *et al.*, 2010; Campbell & Griffiths, 2014). As with komatiite liquidus temperatures, this debate has been complicated by the advancement of wet plume models. These suggest Archaean T_p may have been overestimated by modelling assuming anhydrous conditions (Sobolev *et al.*, 2016), and combined with observations of exceptionally hot Phanerozoic lavas (Thompson & Gibson, 2000; Trela *et al.*, 2017), calls into question whether some portions of the mantle have cooled appreciably since the Archaean. One of the major outstanding issues with the use of komatiites to trace the evolution of mantle T_p is the lack of recognised komatiites from the Proterozoic. This aeon is the period in Earth history during which models of T_p evolution diverge the most, with differences in T_p relative to modern mantle (ΔT) varying by up to 170 °C in the Palaeoproterozoic (Davies, 1999; Herzberg *et al.*, 2010), yet few (if any) komatiites of this age are recognised.

The use of komatiites to investigate the PGE systematics of the mantle was first suggested by Keays (1982), who recognised their advantages as primitive melts which do not reach sulphide saturation until a late stage of crystallisation. As high degree melts komatiites also have the potential to provide representative chemical samples of the mantle (Puchtel *et al.*, 2004), while avoiding strong nugget effects (Aulbach *et al.*, 2015), and repeated depletion, enrichment and metasomatism that affect direct mantle samples (Pearson *et al.*, 2004; Seyler *et al.*, 2007). However, research into this question only became widespread with increasing availability of precise NiS fire assay (e.g., Puchtel & Humayun, 2000; Maier *et al.*, 2003) and Carius tube isotope dilution (e.g., Puchtel *et al.*, 2004) techniques. Since then, a number of studies (Puchtel *et al.*, 2007, 2009b, 2014, 2016a,b; Maier *et al.*, 2009; Fiorentini *et al.*, 2011) have found large variations in komatiite PGE abundances, generally interpreted to reflect differences in their mantle source PGE contents. However, the reasons behind these variations are not clear. Some authors (Maier *et al.*, 2009; Fiorentini *et al.*, 2011) argue that komatiite PGE abundances systematically increase between 3.5 – 2.7 Ga, reflecting slow mixing of PGE late veneer. However, Puchtel *et al.* (2014, 2016a,b) have argued that there is no systematic trend, and that variable PGE abundances in Archaean komatiites are best

explained by sluggish mixing of variably PGE-enriched post-magma ocean domains. Once again, the record of komatiite PGE abundances is punctuated by a significant and striking paucity of data between ∼2.7 – 0.1 Ga.

1.1.3 Thesis outline

The above review highlights a number of outstanding questions in komatiite research. Basic aspects of komatiite formation such as their liquidus temperatures, volatile contents, and relationship to associated rocks remain unclear. Furthermore, the use of komatiites as probes of the chemical and thermal structure of the mantle is severely hampered by large temporal gaps between studied komatiites, particularly during the Proterozoic.

In light of these outstanding questions, this thesis comprises a comprehensive petrological, geochemical, and geochronological study of the Winnipegosis komatiites, and associated basalts and dunites from the Winnipegosis Komatiite Belt (WKB; Hulbert *et al.*, 1994). The komatiites are exceptionally well preserved and have received precious little attention in the academic literature. Their ∼1.9 Ga age places them in the komatiite-poor Proterozoic aeon, and presents an excellent opportunity to begin to fill large temporal gaps in the komatiite record. Compositionally and thermally, the Winnipegosis komatiites form intermediaries between Archaean komatiites and modern picrites, and between the Al-depleted and Al-undepleted komatiite types, providing an invaluable opportunity to investigate the factors driving differences between these various rock types. The main aims of this thesis are as follows:

1. To describe the WKB and provide a summary of (largely unpublished) existing data and work on these rocks.

2. To petrographically characterise the available samples from the WKB, with an emphasis on textures in massive komatiite flows and why some flows differentiated and others did not.

3. To provide a definitive age for the WKB, and place the Winnipegosis komatiites in the context of the broader regional geology.

4. To geochemically characterise the Winnipegosis komatiites and outline the processes required for their formation.

5. To devise a tectonic model that can explain the formation of komatiite during the Proterozoic, and discuss this in relation to Proterozoic mantle potential temperatures.

6. To investigate controls on the PGE systematics of the Winnipegosis komatiites, and how these influence the interpretation of temporal trends in the PGE contents of komatiite source regions.

7. To produce a comprehensive crystallisation model for the Winnipegosis komatiites, and link this to the generation of basalts and dunites in the same greenstone belt.

This chapter (Chapter 1) aims to review the existing data and available samples from the WKB, and act as an introduction to the rocks of the WKB that will form a basis for subsequent chapters. The regional geological setting and tectonic processes in operation at the time of WKB formation are outlined in Section 1.2. A description of the large number of samples and existing data available for this thesis, along with summaries of published and unpublished core logs is given in Section 1.3. Section 1.4 contains detailed petrographical descriptions of the major rock types, with a particular focus on the komatiites. The quality of a large, unpublished database of WKB geochemistry from the Geological Survey of Canada ('GSC database') is assessed in Section 1.5, and some preliminary results from this database follow in Section 1.6. Finally, some interpretations of the petrographical observations in relation to the formation of massive and differentiated komatiite flows are given in Section 1.7. Much of the interpretation of the results presented in this chapter is reserved for Chapters 2, 3, and 4.

New bulk rock geochemical data and olivine and chromite chemistry for the Winnipegosis komatiites, and zircon U-Pb dating of associated mafic rocks is presented in Chapter 2. Geochemical data is used to calculate parental melt compositions and temperatures of crystallisation of the Winnipegosis komatiites, and argue that these rocks represent komatiites (*sensu stricto*). These data are further used to understand processes such as crustal contamination, metamorphism, and liquid-crystal mixing that influenced their geochemistry, and compare the Winnipegosis komatiites to previously studied komatiite localities. The new U-Pb age for the WKB is combined with geochemical observations to argue that the Winnipegosis komatiites form part of the Circum-Superior Belt, and a model for their formation that satisfies the available geological and geochemical evidence is presented.

Platinum Group Element (PGE) abundances and Re-Os isotopic data for the Winnipegosis komatiites are presented in Chapter 3. A whole rock Re-Os isochron suggests the komatiites are the same age as the mafic rocks dated in Chapter 2, and that the PGE systematics of the komatiites were relatively undisturbed. PGE abundance data are used to calculate the PGE contents of the Winnipegosis komatiite parental melt, and in depth geochemical modelling is employed to investigate how PGEs are fractionated between komatiites and their mantle sources. The results of this modelling are compared to a compilation of komatiite whole rock major- and platinum group-element data to question whether komatiite PGE abundances can be used as a proxy for the PGE abundances of the mantle sources. Finally, the implications for models of Earth accretion are discussed.

New bulk rock major element data for dunites and basalts from the WKB is presented in Chapter 4, along with mineral chemistry of clinopyroxene from the Winnipegosis komatiites. These data are combined with geochemical data and calculated parental melt compositions from Chapter 2, and trace element data for the basalts from the GSC database, in an attempt to investigate the relationships between the different types of igneous rocks in the WKB. Thermodynamic modelling is tested against observations of komatiite bulk rock and mineral geochemistry, before being used to model whether WKB komatiites, basalts, and dunites can be related by crustal differentiation processes (such as fractional crystallisation). The results of this modelling are used to reconstruct the petrogenesis of the WKB igneous sequence, and answer long standing questions regarding the relationship between tholeiitic and komatiitic rocks.

1.2 Geological Setting

The Winnipegosis Komatiite Belt (WKB; Hulbert *et al.*, 1994) is located in the Superior Boundary Zone, in Manitoba, Canada, adjacent to the subsurface extension of the Thompson Nickel Belt (Figures 1.1, 1.2). The Superior Boundary Zone lies along the northwestern margin of the Archaean Superior Craton, and forms a narrow foreland marking the eastern extent of deformation associated with the $\sim$ 1.8 Ga Trans-Hudson Orogen (e.g., White *et al.*, 2002). The Trans-Hudson Orogen was formed during the closure of the Manikewan Ocean (Stauffer, 1984), and resulted in the juxtaposition of the Superior Craton with the amalgamated Rae and Hearne Cratons, and a number of continental fragments including the Archaean – Palaeoproterozoic Sask Craton (Lucas

et al., 1993; Corrigan *et al.*, 2009). The Trans-Hudson Orogen is similar in size and tectonic architecture to the modern Himalayan orogen, and recent discovery of eclogite in the Trans-Hudson confirms it was formed by modern-style plate tectonic processes (Weller & St-Onge, 2017). Closure of the Manikewan Ocean is believed to have begun by 1915 Ma, as evidenced by the oldest oceanic arc rhyolites in the juvenile portion (Reindeer Zone) of the Trans-Hudson Orogen (Baldwin *et al.*, 1987). However, arc-related rocks are not apparent along the western Superior margin until the ca. 1.89 Ga initiation of magmatism in the Snow Lake Arc, interpreted as a pericratonic arc outboard of the Superior Boundary Zone on the basis of negative ϵNd and inherited Archaean zircon grains (David *et al.*, 1996; Percival *et al.*, 2005; Corrigan *et al.*, 2009).

Bimodal mafic/ultramafic and felsic magmatism within the Thompson Nickel Belt at ca. 1.88 Ga (Heaman *et al.*, 1986; Hulbert *et al.*, 2005; Heaman *et al.*, 2009) and mafic/ultramafic magmatism in the WKB at ca. 1.87 Ga (Section 2.4.3) are contemporaneous with ongoing magmatism in the Snow Lake Arc and continued closure of the Manikewan Ocean, implying their formation along a convergent margin (Corrigan *et al.*, 2009; Heaman *et al.*, 2009). Due to their age and predominance of mafic magmatism, the Thompson Nickel Belt and WKB are widely considered to form part of the Circum-Superior Belt (CSB; Baragar & Scoates, 1981; Heaman *et al.*, 1986, 2009; Minifie *et al.*, 2013; Ciborowski *et al.*, 2017), a ~3000 km long ca. 1.88 Ga bimodal magmatic system that wraps around the northern and western margins of the Superior Craton. In addition to the Winnipegosis Komatiites, the CSB features rocks of komatiitic affinity at several widely spaced localities, including the Ottawa Islands (Arndt *et al.*, 1987), Cape Smith Belt (Hynes & Francis, 1982; Lesher, 2007), and the Fox River Belt (Minifie *et al.*, 2013). The CSB is considered a Large Igneous Province (LIP; Ernst & Bleeker, 2010), though interpretations of its mode of formation are divided (e.g., Heaman *et al.*, 2009; Minifie *et al.*, 2013).

Arc magmatism and associated sedimentation continued in the juvenile Reindeer Zone of the Trans-Hudson Orogen until ca. 1.82 Ga (Machado *et al.*, 1999; Hollings & Ansdell, 2002), before the terminal collision of the Superior craton with the Rae, Hearne, and Sask cratons, and other amalgamated terranes at ca. 1.83 – 1.80 Ga (Ansdell *et al.*, 1995; Corrigan *et al.*, 2009).

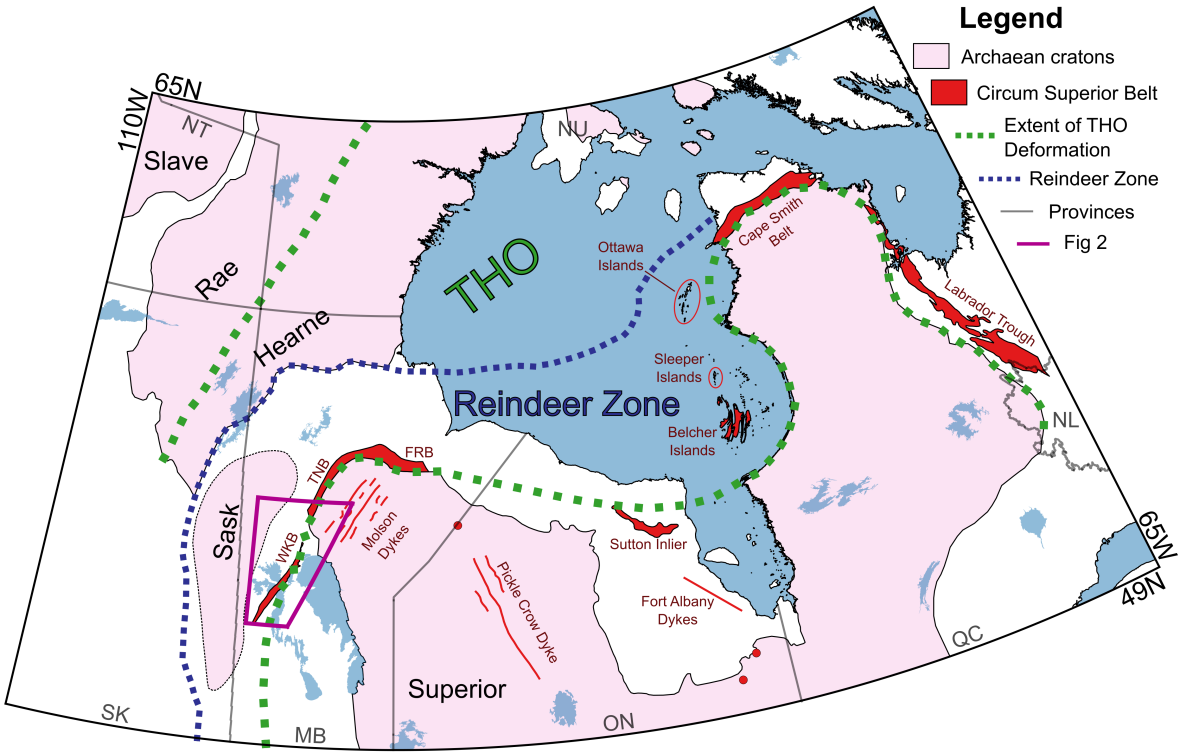

Figure 1.1: Location of the Winnipegosis Komatiite Belt in relation to the Circum-Superior Belt (CSB) and Trans-Hudson Orogen (THO), modified from Baragar & Scoates (1981), Corrigan (2012), and Minifie *et al.* (2013). CSB exposures on the Ottawa and Sleeper Islands are circled, as they are too small to appear on this map. CSB related mafic dykes are identified as thick lines, widths are not to scale. Red dots mark locations of Circum-Superior related carbonatite complexes. Boundaries of cratons and CSB shown are surface exposures except Sask craton and WKB, which are have little and no surface outcrop respectively; approximate subsurface extents identified geophysically are shown. All other geology is not subdivided (white areas). Blue areas indicate water bodies. WKB = Winnipegosis Komatiite Belt, TNB = Thompson Nickel Belt, FRB = Fox River Belt.

1.2.1 The Winnipegosis Komatiite Belt

The WKB lies beneath 120 – 500 m of Palaeozoic cover (McGregor, 2011), and was first identified as a $\sim$ 150 $\times$ 30 km linear magnetic high in the southern, subsurface extension of the Superior Boundary Zone, centred beneath Lake Winnipegosis (Hulbert *et al.*, 1994). Use of the local term 'Thompson Nickel Belt' for the entire Manitoba portion of the Superior Boundary Zone is avoided here as previous studies have stressed that the WKB and Thompson Nickel Belt (*sensu stricto*) are not cogenetic. During the 1990s Cominco drilled 27 geophysical targets within the belt as part of an exploration program for Thompson Nickel Belt style Ni-Cu deposits (McGregor, 2011). The

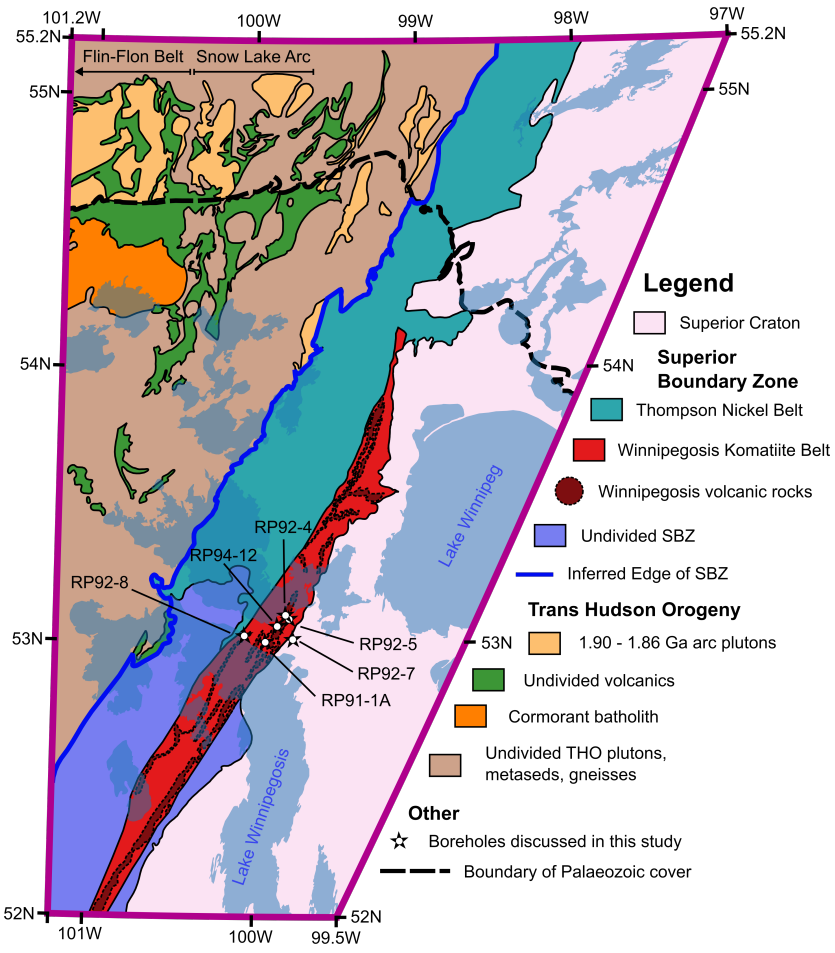

Figure 1.2: Map of the Superior Boundary Zone on the Western Superior Craton, modified from McGregor (2011) and Corrigan (2012). The portion of the map south of the thick dashed line lies beneath Palaeozoic cover: burial depth increases to southwest. Units in this region are interpreted based on aeromagnetic signatures supplemented with borehole data; 1.90 – 1.86 Ga arc plutons are only identified where aeromagnetic signatures match those in outcropping parts of Flin Flon – Snow Lake Belt (McGregor, 2011).

magnetic high was found to comprise a greenstone belt dominated by tholeiitic basalt and komatiite, intercalated with subordinate carbonate and shale sediments (Figure 1.3). These overlie a thin interval of discontinuous basal conglomerate and sandstone, which rests unconformably on Superior Craton tonalite dated at 2792 ± 1.6 Ma in borehole RP92-5 (McGregor, 2011). Komatiite was intersected in ten of the 27 boreholes drilled. Lava flow-tops dip consistently to the West (McGregor, 2011). A single borehole (RP92-8) intersected further basaltic rocks structurally up-section from the komatiites. Lucas *et al.* (1996) divided the igneous rocks of the WKB into three suites, from top to bottom: the Upper tholeiite, Winnipegosis komatiite, and Grand Island

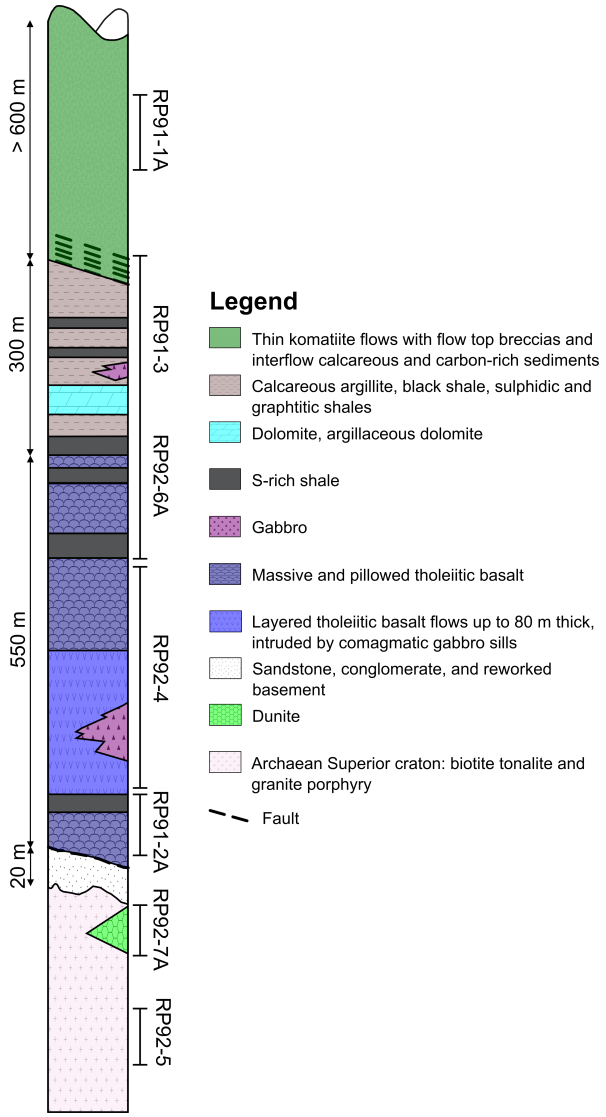

Figure 1.3: Reconstructed stratigraphy of the Winnipegosis Komatiite Belt, based on core logging by Larry Hulbert at the Geological Survey of Canada (Waterton *et al.*, 2017).

tholeiite. However, the Upper tholeiite is similar to the Grand Island tholeiite, and it is not certain whether it represents a stratigraphically distinct unit or a thrust repetition of the sequence (Burnham *et al.*, 2009; McGregor, 2011). The entire belt has undergone sub-greenschist to greenschist facies metamorphism (Section 1.4.3), which likely occurred during the terminal collision phase of Trans-Hudson Orogeny. The lower degree of metamorphism and deformation in the region of the WKB compared to the Thompson Nickel Belt has previously been ascribed to the WKB's position in a re-entrant adjacent to the Thompson promontory (White *et al.*, 2002; Ansdell, 2005).

1.3 Sample availability and core descriptions

A large body of samples used during previous characterisation of the rocks by both Cominco and the Geological Survey of Canada (GSC), was obtained from the GSC archives in Ottawa for the work presented in this thesis. Of these, 157 samples were available from borehole RP91-1A, 16 from borehole RP92-7A, 10 from borehole RP92-8, and 77 from borehole RP94-12. In this borehole numbering scheme, 'RP' is the Cominco property name (Rabbit Point), the digits before the dash indicate the year in which the boreholes were drilled, and the final digit(s) and letter represent the hole number in the property. For brevity, these boreholes are referred to as RP1A, RP7, RP8, and RP12 hereafter. Core samples with masses on the order of 10s to 100s of grams, and rock powders with masses on the order of 10s of grams were available for almost every sample. Some rock powder jar lids had cracked during storage and were potentially contaminated by ambient dust in the GSC archives; these may be unfit for geochemical use. Covered thin sections were available for most samples, with polished thin sections available for a limited number of samples. Finally, zircons separated from borehole RP92-4 (RP4) during previous U-Pb work on the Winnipegosis Komatiite belt (Hulbert *et al.*, 1994) were also made available from the GSC geochronology labs (Section 2.4.3). Complete core sections could not be located; previous core logging is used where available (Hulbert *et al.*, 1994; McGregor, 2011). A full list of samples available for further work is given in Appendix A.

A large database (hereafter the 'GSC database') of unpublished geochemical data collected during the 1990s was also made available for this thesis (Larry Hulbert, personal communication, 2013). These data include: whole rock major and minor element data measured by XRF; whole rock Fe_2O_3:FeO, H_2O_t, and CO_2 determined by wet chemical methods; whole rock trace element data thought to be measured by XRF on pressed powder pellets; whole rock Rare-Earth Element (REE) and selected trace element data measured by solution Inductively Couple Plasma-Mass Spectrometry (ICP-MS); whole rock platinum group element (PGE) data analysed by ICP-MS following fire assay separation; *in-situ* mineral analyses by Electron-Probe Micro Analysis (EPMA); stable isotope data ($\delta^{13}C$ and $\delta^{18}O$) for bulk rocks and some mineral separates; and a variety of bulk rock radiogenic isotope data (Rb-Sr, ^{147}Sm-^{143}Nd, and Pb-Pb). Unfortunately, details of the methods used and checks on data quality were not available for the vast majority of data in the GSC database, thus the reliability of the data cannot

be assessed. Furthermore, some of the data (e.g., PGE data) was either consistently close to or below detection limits, and other data appeared quantised, potentially due to errors introduced during copying and storage of the data over ∼20 years. As such, the majority of the GSC data is not discussed in this thesis. However, bulk rock major element, H_2O_t, and CO_2, rare-earth element, and mineral EPMA data show good agreement with new analyses presented in Chapter 2 (Sections 1.5 and 2.4.2). These are used to provide more representative geochemical trends and averages than possible from the smaller number of samples analysed for this thesis.

1.3.1 Borehole RP1A

Borehole RP1A was the first borehole drilled in the WKB, with the objective of testing whether geophysically identified conductors below Palaeozoic cover were due to Thompson Nickel Belt style Ni-Cu sulphide mineralisation. RP1A is a 548 m long borehole that intersected a large section of komatiite. The upper portions of the borehole comprise overburden and extensive Palaeozoic sedimentary rocks, before a sharp, unconformable contact to an underlying, ∼1 m thick zone of ultramafic regolith (all thicknesses given are borehole depths, not stratigraphic thicknesses). Below this regolith is a ∼254 m thick interval of komatiite, the base of which was not reached during drilling (unpublished Cominco drill logs). Previous core logging and petrographical examination of RP1A (Larry Hulbert, personal communication, 2013; Hulbert *et al.*, 1994) identified at least 28 komatiite flows ranging between ∼3 m and ∼36 m in thickness, with a median thickness of 6 m. A mineralised horizon containing up to 1.6 wt% Ni was also discovered towards the base of the borehole. Samples from this borehole cover the entire depth range of komatiite drilled, with the majority comprising unmineralised komatiite, and seven samples available from the mineralised horizon.

1.3.2 Borehole RP4

The Palaeoproterozoic portion of borehole RP4 intersected a ∼286 m thick section of mafic rock from the Grand Island tholeiite. These mafic rocks comprise fine grained and variably sheared tholeiitic pillow basalts, sheet flows, and thick layered flows, metamorphosed to sub-greenschist grade (unpublished Cominco report, 1992). Thin layers of interflow sediments are present, and contain up to 50% sulphide (McGregor, 2011). Zircons separated by Hulbert *et al.* (1994) are likely to have been separated from coarse

grained gabbro from a > 75 m thick layered sill or flow. However, the exact interval from which they were separated is uncertain.

1.3.3 Borehole RP7

Borehole RP7 is a 506 m long borehole drilled to investigate a doughnut-like magnetic feature. Below Palaeozoic cover, a ∼14 m thick zone of ultramafic regolith grades into a > 300 m thick body of dunite, likely intrusive (unpublished Cominco report, 1992). The dunite is serpentinised throughout and is cut by numerous faults, represented by fault gouge and brecciated peridotite. The base of this dunite was not reached during drilling (unpublished Cominco drill logs). The 16 samples from borehole RP7 are all serpentinised dunites and come from a wide depth range in the borehole.

1.3.4 Borehole RP8

Borehole RP8 is the only borehole in the WKB to intersect the Upper tholeiite. Below Palaeozoic cover, core was recovered from a ∼314 m thick section of mafic rock, predominantly tholeiitic pillow basalts, sheet flows, and thick layered flows, and fine grained metabasalts and metagabbros (unpublished Cominco report, 1992; McGregor, 2011). RP8 volcanics differ from those intersected in RP4 primarily due to a higher metamorphic grade of greenschist facies. No record could be found of the depth from which the ten samples from RP8 were taken, though it is assumed that sample number increases with depth, as for the other boreholes from which samples were available. Metabasalts from this borehole are frequently referred to as 'basalts' in this thesis for simplicity.

1.3.5 Borehole RP12

Borehole RP12 intersected a ∼230 m thick section of komatiite, overlain by a thin zone of regolith below Palaeozoic cover. The base of this komatiite was not reached. Unlike for borehole RP1A, this section was not divided into flows during logging, but a prominent spinifex horizon was noted towards the top of the komatiite section (McGregor, 2011). The 77 samples from this borehole span the whole depth range of komatiite that was cored, though RP12 was not as densely sampled as RP1A.

1.4 Petrographical observations

1.4.1 Massive komatiites flows (RP1A and RP12)

Two main types of lava flow were identified during petrographical investigation of the Winnipegosis Komatiites. The first type are massive olivine porphyritic flows, which comprise all of the flows intersected by borehole RP1A, and likely represent the majority of flows in RP12. Olivine and chromite are the only phenocryst phases, and are relatively evenly distributed throughout the depth profile of each flow. There is no large-scale settling of olivine to form a cumulate layer, and no spinifex textures are observed. Olivine phenocrysts most commonly occur as subhedral, equant grains typically 0.1 – 2 mm in length, which may be fractured or rounded, and may show skeletal overgrowths (Figure 1.4). These olivines may contain inclusions of melt or chromite. Olivines also form large (up to ∼10 mm) semi-skeletal grains with large embayments; these are rarer in samples from near the base of flows and do not contain chromite phenocrysts as inclusions. Chromites are found as euhedral microphenocrysts typically $<$ 200 μm across, and commonly form 3 – 100 μm euhedral or rounded, equant inclusions within olivine phenocrysts.

Clinopyroxene, devitrified glass, and pseudomorphs after olivine can be found as groundmass phases throughout the massive flows. Clinopyroxene is well preserved in most samples, with even extremely fine grained clinopyroxene spherulites and dendrites retaining primary optical continuity and extinction features. Glass in most samples appears brown to black in colour and somewhat opaque. Individual grains in the devitrified material are commonly optically unresolvable. However, an extensive search for remnants of primary glass using backscattered electron (BSE) imaging and wavelength dispersive spectroscopy (WDS) found that the glass phase was pervasively devitrified. The opacity of the devitrified glass is attributed to the formation of sub-microscopic crystal of magnetite, of which larger grains can be seen in the more altered samples. Groundmass olivine, including skeletal overgrowths on phenocrystic olivine, skeletal fragments, hopper olivines, and chain olivine dendrites, is pervasively serpentinised, but is referred to as groundmass olivine below for simplicity.

Despite the same groundmass phases being encountered in most samples, their size and habit varies significantly with depth in each flow. To aid the description of these textural variations, massive flow samples were divided into four main types. The divisions between these textural types are arbitrary and gradational; intermediate textures

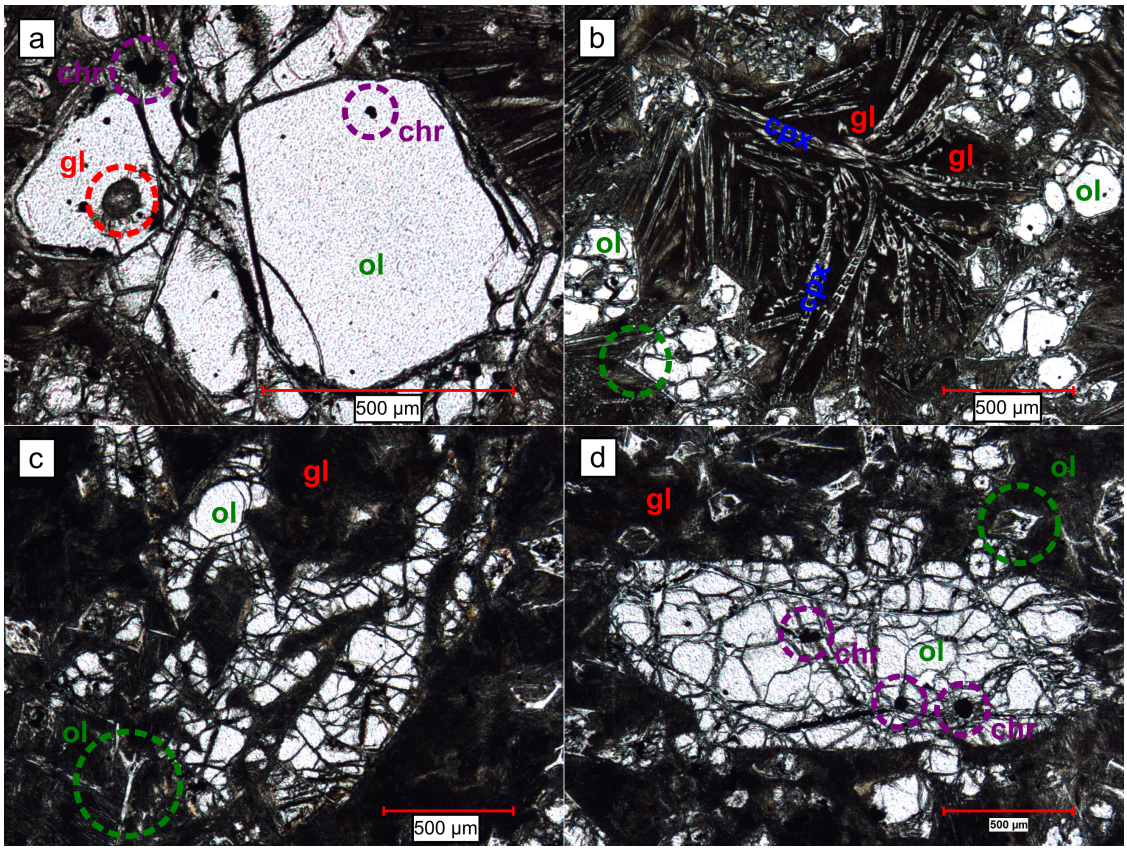

Figure 1.4: Photomicrographs of olivine and chromite phenocrysts in plane polarised light (PPL), with olivine ('ol', green), chromite ('chr', purple), clinopyroxene ('cpx', blue) and glass ('gl', red) labelled. a) Well preserved olivine phenocryst from samples RP1A-111 with rounded melt inclusion (red circle, labelled 'gl') and a small euhedral chromite inclusion. This included chromite was used for Al-in-olivine thermometry (Section 2.3.2). Chromite phenocrysts are also visible in close association with, but not included in, the olivine. b) Subhedral olivine phenocrysts from 'type 1' sample RP1A-66, showing serpentinised skeletal overgrowths (e.g., circled in green). Olivines set in a matrix of clinopyroxene dendrites and devitrified glass (brown). c) Large, embayed, semi-skeletal olivine phenocryst from 'type 3' sample RP1A-4, surrounded by serpentinised skeletal olivine fragments in a matrix of devitrified glass and extremely fine grained clinopyroxene. d) Large olivine grain from 'type 2' sample RP1A-99, with serpentinised cracks and inclusions of both euhedral and rounded chromite. Also visible are serpentinised hopper olivines, set in a matrix of devitrified glass and clinopyroxene.

can generally be identified between the different types.

Type 1 samples

Type 1 massive flow samples are identified on the basis of their large clinopyroxene dendrites and extensive patches of devitrified glass (Figures 1.4b, 1.5, 1.6). Clinopy-

roxene dendrites are typically < 200 μm but rarely range up to 1 mm wide; lengths are typically dictated by spacing between olivine phenocrysts. Clinopyroxene is also found as delicate 'plumose' growths in the groundmass (Figure 1.5b). Olivine phenocrysts are typically small < 500 μm, rounded, and fragmented compared to other textural types, frequently showing skeletal overgrowths. Groundmass olivine is rare, and exists as skeletal fragments (frequently chevron shaped; Figure 1.6). Clinopyroxene dendrites generally do not appear to nucleate on olivine phenocrysts, often appearing to terminate before olivine crystals. However, there is some evidence of small cpx overgrowths on skeletal olivine fragments (Figure 1.6)

Type 2 samples

Type 2 samples (Figures 1.4d, 1.7, 1.8) are distinguished from type 1 samples by a much greater proportion of skeletal hopper olivine, and the appearance of rare chain olivine dendrites (Figure 1.7). They generally contain much finer grained clinopyroxene dendrites, which form straight, parallel, optically continuous arrays in the groundmass (Figure 1.8). This reduction in clinopyroxene dendrite size is accompanied in a reduction in the size of glass patches as the spacing between dendrites grows smaller. These samples show a larger range in olivine phenocryst size, including phenocrysts up to 2 mm in length and rare large embayed/semi-skeletal grains (Figure 1.8), which are absent in type 1 samples. Olivine phenocrysts are generally subhedral and not rounded. Intermediate textures between type 1 and 2 are observed in some thin sections, in which the groundmass is dominated by very fine grained clinopyroxene dendrites with relatively abundant hopper olivines, but rare patches show coarser grained clinopyroxene dendrites and glass.

Type 3 samples

Type 3 samples (Figures 1.4c, 1.9) are distinguished from type 2 by a much greater abundance of chain olivine dendrites and hopper olivine. There is a gradational transition between type 2 and 3, as the proportions of dendritic and hopper olivines increase. Clinopyroxene dendrites are also very fine grained, and generally difficult to distinguish from those seen in type 2 samples. However, unlike type 2 samples, patches of coarser grained clinopyroxene dendrites (transitional to type 1 samples) are never seen in type 3 samples, and all large dendrites in this type are pseudomorphs after olivine (Figure 1.9). Large semi-skeletal olivines are also observed in this textural type (Figure 1.4c).

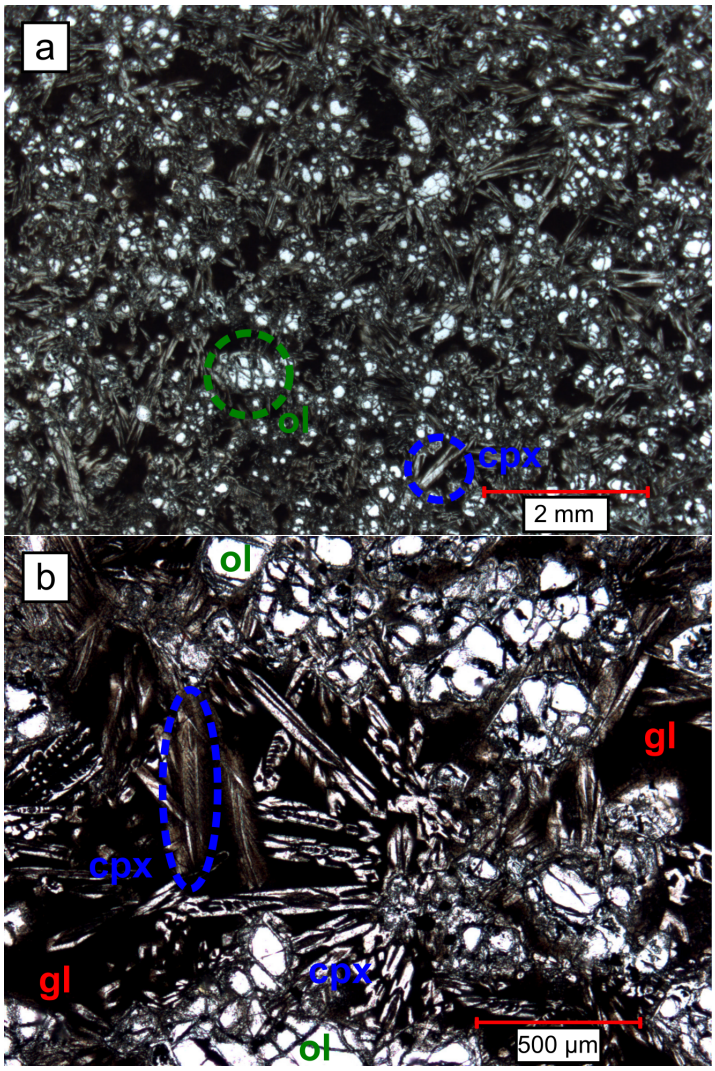

Figure 1.5: PPL Photomicrographs of type 1 massive komatiite samples. a) Wide angle (12.5× zoom) photomicrograph of sample RP1A-30 (∼24 wt% MgO), showing rounded olivines and large, straight cpx dendrites, and large devitrified glass patches. Note relatively low volume of olivine phenocrysts despite high MgO content. b) Clinopyroxene dendrites from sample RP1A-111, showing both large chain or ladder-like dendrites and fine, plumose growths (blue ellipse).

Type 4 samples

Type 4 samples are identified by a continuous 'web' of chain olivine dendrites, not observed in type 3 samples (Figure 1.10). Olivines are typically less than 2 mm in length, and divide patches of exceptionally fine grained dendritic and spherulitic clinopyroxene (on the order of 1 μm wide) and devitrified glass. This olivine 'microspinifex' texture is extremely similar to that seen in the chill margins of Archaean komatiites (Renner, 1989;

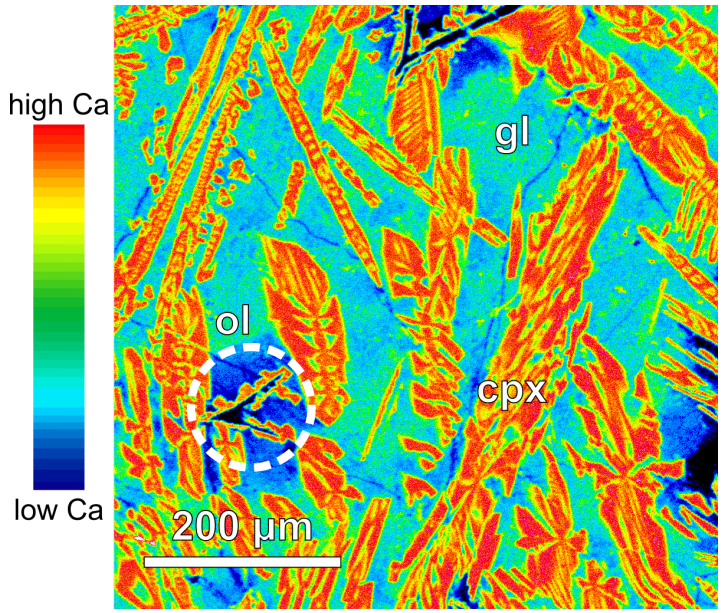

Figure 1.6: Semi-quantitative energy dispersive spectrospcopy (EDS) Ca compositional map from sample RP1A-66. Well preserved dendritic clinopyroxene grains have high Ca cores (red), with fine lower Ca rims (yellow). Very dark blue (Ca-free) chevron shapes (example circled in white) are skeletal olivine fragments, pseudomorphed by serpentine. These are mantled with small cpx growths that appear to have nucleated on them. Micro-crystalline devitrified glass is intermediate in Ca, and appears green/blue.

Arndt *et al.*, 2008). Hopper olivine is rare, and generally shows chain olivine growths extending from its edges. In some samples chain olivine dendrites grade towards shorter, stubbier shapes and fine grain sizes. This may represent an extremely rapid quenching texture. Spherulitic clinopyroxenes form optically continuous sprays with undulose extinction, also indicative of very rapid crystallisation. These can occasionally be seen to radiate from chromite grains, suggesting they sometimes nucleated on this phenocryst phase.

1.4.2 Differentiated komatiite flows (RP12)

'Flow A'

Two strongly differentiated flows are recognised in borehole RP12. The first of these (flow A) is at least 6.7 m thick and located near the top of the komatiite section, with characteristics similar to those observed in basaltic komatiites from the Ottawa Islands (Arndt, 1982). The upper chill margin of the flow has similar groundmass textures to those in the undifferentiated flows (type 4 samples above), although chain olivine

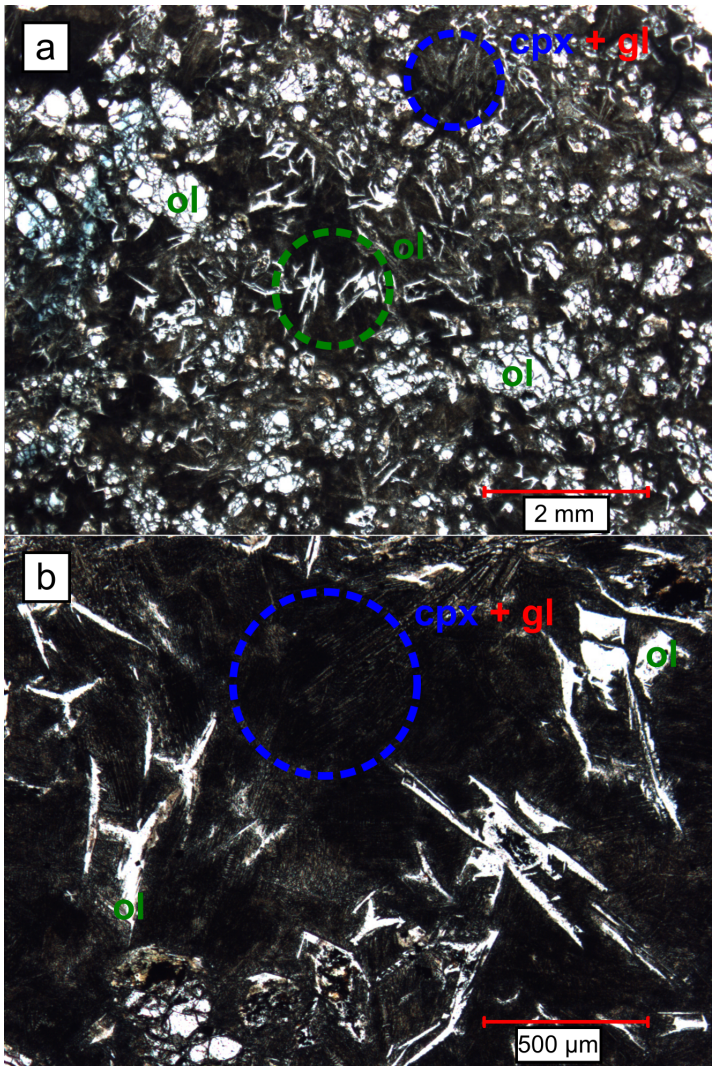

Figure 1.7: PPL Photomicrographs of type 2 massive komatiite samples. a) Wide angle photomicrograph of sample RP1A-1, showing subhedral olivine phenocrysts and serpentinised hopper olivine, set in a groundmass of clinopyroxene and glass. Rare chain olivine dendrites are visible and large glass patches are absent. b) Detail in sample RP1A-1, showing skeletal hopper olivines and fine grained arrays of clinopyroxene dendrites in glass.

dendrites are typically longer, and many olivine phenocrysts are skeletal in habit or have skeletal overgrowths (Figure 1.11a).

Approximately 0.5 m below this chill margin is a $>$ 0.8 m thick phenocryst-free olivine spinifex zone (Figure 1.11b). This spinifex zone retains a 'web' of randomly orientated olivine dendrites dividing patches of finer grain clinopyroxene dendrites and devitrified glass; the main difference from the chill margin is an increase in the length of chain olivine (up to $\sim$10 mm in length) and the absence of olivine phenocrysts. It

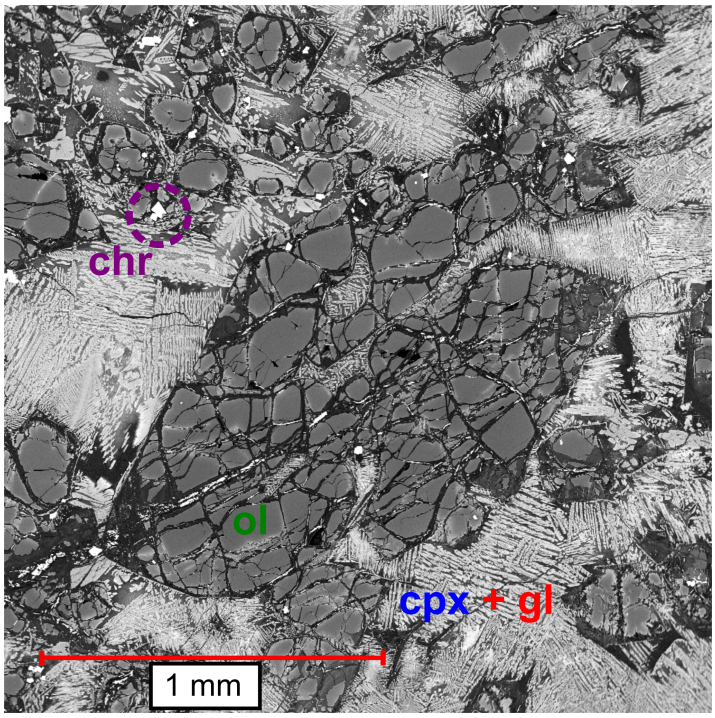

Figure 1.8: Backscattered electron (BSE) map of a large embayed semi-skeletal olivine in a matrix of clinopyroxene dendrites and glass from type 2 massive komatiite sample RP1A-8. Brighter regions indicate high average atomic number, from brightest to darkest: chromite > high Ca clinopyroxene > olivine ∼ devitrified glass > serpentine. Clinopyroxene forms parallel arrays that are optically continuous in cross polarised light. These dendrites are also found in the olivine embayments.

is uncertain whether the transition from chill margin to olivine spinifex is gradational or abrupt due to a lack of intervening samples. Some chromites in this layer show a cruciform habit typical of chromite in spinifex textured komatiites (Figure 1.12; Zhou & Kerrich, 1992; Barnes, 1998).

Less than 1.2 m below the base of this olivine spinifex zone is a > 1 m thick layer of acicular to subhedral pyroxene phenocrysts, < 4 mm in length ('acicular pyroxene zone'), set in a matrix of pyroxene, plagioclase, and small patches of devitrified glass (Figure 1.11c). Phenocryst pyroxene grains have a slightly skeletal habit and 'hollow' appearance due to the presence of fine grained minerals in their cores. Interpretation of the nature of these cores is hampered by alteration of the pyroxene along irregular fractures, but in some cases these cores are continuous with, and texturally similar to, the groundmass; these appear to represent melt embayments resulting from the skeletal crystal habit. Elsewhere, cores of fine grained alteration minerals are isolated and texturally distinct from the groundmass. It is possible that these represent composite

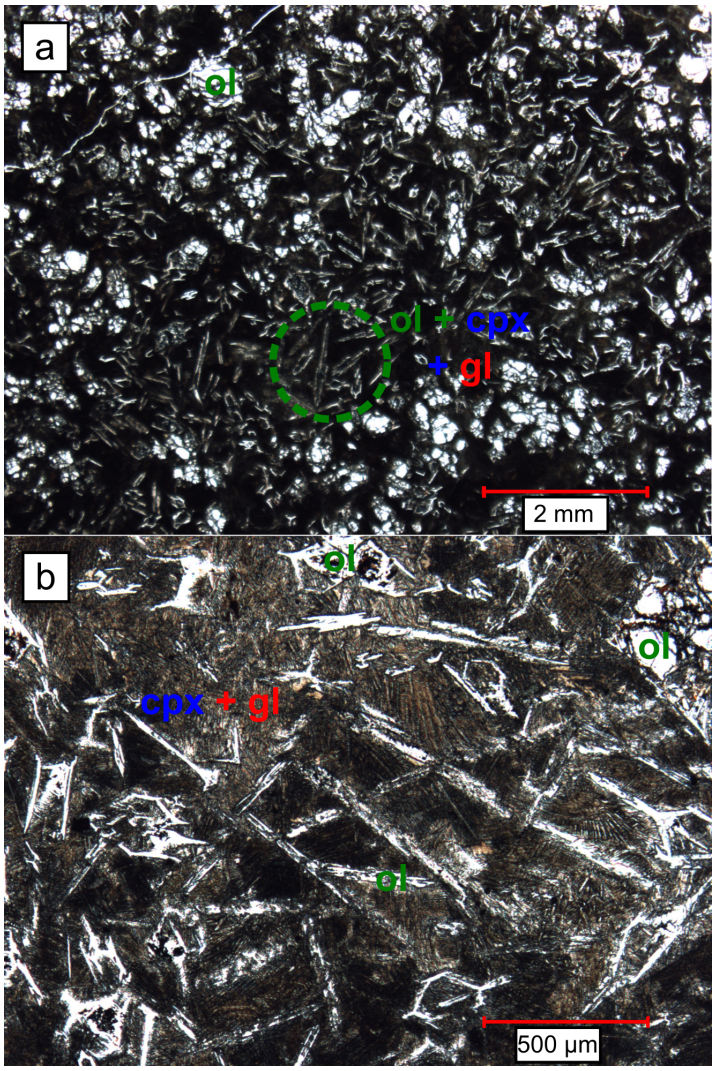

Figure 1.9: PPL Photomicrographs of type 3 massive komatiite samples. a) Wide angle photomicrograph of type 3 samples RP1A-67, showing abundant hopper olivine, with some skeletal grains showing a more elongate habit transitional to chain olivine dendrites. All large dendrites in this image are pseudomorphs after olivine and no large clinopyroxene dendrites are present. b) Hopper and chain olivine from samples RP1A-4, set in a matrix of extremely fine grained clinopyroxene dendrites and glass. Chain olivine dendrites are common but do not form an interconnected web as observed in type 4 samples.

pyroxenes, with altered pigeonite cores mantled by augite (Arndt & Fleet, 1979; Wilson *et al.*, 1989). However, no large chloritised cores similar to those reported by Lowrey *et al.* (2017) are observed, and pigeonite, if originally present, represented a minor and possibly metastable (Arndt & Fleet, 1979) component of the pyroxene grains. This zone corresponds to the 'randomly orientated pyroxene needle' layer that forms the base of

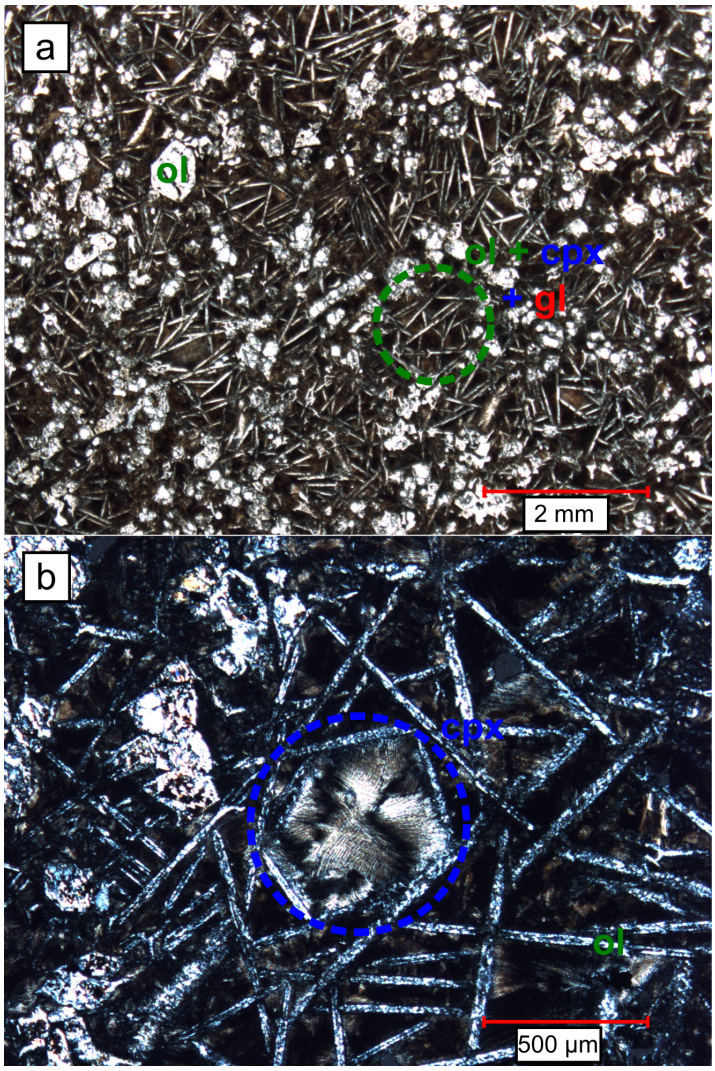

Figure 1.10: Photomicrographs of type 4 massive komatiite samples. a) PPL Wide angle photomicrograph of type 4 sample RP1A-17. All large dendrites are serpentinised chain olivine dendrites, which divide spaces between olivine phenocrysts to produce a web-like texture. Clinopyroxene dendrites are too small to be individually visible, but brown patches between olivine dendrites are extremely fine grained clinopyroxene dendrites and spherulites, and glass. b) Cross Polarised Light (CPL) photomicrograph of RP1A-17 groundmass. Circled pyroxene spherulite shows curving grains and undulose extinction.

the upper flow immediately above the cumulate layer in the Ottawa Island basaltic komatiites (Arndt, 1982).

The lowermost sample obtained from this flow (< 3.2 m from the base of the acicular pyroxene zone) contains large (up to ∼10 mm in length) hopper olivine crystals set in a matrix of clinopyroxene dendrites and glass (Figure 1.11d). Previous core logging

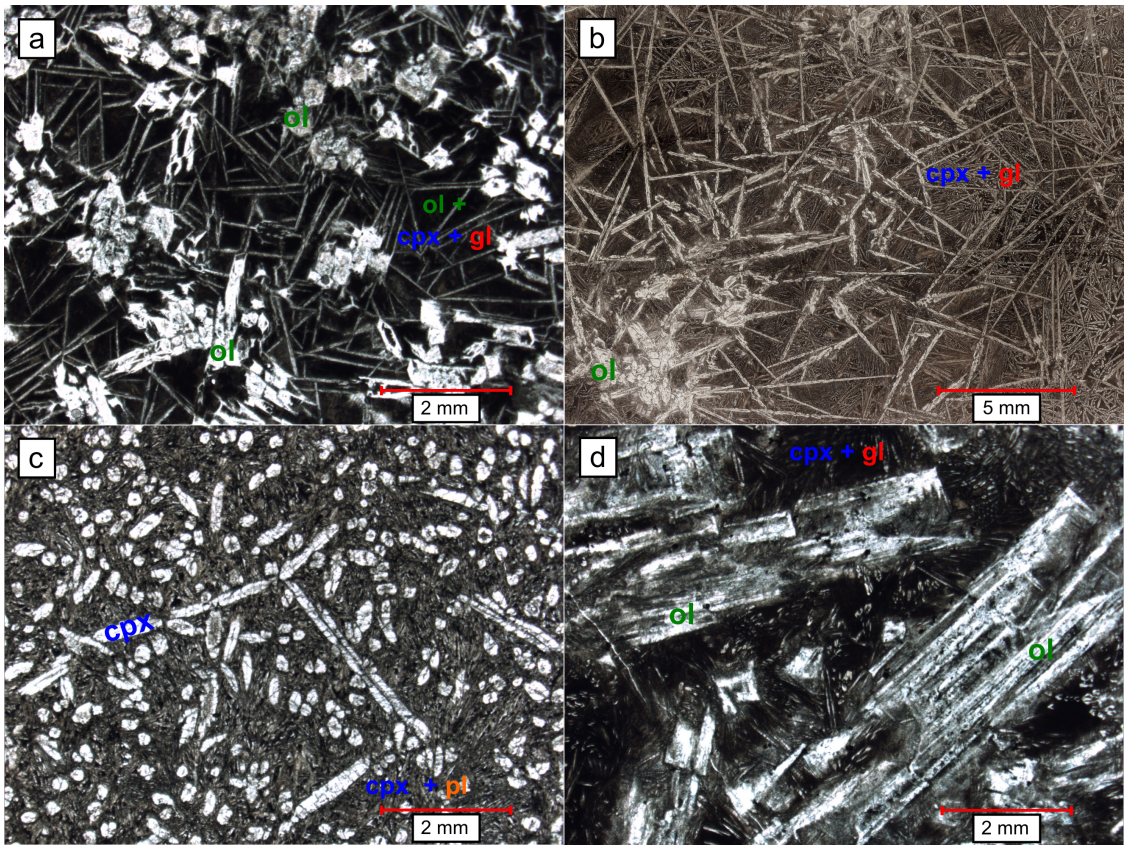

Figure 1.11: PPL photomicrographs and thin section scans of samples from differentiated flow A in borehole RP12. a) Chill margin sample RP12-304.8 showing pseudomorphed granular olivine phenocrysts and hopper olivine in a matrix of chain olivine dendrites, clinopyroxene, and glass. Clinopyroxene dendrites are fine grained and not visible at this scale. b) Olivine spinifex sample RP12-306.1, note larger scale. Long (1 – 10 mm) dendrites are pseudomorphs after olivine, these divide patches of shorter but relatively coarse pyroxene dendrites and glass. c) Acicular pyroxene sample RP12-308.3. Large white grains are semi-skeletal, possibly composite pyroxene grains primarily composed of augite. Darker cores are hollow and continuous with the groundmass in some grains, but elsewhere indicative of alteration, possibly after pigeonite. Mottled brown and white matrix consists of finely intergrown plagioclase and clinopyroxene. d) Hopper olivine cumulate sample RP12-311.5, comprising large pseudomorphed hopper olivine crystals set in a matrix of coarse clinopyroxene dendrites and glass.

indicates a sharp boundary between the acicular pyroxene and hopper olivine layers (McGregor, 2011). This zone is considered the equivalent of the B1 zone of layered Archaean komatiite flows (Arndt, 1982). Though no samples were available from the base of the flow, previous core logging (McGregor, 2011) indicates the presence of an olivine cumulate with approximately 40% olivine below the hopper olivine layer.

Three other olivine spinifex layers are recognised elsewhere in borehole RP12, but

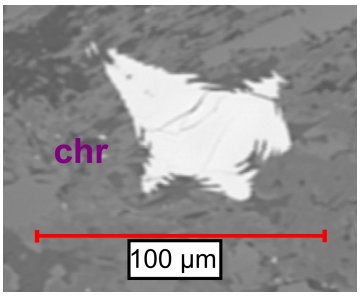

Figure 1.12: Backscattered electron (BSE) map of a cruciform chromite (white) from the olivine spinifex layer in the strongly differentiated flow (sample RP12-306.1).

both are underlain (within < 10 m) by rapidly cooled (type 3 or type 4) massive flow samples. It is unclear whether these represent thinner differentiated flows, flows which did not differentiate as strongly as the two discussed above, or strongly differentiated flows that simply were not sampled throughout.

'Flow B'

The second strongly differentiated flow (flow B) is found lower in the section, and has considerably different characteristics to flow A. Textures at the top of the flow are difficult to identify as uppermost sample was heavily intruded by carbonate veins. However, the least altered parts of this sample have a similar appearance to type 4 chill margin samples from the massive flows.

Less than 2.5 m below this chill margin is a sample with some characteristics similar to both the hopper olivine cumulate and acicular pyroxene samples, but also contains pyroxene spinifex. This sample contains patches with large hopper olivine grains (> 1 mm in length; Figure 1.13a), closely associated with coarse acicular to skeletal pyroxene phenocrysts. Away from these hopper olivines, the sample is dominated by long, narrow pyroxene dendrites, which form a web-like spinifex texture (Figure 1.13b). These are interspersed with shorter pyroxene dendrites. The groundmass comprises fine grained pyroxene and plagioclase throughout. It is possible that this sample represents the base of a pyroxene spinifex zone at the transition to a hopper olivine cumulate below (Silva *et al.*, 1997). Despite these textural differences, this pyroxene spinifex/hopper olivine sample is geochemically very similar to the acicular pyroxene samples from flow A (Figure 1.13, Section 1.6).

The cumulate zone begins less than 1.8 m below this sample. Five samples spanning 7.2 m show relatively consistent olivine phenocryst contents. Most of these sample

have textures similar to type 1 samples from the massive komatiite flows, with coarse pyroxene dendrites or semi-skeletal pyroxene and large glassy patches interstitial to olivine phenocrysts (Figure 1.13c). One sample from near the base of the flow does not contain glassy patches; instead the melt completely crystallised to a fine grained intergrowth of acicular plagioclase and pyroxene. The pyroxene needles appear to have nucleated on existing pyroxene in the groundmass (Figure 1.13d). This texture may represent a particularly slow cooling rate near the base of this flow; experiments using Munro basaltic komatiite compositions suggest that plagioclase can only nucleate at cooling rates below 3 °C per hour (Kinzler & Grove, 1985), and groundmass plagioclase did not crystallise in most Winnipegosis samples.

1.4.3 Metamorphism and alteration of komatiites

Samples from borehole RP1A are generally very well preserved, with approximately one third of samples retaining $\geq 70\%$ fresh olivine phenocrysts. A few samples show virtually no breakdown of phenocrystic olivine except along serpentinised cracks. However, as reported in previous studies of komatiite (Parman *et al.*, 1997), some areas of apparently fresh olivine appear zoned, with Fe increasing towards serpentinised cracks rather than the original crystal edges (Figure 1.14). Waterton *et al.* (2017) interpreted this as a metamorphic effect, due to diffusion of Fe into the olivine and/or diffusion of Mg out of the olivine during serpentinisation. However, it is also possible that this decrease in Fe content measured by EPMA is in fact an analytical artefact caused by rounding of the edges of olivine fragments during polishing. In either case, these rims must be avoided during EPMA analysis of olivine to avoid spuriously low Mg#s (Section 2.4.2).

Groundmass olivine is pervasively altered to talc and serpentine, but clinopyroxene appears stable in most samples, with preservation of even the finest pyroxene dendrites and spherulites. Chromite appears unaltered in most samples, but phenocrysts may show magnetite overgrowths, as previously observed by Arndt & Lesher (1992). Metamorphism is largely restricted to hydration along cracks and veins, and the metamorphic assemblage of serpentine, talc, chlorite and magnetite (plus pyroxene) corresponds to the prehnite-pumpellyite facies of Jolly (1982).

Complete destruction of primary igneous mineralogy is only observed adjacent to large veins, which can be roughly divided into hydrous and carbonate veins. Several generations of each vein type are apparent from cross cutting relationships. Hydrous veins are commonly observed throughout borehole RP1A, and are primarily composed

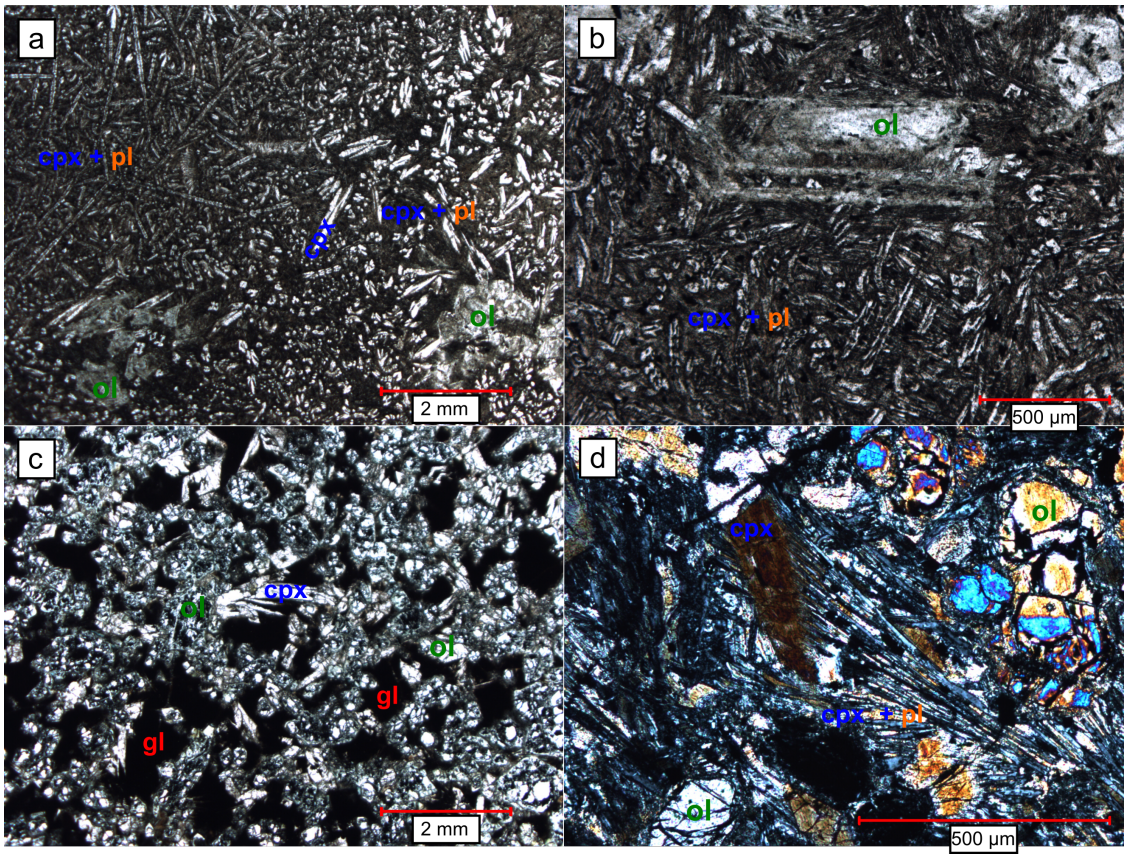

Figure 1.13: Photomicrographs from differentiated flow B in borehole RP12. a) PPL image of the hopper olivine/pyroxene spinifex textured sample RP12-426.7. The upper left part of the image shows a pyroxene spinifex texture defined by long narrow pyroxene dendrites, with interspersed shorter and sometimes curving pyroxene dendrites. The bottom right part of image contains clumps of large, pseudomorphed hopper olivines surrounded by coarse acicular pyroxene grains with a stubbier habit. b) PPL image of a $>$ 1 mm long pseudomorph after hopper olivine from RP12-426.7, surrounded by dendritic pyroxene and set in a groundmass of pyroxene and plagioclase. c) PPL image of typical 'cumulate' texture in sample RP12-428.5, from the lower part of the flow. The texture is similar to type 1 massive flow samples, with coarse, semi-skeletal pyroxene and large glassy patches interstitial to altered olivine phenocrysts. d) CPL image of a fine intergrowth of pyroxene and plagioclase from sample RP12-433.6, with acicular pyroxene appearing to nucleate on a larger pyroxene crystal in the groundmass.

of serpentine, talc, chlorite and opaque oxides (likely magnetite). Deformation features including alignment of talc crystals indicate that these veins formed prior to or during deformation during the Trans-Hudson Orogen. Olivines near the veins are often completely serpentinised and in some cases are replaced by serpentine + chlorite. Sulphide is generally not observed in these veins, but small, $\sim$20 μm sulphides were observed in

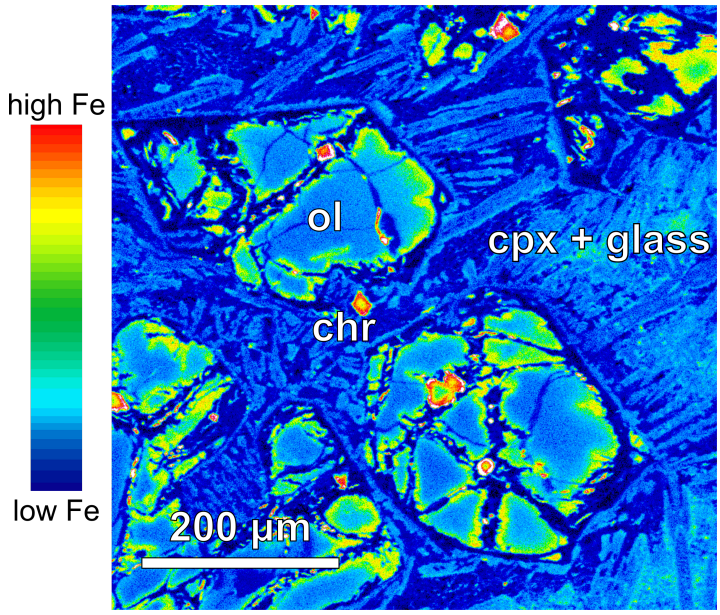

Figure 1.14: Semi-quantitative energy dispersive spectrospcopy (EDS) map of relative Fe content in an olivine from sample RP1A-66. Bright green and red equant grains are chromite with magnetite-rich metamorphic overgrowths. Olivine fragments show low Fe (blue colours) in their cores, zoning to high Fe (yellow) adjacent to serpentinised cracks.

a hydrous vein in sample RP1A-99. Formation of this sulphide bearing hydrous vein may have been associated with Pt and Pd re-mobilisation (Section 3.5.2).

Carbonate veins are more sparsely distributed in borehole RP1A, and tend to be concentrated along certain horizons. The largest of these is the mineralised section identified by Hulbert *et al.* (1994), where Fe, Ni, and Cu bearing sulphides are associated with one of the generations of carbonate veining. Carbonate veins are primarily composed of calcite, also contain significant quantities of quartz and sulphide in the larger horizons. These veins are complex and multi-generational, showing variations in grain size and quartz content, and void-infill textures (Figure 1.15). Carbonate veins often offset or form the cores of hydrous veins, suggesting that they generally formed later. However, calcite and quartz are frequently deformed, showing deformation twins and undulose extinction respectively, indicating that these veins also formed before or during the terminal Trans-Hudson Orogen. Carbonate veins frequently have large alteration haloes, and appear to be associated with oxidation of the primary minerals; for example, groundmass olivine is often psuedomorphed by opaque oxides.

Samples from borehole RP12 are generally more altered, with many samples retaining little or no olivine. Both hydrous and carbonate veins are also observed. Though

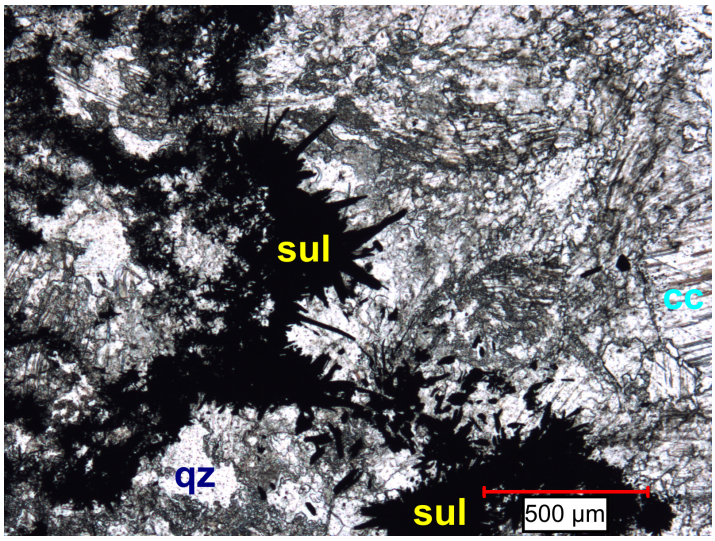

Figure 1.15: PPL photomicrograph of void-filling sulphide ('sul') from a large quartz-carbonate ('qz'; 'cc') vein in the mineralised horizon. Sulphides appear to have grown from a previous vein edge (left side) towards the centre of the vein (right).

some samples appear to preserve up to 80% of phenocrystic olivine, these olivine crystals often have a 'mottled' appearance and contain tiny, unidentified metamorphic grains, suggesting their incipient breakdown. The metamorphic assemblage consists of chlorite, tremolite-actinolite, talc, and magnetite. Although pyroxene is preserved in most samples, it is occasionally replaced by tremolite-actinolite, indicative of lower greenschist facies (Jolly, 1982).

1.4.4 RP7 Dunites

Dunites from borehole RP7 are pervasively altered to fine grained serpentine, brucite, and magnetite, with no primary olivine preserved. Igneous chromite is preserved, but almost ubiquitously overgrown by metamorphic magnetite. However, it can still be distinguished from metamorphic magnetite by its subhedral chromite habit and relatively even distribution in the dunites. Magnetite forms thin, undulating bands dividing large patches of serpentine and brucite; these appear to partially outline a previous cumulate mesh texture (Figure 1.16). This is similar to transitional textures between 'pseudomorphic' and 'non-pseudomorphic' pervasively serpentinised dunite described by Burnham *et al.* (2009). Despite these bands, the incomplete nature of the mesh textures makes it difficult to confidently identify the grain sizes of the primary olivines.

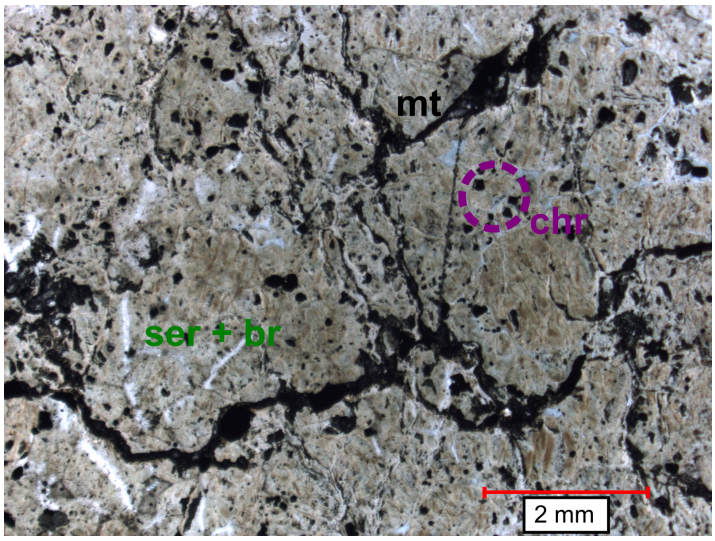

Figure 1.16: PPL photomicrograph of dunite from borehole RP7. Undulating bands of opaque magnetite ('mt') divide large patches of brown-yellow serpentine and brucite ('ser + br'). Magnetite bands may outline the previous cumulate mesh texture. Relict chromites are overgrown by metamorphic magnetite but retain a subhedral chromite habit.

1.4.5 RP8 Metabasalts

Metabasalts from borehole RP8 are green in core samples and pervasively altered to greenschist minerals in thin section. The samples are homogeneous, and no primary minerals or textures are preserved. The greenschist mineral assemblage consists of actinolite, hornblende, epidote, quartz, and sphene, with minor chlorite and opaque oxides. With the exception of epidote, which is present in samples from nearer the top of the the cored section, but absent from samples deeper in the section, the mineral assemblage is consistent throughout. However, the grain size increases considerably with depth in the section, suggesting the deeper parts of borehole RP8 experienced higher peak metamorphic conditions. Quartz veins with minor carbonate were observed in several samples.

1.5 Assessment of GSC database quality

A large quantity of new whole rock major, trace, and transition element data was collected during this thesis, with a particular focus on komatiite samples from boreholes RP1A and RP12. Details of the methods used, and accuracy and repeatability of the measurements is presented in Sections 2.3.1 and 4.3.1. Komatiite data is presented

in Section 2.4.1 and discussed in detail in Section 2.5, and major element data from the RP7 dunites and RP8 basalts is presented in Sections 4.4.1 and 4.4.2. However, the GSC database contains data from a much greater number of samples than it was possible to analyse during this thesis, along with trace element data for RP7 dunites and RP8 basalts that were not analysed for this work. It is therefore desirable to evaluate the quality of the data contained in the GSC database for use in this study. Though details of the methods used and checks on data quality were not available (Section 1.3), all of the samples analysed for this thesis had also been analysed for major, minor, and limited trace elements by XRF in the GSC database; about half of the samples had also been analysed for rare-earth elements by solution ICP-MS, and some RP12 samples had additional trace element data measured by ICP-MS. The quality of the GSC database analyses can therefore be tested against the new precise and accurate major, trace, and transition element data. Plots of GSC data against new data collected for this thesis are shown in Figures 1.17, 1.18, 1.19, and 1.20. Given the demonstrated accuracy and precision of the new analyses (Sections 2.3.1, 4.3.1), data arrayed along 1:1 lines can generally be considered accurate, and lower amounts of scatter corresponds to higher precision data.

1.5.1 Major and minor element XRF data

Major and minor element XRF data from the GSC database generally shows an excellent match to the new data collected for this thesis (Figure 1.17). However, there are a number of exceptions. Elements present in low concentrations, particularly Na_2O, K_2O, and P_2O_5 show more scatter. Though the low-concentration elements K_2O and P_2O_5 are less precise than other elements in the new analyses, repeatabilities of $< 5\%$ (1σ; Section 2.4.1) in the new data cannot explain some of the large degrees of scatter at low concentrations. The observation that some of the GSC Na_2O and K_2O data is recorded as zero suggests that concentrations in some samples were below, or close to, the LOD. It is therefore likely that GSC data for these elements is quite imprecise in low concentration samples. Additionally, GSC P_2O_5 data is systematically high relative to the new data and appears quantised, with small variations about each 'step' only caused by differences in the major element totals used for data normalisation. It is uncertain whether these quanta represent the maximum precision of the method, or an error in data storage or transfer since their analyses. GSC SiO_2 data, particularly for the komatiites and dunites, shows a systematic offset towards higher values compared

to the new data. The sum of GSC CO_2 and H_2O data shows a good match to the new dunite LOI data, though it appears to slightly overestimate the total volatile content at lower concentrations. Finally, data for the dunites generally show more scatter against the new data than data for the komatiites and basalts, even for high concentration elements.

1.5.2 Minor and trace element XRF data

Minor and trace element XRF data from the GSC database is of variable quality compared to new data collected for this thesis (Figure 1.18). Transition metal elements for which the new data was also measured by XRF (Cr and V), show a good agreement with the GSC data. However, Sc, Co, Ni, and Cu, which were measured by XRF on pressed powders pellets in the GSC database, and by ICP-MS for this thesis (due to a lack of sample powder for XRF analysis on pressed powder pellets), show consistently lower values in the GSC data than the new data. This discrepancy can be attributed to uncorrected-for interferences in the ICP-MS data; these elements were up to 10% too high relative to accepted values in repeated measurements of the OKUM certified reference material (Section 2.3.1). The GSC transition metal data may therefore be more accurate than the new data, though this is difficult to evaluate due to the inaccuracies in the new data. However, the degree of scatter, particularly in data from RP1A samples, is far larger than expected given the $\sim$3% (1σ relative) repeatability of the new transition metal analyses by solution ICP-MS, suggesting that the GSC RP1A transition metal data is less precise than the new ICP-MS data. GSC transition metal data shows a similar quantisation to the P_2O_5 data; elements with concentrations of $>$ 1000 ppm in a given sample only vary in increments of 100 ppm, and elements with concentrations between 1000 ppm and 100 ppm appear rounded to the nearest 10 ppm.

In contrast to the transition metal elements, the majority of the data for other trace elements analysed by XRF appears both imprecise and inaccurate. Rb, Nb, and Ba are all widely scattered, show evidence of quantisation, and lie well above 1:1 lines. Zr shows a similar behaviour for RP12 samples, though Zr for RP1A samples is too low relative to the new solution ICP-MS data. Only Sr and Y show a reasonable agreement to the new data, though data for Y is also quantised. As such, the GSC XRF trace element data will not be further used in this thesis.

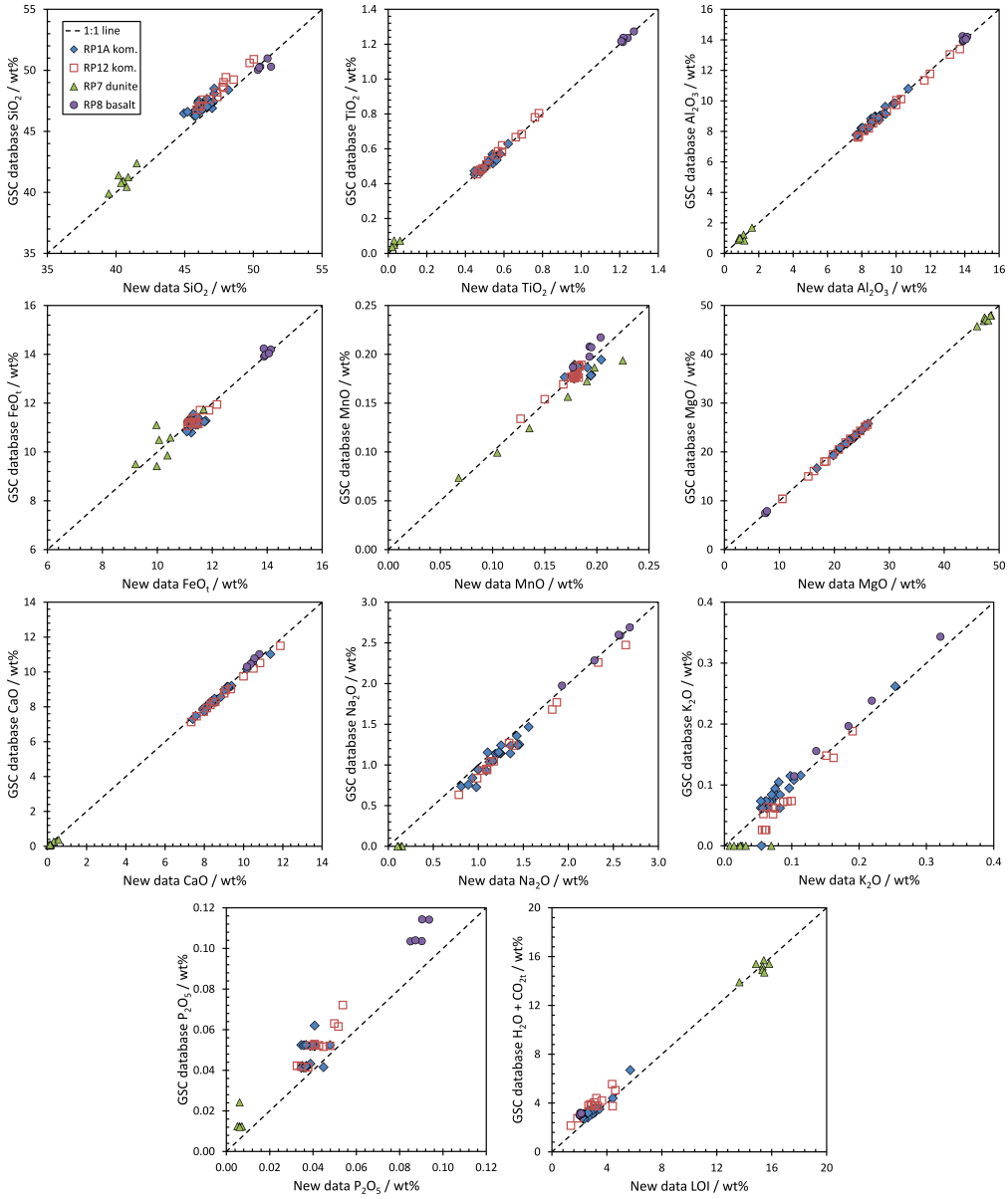

Figure 1.17: A comparison of bulk rock major and minor element XRF data from the GSC database against new bulk rock XRF data obtained for this thesis on the same samples (Sections 2.4.1, 4.4.1, 4.4.2). Accuracy and precision of CO_2 and H_2O data from the GSC database was assessed by comparing their sum (expected to represent the majority of the volatile content of the samples) to the loss on ignition (LOI) from the new analyses.

1.5.3 Trace and rare-earth element ICP-MS data

Solution ICP-MS REE data from the GSC database shows a moderately good agreement to the new solution ICP-MS data from this thesis (Figure 1.19). The data are

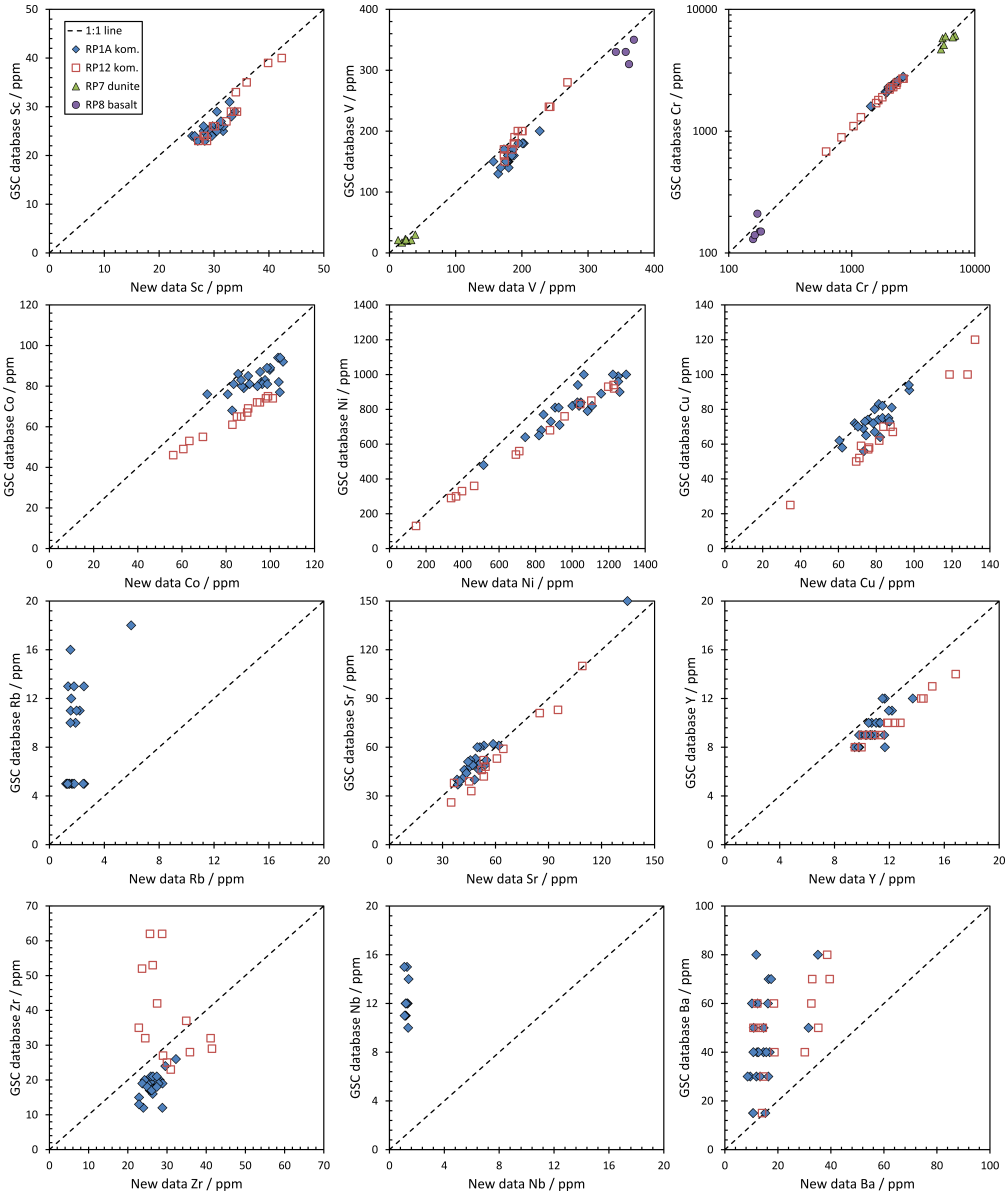

Figure 1.18: A comparison of bulk rock minor and trace element data from the GSC database against new XRF and solution ICP-MS data obtained for this thesis on the same samples (Sections 2.4.1, 4.4.1, 4.4.2). New data for Cr and V was analysed by XRF on $Li_2B_4O_7$ fusion disks; all other elements were analysed by solution ICP-MS with medium resolution employed for the transition elements Sc, Co, Ni, and Cu. Note logarithmic scale for Cr.

accurate, lying close to 1:1 lines, but show a moderate amount of scatter, indicating low precision relative to the new data (repeatable to $\leq 2\%$; 1σ relative). Despite the relative imprecision, these data are likely sufficiently precise and accurate to determine approximate absolute REE concentrations and the shape of REE patterns.

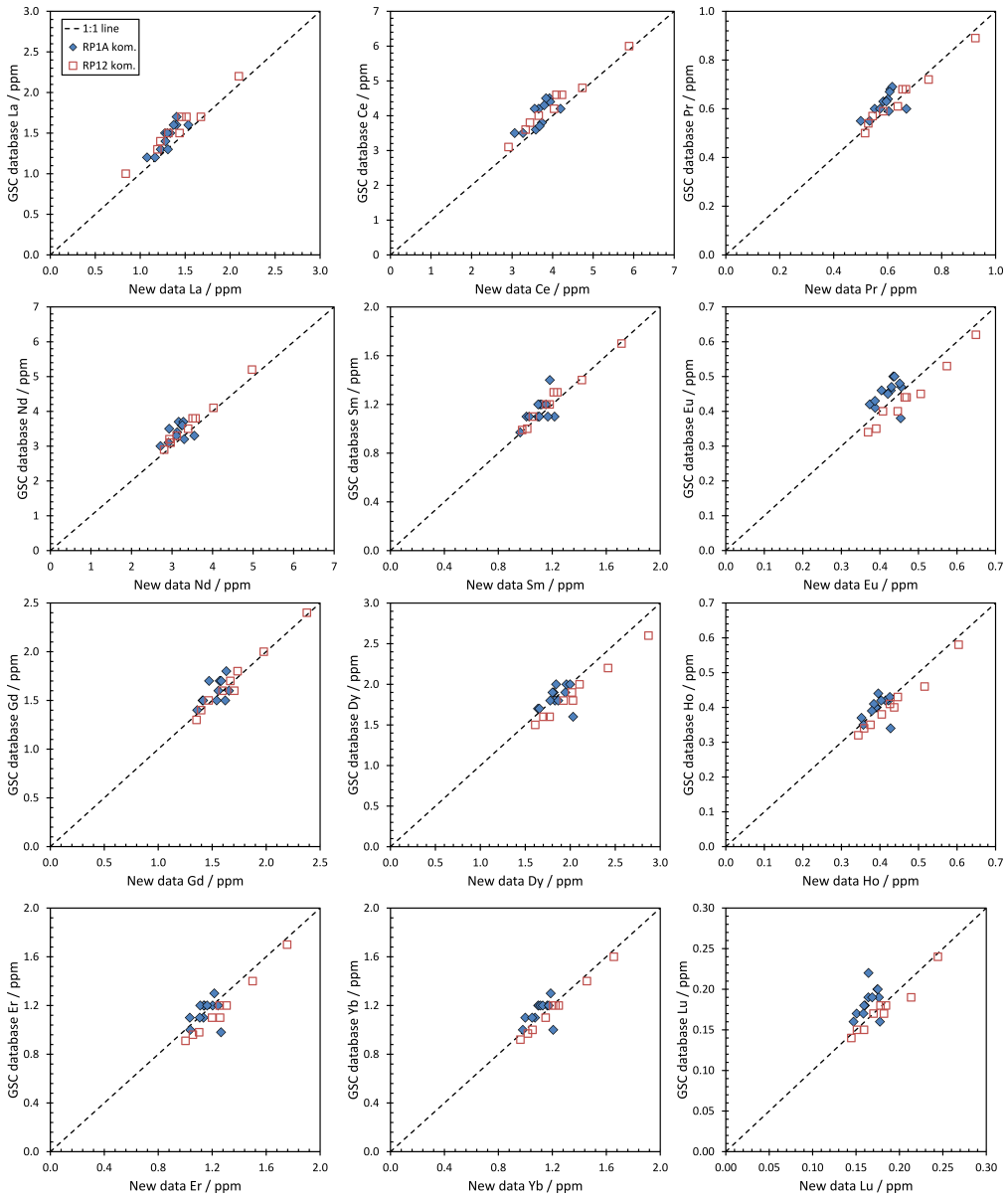

Figure 1.19: A comparison of bulk rock rare-earth element (REE) ICP-MS data from the GSC database against new bulk rock solution ICP-MS data obtained for this thesis on the same samples (Section 2.4.1). Data for Tb is not shown, but shows a similar distribution to Ho.

Additional trace element solution ICP-MS data for RP12 is of variable quality (Figure 1.20). Rb, Y (measured for all samples for which REEs were measured, including some RP1A samples), Nb, and Cs all show good agreement with the new ICP-MS data. However, Hf, Th, and U all show considerable scatter and lie above 1:1 lines, and are considered inaccurate and imprecise.

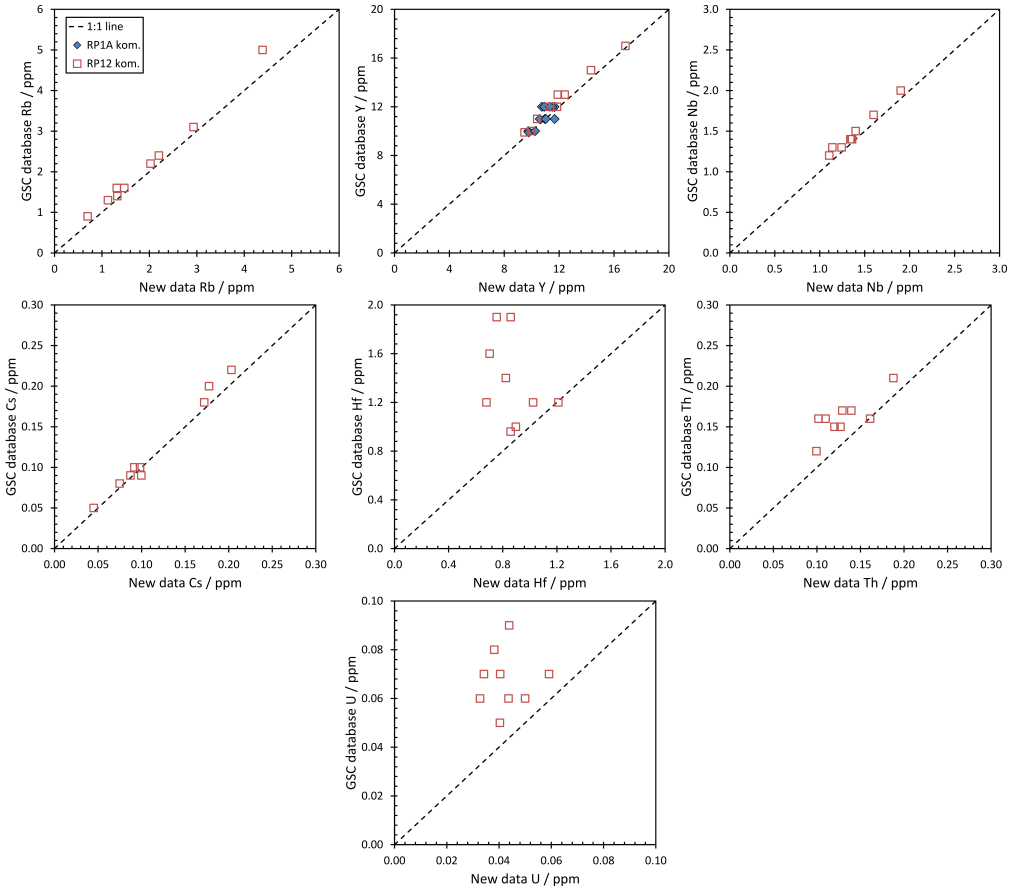

Figure 1.20: A comparison of bulk rock trace element element ICP-MS data from the GSC database against new bulk rock solution ICP-MS data obtained for this thesis on the same samples (Section 2.4.1).

In summary, major and minor element oxides from the GSC database, with the exception of low concentration elements, may be considered precise and accurate. Transition element analyses from the GSC database are likely to be of reasonable quality, though this cannot be ascertained with great confidence. GSC analyses of the REEs, Rb, Y, Nb, and Cs by solution ICP-MS may be of low precision compared to modern analytical techniques, but should give a reasonable indication of elemental concentrations and the shape of REE patterns. All other XRF and ICP-MS trace element data from the GSC database are imprecise and inaccurate and will not be further used in this thesis.

1.6 Geochemical results from the GSC database

1.6.1 Excluding altered komatiite samples

Effects of carbonate veining

Petrographical observations suggest that the most altered Winnipegosis komatiite samples are those intruded by large multi-generational carbonate veins (Section 1.4.3). These can be identified geochemically in the GSC database by elevated CO_2 content, which in the extreme case of the 'mineralised' samples identified by Hulbert *et al.* (1994) can reach CO_2 contents of up to 27.5 wt%. Komatiite samples intruded by these veins form an array between unaltered komatiite with low CO_2 contents and mineralised samples which approach calcite compositions (Figure 1.21).

This addition of calcite may effectively be a 'dilution' process in which calcite is added to the rock without significantly altering the composition of its komatiite host, or it could be associated with significant elemental mobility and exchange between the fluid from which calcite crystallised and the surrounding komatiite. In the case of incompatible elements forming ratios that are invariant during fractional crystallisation and crystal-liquid remixing (Section 2.5.5), such as Al_2O_3/TiO_2, these processes can be distinguished by plotting the ratio as a function of CO_2 content. Figure 1.21 also shows that the Al_2O_3/TiO_2 of komatiites appears approximately constant with increasing CO_2 content, even as the absolute Al_2O_3 and TiO_2 contents fall as the volume sampled is increasingly dominated by calcite. This suggests that, at least for Al_2O_3 and TiO_2, the intrusion of calcite veins effectively diluted the amount of komatiite present in bulk rock samples without significantly mobilising these elements.

However, Al_2O_3 and TiO_2 are among the least susceptible elements to alteration in the Winnipegosis Komatiites (Section 2.5.1), and similar tests cannot be performed for elements that do not form invariant ratios during komatiite crystallisation and subsequent liquid-crystal remixing. Furthermore, even in the unlikely case that carbonate vein infiltration had not significantly altered the host komatiite composition in any way, bulk rock compositions of carbonate veined samples would still need to be corrected for calcite addition. As such, an attempt is made below to screen out samples whose chemistry has been modified by carbonate veining.

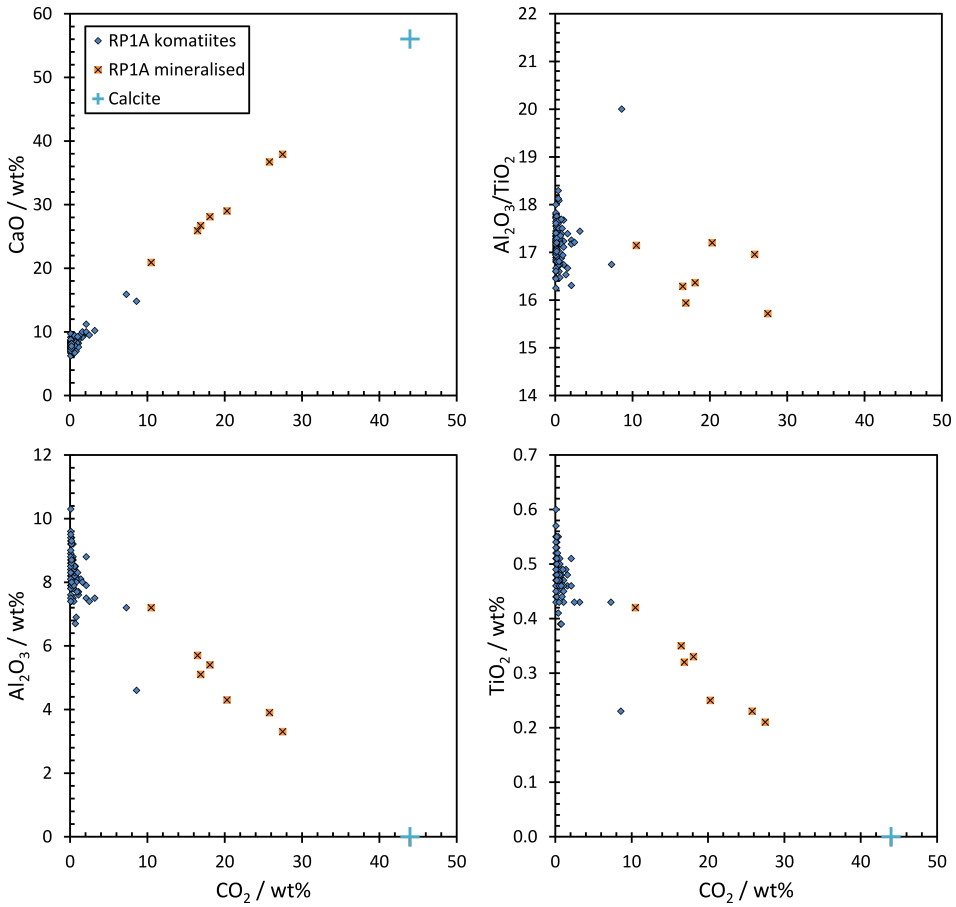

Figure 1.21: Effect of carbonate veining on bulk rock geochemistry. Bulk rock compositions form a trend between low CO_2 unaltered komatiite and calcite compositions on a plot of CaO against CO_2. Al_2O_3/TiO_2 remains approximately constant with increasing CO_2, whereas absolute Al_2O_3 and TiO_2 contents decrease with increasing CO_2, suggesting that Al_2O_3 and TiO_2 were diluted but not significantly remobilised by intrusion of carbonate veins. All major element contents are shown on a hydrous, CO_2 bearing basis, and not renormalised to anhydrous totals.

CO_2 filter

Many elements in Winnipegosis Komatiite samples are arrayed along olivine (or olivine + chromite) control lines when plotted against MgO (Section 2.5.1). As the highest CO_2 samples in the GSC database generally show the greatest deviations from olivine control lines, it is suggested that an optimal CO_2 content for screening out altered samples can be selected by investigating how the scatter about olivine control lines varies with CO_2 threshold value. The regression coefficient (R^2 value) for regressions of various elements against MgO is used as a proxy for scatter around olivine control

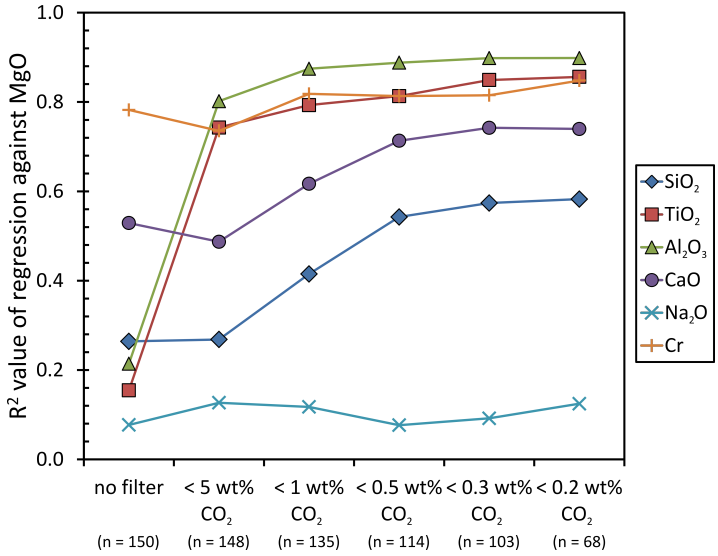

Figure 1.22: Plot of regression coefficient (R^2 value) of olivine control lines (regressions of elements against MgO) for RP1A samples in the GSC database, as a function of CO_2 threshold value. Samples above the CO_2 threshold value are progressively removed from regressions. Samples identified as 'mineralised' by Hulbert *et al.* (1994) are excluded from all regressions.

lines, and plotted as a function of CO_2 threshold value in Figure 1.22. Only samples from the lower metamorphic grade borehole RP1A are used in the regressions.

Progressive removal of high CO_2 samples generally reduces the scatter about olivine control lines (increased R^2 value), though there are some differences in the behaviour of different elements. For conservative elements, such as TiO_2 and Al_2O_3, removal of only the highest CO_2 samples ($\geq$ 5 wt% CO_2) considerably increases the R^2 value of their regressions against MgO. Further removal of the highest CO_2 remaining samples causes little improvement. The least conservative element shown here, Na_2O, shows no improvement with progressive removal of high CO_2 samples, as it does not follow an olivine control line even in relatively unaltered samples (Section 2.5.1). However, the degree of scatter around regressions of CaO and SiO_2 against MgO continues to fall until a CO_2 threshold value of $<$ 0.3 wt% CO_2 is reached. This threshold will therefore be used to select unaltered samples for this thesis, as using a $<$ 0.2 wt% CO_2 threshold excludes many more samples without providing significant improvements to the quality of olivine control lines.

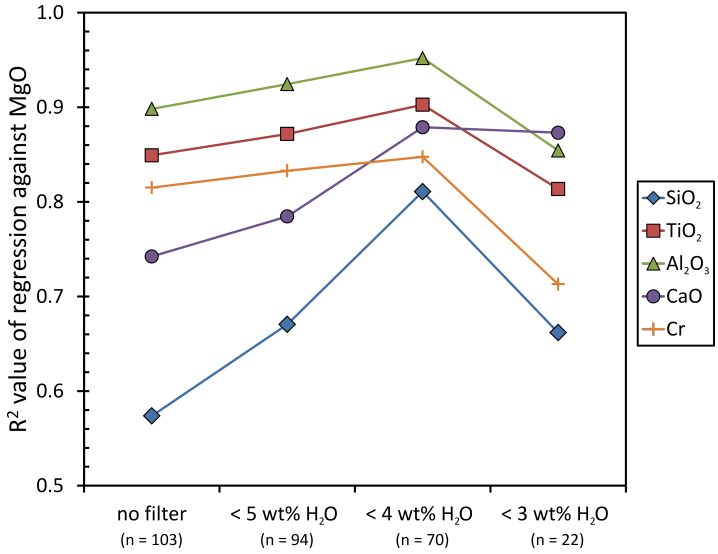

Figure 1.23: Plot of regression coefficient (R^2 value) of olivine control lines (regressions of elements against MgO) for RP1A samples in the GSC database, as a function of H_2O threshold value. Samples above the H_2O threshold value are progressively removed from regressions. Only samples with < 0.3 wt% CO_2 are used in all regressions.

H_2O filter

As Winnipegosis komatiites also contain hydrous veins, a similar filter can be applied based on the H_2O content of samples in the GSC database. As the presence of carbonate veins appears to exert a first order control on komatiite alteration, only samples with $<$ 0.3 wt% CO_2 were considered. The R^2 value for regressions of various elements against MgO is plotted as a function of H_2O threshold value in Figure 1.23.

As with the CO_2 filter, progressive removal of the highest H_2O samples generally increases the R^2 value of regressions. A major exception to this is for a filter of < 3 wt% H_2O, at which point so few samples remain that the R^2 value falls as a consequence of the reduced range in MgO of the remaining samples. Though the R^2 value of the regression of Na_2O against MgO also increased with removal of high H_2O samples, this is not plotted as the less scattered regression still did not correspond to an olivine control line (Section 2.5.1). An optimal threshold value of < 4 wt% H_2O was applied to identify unaltered RP1A samples for this thesis. However, this filter could not be applied to RP12 samples due to their higher metamorphic grade and H_2O contents. Instead, an attempt was made to select samples with as low H_2O contents as possible for reanalysis for this thesis (Section 1.3).

1.6.2 Depth trends in WKB boreholes

RP1A

Geochemical depth profiles constructed using data from the GSC database, and a profile of petrographically estimated olivine alteration, are shown for RP1A in Figure 1.24. Samples with < 0.3 wt% CO_2 show a range of MgO contents between 16.7 and 25.8 wt%; samples with lower MgO are associated with high CO_2 contents and carbonate veining. A 9-point moving average of bulk rock MgO content was constructed to smooth variations due to variable olivine fractionation (Section 2.5.1), using only samples with < 0.3 wt% CO_2. This moving average remains relatively constant around ∼22.5 wt% MgO, and shows no systematic trend with depth. A similar result is obtained by averaging the MgO content of samples with < 0.3 wt% CO_2 in each flow; there is no trend in the average MgO content of flows with depth, and the average MgO content of flows with three or samples with < 0.3 wt% CO_2 shows a limited range between 20.6 and 23.7 wt% (22.5 ± 0.9 wt%, uncertainty quoted as 1σ absolute). As the behaviour of many elements in the Winnipegosis Komatiites are consistent with olivine control (Section 2.5.1), the restricted range and lack of trends in MgO content in RP1A suggests that the composition of erupted komatiite was relatively invariant across all 28 lava flows intersected by this borehole.

Bulk rock Ni contents are also relatively constant throughout borehole RP1A, with the exception of the mineralised horizon identified by Hulbert *et al.* (1994). This horizon contains very high Ni and S contents, up to maximum values of 12000 ppm and ∼9000 ppm respectively, and is associated very high CO_2 contents due to intense carbonate veining. Despite this association with carbonate veins, high Ni and S contents are not found in any other high CO_2 samples; in fact, sample RP1A-34 from the uppermost high CO_2 horizon in Figure 1.24, shows lower Ni and S contents than unaltered komatiite samples. Conversely, high S contents are found in samples RP1A-114 – RP1A-116 (at a depth of ∼465 m), yet high Ni or CO_2 contents are not observed. Alteration in these samples generally appears associated with hydrous veins, with the exception of a single, relatively small carbonate vein in sample RP1A-115. These observations suggest that high CO_2 or S contents alone are not reliable indicators of mineralisation in these komatiites.

Though carbonate veining produced the largest alteration effect on bulk rock compositions (Section 1.6.1), high CO_2 horizons are not always associated with complete

alteration of olivine phenocrysts. Instead, the petrographically estimated percentage of altered olivine phenocrysts appears to show a stronger correlation with H_2O contents. The two largest sections showing complete alteration of olivine phenocrysts, at depths of ∼320 – 355 m, and ∼460 – 480 m, are both associated with high H_2O contents of >5 wt%. This is consistent with the petrographical observations that olivine is predominantly altered to serpentine (Section 1.4.3), and that unaltered olivine phenocrysts can be found even in thin sections dominated by carbonate veining. Considering all three indicator of alteration (CO_2, H_2O, and olivine alteration), the least altered sections of RP1A appear to be near the top of the komatiite sequence (samples RP1A-1 – RP1A-19, depth range ∼274 – 300 m), and near the base of borehole (RP1A-138 – RP1A-154, depth range ∼501 – 524 m).

RP12

Borehole RP12 was not as densely sampled as borehole RP1A, and was not divided into flows during core logging (McGregor, 2011). Furthermore, geochemical data is not available for any of the samples where intense carbonate veining similar to the mineralised section in RP1A was observed petrographically, and some samples for which geochemical data was available do not have corresponding thin sections. Trends in the geochemical data are therefore harder to identify and interpret than in RP1A.

In general, massive komatiite flow samples appear to have similar MgO contents to those in borehole RP1A. There is an apparent drop in MgO content towards the top of the borehole. However, there is insufficient data to determine whether this represents a fall in erupted MgO content or a relative oversampling of the upper portions of differentiated flows. The highest MgO contents are found in cumulate samples from the base of flow B, consistent with a net accumulation of olivine relative to the massive flows.

Samples in RP12 tend to show more evidence of alteration than those in RP1A. Although geochemical data was not obtained for the samples most infiltrated by carbonate veins, H_2O contents lower than 4 wt% are rare, and only the chemically distinct acicular pyroxene samples have $H_2O < 3$ wt%. The proportion of olivine phenocrysts that are altered also tends to be higher; in contrast to RP1A (Section 1.4.3), samples with ≥ 70 % fresh olivine phenocrysts (< 30 % olivine altered) are rare.

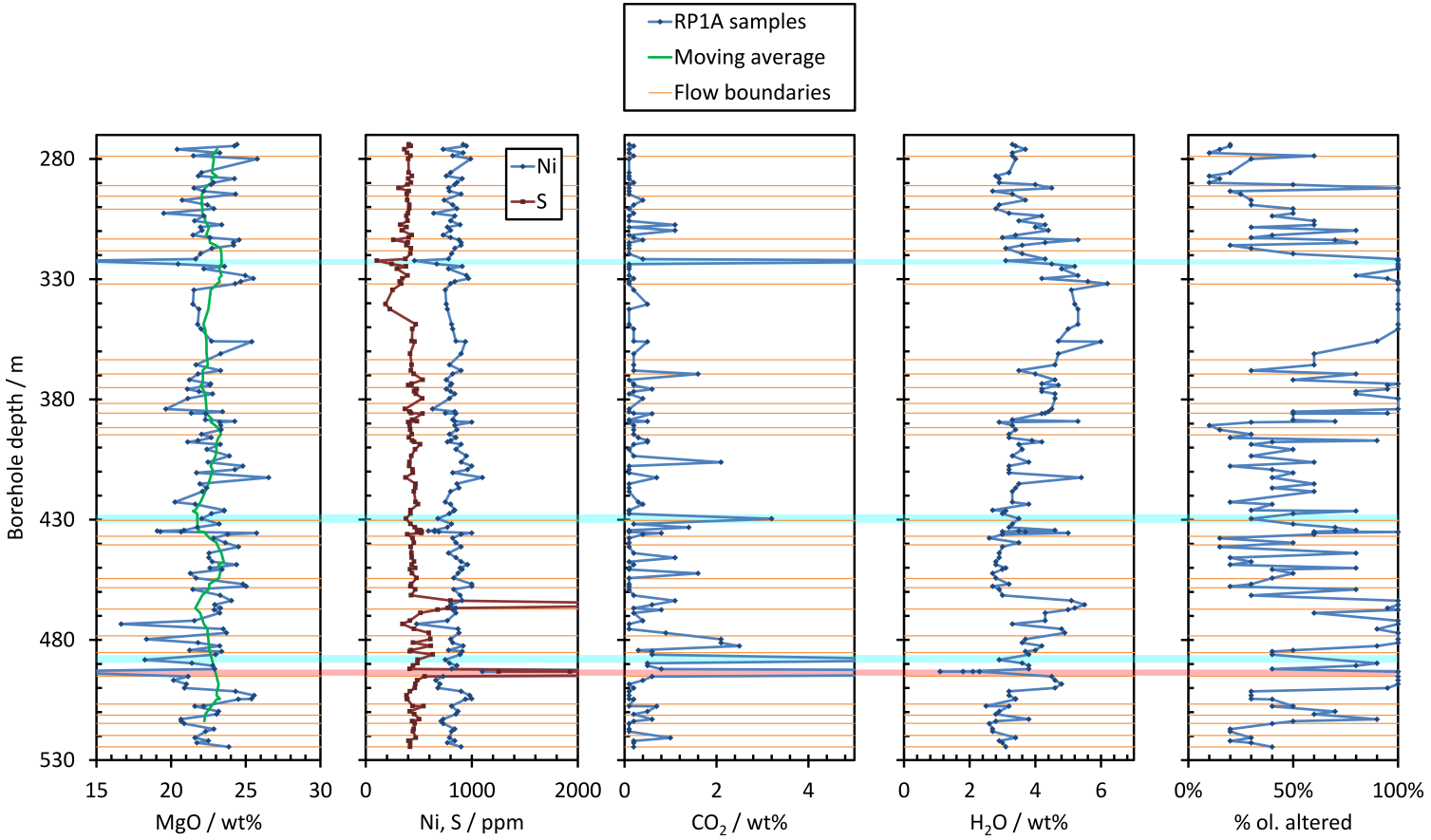

Figure 1.24: Geochemical and petrographical depth profiles for borehole RP1A. Lines joining data from individual samples are to help visualisation and are not intended to imply that the data can be interpolated between sampled locations. Green line in the depth vs. MgO plot is a 9 point moving average from samples with < 0.3 wt% CO_2. Flow boundaries are from logging by Hulbert *et al.* (1994). The red shaded field indicates the mineralised horizon of Hulbert *et al.* (1994); blue shaded fields indicate other horizons with high CO_2 contents that do not show similarly elevated Ni and S contents. '% ol. altered' is the petrographically estimated percentage of olivine phenocrysts that have been serpentinised or otherwise altered to metamorphic assemblages. Groundmass olivine is excluded from this estimate as it was pervasively altered throughout RP1A.

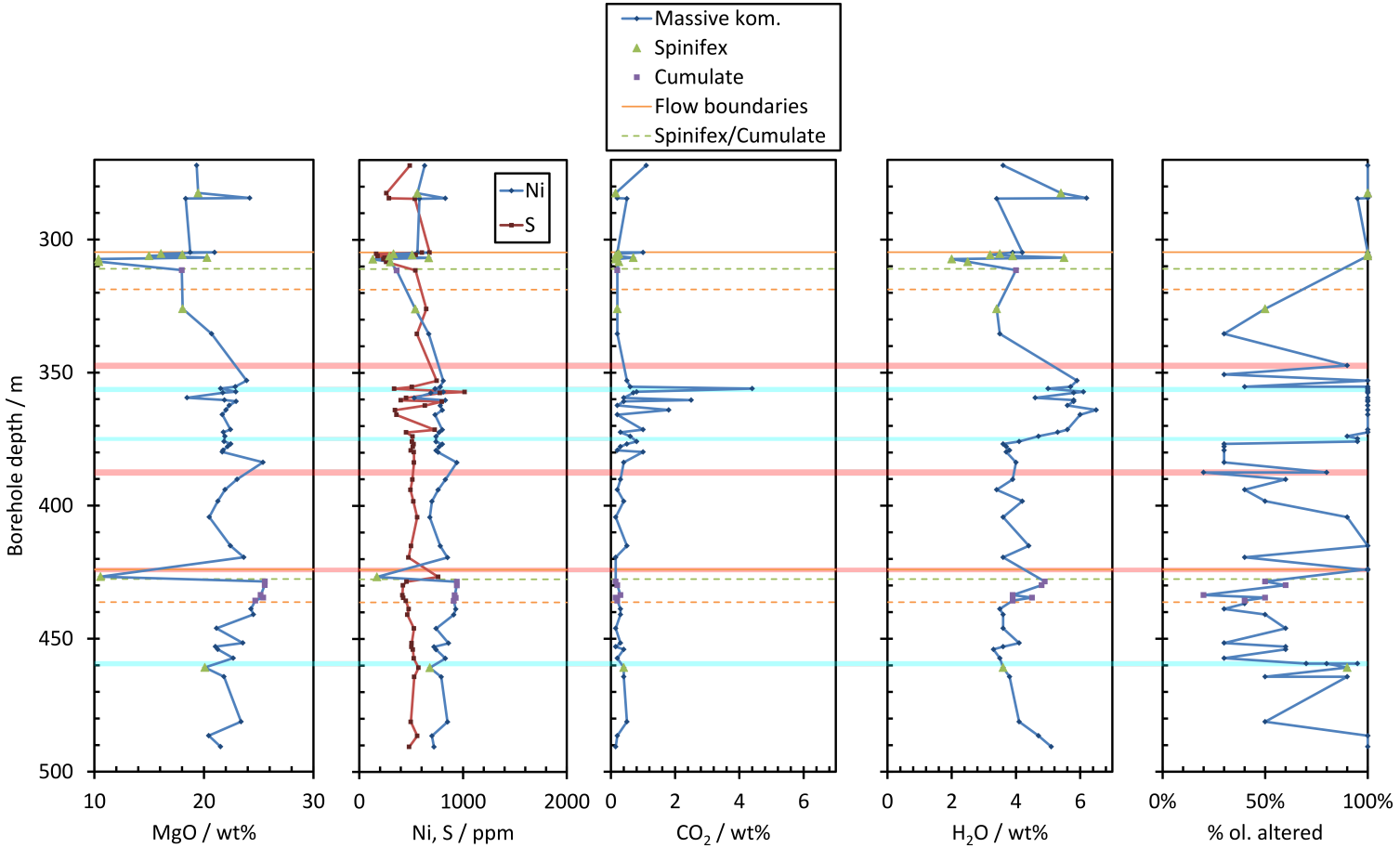

Figure 1.25: Geochemical and petrographical depth profiles for borehole RP12. Symbols as in Figure 1.24, except for identification of spinifex and cumulate samples in differentiated flows. Flow boundaries and boundaries between spinifex and cumulate layers (Spinifex/Cumulate) are from Sections 1.4.2 and 1.7.2, dashed lines indicate uncertainty. Red shaded fields indicate mineralised horizons identified based on petrographically observed sulphide content (as there is no geochemical data for these samples in the GSC database), blue shaded fields indicate carbonate veined samples in which sulphide was not observed.

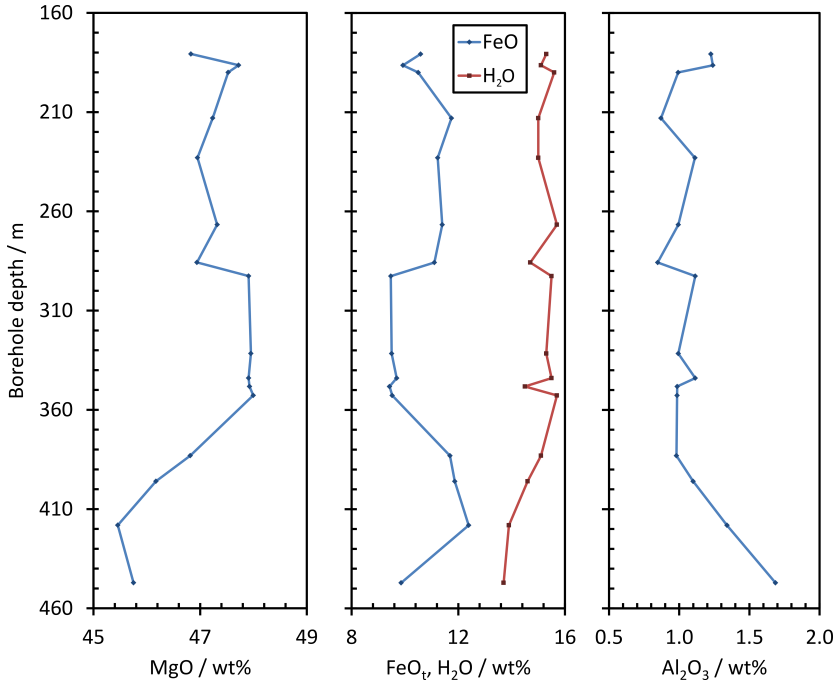

Figure 1.26: Geochemical depth profiles for dunites from borehole RP7.

RP7 Dunites

The dunites intersected by borehole RP7 show a small range in MgO contents between ∼45 and ∼48 wt% (Figure 1.26). MgO contents are highest at the top and middle of the borehole, and show a marked decrease towards the base. This is mirrored by variations in their FeO_t contents, which vary from ∼9.5 to ∼12.5 wt%; higher MgO samples show lower FeO_t. Samples from RP7 also show a trend towards decreasing H_2O contents, and increasing Al_2O_3 contents towards the base of the borehole. Interpretations of these variations are given in Section 4.5.

RP8 Basalts

Though absolute depths were not available for the RP8 basalts (Section 1.3), they show an extremely constant major element composition with relative depth in the borehole, and no depth trends could be discerned. This notable consistency in basalt chemistry is discussed further in Section 4.7.1.

1.7 Formation of massive and differentiated komatiite flows

1.7.1 Cooling and crystallisation in massive flows

In all sample types from the massive flows, the same cross cutting relationships between crystallising phases are observed. Olivine and chromite phenocrysts (including the embayed semi-skeletal olivines) were the first phases to crystallise. Though chromite is frequently included in olivine, the relative timing of crystallisation of these two phases cannot be established petrographically. Next to crystallise were various groundmass olivines, these either mantle existing olivine grains in the case of the skeletal overgrowths in type 1 samples, or are interstitial to olivine and chromite phenocrysts in the case of hopper olivines and chain olivine dendrites. Dendritic and spherulitic clinopyroxenes are always interstitial to groundmass olivine, mantling skeletal olivine fragments in type 1 samples and terminating against groundmass olivine in all other sample types. As groundmass olivine never terminates against groundmass clinopyroxene, it is inferred that these two groundmass phases cannot have been crystallising simultaneously, and that a gap in temperature and time separates their crystallisation (Faure & Tissandier, 2014).

The textural differences between the sample types identified can largely be explained by differences in the cooling rate (or degree of undercooling) experienced by different samples. Experimental studies have shown that granular olivine (i.e. phenocrysts) form at the slowest cooling rates (or lowest degree of undercooling), with hopper olivine and chain (or 'swallowtail') olivines forming at progressively higher cooling rates (higher degrees of undercooling; Donaldson, 1976; Faure *et al.*, 2003). Type 4 samples, defined by their abundant chain olivine dendrites therefore formed under the highest cooling rates. The additional presence of hopper olivine in type 3 samples implies a slower cooling rate, though these samples crystallised faster than type 1 and 2 samples in which chain olivine is absent. Type 2 samples probably cooled faster than type 1 samples given the rarity of hopper olivine in type 1 samples. The progressive decrease in clinopyroxene dendrite size from type 1 to type 4, with the appearance of clinopyroxene spherulites in type 4 samples supports this interpretation (Figure 1.27).

Although type 1 samples appear to have undergone the slowest cooling, they still retain large glassy patches in almost all samples. This is attributed to the frequently documented 'reluctance' of plagioclase to crystallise at even relatively low cooling rates (Kinzler & Grove, 1985; Faure & Tissandier, 2014).

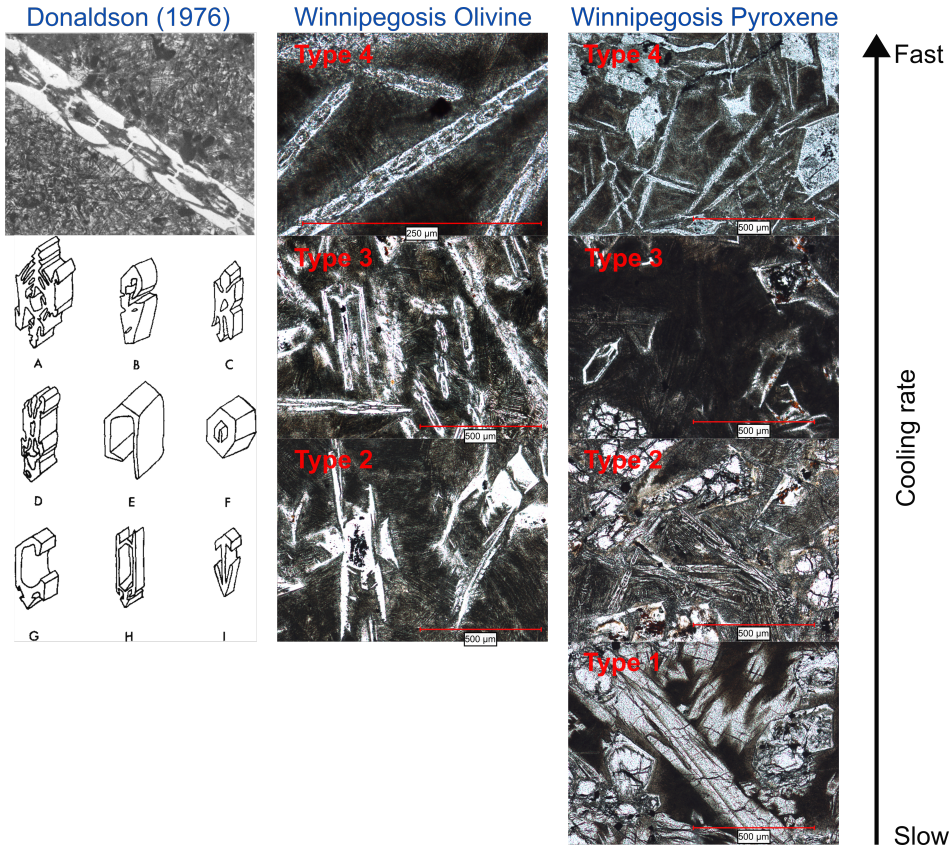

Figure 1.27: Comparison of morphology and size of Winnipegosis groundmass olivine and pyroxene, indicating differences in cooling rate. Olivine morphology changes from predominantly hopper olivine in type 2 samples, to predominantly chain olivine dendrites in type 4 samples. Pyroxene dendrite size progressively decreases from type 1 to type 4 samples, with the appearance of pyroxene spherulites in type 4 samples. Experimentally grown chain olivine and sketches of natural hopper olivine from Donaldson (1976) are shown for comparison.

Relation of cooling rates to depth in flow

In some flows identified by Hulbert *et al.* (1994), such as flow 21 and flow 5, cooling rates inferred petrographically vary systematically, with a general decrease in cooling rate (transition from type 4 to type 1 samples) observed with increasing depth in the flow (Figure 1.28). However, in other flows, such as the ~36 m thick flow 14, the largest flow identified by Hulbert *et al.* (1994), cooling rates do not appear to vary in a uniform manner and multiple type 4 chill margin horizons are observed within the flow (thicknesses are given as the apparent thickness down borehole, not the true stratigraphic thickness of the flows). It is suggested that either this is a feature caused by repeated inflation of partially cooled lava flows (Arndt, 1982; Hon *et al.*, 1994; Self

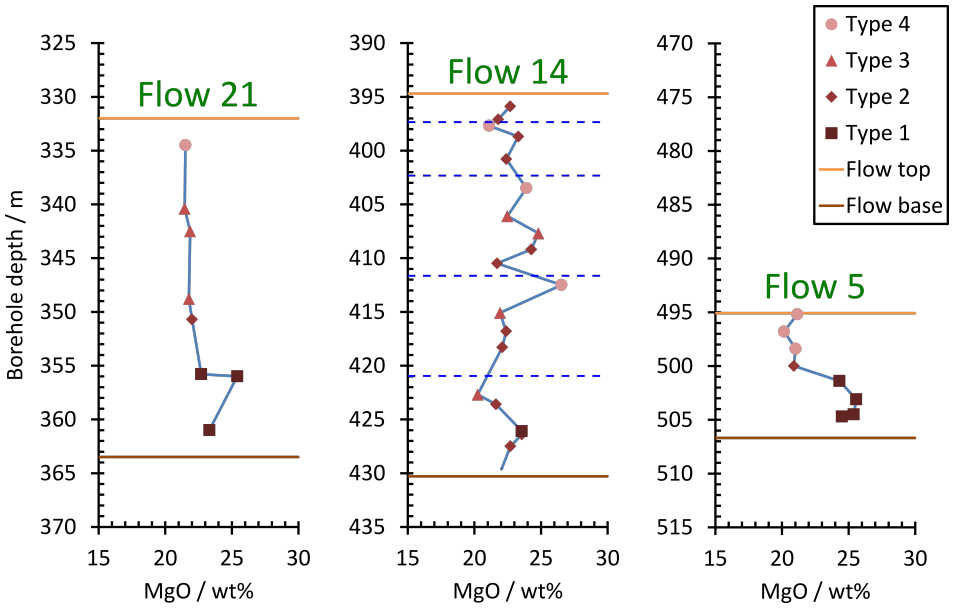

Figure 1.28: Variations in MgO content (from the GSC database) and textural type in three komatiite flows identified by Hulbert *et al.* (1994) from borehole RP1A. Flow 21 and flow 5 both show consistent changes in cooling rate with depth in the flow; sample types vary from type 4 (chill margins) near the top of the flow to type 1 near the base of the flow. Flow 21 has a largely consistent MgO content throughout, whereas flow 5 shows minor evidence of olivine settling in the increased MgO content of type 1 samples from near the base of the flow. Flow 14 shows three distinct type 4 chill margin textured samples, which may indicate that it was formed by multiple cycles of cooling and inflation, or is comprised of a number of smaller lava flows unidentified during core logging (indicated by blue dashed lines).

et al., 1996), or that this section of borehole in fact represents multiple smaller flows that could not be distinguished during core logging. If flow 14 is in fact comprised of a number of unidentified smaller flows, the thickest flow in RP1A is the ~31 m thick flow 21 of Hulbert *et al.* (1994).

Reconstruction of a generic Winnipegosis massive komatiite flow

Considering all the above petrographical observations, a 'generic' massive flow structure can be reconstructed (Figure 1.29). In general, olivine and chromite phenocrysts are evenly distributed throughout the flow, though there may be some slight settling of olivine to produce an MgO-enriched lower portion, and slightly MgO-depleted upper portion of the flow. Olivine phenocrysts tend to be smallest and most rounded in slowly cooled samples from near the base of the flow. It is speculated that this reflects abrasion and fragmenting of the grains during turbulent transport in the lava flow (Huppert *et al.*,

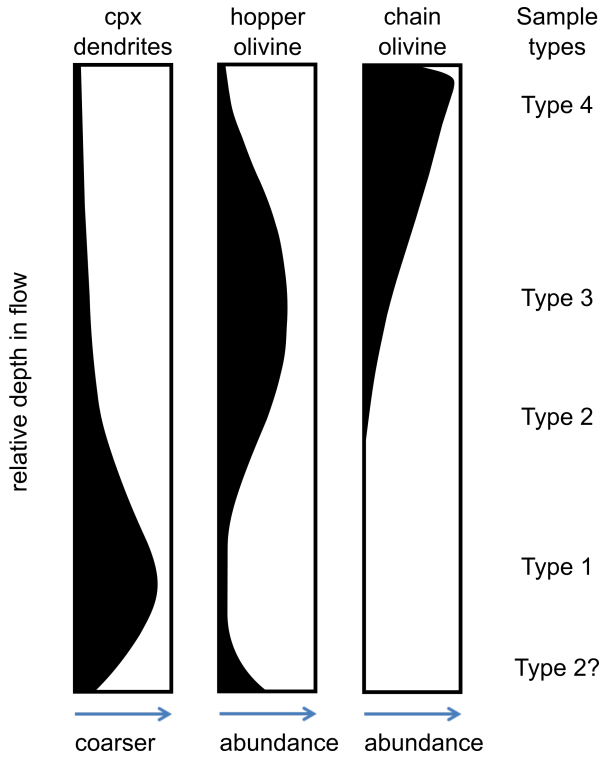

Figure 1.29: Schematic reconstruction of a Winnipegosis komatiite massive flow, showing size of clinopyroxene dendrites and relative abundance of chain and hopper olivine with relative depth in the flow.

1984) and possibly saltation along the flow base. No systematic variations in chromite size or shape are observed with depth in flow.

Discounting possible composite flows such as flow 14 (above), systematic variations in cooling rate are observed reflected in the transition from type 4 to type 1 samples with depth in flow. Rapidly cooled type 4 samples can be observed several metres from the tops of flows (e.g., flow 5 in Figure 1.28), indicating that these massive flows had thick chill margins. Thick (1 – 3 m) chill margins are also observed in Proterozoic basaltic komatiites from the Ottawa Islands, which also form part of the Circum-Superior Belt, but are distinct from the thin (5 – 10 cm) chill margins typically observed in Archaean komatiites (Arndt, 1982). Though samples from the basal chill margins of flows were not unequivocally identified, many flows identified by Hulbert *et al.* (1994) appear to revert to type 2 textures or transitional textures between type 1 and 2 immediately above their basal contacts, consistent with an increase in cooling rate at the flow base.

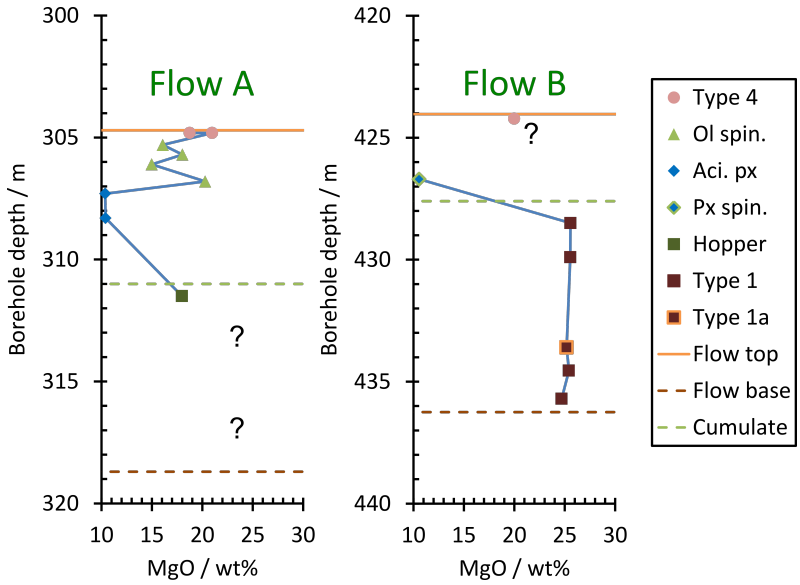

Figure 1.30: Variations in MgO content (from the GSC database) and textural type in two differentiated komatiite flows identified in borehole RP12. 'Type 4' = chill margins, similar to those seen in the massive komatiite flows, 'Ol spin.' = random olivine spinifex, 'Aci. px' = acicular pyroxene samples, 'Px spin.' = pyroxene spinifex with large hopper olivines, 'Hopper' = hopper olivine cumulate, 'Type 1' = olivine phyric samples with similar textures to type 1 massive flow samples, 'Type 1a' = type 1 sample with groundmass fully crystallised to a fine intergrowth of plagioclase and pyroxene, no glass remaining. Green 'Cumulate' lines indicate the estimated position of the boundary between spinifex and cumulate zones within the flow. Dashed lines indicate where depths of flow bases or spinifex cumulate boundaries have been estimated. No samples are available from the base of flow A, and the chill margin sample from the top of flow B has no geochemical data available (indicated by questions marks). An estimated MgO content of ~20 % is shown for the flow B chill margin for illustrative purposes.

1.7.2 Why did some komatiite flows differentiate?

Depth profiles through the differentiated flows 'A' and 'B' are shown in Figure 1.30. It is clear that these flows show much greater geochemical variations than the massive flows, with the low MgO contents present in the upper portion of the flows corresponding to large scale removal of olivine from the pyroxene spinifex and acicular pyroxene zones. However, it is not immediately apparent why the majority of komatiite flows did not differentiate, but some flows in borehole RP12 were able to differentiate into spinifex and cumulate layers, especially given the geochemical similarity between the massive and differentiated flows (Section 2.4). A number of models are considered below.

Gravitational settling of olivine phenocrysts

Early models for the formation of differentiated komatiite flows invoked gravitational settling of olivine grains in a conductively cooling flow to form a crystal-poor upper portion of the flow into which spinifex textures could grow (Pyke *et al.*, 1973; Arndt *et al.*, 1977). More recently, these models have fallen out of favour for the formation of Archaean differentiated komatiite flows, due to low calculated viscosities that are thought to have enabled turbulent flow (Bickle, 1982; Huppert *et al.*, 1984; Huppert & Sparks, 1985) with convective velocities exceeding the settling velocity of olivine phenocrysts (Turner *et al.*, 1986) and preventing settling. However, given the lower MgO contents and temperatures of the Winnipegosis Komatiites relative to Archaean komatiites (Section 2.5.4), these arguments may not necessarily apply.

If spinifex formation was controlled by gravitational olivine settling, the development of spinifex texture depends primarily on the settling rate of olivine and the time available before the flow cools sufficiently to impede crystal settling. From Stokes' law, the settling velocity of olivine is controlled by its size (and shape), the viscosity of the liquid (controlled by magma temperature and composition), and the density difference between olivine and liquid. For a conductively cooling flow, the time taken to cool enough to prevent further crystal settling is primarily governed by the thickness of the flow (Pyke *et al.*, 1973). Given that no differences can be discerned in geochemistry of massive and differentiated flows (Section 2.4), or phenocryst characteristics between the massive flows and lower portion of differentiated flow B, this model predicts that differentiated flows in the Winnipegosis sequence should be thicker than the massive flows.

Calculated as the difference in borehole depth from the uppermost to lowermost sample in a flow, the differentiated flows A and B are a minimum of 6.7 m and 11.5 m thick, respectively. Note that this is likely to be a large underestimate of the thickness of flow A as this only represents the thickness between the chill margin and hopper olivine cumulate; almost the entire cumulate zone was not sampled. Calculated as the difference in borehole depth from the top of the flows to the first sample from a lower flow, the differentiated flow A has a maximum thickness of 21.2 m, and flow B has a maximum thickness of 12.6 m. The poorly constrained thickness of flow A can be better estimated by analogy to differentiated basaltic komatiites flows from the Ottawa Islands (Arndt, 1982), whose upper portions are texturally very similar to those of flow A. The type example given by Arndt (1982) is 14 m thick, with a ~6.5 m interval

between the upper chill margin and hopper olivine cumulate layer. This is similar to the thickness (from borehole depth) of flow A, and so the thickness of flow A is roughly estimated as ∼14 m. Given the identification of > 30 m thick (borehole depth) massive flows in borehole RP1A by Hulbert *et al.* (1994), gravitational olivine settling likely cannot explain why some Winnipegosis komatiite flows differentiated and others did not, unless flow boundaries were incorrectly assigned during core logging or the dip of the boreholes and/or komatiite flows was vastly different between RP1A and RP12.

A number of models that do not require gravitational settling of olivine to facilitate the formation of spinifex texture are considered below. These more recent models of spinifex formation are compatible with the prediction that komatiites flowed turbulently and may have convected vigorously, and generally interpret spinifex textures as having grown simultaneously with, or even before, the settling of olivine to form a cumulate layer (Lajoie & Gelinas, 1978; Turner *et al.*, 1986; Arndt, 1986; Silva *et al.*, 1997; Shore & Fowler, 1999; Faure *et al.*, 2006). Shared features of all of these models include downward growth of spinifex from the flow top, such that the latest formed spinifex at the base of the spinifex zone has the most evolved, MgO-poor compositions, and gradual settling of olivine phenocrysts initially held in suspension by thermal convection and/or turbulent flow. However, the mechanisms driving downward spinifex growth differ substantially between different models.

Presence of strong thermal gradients

Recent petrographical and experimental studies have highlighted the importance of strong thermal gradients in the upper portion of komatiite flows in producing spinifex textures (Shore & Fowler, 1999; Faure *et al.*, 2006). In this light, differentiated flows might have formed where strong thermal gradients were present, whereas massive flows might reflect an absence of strong thermal gradients. Two possible mechanisms are considered for generating differences in thermal gradients between different komatiite flows.

Turner *et al.* (1986) suggested that rapid emplacement of successive komatiite flows could impede spinifex formation, as the formation of spinifex texture might require that strong thermal gradients are maintained for hours or days (Arndt *et al.*, 2008). Flows that erupted and had sufficient time to cool and crystallise (for instance, through contact with seawater) before the eruption of a subsequent flow would produce spinifex textures. However, if a cooling komatiite flow was quickly covered by a second komatiite

flow, the overlying flow would produce an 'insulating' effect and reduce or eliminate the thermal gradient generated in the crystallising flow, leading to formation of a massive komatiite flow. This mechanism is considered unlikely for the Winnipegosis komatiites, as core logging of RP1A (Hulbert *et al.*, 1994) identified the presence of calcareous and carbon rich sediments between flows. This suggests that a substantial (though unconstrained) amount of time passed between the emplacement of successive massive komatiite flows encountered in borehole RP1A, and it is likely that flows had fully cooled and crystallised by the time overlying flows were emplaced. Furthermore, no evidence of partial melting and recrystallisation of igneous textures are observed in the massive flows, as has been documented in the rapidly emplaced Honeymoon Well komatiites (Gole *et al.*, 1990).

Alternatively, Shore & Fowler (1999) suggest that strong thermal gradients could be generated in flow interiors by a self-propagating process of hydrothermal cooling and cracking. In their model, rapid cooling of the flow top through contact with seawater causes thermal contraction and extensive fracturing. The formation of fractures allows further downward ingress of seawater into the flow, causing further contraction and cracking and generating extremely large thermal gradients. For this model to explain the formation of both massive and differentiated flows, the massive komatiites would be predicted to have erupted sub-aerially to limit hydrothermal cooling and generation of strong thermal gradients, whereas differentiated komatiites would be predicted to have erupted sub-aqueously. This model can potentially explain why differentiated komatiites are found only in borehole RP12, if the palaeosurface at this location was below sea level, whereas the palaeosurface in the location of RP1A was not. However, some changes in sea level relative to the palaeosurface at RP12 would be required to explain why some flows intersected by RP12 did not differentiate. Unfortunately, the hypothesis that differentiated komatiite flows erupted sub-aqueously, whereas massive komatiites flows erupted sub-aerially, cannot be rigorously tested due to the small size and lack of geologically context for the core samples, and a lack of interflow sediment samples. However, the presence of calcareous interflow sediments in borehole RP1A suggests that these flows may have also erupted sub-aqueously.

Ponding of turbulent lava flows

The model of Arndt (1986) attributes the difference between massive and differentiated komatiite to how far the komatiite lava is able to flow and cool before ponding. In

this model, turbulent flow of komatiite lava causes very efficient heat loss, and prevents formation of thick chill margins (Huppert *et al.*, 1984; Turner *et al.*, 1986). This heat loss also promotes rapid crystallisation of olivine, as phenocrysts transported in the turbulently flowing lava (Arndt, 1986). If flow continues, the proportion of olivine phenocrysts increases until it reaches ∼50% (by volume). At this point the high proportion of phenocrysts causes a drastic increase in viscosity of the lava, and the flow stops moving (Marsh, 1981). Olivine phenocrysts remain suspended within the flow with minimal settling, and a massive flow is produced. Alternatively, if the flow ponds before sufficient cooling and olivine crystallisation, a spinifex layer is able grow downwards from the roof of the convecting flow, while phenocrystic olivine crystallises in the lower portion of the flow. Spinifex growth from the top of the flow and phenocryst growth in the base of the flow continues until the proportion of phenocrysts becomes high enough to inhibit convection.

This model therefore predicts that differentiated flows should form closer to the vents from which the komatiites erupted, such that olivine phenocryst crystallisation could not progress significantly before the komatiites ponded, or in areas where the local topography aided ponding of flows. This model has the potential to explain why multiple komatiite flows intersected by borehole RP12 were able to differentiate, but none of those in borehole RP1A did; perhaps borehole RP12 intersected komatiite flows closer to the vent through which they erupted, or in a region with favourable topography for flow ponding. However, due to the essentially one-dimensional nature of the boreholes, these predictions cannot be rigorously tested.

Some predictions of this model are not compatible with petrographical observations. Firstly, none of the massive flows contain phenocryst contents as high as 50 vol%. Secondly, this model predicts that the majority of olivine phenocryst crystallisation occurs after eruption within the flow. This is not consistent with calculated olivine crystallisation temperatures (Section 2.5.4), which suggest that olivine phenocryst crystallisation essentially ceased upon eruption, with olivine crystallisation continuing only as skeletal and dendritic olivine (Silva *et al.*, 1997). However, the Winnipegosis komatiites are likely to have had higher viscosities than Archaean komatiites for which this model was developed. As such, it is possible that flow cessation might occur due to cooling and increasing viscosity during flow, accompanied by minor skeletal olivine crystallisation. If this is the case, this model remains a viable option for explaining why only some Winnipegosis komatiite flows differentiated.

Differences in phenocryst load upon eruption

Arndt *et al.* (2008) suggest that massive komatiite flows might form when komatiite is erupted with a high proportion of olivine phenocrysts upon eruption, leading to an 'olivine choked' flow with a high effective viscosity. By contrast, differentiated flows would form where little olivine crystallisation had occurred before eruption, allowing the flow to convect and generate spinifex textures. This model can be tested by examining the olivine phenocryst content in chill margins. The chill margin of differentiated flow A (sample RP12-304.8) contains an estimated ∼10 vol% phenocrysts. Phenocryst contents in the chill margin of differentiated flow B appear low (∼5 vol%; sample RP12-424.22B) but are very difficult to ascertain with any confidence due to extensive carbonated veining throughout the sample. These estimates do not appear unusually low compared to the massive komatiites flows, whose chill margins contain between ∼5 – 20 vol% olivine phenocrysts.

Summary

Many models of komatiite flow differentiation focus on the prerequisites for spinifex formation, but do not consider why most komatiite flows do not differentiate (Arndt *et al.*, 2008), despite attaining considerable thicknesses. The observation that some, but not all, Winnipegosis komatiite flows differentiated is unlikely to be attributable to gravitational settling of olivine phenocrysts (Pyke *et al.*, 1973; Arndt *et al.*, 1977). This model predicts, contrary to the flow identifications of Hulbert *et al.* (1994), that thicker flows should develop spinifex texture, while thinner flows should not. Although strong thermal gradients are likely a prerequisite for the formation of spinifex texture (Shore & Fowler, 1999; Faure *et al.*, 2006), no evidence is found to suggest that the differentiated flows experience higher internal thermal gradients than the massive flows. Furthermore, no evidence can be found to indicate that differentiated flows erupted with lower olivine phenocryst contents. Although not all predictions of the flow ponding model of Arndt (1986) can be tested, this is the only model compatible with the petrographical and geological observations. This model suggests that flows differentiated to form spinifex and cumulate zones where they were able to pond soon after eruption, whereas flows that flowed extensively from the vent cooled and crystallised until the viscosity was too high to allow formation of a spinifex zone. Differences in the prevalence of differentiated flows in boreholes RP1A and RP12 can be explained by borehole RP12 intersecting a komatiite sequence closer to an eruption vent, or by local palaeo-topography near RP12

favouring earlier ponding of flows.

1.8 Conclusions

The Winnipegosis Komatiite Belt (WKB) comprises part of the Circum-Superior Belt large igneous province, formed along a convergent margin during destruction of the Palaeoproterozoic Manikewan Ocean. Shortly after it's formation, the entire belt was metamorphosed at sub-greenschist to greenschist grade during the Trans-Hudson Orogeny. Rock samples available for this thesis are from four boreholes drilled during mineral exploration in the belt: komatiites from boreholes RP1A and RP12, dunites from borehole RP7, and basalts from borehole RP8. Additional zircon separates are available from a coarse gabbroic unit from borehole RP4.

Petrographical investigations identify that the majority of komatiites are present as massive flows, while a small number differentiated to form spinifex and cumulate layers. Komatiites from borehole RP1A are exclusively massive flows, which contain only olivine and chromite as phenocryst phases. These flows are excellently preserved, having only been metamorphosed to sub-greenschist grade, and are primarily altered around hydrous and carbonate veins. A variety of groundmass textures identified in skeletal olivine and pyroxene are likely driven by difference in cooling rate or degree of undercooling at the time of groundmass crystallisation. Borehole RP12 features both massive and differentiated komatiite flows, and has undergone higher grade metamorphism. Differentiated komatiites show a range of textural and compositional variations, including hopper olivine cumulates, pyroxene phenocryst-bearing layers, and olivine spinifex. The presence of differentiated and massive flows in the same sequence might be attributable to how far flows were able to travel and cool before finally ponding and crystallising. RP7 dunites retain only chromite as a primary igneous mineral; olivine is entirely serpentinised and igneous textures are difficult to discern. RP8 basalts comprise a greenschist mineral assemblage, with primary minerals and textures completely destroyed by metamorphism.

A large database of unpublished geochemical data ('GSC database') is used to construct depth profiles for the boreholes studied in this thesis. In general, the komatiites, basalts, and dunites show only minor geochemical variations with depth in each borehole. The largest geochemical anomalies are associated with carbonate veining in boreholes RP1A and RP12, and the formation of differentiated flows in borehole RP12.

Chapter 2

Age, Origin and Thermal Evolution of the Winnipegosis Komatiite

Chapter Summary

The Proterozoic spans the longest portion of Earth's history, yet in contrast to the Archaean, the record of komatiites and related high MgO igneous rocks from this Aeon is sparse. This chapter presents mineral and bulk rock geochemistry, and Al-in-olivine thermometry for the Winnipegosis Komatiites, with a view to understanding komatiite formation and the thermal state of the mantle during the Palaeoproterozoic. New U-Pb SHRIMP dating of mafic zircons is also presented, yielding an age of 1870.3 ± 7.1 Ma for the Winnipegosis Komatiite Belt. The komatiites are Al-undepleted, and trace element data indicate they were derived from depleted mantle, subsequently contaminated with 2 – 3% continental crust. Temperatures from Al-in-olivine thermometry are consistent with a nominally dry melt, and combined with olivine-melt Mg-Fe partitioning, suggest a parental melt with ∼24 wt% MgO and a liquidus (olivine) temperature of ∼1501 °C, approximately 100 °C cooler than their hottest Archaean counterparts. At ∼1424 °C chromite joined olivine as a crystallising phase. Olivine and chromite phenocrysts were re-mixed with residual melt shortly before or during komatiite eruption, which occurred by the time the magma had cooled to ∼1321 °C. Combined geochemical and geological evidence requires that the Winnipegosis Komatiites erupted onto rifting continental crust. Their high liquidus temperatures require anomalously hot mantle. Considering the Winnipegosis Komatiites in the context of the broader Circum-Superior Belt, it is suggested that these magmas formed from a mantle plume that was deflected towards the margins of the Superior craton by strong gradients in lithospheric thickness. This interpreta-

tion of the mode of formation of the Circum-Superior Belt casts doubt on ambient mantle potential temperatures as high as 1600 °C during the Proterozoic.

2.1 Introduction

Komatiites are generally believed to represent high-temperature, large-degree melts of the mantle (Nisbet *et al.*, 1993; Arndt *et al.*, 2008). As such, they have long been used as probes of both the chemical and thermal evolution of the mantle through time (Bickle *et al.*, 1976; Maier *et al.*, 2009; Campbell & Griffiths, 2014). However, the temporal record of mantle temperature and chemistry provided by komatiites is irregular; the vast majority of komatiites erupted during the Archaean (Arndt *et al.*, 2008), with only two occurrences known from the Phanerozoic (Echeverria, 1980; Hanski *et al.*, 2004). Despite comprising almost half of Earth history, only a handful of komatiites and related high MgO igneous rocks have been reported from the Proterozoic Aeon, including: Ti-rich komatiites of the Karasjok and Central Lapland Greenstone Belts (Barnes & Often, 1990; Hanski *et al.*, 2001); basaltic komatiites of the Vetreny Belt (Puchtel *et al.*, 1997); and a number of basaltic komatiites and compositionally similar intrusions from the Circum-Superior Belt (Arndt, 1982; Arndt *et al.*, 1987; Hynes & Francis, 1982; Minifie *et al.*, 2013).

In light of the paucity of Proterozoic komatiites, this chapter describes the well preserved ∼1.87 Ga Winnipegosis Komatiites from Manitoba, Canada. The minimally altered nature of the Winnipegosis Komatiite sequence provides an excellent opportunity both to study komatiite formation during the Proterozoic, and to compare the chemical and thermal state of Archaean and Proterozoic mantle. Geochemical observations are presented with a view to understanding the mode of formation and thermal evolution of the Winnipegosis Komatiites. The Winnipegosis lavas are demonstrated to be komatiites by any definition, showing spinifex textures (Section 1.4.2) and derivation from a liquid with > 18 wt% MgO (Kerr & Arndt, 2001). The Winnipegosis Komatiites show many geochemical similarities to Archaean Al-undepleted komatiites, and formed from a nominally dry, depleted mantle source. Their high liquidus temperatures are ∼100 °C lower than their hottest Archaean counterparts, but still require thermally anomalous mantle for their formation. Finally, possible modes of formation of the Winnipegosis Komatiites are discussed in light of these findings and the regional geological context.

2.2 Background and sample selection

Details on the geological setting of the Winnipegosis Komatiite belt, along with petrographical descriptions of Winnipegosis Komatiites can be found in Chapter 1. Komatiite samples chosen for re-analysis were screened to exclude those with ≥ 0.3 wt% CO_2 and high H_2O_t (Section 1.6.1), as these represent those most infiltrated by carbonate and talc-serpentine veins identified petrographically (Section 1.4.3), and hence most affected by fluid flow during metamorphism. Based on this screening, and attempting to maintain a large range in both MgO contents and stratigraphic position, a subset of 20 komatiite samples from borehole RP1A and 14 komatiite samples from RP12 were chosen for new geochemical analysis.

2.3 Methods

2.3.1 Bulk rock major and trace elements

Whole rock major and minor element geochemistry was measured by X-Ray Fluorescence (XRF) on $Li_2B_4O_7$ fusion disks at Franklin and Marshall College (Mertzman, 2000). Ten replicates of the OKUM (Ontario komatiite) certified reference material (CRM) were measured to assess the repeatability under measurement conditions (hereafter 'repeatability'; JCGM, 2012) and accuracy of the method. Most major and minor elements were repeatable to a precision of $< 2\%$ (1σ relative); K_2O, P_2O_5, and V, present in low concentrations in OKUM, had repeatabilities of $< 5\%$ (Table 2.1). Loss on ignition (LOI) was variable, with a repeatability of $\sim$8%. All elements except for TiO_2 and Cr overlap with the certified 95% confidence limits (IAG, 2015) within two standard deviations, and are therefore considered accurate at the level of precision of the measurements. TiO_2 and Cr are about both $\sim$5% (relative) lower than the certified values, and lie just outside the certified 95% confidence limits. Ni measurements in OKUM were not reproducible using this method, and are excluded from this study.

Trace elements, including rare-earth elements (REEs), were measured following a procedure similar to Ottley *et al.* (2003) at the Arctic Resources Geochemistry Laboratory at the University of Alberta. A mass of 0.1 ± 0.01 g of rock powder per sample was dissolved in Savillex PFA beakers with 4 mL of concentrated HF (28.7 M) and 1 mL of concentrated HNO_3 (15.4 M, both acids Teflon distilled in-house) and refluxed on a hotplate at 150 °C for > 120 hours. Due to incomplete dissolution of some samples

at this stage, all samples were dried down and again refluxed in 2 mL of concentrated HF and 2 mL concentrated HNO_3 at 150 °C for > 120 hours, after which all samples appeared fully dissolved. Samples were then dried down before being evaporated to near dryness three times in concentrated HNO_3, and diluted in 3% HNO_3 for measurement. Most trace elements were analysed at a mass resolution of 300 (10% peak-valley definition) on a Nu Attom ICP-MS, with the exception of the transition metals (Sc, Cr, Co, Ni, Cu), which were measured on a Thermo Fisher Element 2 ICP-MS at a mass resolution of 4000.

Twelve replicate dissolutions of the OKUM CRM were analysed to monitor repeatability and accuracy. All REEs, Rb, Sr, and Y were repeatable to $\leq$ 2% (1σ relative) over 3 analytical sessions (Table 2.1). Cs, Ba, Hf, Th, and U had repeatabilities of < 4%; Zr and Pb had repeatabilities of ∼7%. All of these elements overlap with the certified values within 95% confidence limits, and are therefore deemed accurate at the level of precision of the analyses. However, it is noted that Zr in these measurements is about 7% below the certified value, despite the agreement within confidence limits. Transition metal analyses were repeatable to ∼3% (1σ relative). Sc and Cu data overlap are within two standard deviations of the certified 95% confidence limits, and are considered accurate. Co and Ni data are ∼10% too high relative to the certified OKUM values, lying just outside the certified 95% confidence limits. Cr data measured by ICP-MS was systematically high compared to both the certified OKUM value and XRF data from this study, likely due to an uncorrected interference during measurement, and is not used further as it is both less repeatable and less accurate than the data measured by XRF. However, it shows a strong correlation with the XRF data (Figure 2.1), which is interpreted as evidence that chromite was fully dissolved in both the OKUM standard and Winnipegosis samples.

2.3.2 Mineral EPMA Analyses

Major, minor, and trace element compositions of fresh olivine and co-existing olivine-chromite pairs from thin sections of the Winnipegosis Komatiite, were analysed using a JEOL 8900R electron microprobe at the University of Alberta. These measurements can be divided into 'routine' measurements performed to obtain major element compositions only, and 'high precision' measurements designed to measure trace elements, in particular for the application of the Al-in-olivine – spinel thermometer (Wan *et al.*, 2008; Coogan *et al.*, 2014). Routine measurements were performed with peak measurement

Table 2.1: Bulk rock major and minor element data measured by XRF (above line), and minor and trace element data measured by ICP-MS (below line) for the OKUM certified reference material. 'Average OKUM' data ± 2 standard deviations (2σ abs., n = 10) from this study are compared to the OKUM certified values ('OKUM cert') and 95% confidence limits (IAG, 2015). Data for oxides, V, and Cr was renormalised to 100% totals on an anhydrous basis, with FeO_t calculated assuming all Fe is present as FeO. LOI and elements measured by ICP-MS were not renormalised. Raw totals are given as an indication of data quality. Repeatability under measurement conditions for each element is shown as 1 relative standard deviation of the data. 'LOI' = loss on ignition. Average Cr data measured both by XRF and ICP-MS is shown; Cr measured by ICP-MS is ∼15% higher than the certified value (Figure 2.1).

	Average OKUM	2σ abs.	OKUM cert.	95% conf.	Repeatability (1σ rel.)
SiO_2 *(wt%)*	46.76	0.74	47.14	0.15	0.8%
TiO_2	0.390	0.010	0.406	0.004	1.2%
Al_2O_3	8.47	0.11	8.51	0.04	0.6%
FeO_t	11.52	0.26	11.35	0.05	1.1%
MnO	0.188	0.003	0.194	0.003	0.7%
MgO	22.93	0.40	22.73	0.11	0.9%
CaO	8.44	0.09	8.38	0.06	0.6%
Na_2O	1.229	0.030	1.213	0.023	1.2%
K_2O	0.047	0.003	0.047	0.002	3.7%
P_2O_5	0.025	0.002	0.028	0.002	3.5%
Total	99.37	0.19	99.32		0.1%
LOI	4.50	0.68	4.49	0.14	7.6%
V (ppm)	167	11	168	3	3.2%
Cr	2339	45	2460	31	1.0%
Sc	30.2	1.9	27.9	1.5	3.2%
Cr	2846	140	2460	31	2.5%
Co	97.2	5.9	88.9	1.5	3.0%
Ni	976	64	886	10	3.3%
Cu	47.1	3.1	43.5	1.2	3.3%
Rb	0.89	0.03	0.96	0.06	1.4%
Sr	15.7	0.6	16.1	1.0	2.0%
Y	9.43	0.33	9.08	0.29	1.7%
Zr	15.9	2.0	17.0	1.4	6.4%
Nb	0.37	0.03	0.37	0.06	3.9%
Cs	0.173	0.008	0.184	0.003	2.2%
Ba	5.84	0.29	6.20	0.50	2.5%
La	0.39	0.01	0.41	0.02	1.7%
Ce	1.25	0.03	1.27	0.03	1.4%
Pr	0.23	0.01	0.24	0.01	1.7%
Nd	1.46	0.05	1.49	0.02	1.6%
Sm	0.70	0.02	0.72	0.01	1.6%
Eu	0.30	0.01	0.30	0.01	1.5%
Gd	1.17	0.03	1.17	0.07	1.4%
Tb	0.22	0.01	0.23	0.01	1.9%
Dy	1.56	0.06	1.61	0.04	1.9%
Ho	0.34	0.01	0.36	0.01	1.5%
Er	1.01	0.04	1.04	0.01	2.0%
Yb	0.99	0.03	1.01	0.02	1.6%
Lu	0.15	0.00	0.15	0.01	1.5%
Hf	0.54	0.03	0.55	0.02	3.1%
Pb	0.22	0.03	0.26	0.02	7.7%
Th	0.027	0.002	0.031	0.004	3.5%
U	0.010	0.001	0.012	0.005	3.5%

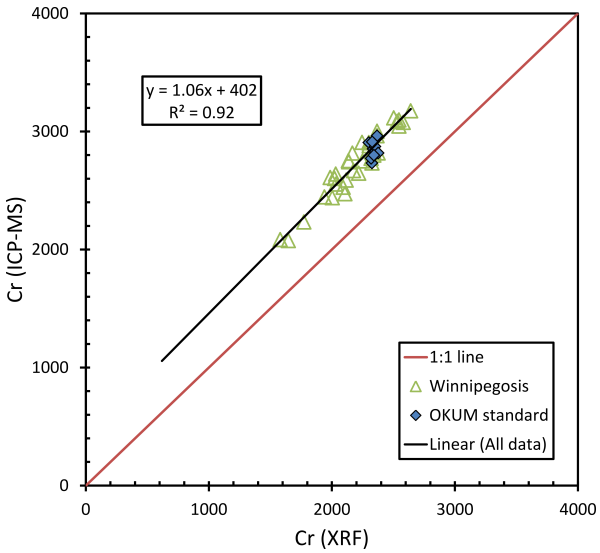

Figure 2.1: A comparison of Cr data (in units of ppm) obtained by ICP-MS following HF + HNO_3 sample dissolution, and XRF on $Li_2B_4O_7$ fusion disks. The ICP-MS data is systematically higher than the XRF data, which likely results from an uncorrected interference at the time of measurement. Despite this, the two datasets show a strong correlation. This is interpreted as evidence that chromite was fully dissolved during the sample dissolution procedure, as incomplete dissolution might be expected to produce values below the 1:1 line, or strongly varying ICP-MS data in comparison to that obtained by XRF.

times of 30 s for most elements using a beam current of 20 nA. High precision measurements were carried out using a beam current of 100 nA, and much longer analysis times. Aluminium was measured for 240 s on peak, with upper and lower backgrounds of 120 s each. These conditions yielded an average limit of detection of 0.0019 wt% Al_2O_3 (10 ppm Al), with the Potts (1992) limit of determination (blank + 6σ) at 0.0039 wt% Al_2O_3 (21 ppm Al). All measurements used an accelerating voltage of 20 kV. Further details on high resolution measurement conditions are given in Appendix B.1.

Due to the lack of a CRM for trace elements in olivine, data is reported from two different in-house San Carlos olivine standards to assess the precision and the accuracy of the method (see Appendix B.2 for details). The first, SC-BK, was characterised by LA-ICP-MS to have an Al-content of 80.4 ± 2.3 ppm. Repeated high precision EPMA analyses, standardised against a Frank Smith pyrope, yielded an average Al content of 78.3 ± 5.9 ppm (1σ, n = 41). The use of a plagioclase Al calibration standard rather than pyrope increases the average Al concentration by ∼4.5%, which is smaller than the effect of using Si or Mg as an internal standard in the LA-ICP-MS data. This suggests that Al concentrations in olivine can be measured accurately, with repeatability of 7.6%

(1σ relative) at ~80 ppm Al. The second in-house reference material, SC/KA, does not have an 'accepted' Al concentration, but is homogeneous in Ca (Köhler & Brey, 1990). Repeated analyses yielded an average Al content of 89.7 ± 5.2 ppm (1σ, n = 15), or a repeatability of 5.8% (1σ relative) at ~90 ppm Al. The Al-in-olivine measurements from Winnipegosis Komatiite samples are expected to be of higher precision than this due to their higher Al contents of ~250 – 450 ppm (Section 2.4). A comparison of the measured and theoretical precisions for several trace elements in the two olivine standards demonstrates that the repeatability of trace element measurements in olivine using the EPMA are dominated by counting statistics, at least at low concentrations (Appendix B.3). Using the formula of Cox (1983), the uncertainty on an individual measurement of Al in the Winnipegosis Komatiite olivine is conservatively estimated to be ~2.5% (1σ relative).

For the application of the Al-in-olivine thermometer (Wan *et al.*, 2008; Coogan *et al.*, 2014), olivine-chromite pairs were selected in which the chromite was entirely enclosed in fresh olivine, in the two dimensions observable (Figure 1.4). To minimise the possible effects of secondary fluorescence from the chromite, Al-in-olivine analyses were located approximately 40 microns from the chromite grain boundaries. To account for the effects of Al zoning, 5 spots were analysed in each olivine from a range of positions around the included chromite grain. Temperatures were determined for each olivine spot using the average Cr# obtained for the enclosed chromite, and an average temperature calculated for each olivine.

2.3.3 Zircon U-Pb methods

Previous Thermal Ionisation Mass Spectrometry (TIMS) U-Pb zircon dating of mafic rocks from the Winnipegosis Komatiite Belt yielded an age initially interpreted as 1864 $^{+6}_{-4}$ Ma (Hulbert *et al.*, 1994). However, these data were never formally published, and a re-analysis of the original zircons and U-Pb data suggest that the precision indicated by this age is overly optimistic (Section 2.4.3). As such, the methods used in the original analysis of Hulbert *et al.* (1994) are presented here, in addition to the methods used during re-analysis of the zircons by U-Pb Sensitive High Resolution Ion Microprobe (SHRIMP) dating. Results and interpretation of the data from both methods is presented in Section 2.4.3.

A section of coarse grained pyroxene cumulate from borehole RP92-4, representing either a thick flow or sill (Burnham *et al.*, 2009), was crushed and zircons were

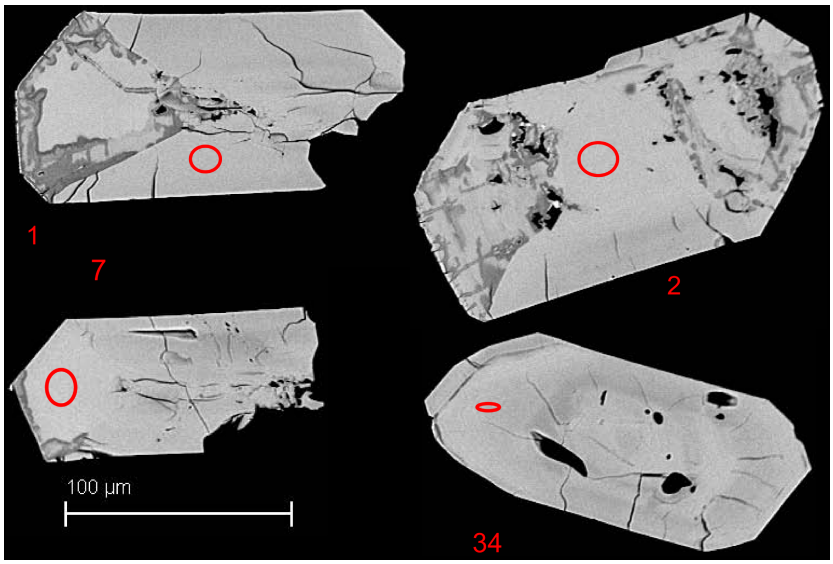

Figure 2.2: Typical zircons used for SHRIMP dating, taken from same population used for TIMS dating by Hulbert *et al.* (1994). Approximate locations of analytical spots are shown by red ellipses. Red numbers indicate zircon number, e.g. spot 034.1 (Table 2.4) is the first spot measured on zircon 34.

extracted using standard separation techniques at the Geological Survey of Canada (GSC) Geochronology Labs in 1993. This zircon separate was used both for the initial TIMS U-Pb analysis of Hulbert *et al.* (1994), and the new SHRIMP analyses (Waterton *et al.*, 2017). The zircons were investigated petrographically, mounted, and imaged using backscattered electron (BSE) imaging before SHRIMP analysis.

Zircons isolated by Hulbert *et al.* (1994) are moderately well preserved, stubby to elongate prismatic crystals and fragments, with sharp crystal edges, ~50 – 200 μm in size. Backscattered electron (BSE) images reveal broad, faint igneous zoning in some grains. However, the zircons are heavily fractured, and many show regions of mottled and irregular dark patches in BSE, indicative of metamictisation and alteration. Small, very bright spots may represent Th or U rich secondary phases crystallising following alteration (Figure 2.2).

Age data presented in Hulbert *et al.* (1994) was acquired using TIMS by Richard Stern, also at the GSC Geochronology Labs. Details of the exact chemical procedure and analytical methods used are unknown. During re-analysis, SHRIMP was used to obtain U-Th-Pb data for a total of 17 spots located on the igneous portions of 15 zircons from the zircon separate described above, with care taken to avoid zones of metamictised and altered zircon.

2.4 Results

2.4.1 Bulk Rock Geochemistry

XRF major and minor elements

Bulk rock major, minor, and trace element data for Winnipegosis Komatiites is summarised in Table 2.2, and also available in the supplementary information to Waterton *et al.* (2017). Variations of elements measured by XRF against MgO are shown in Figure 2.3. Some incompatible elements, such as Al_2O_3 and TiO_2, show extremely tight correlations which extrapolate through measured olivine compositions. Others show more scatter and regression lines extend to higher (e.g., CaO) or lower (e.g., Na_2O) MgO than Winnipegosis olivine. Samples from borehole RP12 lie along the same regression trends as the RP1A samples, but are generally more scattered.

The elements SiO_2, FeO, and MnO show less variability with MgO, but all show slightly negative correlations. Cr_2O_3, compatible in both olivine and chromite, shows a strong positive correlation with MgO. A regression of Cr_2O_3 against MgO from RP1A intersects a mixing line between the average olivine composition and the average chromite composition at approximately 1.1% chromite.

Samples from massive flows contain between 16.8 and 26.1 wt% MgO. Samples from the upper portion of differentiated flows generally show lower MgO contents: random olivine spinifex samples contain 15.3 – 19.8 wt% MgO, the hopper olivine cumulate sample contains 18.2 wt% MgO, and two acicular pyroxene zone samples both contain ~10.5 wt% MgO. Data from the GSC database indicate that most of the komatiites sampled form a tight range in MgO, with a mean of 22.2 ± 2.2 wt% (1σ absolute), and a median MgO content of 22.4 wt% MgO (n = 189 samples with < 1 wt% CO_2).

ICP-MS minor and trace elements

Many trace elements measured for this study show broad negative correlations with MgO (Figure 2.4), though the degree of data scatter about these correlations varies considerably. In general, the heavy REEs (HREEs) and middle REEs (MREEs) show tighter correlations with MgO, and intersect the MgO axis closer to measured olivine MgO than the light REEs (LREEs). Data for the large ion lithophile elements (LILEs) and Pb are generally very scattered; U, Th and Nb show moderate degrees of scatter, whereas Zr, Hf, V, and Sc show tight correlations with MgO. Nickel and Co show strong

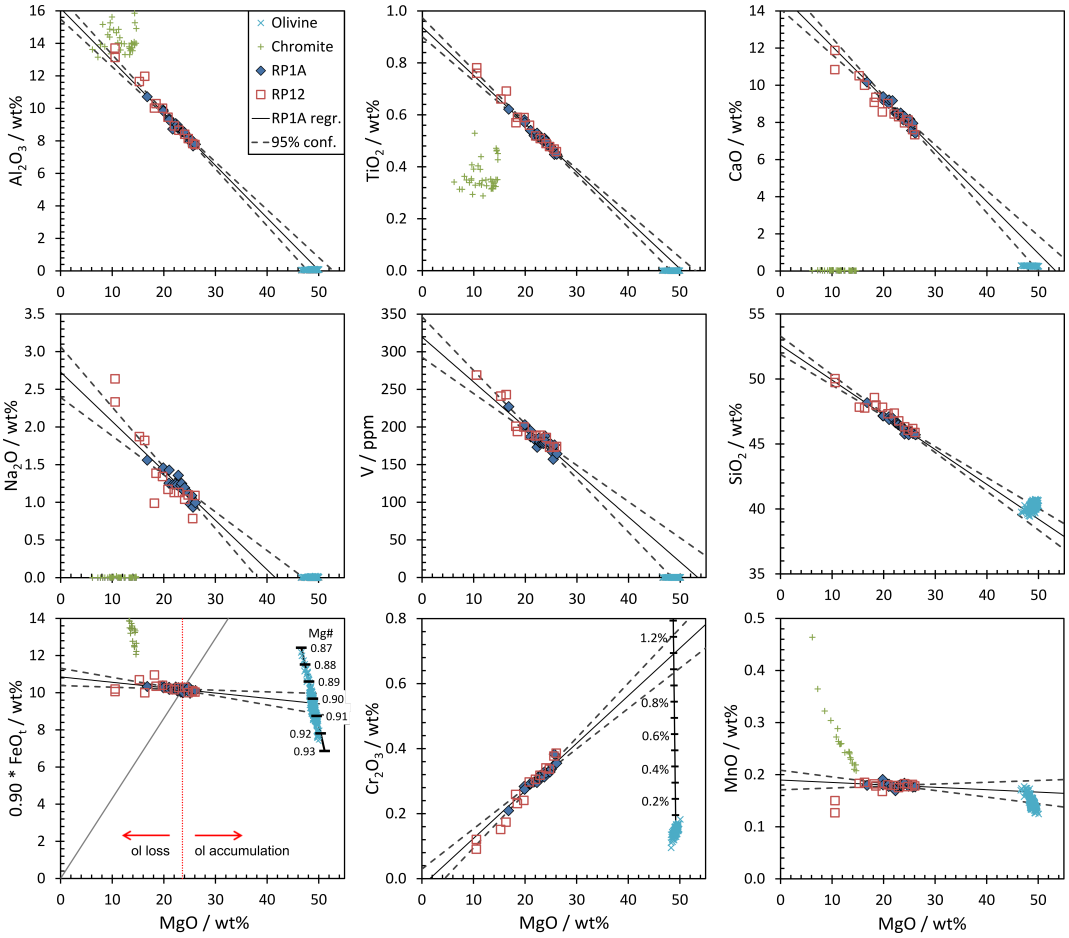

Figure 2.3: Variation of major and minor elements as a function of MgO. All plots show linear regressions of RP1A data (solid black lines), along with 95% confidence limits about the regression (dashed grey curves). Cr_2O_3 against MgO plot shows a mixing line between the average olivine and chromite compositions measured by EPMA, ticks indicate percentage of chromite in mixture. FeO is plotted as $0.90 * FeO_t$, based on the best estimate of the $Fe^{2+}/\Sigma Fe$ at the time komatiite crystallisation (see Section 2.5.3 for details); plot also shows model olivine compositions as a thick black line, tick marks indicate olivine Mg#. Thin grey line represents the FeO/MgO ratio of the liquid in equilibrium with the highest Mg# olivine, and the dashed red line indicates the calculated parental liquid MgO.

positive correlations with MgO.

Primitive upper mantle (PUM; Hofmann, 1988) normalised spidergrams (Figure 2.5) show a generally depleted pattern, with LREE < MREE, low Nb, U and Th, and trace element concentrations approximately $2 * PUM$. The samples also show a modest HREE depletion relative to the MREEs, defining 'hump' shaped REE patterns. The LILEs and Pb are variably enriched. Trace element patterns for massive flows from RP1A and RP12 are extremely consistent and there is no significant difference between boreholes.

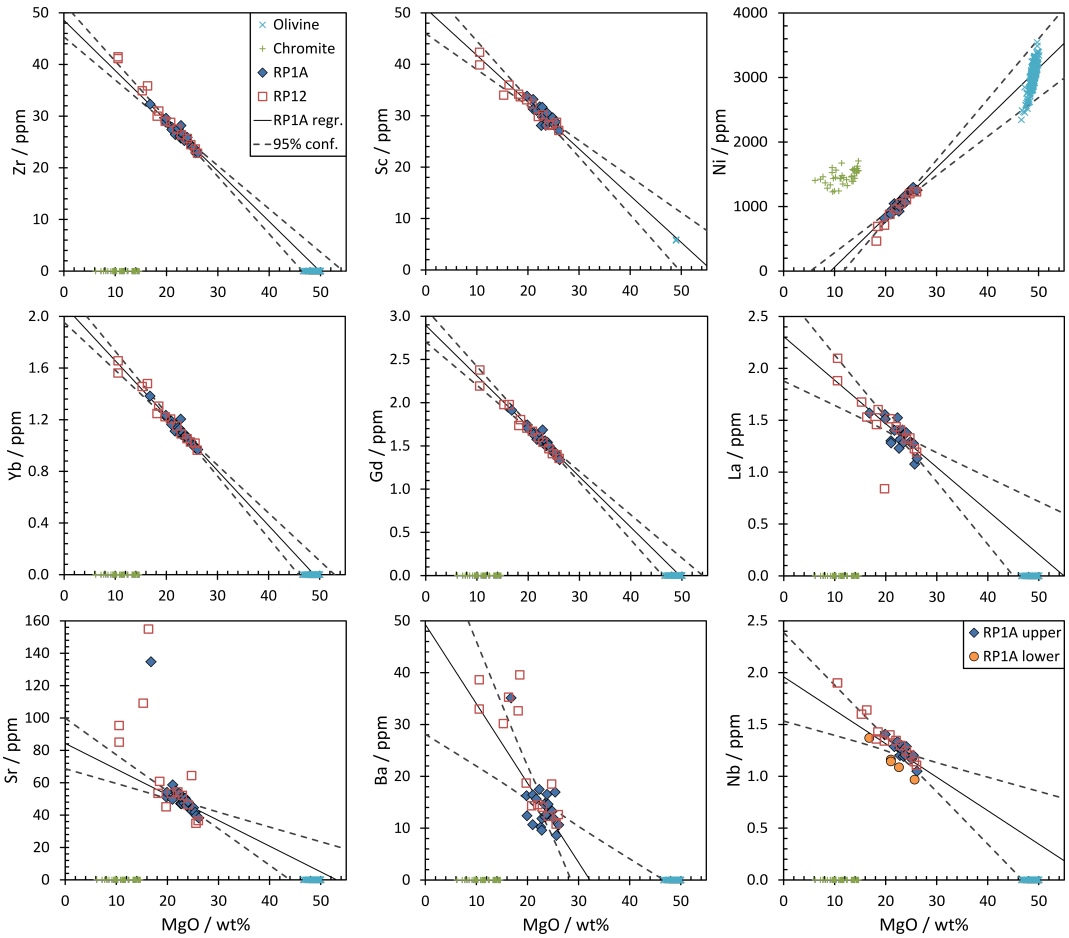

Figure 2.4: Variation of trace elements as a function of MgO, showing linear regressions of all RP1A data with 95% confidence limits. RP1A data for Nb is split into samples from the lowermost 50 m of the borehole ('RP1A lower', orange circles) and samples from the remainder of the borehole ('RP1A upper', blue diamonds). An average value of 5.8 ppm Sc measured from LA-ICP-MS analyses of Winnipegosis Komatiite olivine (Pedro Waterton, unpublished data) is plotted at the average olivine MgO of 49 wt%. Scandium in chromite was not measured; although previous work has indicated up to 16 ppm Sc in chromite from high MgO volcanic rocks (Pagé & Barnes, 2009), this is not expected to have a large effect on the whole rock budget of Sc due to the low proportion of chromite. Nickel in olivine and chromite were measured by EPMA. All other trace elements plotted were present in negligible quantities in Winnipegosis olivine, and assumed to be negligible in chromite; their MgO ranges are plotted at 0 ppm trace element concentration.

Samples from differentiated flows from RP12 show more variable patterns, and slight positive Eu anomalies are observed in two spinifex-textured samples (RP12-282.5 and RP12-305.3). Sample RP12-282.5 also shows significantly more depleted LREEs than any other sample.

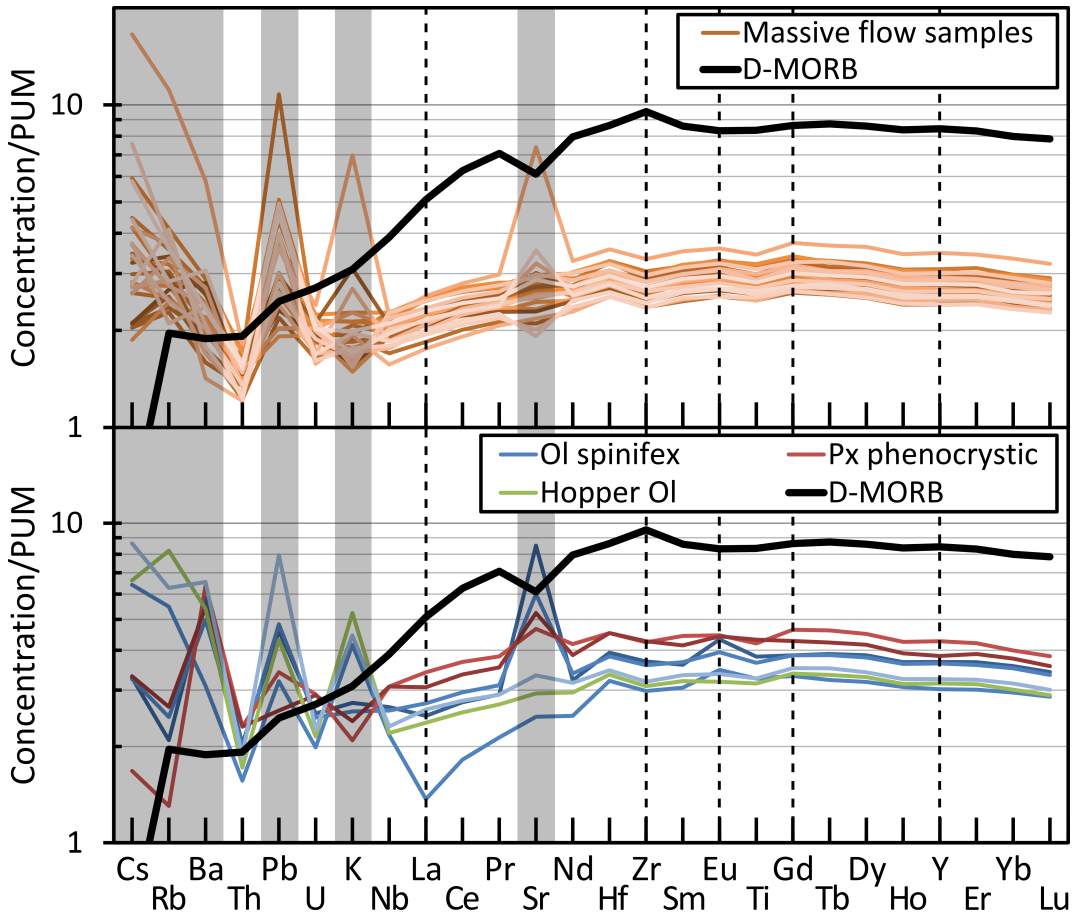

Figure 2.5: Trace element spidergram normalised to PUM (Hofmann, 1988). Element order after Sun & McDonough (1989), except for the position of Pb, which follows Salters & Stracke (2004). All massive flow samples (n = 27) analysed are shown in the top diagram, samples from differentiated flows are subdivided in the lower plot. Fluid mobile elements are highlighted in grey. Thick black line is the average DMORB of Gale *et al.* (2013). Slight negative Zr anomalies are likely an analytical artefact (Section 2.3).

Table 2.2: Bulk rock major and minor element data measured by XRF, and minor and trace element data measured by solution ICP-MS for Winnipegosis Komatiites. Data normalisation and table layout as in Table 2.1. Rock types: 'Mass. K.' = massive komatiite, 'Min. K.' = mineralised komatiite, 'Serp. dun.' = serpentinised dunite, 'D.K.' = differentiated komatiite. Subtypes within differentiated komatiite flows: 'ol spin.' = olivine spinifex, 'chill' = chilled margin, 'aci. px' = acicular pyroxene zone, 'hopper' = hopper olivine cumulates.

	RP1A-8a	RP1A-8b	RP1A-8c	RP1A-8av.	RP1A-15	RP1A-18	RP1A-20
Rock Type	Mass. K.	Mass. K.	Mass. K.	Mass. K.	Mass. K.	Mass. K.	Mass. K.
SiO_2 *(wt%)*	45.21	46.12	45.78	45.70	46.47	46.57	47.15
TiO_2	0.45	0.45	0.45	0.45	0.51	0.51	0.57
Al_2O_3	7.83	7.74	7.79	7.79	8.78	8.79	9.83
FeO_t	11.24	11.20	11.26	11.24	11.41	11.29	11.40
MnO	0.18	0.18	0.18	0.18	0.18	0.18	0.18
MgO	26.53	25.84	26.04	26.14	22.81	22.80	19.91
CaO	7.45	7.39	7.41	7.42	8.38	8.40	9.39
Na_2O	1.01	0.99	0.99	0.99	1.36	1.36	1.46
K_2O	0.064	0.073	0.069	0.069	0.055	0.062	0.070
P_2O_5	0.036	0.035	0.035	0.035	0.036	0.045	0.040
Total	99.52	99.48	99.32	99.44	99.16	99.33	99.49
LOI	3.04	3.10	3.02	3.01	2.18	2.40	2.67
V (ppm)	169	154	170	164	180	179	203
Cr	2546	2503	2546	2532	2167	2117	1879
Sc	26.9	27.6	26.6	27.1	31.7	29.7	30.5
Co	105.8	103.7	101.0	103.5	104.3	96.0	80.7
Ni	1237	1266	1254	1252	1084	1001	743
Cu	70.8	107.1	68.1	82.0	85.9	79.1	81.3
Rb	1.34	1.38	1.37	1.36	1.26	1.22	1.63
Sr	37.4	38.7	38.5	38.2	50.6	47.0	54.1
Y	9.26	9.59	9.56	9.47	11.63	10.71	12.19
Zr	22.5	23.2	23.0	22.9	28.2	25.7	29.6
Nb	1.03	1.06	1.05	1.05	1.27	1.20	1.41
Cs	0.055	0.058	0.056	0.057	0.056	0.055	0.080
Ba	10.3	11.0	10.6	10.6	11.8	9.6	12.4
La	1.11	1.14	1.14	1.13	1.41	1.31	1.51
Ce	3.18	3.25	3.22	3.22	4.02	3.74	4.24
Pr	0.51	0.52	0.52	0.51	0.63	0.59	0.67
Nd	2.67	2.78	2.76	2.74	3.42	3.13	3.57
Sm	0.94	0.96	0.95	0.95	1.20	1.08	1.22
Eu	0.36	0.38	0.37	0.37	0.46	0.42	0.48
Gd	1.34	1.35	1.34	1.34	1.68	1.54	1.71
Tb	0.24	0.25	0.24	0.24	0.30	0.27	0.31
Dy	1.56	1.64	1.62	1.61	1.99	1.80	2.06
Ho	0.34	0.35	0.34	0.34	0.43	0.39	0.44
Er	0.98	1.02	1.01	1.00	1.24	1.12	1.30
Yb	0.95	0.98	0.98	0.97	1.20	1.09	1.23
Lu	0.14	0.15	0.14	0.14	0.18	0.16	0.18
Hf	0.67	0.69	0.68	0.68	0.86	0.77	0.88
Pb	0.34	0.36	0.45	0.38	0.89	0.87	1.89
Th	0.095	0.101	0.101	0.099	0.121	0.109	0.135
U	0.031	0.034	0.034	0.033	0.040	0.034	0.039

Table 2.2: continued

	RP1A-31	RP1A-53	RP1A-65	RP1A-79	RP1A-87	RP1A-90	RP1A-95
Rock Type	Mass. K.	Mass. K.	Mass. K.	Mass. K.	Mass. K.	Mass. K.	Mass. K.
SiO_2 *(wt%)*	46.26	46.02	46.15	46.62	45.76	44.95	47.16
TiO_2	0.50	0.54	0.50	0.53	0.50	0.48	0.58
Al_2O_3	8.54	9.02	8.57	9.06	8.50	8.23	9.92
FeO_t	11.40	11.76	11.37	11.45	11.40	11.24	11.53
MnO	0.18	0.20	0.18	0.17	0.18	0.20	0.19
MgO	23.49	22.97	23.83	22.31	24.04	22.50	19.82
CaO	8.28	8.55	8.13	8.50	8.32	11.37	9.24
Na_2O	1.25	0.81	1.16	1.24	1.19	0.89	1.44
K_2O	0.067	0.096	0.075	0.077	0.055	0.103	0.083
P_2O_5	0.036	0.037	0.036	0.039	0.037	0.039	0.041
Total	99.69	98.89	99.43	99.38	99.32	99.15	99.34
LOI	3.10	4.43	2.50	2.54	2.31	5.70	2.29
V (ppm)	178		188	173	180		201
Cr	2218		2250	2023	2219		1940
Sc	28.1		28.9	31.7	26.0		33.8
Co	97.6	85.4	99.8	96.3	90.6	82.7	88.0
Ni	1048	907	1064	1038	1029	831	819
Cu	75.6	68.6	74.0	81.1	73.1	73.5	97.4
Rb	1.35	2.54	1.90	2.21	1.46	2.46	1.55
Sr	50.4	38.7	48.7	53.5	48.2	61.9	51.2
Y	10.35	10.96	10.49	11.25	10.64	11.67	11.96
Zr	25.3	26.4	25.6	27.6	25.9	28.8	28.9
Nb	1.19	1.23	1.20	1.33	1.29	1.41	1.40
Cs	0.070	0.230	0.120	0.159	0.099	0.116	0.112
Ba	12.2	31.6	16.5	17.5	14.6	15.3	16.3
La	1.28	1.33	1.37	1.52	1.38	1.54	1.55
Ce	3.65	3.66	3.70	4.21	3.79	4.20	4.35
Pr	0.57	0.58	0.58	0.66	0.60	0.67	0.68
Nd	3.03	3.13	3.10	3.45	3.15	3.55	3.60
Sm	1.07	1.09	1.07	1.18	1.08	1.22	1.23
Eu	0.41	0.40	0.41	0.45	0.42	0.45	0.48
Gd	1.50	1.47	1.51	1.65	1.50	1.62	1.74
Tb	0.26	0.28	0.26	0.28	0.27	0.31	0.31
Dy	1.76	1.84	1.77	1.91	1.79	2.03	2.03
Ho	0.37	0.39	0.38	0.41	0.38	0.43	0.44
Er	1.08	1.14	1.10	1.18	1.11	1.27	1.25
Yb	1.07	1.10	1.08	1.14	1.06	1.21	1.23
Lu	0.16	0.16	0.16	0.17	0.16	0.18	0.18
Hf	0.74	0.78	0.75	0.82	0.76	0.85	0.87
Pb	0.53	2.49	0.70	0.77	0.50	0.24	0.66
Th	0.110	0.110	0.116	0.140	0.124	0.124	0.139
U	0.037	0.036	0.037	0.044	0.041	0.045	0.045

Table 2.2: continued

	RP1A-99	RP1A-101	RP1A-105	RP1A-111	RP1A-112	RP1A-113	RP1A-120
Rock Type	Mass. K.	Mass. K.	Mass. K.	Mass. K.	Mass. K.	Mass. K.	Mass. K.
SiO_2 *(wt%)*	46.36	45.97	45.71	45.93	47.00	46.28	48.18
TiO_2	0.51	0.47	0.48	0.47	0.52	0.51	0.62
Al_2O_3	8.66	7.97	8.20	8.04	8.72	8.57	10.71
FeO_t	11.14	11.08	11.43	11.22	11.32	11.11	11.48
MnO	0.18	0.18	0.18	0.18	0.18	0.18	0.18
MgO	23.31	25.09	24.85	25.42	21.71	23.74	16.79
CaO	8.50	8.16	7.94	7.56	9.17	8.33	10.17
Na_2O	1.22	0.98	1.12	1.09	1.23	1.16	1.56
K_2O	0.077	0.064	0.054	0.057	0.113	0.083	0.254
P_2O_5	0.037	0.037	0.036	0.035	0.037	0.037	0.048
Total	99.42	99.34	99.24	99.47	99.28	99.27	99.38
LOI	2.30	2.94	2.45	2.62	2.05	2.55	2.96
V (ppm)	179	168	178	157	184	179	227
Cr	2135	2301	2245	2367	2031	2137	1430
Sc	29.6	28.3	29.6	28.8	31.0	30.5	32.8
Co	98.6	103.9	105.8	104.5	95.4	100.0	71.5
Ni	1109	1260	1253	1296	1045	1159	515
Cu	83.3	78.4	79.2	74.6	86.5	87.0	97.2
Rb	1.71	1.47	1.31	1.43	1.82	1.33	5.96
Sr	47.4	44.6	42.3	41.7	54.8	45.8	134.7
Y	10.75	9.81	9.93	9.75	10.92	10.59	13.71
Zr	26.4	24.0	24.3	23.7	26.4	25.9	32.3
Nb	1.29	1.17	1.18	1.20	1.29	1.27	1.37
Cs	0.089	0.074	0.050	0.056	0.087	0.076	0.443
Ba	14.6	11.9	13.3	16.9	15.6	12.7	35.1
La	1.41	1.27	1.29	1.28	1.40	1.37	1.57
Ce	3.92	3.57	3.63	3.56	3.94	3.84	4.47
Pr	0.61	0.55	0.57	0.55	0.62	0.60	0.72
Nd	3.24	2.94	2.98	2.93	3.24	3.17	3.90
Sm	1.11	1.02	1.03	1.01	1.12	1.10	1.36
Eu	0.43	0.39	0.39	0.39	0.43	0.42	0.52
Gd	1.56	1.41	1.45	1.41	1.57	1.54	1.91
Tb	0.27	0.24	0.25	0.25	0.27	0.27	0.34
Dy	1.82	1.66	1.68	1.64	1.83	1.80	2.32
Ho	0.39	0.36	0.36	0.36	0.40	0.38	0.49
Er	1.14	1.04	1.05	1.03	1.14	1.11	1.43
Yb	1.10	1.01	1.03	1.00	1.11	1.07	1.38
Lu	0.16	0.15	0.15	0.15	0.16	0.16	0.20
Hf	0.77	0.71	0.73	0.71	0.78	0.75	0.95
Pb	0.88	0.45	0.34	0.40	0.52	0.36	0.64
Th	0.127	0.114	0.119	0.119	0.125	0.122	0.147
U	0.044	0.037	0.039	0.039	0.043	0.041	0.049

Table 2.2: continued

	RP1A-140	RP1A-141	RP1A-147	RP1A-148	RP1A-150	RP1A-153
Rock Type	Mass. K.	Mass. K.	Mass. K.	Mass. K.	Mass. K.	Mass. K.
SiO_2 *(wt%)*	45.79	45.21	47.09	46.87	46.64	45.99
TiO_2	0.45	0.50	0.54	0.54	0.52	0.56
Al_2O_3	7.69	8.44	9.37	9.28	8.98	9.39
FeO_t	11.23	11.48	11.43	11.30	11.22	11.71
MnO	0.18	0.19	0.18	0.18	0.18	0.19
MgO	25.67	25.05	21.02	21.05	22.61	22.12
CaO	7.95	8.01	9.02	9.21	8.52	8.84
Na_2O	0.94	1.00	1.25	1.43	1.23	1.10
K_2O	0.070	0.081	0.060	0.098	0.062	0.054
P_2O_5	0.035	0.036	0.041	0.041	0.040	0.037
Total	99.59	99.16	99.40	99.30	99.67	99.08
LOI	3.47	3.17	2.40	2.36	2.22	2.63
V (ppm)	176		195	187	185	
Cr	2620		1987	2004	2107	
Sc	26.5		33.2	31.3	28.1	
Co	98.5	90.0	94.2	87.1	86.8	83.4
Ni	1224	1031	931	883	926	843
Cu	62.0	60.5	88.2	83.3	69.5	70.3
Rb	1.98	2.52	1.59	1.79	1.53	1.53
Sr	39.6	43.6	49.7	58.7	47.1	44.4
Y	9.79	10.25	11.67	11.50	11.03	11.33
Zr	22.9	25.0	27.9	27.4	26.1	27.4
Nb	0.97	1.11	1.16	1.14	1.09	1.13
Cs	0.111	0.113	0.093	0.070	0.073	0.099
Ba	8.6	10.8	10.7	16.4	10.2	10.9
La	1.08	1.16	1.30	1.28	1.23	1.31
Ce	3.06	3.27	3.79	3.74	3.59	3.68
Pr	0.50	0.53	0.61	0.60	0.57	0.60
Nd	2.72	2.91	3.28	3.25	3.11	3.30
Sm	0.96	1.03	1.18	1.15	1.10	1.17
Eu	0.37	0.39	0.46	0.45	0.43	0.44
Gd	1.36	1.42	1.66	1.63	1.57	1.58
Tb	0.25	0.27	0.29	0.29	0.28	0.30
Dy	1.66	1.78	1.96	1.95	1.87	2.00
Ho	0.35	0.38	0.42	0.41	0.40	0.43
Er	1.04	1.11	1.22	1.20	1.16	1.24
Yb	0.98	1.05	1.19	1.16	1.13	1.17
Lu	0.15	0.16	0.18	0.17	0.17	0.18
Hf	0.68	0.76	0.82	0.81	0.78	0.83
Pb	0.67	0.62	0.48	0.42	0.53	0.71
Th	0.098	0.096	0.110	0.109	0.103	0.101
U	0.032	0.035	0.038	0.034	0.035	0.038

Table 2.2: continued

	RP12-282.5	RP12-305.3	RP12-306.1	RP12-307.3	RP12-308.3	RP12-311.5	RP12-326
Rock Type	D.K. (ol spin.)	D.K. (ol spin.)	D.K. (ol spin.)	D.K. (aci. px)	D.K. (aci. px)	D.K. (hopper)	D.K. (ol spin.)
SiO_2 *(wt%)*	47.82	47.77	47.83	49.73	50.03	48.57	48.00
TiO_2	0.59	0.69	0.66	0.76	0.78	0.57	0.59
Al_2O_3	10.01	11.97	11.65	13.13	13.71	10.02	10.29
FeO_t	11.56	11.10	11.88	11.33	11.18	12.17	11.49
MnO	0.17	0.19	0.18	0.15	0.13	0.18	0.18
MgO	19.76	16.31	15.27	10.56	10.55	18.19	18.50
CaO	8.56	10.00	10.51	11.87	10.84	9.08	9.35
Na_2O	1.34	1.82	1.87	2.33	2.64	0.99	1.39
K_2O	0.152	0.100	0.094	0.076	0.087	0.190	0.162
P_2O_5	0.041	0.050	0.048	0.052	0.054	0.043	0.045
Total	99.87	99.60	99.52	99.60	99.76	99.58	99.42
LOI	4.39	4.42	3.07	1.38	1.86	3.24	2.67
V (ppm)	200	243	241	269	269	201	194
Cr	1646	1188	1034	825	619	1773	1580
Sc	33.1	36.0	34.0	39.9	42.3	34.2	33.7
Co	84.9	60.6	63.3	56.1	69.5	86.8	82.8
Ni	711	397	338	146	364	464	692
Cu	128.3	34.6	72.0	132.2	118.7	83.8	87.5
Rb	2.93	1.12	1.32	0.70	1.42	4.39	3.36
Sr	45.1	155.0	109.2	85.1	95.4	53.4	60.8
Y	11.90	14.48	14.32	16.84	15.13	12.40	12.80
Zr	29.0	35.9	34.9	41.1	41.5	30.0	31.0
Nb	1.34	1.64	1.60	1.90	1.90	1.36	1.43
Cs	0.172	0.088	0.087	0.045	0.089	0.177	0.232
Ba	18.7	35.3	30.2	38.6	33.0	32.6	39.6
La	0.84	1.53	1.68	2.10	1.88	1.46	1.60
Ce	2.91	4.41	4.73	5.89	5.38	4.09	4.46
Pr	0.52	0.70	0.75	0.93	0.86	0.66	0.70
Nd	2.97	3.84	4.02	4.97	4.59	3.51	3.76
Sm	1.18	1.39	1.42	1.71	1.60	1.24	1.29
Eu	0.51	0.63	0.57	0.65	0.64	0.46	0.49
Gd	1.71	1.98	1.98	2.38	2.19	1.74	1.80
Tb	0.30	0.37	0.36	0.43	0.40	0.31	0.33
Dy	2.03	2.46	2.42	2.87	2.65	2.10	2.18
Ho	0.44	0.52	0.52	0.60	0.56	0.45	0.46
Er	1.26	1.53	1.50	1.76	1.62	1.31	1.35
Yb	1.22	1.48	1.46	1.66	1.56	1.25	1.30
Lu	0.18	0.22	0.21	0.24	0.23	0.18	0.19
Hf	0.86	1.05	1.02	1.21	1.21	0.90	0.93
Pb	0.56	0.81	0.84	0.60	0.45	0.76	1.39
Th	0.127	0.165	0.161	0.188	0.188	0.140	0.151
U	0.040	0.052	0.050	0.059	0.059	0.044	0.046

Table 2.2: continued

	RP12-394	RP12-404.3	RP12-419.4	RP12-428.5	RP12-433.6	RP12-438.8	RP12-457.3
Rock Type	Mass. K.	Mass. K.	Mass. K.	Mass. K.	Mass. K.	Mass. K.	Mass. K.
SiO_2 *(wt%)*	47.38	47.33	46.32	45.88	46.19	46.05	46.78
TiO_2	0.52	0.56	0.49	0.46	0.47	0.48	0.51
Al_2O_3	8.92	9.45	8.41	7.77	7.83	8.14	8.65
FeO_t	11.29	11.37	11.43	11.15	11.23	11.11	11.42
MnO	0.18	0.18	0.18	0.18	0.18	0.18	0.18
MgO	22.04	20.82	24.05	26.04	25.61	24.73	22.91
CaO	8.45	9.02	7.98	7.33	7.61	8.13	8.31
Na_2O	1.13	1.17	1.04	1.09	0.78	1.10	1.13
K_2O	0.058	0.056	0.060	0.064	0.071	0.062	0.072
P_2O_5	0.039	0.041	0.038	0.033	0.033	0.035	0.038
Total	99.44	99.41	99.28	99.38	99.41	99.55	99.47
LOI	2.89	3.34	3.12	4.62	3.64	3.17	2.82
V (ppm)	188	189	186	174	173	173	189
Cr	2092	2034	2330	2641	2580	2304	2176
Sc	29.8	32.3	28.1	27.1	28.7	28.3	30.2
Co	90.0	89.5	95.3	98.1	101.1	99.0	94.0
Ni	959	879	1105	1227	1230	1198	1045
Cu	81.5	88.7	76.2	71.1	69.4	75.7	81.6
Rb	1.47	1.13	1.31	2.02	2.20	1.52	1.92
Sr	54.4	53.3	46.3	36.6	34.9	64.4	52.2
Y	11.35	11.85	10.41	9.48	9.97	10.07	10.95
Zr	27.5	28.8	25.7	22.8	23.6	24.5	26.4
Nb	1.35	1.40	1.24	1.11	1.14	1.20	1.30
Cs	0.098	0.100	0.092	0.203	0.075	0.118	0.156
Ba	14.5	14.3	12.3	12.6	10.8	18.5	14.1
La	1.44	1.51	1.31	1.19	1.22	1.33	1.41
Ce	4.04	4.23	3.66	3.34	3.44	3.67	3.89
Pr	0.64	0.67	0.58	0.53	0.54	0.58	0.61
Nd	3.40	3.58	3.12	2.81	2.94	3.05	3.25
Sm	1.16	1.21	1.06	0.98	1.01	1.03	1.12
Eu	0.45	0.47	0.41	0.37	0.39	0.39	0.43
Gd	1.60	1.67	1.47	1.36	1.40	1.41	1.54
Tb	0.29	0.31	0.26	0.24	0.25	0.26	0.28
Dy	1.93	2.02	1.77	1.61	1.70	1.71	1.86
Ho	0.40	0.43	0.38	0.34	0.36	0.37	0.40
Er	1.20	1.26	1.10	1.00	1.06	1.07	1.15
Yb	1.15	1.21	1.05	0.96	1.02	1.03	1.09
Lu	0.17	0.18	0.16	0.14	0.15	0.15	0.17
Hf	0.82	0.86	0.76	0.68	0.70	0.74	0.79
Pb	0.83	0.63	0.46	0.70	0.49	0.86	0.80
Th	0.120	0.129	0.110	0.099	0.102	0.124	0.126
U	0.040	0.044	0.038	0.033	0.034	0.041	0.041

2.4.2 Mineral chemistry

Olivine

Randomly selected fresh olivine from samples RP1A-8, RP1A-18, RP1A-99, and RP1A-111 show a range of Mg# between 0.923 and 0.889 (where Mg# = molar Mg/[Mg + Fe]), with a strong peak in relative frequency about 0.907 (n = 183; Table 2.3, Figure 2.6). To avoid Fe-enriched domains (Section 1.4.3), only olivine cores were analysed; high Mg# olivine is likely over-represented. A set of 160 olivine core analyses from the GSC database, measured from 62 samples, shows an indistinguishable mode at Mg# 0.905. Olivine grains selected for Al-in-olivine thermometry are excluded from the histogram in (Figure 2.6) to avoid bias in the distribution. However, these show consistently lower Mg# than the randomly selected points, with a range in Mg# from 0.912 to 0.872, and a mode at 0.902 (150 analyses, 30 olivine grains). The maximum olivine Mg# from a given sample does not appear to correlate with bulk rock MgO, though is an apparent trend towards higher Mg# olivine up-sequence (towards lower samples numbers) in the GSC data from borehole RP1A (Figure 2.7).

The elements Ca, Mn, Al, and Co in olivine are negatively correlated with Mg#, whereas Ni and Cr show positive correlations (Figure 2.8). High concentrations of Ca and Cr preclude these olivine grains from being mantle-derived xenocrysts (Simkin & Smith, 1970). Some analyses from chromite-hosting olivine grains show scatter towards higher Cr contents. Modelling using the PENEPMA program (Llovet *et al.*, 2012) shows that this is likely caused by secondary fluorescence from enclosed chromite, which can affect olivine Cr data by > 100 ppm at distances up to 100 μm from the grain boundary (Figure 2.9). These analyses are not excluded from the Al-in-olivine thermometry as they do not show similarly elevated Al contents; modelling shows secondary fluorescence of Al should fall to < 1 ppm levels within 15 microns of the olivine-chromite boundary. Phosphorus was below the limit of determination of 0.01 wt%, and so coupled Al – P $\rightleftharpoons$ Si – Si substitution should have a minimal effect on the calculated temperatures (Coogan *et al.*, 2014). The consistent trends between trace elements in olivine and Mg# indicate that altered Fe-enriched domains (Section 1.4.3) were successfully avoided during analysis.

Table 2.3: Representative EPMA analyses from randomly selected RP1A komatiite olivine (i.e. not from olivine-chromite pairs used for Al-in-olivine temperatures). Both the maximum Mg# (max Mg#) routine and high precision ('high prec.') analyses are shown, along with the minimum Mg# (min Mg#) analysis, 75th percentile (75th %), median, and 25th percentile high precision olivine analyses by Mg#. 'NQ' = not quantifiable, concentrations below limit of determination (Section B.2). The full dataset of olivine analyses can be found in the supplementary information to Waterton *et al.* (2017).

Sample	RP1A-8	RP1A-111	RP1A-111	RP1A-111	RP1A-99	RP1A-111
grain	ol63	ol32	ol08	ol30	ol11	ol23
	max Mg#	max Mg#	75th %	median	25th %	min Mg#
Analysis	routine	high prec.	high prec.	high prec.	high prec.	high prec.
SiO_2 *(wt%)*	40.25	40.231	40.096	39.949	40.182	39.856
TiO_2	NQ	NQ	NQ	NQ	NQ	NQ
Al_2O_3	0.07	0.077	0.075	0.070	0.069	0.074
Cr_2O_3	0.16	0.182	0.157	0.148	0.148	0.111
MnO	0.11	0.125	0.140	0.137	0.146	0.157
FeO	7.42	7.950	8.709	8.985	9.251	10.193
CoO	0.02	0.016	0.014	0.012	0.016	0.015
NiO	0.41	0.425	0.404	0.396	0.379	0.370
MgO	49.90	50.089	49.508	49.161	48.923	48.302
CaO	0.25	0.259	0.259	0.264	0.273	0.281
Na_2O	NQ	NQ	NQ	NQ	NQ	NQ
K_2O	NQ	NQ	NQ	NQ	NQ	NQ
P_2O_5	NQ	NQ	NQ	NQ	NQ	NQ
Total	98.62	99.388	99.375	99.132	99.398	99.376
Mg#	0.923	0.9182	0.9102	0.9070	0.9041	0.8941
Al (ppm)		405	396	368	367	391
Cr		1246	1076	1011	1015	757
Mn		964	1087	1064	1132	1212
Co		126	113	94	127	116
Ni		3341	3174	3113	2981	2908
Ca		1849	1852	1886	1952	2009

Chromite

Chromite grains measured for Al-in-olivine – spinel thermometry have Cr# (Cr# = Cr/[Cr + Al]) in the range 0.64 – 0.72, overlapping the calibrated range of the thermometer (Cr# 0 – 0.69; Coogan *et al.*, 2014). Stoichiometrically determined (Droop, 1987) chromite Fe^{3+} contents (0.12 – 0.20 Fe^{3+} cations per formula unit; pfu) lie slightly outside the thermometer calibration range. However, the correlation between Fe^{3+} and temperature within the calibrated range is considered weak (Coogan *et al.*, 2014) or non-existent (Wan *et al.*, 2008), affecting calculated temperatures by less than the overall uncertainty in the calibration of ± 25 °C. It is also noted that the calculated Fe^{3+} contents of Winnipegosis chromite fall well within the range observed for chromite from

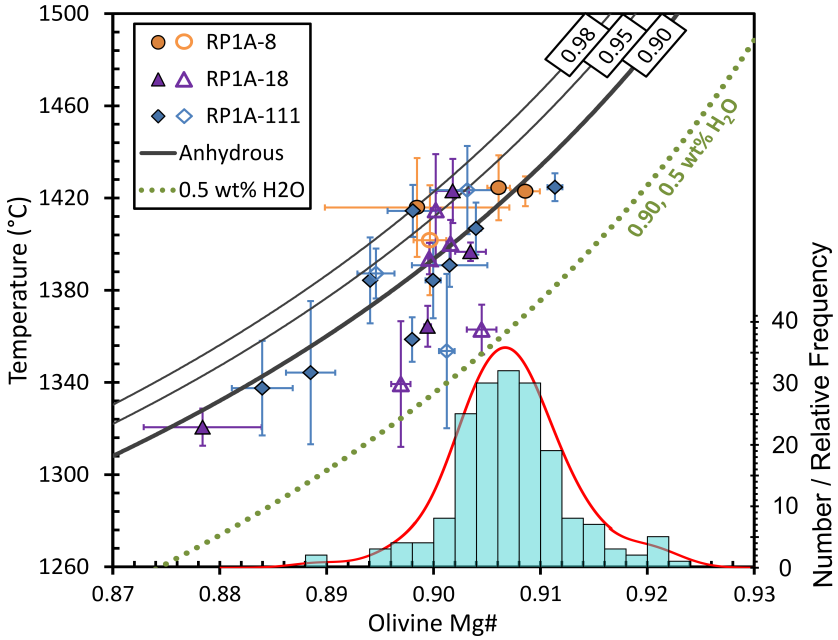

Figure 2.6: Average Al-in-olivine temperatures for olivine-chromite pairs, plotted as a function of olivine Mg#. Olivine-chromite pairs are grouped by sample and Fe-Mg equilibration temperature (Ballhaus *et al.*, 1991); solid symbols indicate high Fe-Mg equilibration temperatures (> 900 °C), open symbols indicate low Fe-Mg equilibration temperatures (< 900 °C). Error bars are 1 standard deviation of the 5 repeated analyses for each olivine. Histogram (light blue blocks) and probability density function (red line) show Mg# of olivine cores (n = 183). Grey curves are temperatures determined from anhydrous olivine Fe-Mg partitioning as a function of Mg#, shown for liquid $Fe^{2+}/\Sigma Fe = 0.90$ (the preferred value), 0.95, and 0.98 (upper bounds determined from V/Sc partitioning). Green dotted curve shows temperature – Mg# relationship for $Fe^{2+}/\Sigma Fe = 0.90$ in a melt containing 0.5 wt% H_2O. See Section 2.5.4 for curve calculation details.

Phanerozoic LIPs (0.07 – 0.23 Fe^{3+} cations pfu; Coogan *et al.*, 2014), and do not show evidence of replacement by metamorphic magnetite (e.g., Evans & Frost, 1975). All chromite grains analysed contain < 0.5 wt% MnO, and pass the Barnes (1998) MnO – Mg# filter for post-eruptive alteration. Some small chromite grains yielded SiO_2 values up to several wt%, significantly higher than those typically expected for komatiitic chromites (up to 0.23 wt%; Barnes, 1998). This is attributed to secondary fluorescence from the host olivine, and an arbitrary cut-off of 0.5 wt% SiO_2 is used to screen out affected analyses.

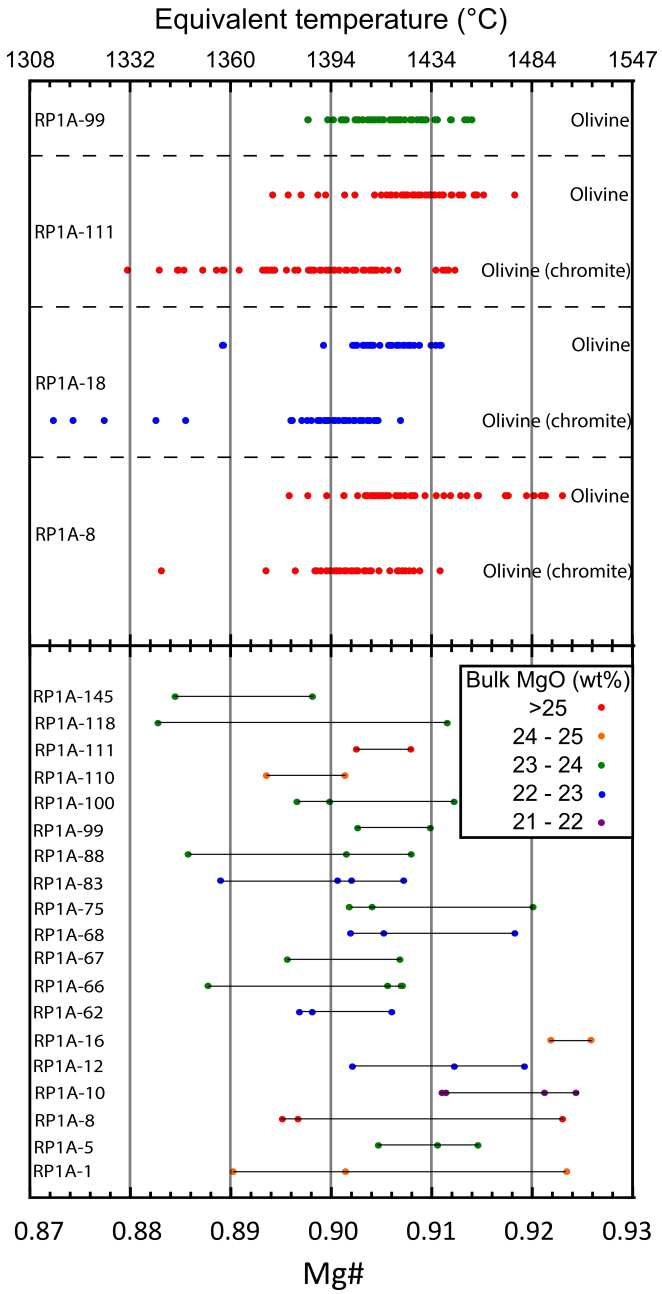

Figure 2.7: Mg# ranges of olivine cores from various Winnipegosis komatiite samples, measured for this study (above), and from samples with multiple analyses in the GSC database (below). Equivalent temperature calculated as described in Section 2.5.4 is shown on the secondary axis at the top of the plot. Data from this study is subdivided into data from randomly selected olivines ('Olivine') and olivines from olivine – chromite pairs used for Al-in-olivine thermometry ('Olivine (chromite)'). Both datasets show wide ranges of olivine Mg# in individual samples, crystallised over a large temperature interval, which do not correlate with the bulk rock MgO. Note that some of the highest Mg# olivines are found in RP1A-10, the lowest bulk rock MgO sample plotted here.

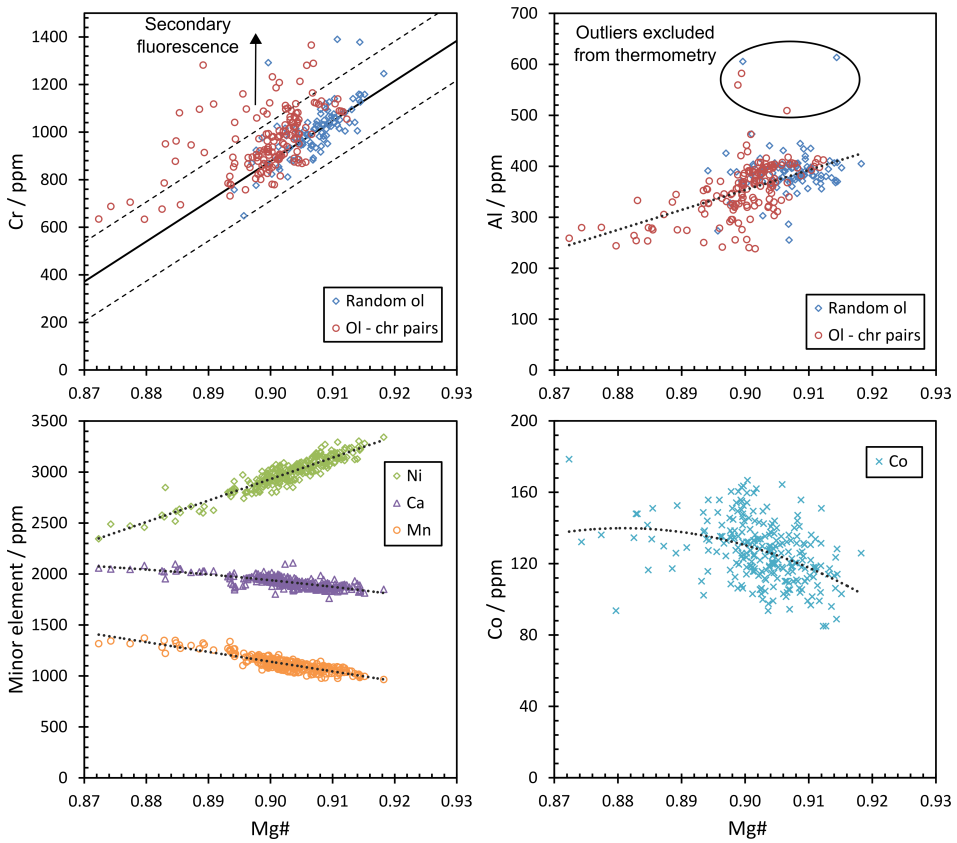

Figure 2.8: Minor and trace elements in olivine measured by high precision EPMA, plotted as a function of Mg#. Solid black line in Cr plot is a regression of the random olivine data, with dashed lines showing 3σ uncertainty about the regression; ~99% of the data should lie within these dashed lines for normally distributed random errors. Only three of the randomly selected olivine data plot outside these bounds, whereas many of the analyses from olivine-chromite pairs show elevated Cr, indicative of secondary fluorescence. No similar distinction can be made for the Al data, except for the lower Mg# of the olivine-chromite pairs, suggesting secondary fluorescence did not affect the Al data. Five high Al outlier points excluded from Al-in-olivine thermometry are indicated. Dotted lines are approximate trends for all other minor and trace elements.

Al-in-olivine temperatures

Average Al-in-olivine temperatures from olivine-chromite pairs are shown in Figure 2.6, plotted as a function of olivine Mg#. The full dataset of high precision olivine-chromite pair analyses can be found in the supplementary information to Waterton *et al.* (2017). The olivine-chromite pairs are grouped by sample and Fe-Mg exchange equilibration temperature (Ballhaus *et al.*, 1991). Open symbols indicate Fe-Mg equilibration temperatures < 900 °C, which suggest that the olivine-chromite pairs underwent extensive

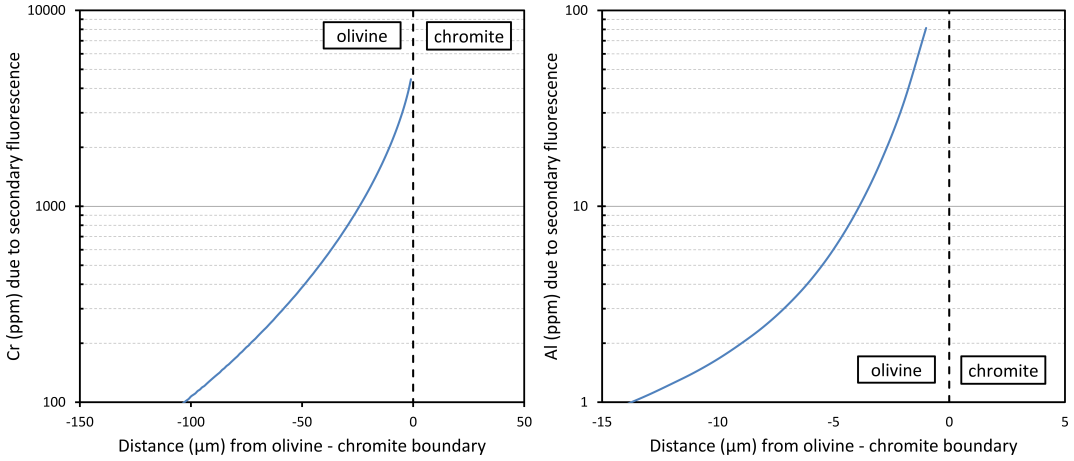

Figure 2.9: Modelling using the PENEPMA program (Llovet *et al.*, 2012) to show the effect of secondary fluorescence of Al and Cr in olivine from an adjacent chromite. The model assumes that the olivine and chromite are touching semi-infinite masses, and is therefore a 'worst case' model for a large chromite (relative to the travel distance of X-rays in the material) included in an olivine; secondary fluorescence effects are smaller for small chromites. Cr shows much stronger secondary fluorescence effects due to its higher atomic number.

subsolidus exchange of Fe and Mg with their host olivines. In general, these pairs retain high, magmatic Al-in-olivine temperatures, confirming that this thermometer is less susceptible to resetting by diffusion than Mg-Fe exchange thermometers (Wan *et al.*, 2008). However, it should be noted that the lowest Al-in-olivine temperatures at a given Mg# are from pairs with low Fe-Mg equilibration temperatures, which may indicate limited subsolidus Al exchange in some cases of extensive subsolidus Fe-Mg exchange. The Al-in-olivine temperatures range from ∼1425 to ∼1320 °C and correlate with Mg#. None of the chromite-hosting olivine crystals analysed had Mg# > 0.912 adjacent to the chromite inclusions.

The average uncertainty (1σ absolute of five Al measurements in each olivine) is ± 14 °C, less than the uncertainty in the thermometer calibration. However, these uncertainties are generally far larger than analytical errors, with the largest uncertainty of ± 33 °C (1σ absolute) reflecting an uncertainty in the measured Al concentration of ± 14% (1σ relative). This, combined with the relative constancy of temperatures determined from other olivine-chromite pairs (as low as ± 4 °C, 1σ absolute) is best explained by zoning in the Al content of some olivine grains (Coogan *et al.*, 2014).

2.4.3 Revised age of the Winnipegosis Komatiite Belt

TIMS U-Pb data

The original zircon U-Pb data acquired and presented in Hulbert *et al.* (1994) is shown in Table 2.4 and Figure 2.10. These data are not straightforward to interpret. Firstly, the analyses contain high contents of common lead, far above the typical blank levels at the GSC geochronology lab at the time (Richard Stern, personal communication, 2016). Given the common presence of metamictised and altered zones in some zircons, this high common lead was likely introduced during alteration. Secondly, the zircon data do not all record the same age. Five of the data (fractions A, B, C, D, F; black error ellipses) are consistent with an age of 1864 $^{+6}_{-4}$ Ma, with a high probability of fit of 0.84, but due to the very large analytical errors for fractions A, B, and D, this is essentially a two point regression. The remaining datum (fraction E, red error ellipse) yields an apparently older $^{207}Pb/^{206}Pb$ age of 1886 ± 8 Ma. If included in the regression an average age of 1869 ± 22 Ma is found, though a high MSWD (6.8) and zero probability of fit suggest that it is not valid to include this point in any average.

One possible interpretation is that the cumulate rock formed at 1864 $^{+6}_{-4}$ Ma, but included a xenocryst of 1886 ± 8 Ma material. This interpretation implies two phases of magmatism in the Winnipegosis. However, as the younger age is primarily constrained by two analyses, and the only concordant, precise analysis contains one of the lowest ratios of radiogenic to common lead, there appears to be insufficient high quality data to make this distinction. Instead, the age of 1864 $^{+6}_{-4}$ Ma is considered to be a minimum crystallisation age, and the age indicated by these data is interpreted to be broadly in the region of 1860 – 1890 Ma. Given the clear evidence of zircon alteration, and the difficulty in interpreting the TIMS U-Pb data, this not considered a robust age.

SHRIMP U-Pb data

SHRIMP analyses show high Th/U (Table 2.4, Figure 2.11), consistent with these being primary magmatic zircons that crystallized from a mafic magma (Wang *et al.*, 2011). A single spot had very low concentrations of U and Th, and a high common lead content, as was excluded from averaging, along with two points with > 5% discordance. The remaining 14 spots with < 5% discordance are consistent with a single age population, and yield a $^{207}Pb/^{206}Pb$ age of 1870.3 ± 7.1 Ma with a probability of fit of 0.17. This age overlaps within error, but is slightly older than the previous age determination.

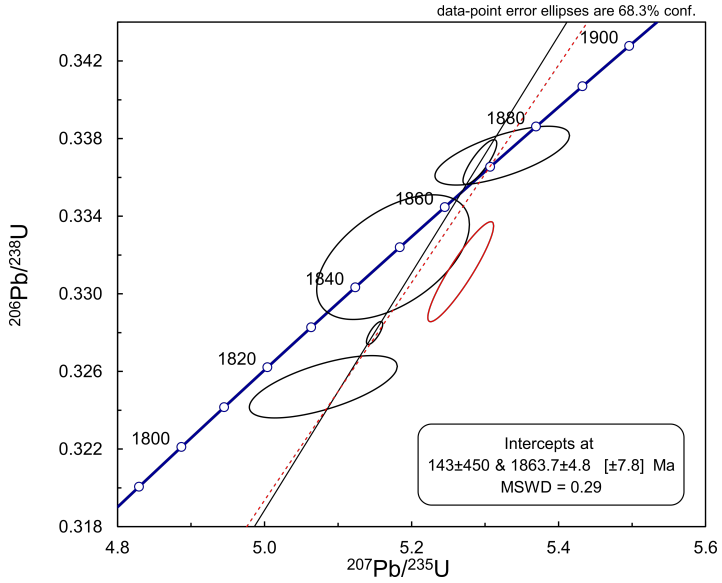

Figure 2.10: All U-Pb single zircon TIMS analyses from RP92-4 coarse pyroxene cumulates (Hulbert *et al.*, 1994). If the red error ellipse is excluded as an outlier, a regression of the data (solid black line) represented by black error ellipses yields an upper intercept age of 1864 $^{+6}_{-4}$ Ma, with an MSWD of 0.29 and a probability of fit of 0.84. If all data points are included in the regression (dashed red line), an upper intercept age of 1869 ± 22 Ma is obtained, with an MSWD of 6.8 and zero probability of fit.

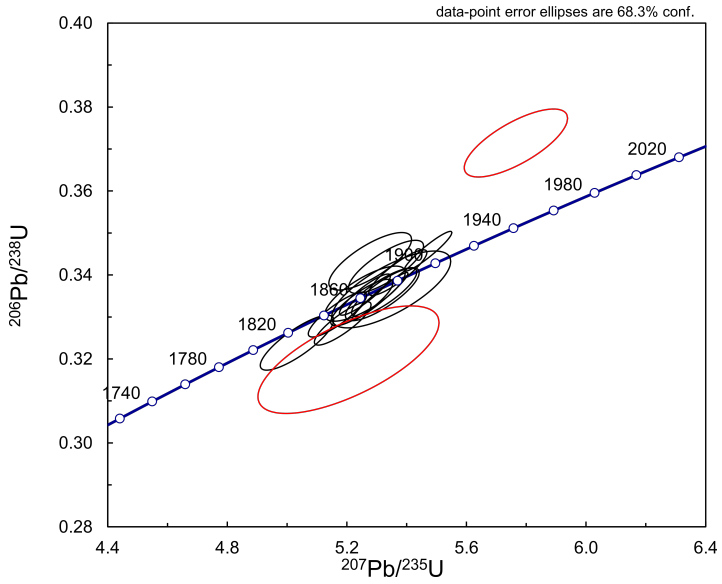

Figure 2.11: Concordia plot of all U-Pb SHRIMP spots on RP92-4 zircons, excluding a spot with high common lead. Black ellipses are $< 5\%$ discordant analyses which were used for the weighted average, red ellipses are $> 5\%$ discordant analyses which were excluded from the weighted average.

Table 2.4: U-Pb zircon data for a coarse grained mafic cumulate from borehole RP92-4. SIMS data from Waterton *et al.* (2017), TIMS data from Hulbert *et al.* (1994). '$1\sigma_{rel}$' = 1σ relative, '$1\sigma_{abs}$' = 1σ absolute, 'ρ' = error correlation coefficient, '%Disc.' = percentage discordance, 'n.d.' = not determined where raw $^{204}Pb/^{206}Pb$ ratios were < 0.

Zircon/ Spot	Type	U / ppm	Th / ppm	^{206}Pb / ppm	$^{232}Th/^{238}U$	$^{204}Pb/^{206}Pb$	$^{208}Pb/^{206}Pb$	$1\sigma_{rel}$ / %	$^{207}Pb/^{235}U$	$1\sigma_{rel}$ / %	$^{206}Pb/^{238}U$	$1\sigma_{rel}$ / %	ρ	$^{207}Pb/^{206}Pb$	$1\sigma_{rel}$ / %	$^{207}Pb/^{206}Pb$ Age / Ma	$1\sigma_{abs}$ / Ma	% Disc.
002.1	SIMS	158	4241	45.6	27.71	$1.6*10^{-5}$	8.253	0.59	5.325	1.4	0.3358	1.1	0.84	0.1150	0.74	1880	13	+0.80
004.1	SIMS	236	6163	66.6	26.98	$4.0*10^{-5}$	8.068	0.47	5.186	1.2	0.3285	1.0	0.86	0.1145	0.62	1872	11	+2.54
005.1	SIMS	86	1073	25.5	12.83	$8.2*10^{-5}$	3.770	1.01	5.278	1.7	0.3433	1.3	0.76	0.1115	1.12	1824	20	–4.94
001.1	SIMS	97	1539	27.8	16.46	$1.0*10^{-4}$	4.961	0.87	5.261	1.7	0.3355	1.3	0.76	0.1137	1.09	1859	20	–0.36
007.1	SIMS	196	5123	55.6	27.04	n.d.	8.016	0.53	5.168	1.2	0.3306	1.1	0.86	0.1134	0.64	1855	12	+0.83
006.1	SIMS	15	90	4.1	6.22	n.d.	1.842	3.33	5.205	3.8	0.3198	2.6	0.69	0.1180	2.79	1927	50	+8.20
013.1	SIMS	115	2091	33.0	18.83	$6.6*10^{-5}$	5.634	0.76	5.319	1.5	0.3354	1.2	0.81	0.1150	0.90	1880	16	+0.93
013.2	SIMS	40	414	11.4	10.81	$1.3*10^{-4}$	3.178	1.63	5.348	2.5	0.3365	1.8	0.73	0.1153	1.68	1884	30	+0.85
042.1	SIMS	624	860	185.3	1.42	n.d.	0.420	1.03	5.471	1.0	0.3456	0.9	0.94	0.1148	0.33	1877	6	–2.28
049.1	SIMS	125	2024	36.6	16.78	$1.2*10^{-4}$	4.938	0.77	5.331	1.6	0.3419	1.2	0.79	0.1131	0.96	1849	17	–2.90
034.1	SIMS	390	71	112.3	0.19	$2.8*10^{-5}$	0.050	6.93	5.260	1.1	0.3353	1.0	0.90	0.1138	0.47	1861	8	–0.22
027.1	SIMS	110	1571	35.2	14.73	$1.5*10^{-4}$	4.563	1.07	5.765	2.0	0.3714	1.4	0.73	0.1126	1.36	1841	25	–12.34
032.1	SIMS	285	6793	83.2	24.66	$1.1*10^{-5}$	7.213	0.51	5.370	1.2	0.3406	1.1	0.88	0.1144	0.56	1870	10	–1.19
042.2	SIMS	633	885	182.0	1.44	$1.8*10^{-5}$	0.423	0.98	5.311	1.2	0.3350	1.1	0.96	0.1150	0.33	1880	6	+1.08
039.1	SIMS	86	1421	23.9	17.06	$8.3*10^{-21}$	5.072	0.93	5.033	1.6	0.3239	1.3	0.83	0.1127	0.91	1844	16	+2.18
038.1	SIMS	167	3716	48.0	22.93	$5.7*10^{-5}$	6.774	0.58	5.250	1.3	0.3334	1.1	0.84	0.1142	0.71	1867	13	+0.75
				Pb / ppm														
A (Z)	TIMS	68		120		$3.6*10^{-3}$	5.05		5.175	1.3	0.3319	0.64	0.52	0.1131	1.13	1849.5	20.2	+0.12
B (Z)	TIMS	82		148		$8.8*10^{-3}$	5.08		5.323	1.1	0.3371	0.30	0.68	0.1145	0.96	1872.4	17.1	–0.02
C (Z)	TIMS	91		170		$7.9*10^{-4}$	5.47		5.150	0.1	0.3280	0.12	0.77	0.1139	0.09	1862.1	1.7	+2.07
D (Z)	TIMS	51		95		$8.9*10^{-3}$	5.53		5.080	1.3	0.3252	0.33	0.66	0.1133	1.12	1852.8	20.0	+2.33
E (Z)	TIMS	48		70		$1.6*10^{-3}$	3.97		5.267	0.6	0.3311	0.51	0.92	0.1154	0.23	1885.5	4.1	+2.54
F (Z)	TIMS	119		237		$1.8*10^{-3}$	5.69		5.293	0.3	0.3368	0.23	0.83	0.1140	0.16	1863.8	2.9	–0.46

2.5 Discussion

2.5.1 Olivine control and the effects of metamorphism

Strong correlations between MgO and many incompatible elements that intersect olivine compositions are indicative of olivine control, consistent with the petrographical observation that olivine was the dominant crystallising mineral. A regression of Cr_2O_3 against MgO for the RP1A samples intersects a mixing line between average olivine and chromite compositions at 1.1 ± 0.1% chromite (95% confidence interval about the regression line), suggesting the spread of data can be explained by the addition/subtraction of a mixture of ∼98.9% olivine and 1.1% chromite phenocrysts (by weight). The proportions in this mixture must have remained relatively constant to produce such a linear trend in Cr_2O_3 against MgO, and were similar for komatiites from both the RP1A and RP12 boreholes.

Without evidence of any further phenocryst phases in the vast majority of samples, deviations from olivine (or olivine + chromite) control lines are interpreted to represent alteration of primary compositions (Lahaye & Arndt, 1996), for example during Trans-Hudson age metamorphism. Pyroxene fractionation could potentially cause deviations from olivine control lines in the differentiated flow samples. However, Sc is negatively correlated with MgO (Figure 2.4), and positively correlated with La (not shown) across all samples, implying there was no significant pyroxene fractionation, even in the differentiated flows. Elements are considered 'unaltered' if regressions against MgO intersect measured olivine compositions, and qualitatively identify increasing degree of alteration by:

1. Increasing scatter about regression lines (relative to the expected scatter from analytical uncertainties).

2. Increasing shift of the extrapolation of these regressions away from measured olivine compositions.

By these measures SiO_2, Al_2O_3, TiO_2, Hf, Zr, the MREEs and HREEs (Sm and heavier), Sc, and Ni are 'unaltered' in RP1A; this also implies that MgO is effectively unaltered in these rocks. Elements showing evidence of alteration, arranged in approximate order of increasing alteration are Nd < Pr < CaO ∼ V < Ce < P_2O_5 < La < Th ∼ Nb ∼ U ∼ Cu < Na_2O < Sr < K_2O ∼ Ba ∼ Rb ∼ Cs ∼ Pb (Figures 2.3 and 2.4).

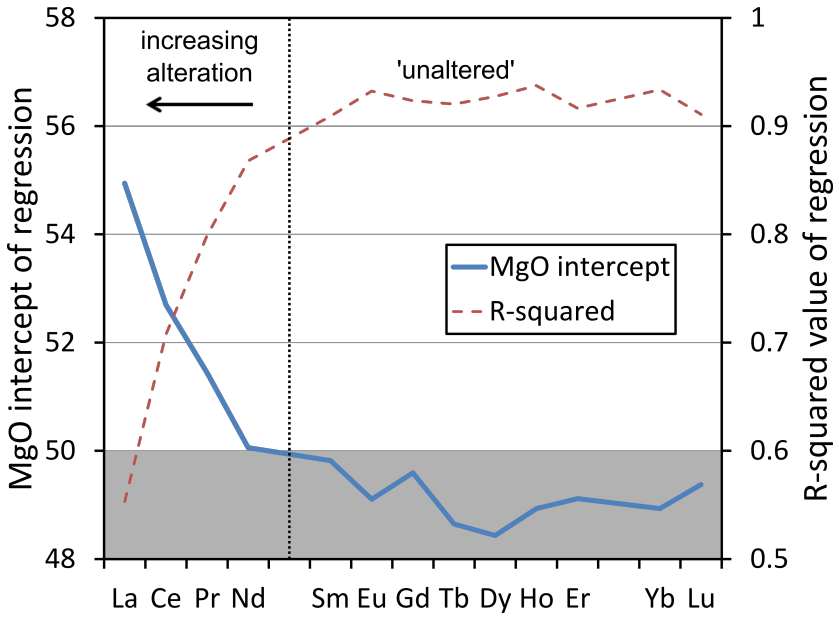

Figure 2.12: 'REE alteration plot' summarising olivine control line regressions for the REEs. Thick solid blue line plots the MgO intercept of regressions of REEs data. Grey box shows range of olivine compositions measured in Winnipegosis Komatiites; to satisfy an olivine control line, the MgO intercept of REE regressions should lie within this range. Thin dashed red line shows R^2 value of regressions against MgO, used here as a proxy for data scatter. MREEs and HREEs have consistently high R^2 values of > 0.9 and intersect measured olivine compositions, indicating they were unaltered. By contrast, R^2 values fall rapidly, and MgO intercepts are shifted to higher values than measured olivine compositions, for LREEs lighter than Sm.

The REE regressions against MgO are summarised in a 'REE alteration plot' (Figure 2.12). This plot is generated by plotting the R^2 value, used as a proxy for data scatter, and MgO intercept of regressions of each REE against MgO in turn. For example, a regression of Yb against MgO (Figure 2.4) intersects the MgO axis at 49 wt%, within the range of measured olivine compositions, and has a high R^2 value > 0.9. The Yb data therefore follow a tight olivine control line, and Yb is considered unaltered. By contrast, a regression of La against MgO extends to an MgO value of 55 wt%, higher than measured olivine compositions, and has a low R^2 value of $\sim$0.55. The La data is not consistent with an olivine control line, and La is therefore considered altered. The rapid shift towards lower R^2 values and higher MgO intercepts for LREEs lighter than Sm is indicative of increasing degrees of alteration.

The surprisingly low degree of alteration of CaO is ascribed to its incorporation primarily into dendritic clinopyroxene, which was unaltered during metamorphism. Al-

teration of elements in which the rock budget is dominated by chromite (Cr_2O_3), or which may be strongly affected by changing olivine partition coefficients (FeO, MnO, Ni) cannot be checked by this method, but the low degrees of scatter about regressions against MgO suggest Cr_2O_3, FeO, MnO, and Ni are also close to unaltered in RP1A samples.

2.5.2 Metamorphism vs. variable mixing with an enriched component

Samples from borehole RP12, metamorphosed at greenschist facies, show far greater scatter in plots of fluid-mobile elements such as Na_2O, Sr, K_2O, Ba, Rb, Cs, and Pb against MgO than the lower grade RP1A samples (prehnite-pumpellyite facies). This seems to indicate that metamorphism is the primary cause of deviations from olivine control lines. However, this fails to explain the scatter in elements such as Nb, U, and Th, given that data for these elements from samples in the higher metamorphic grade RP12 borehole show a tighter correlation with MgO than the less metamorphosed RP1A samples (e.g., Figure 2.4). Significant mobility during metamorphism would be especially surprising for Nb given that all other high field strength elements and even 'more mobile' elements such as Ca show tight correlations against MgO, and Nb is not typically mobile during low grade metamorphism (Cann, 1970).

In an attempt to resolve this issue, it is suggested that both the flat trace element patterns of Winnipegosis Komatiites and the high degree of scatter of fluid immobile elements such as Nb and Th could reflect variable mixing between a depleted komatiite magma and more enriched component: enriched mantle in the source, subduction-zone fluids, or continental crust.

The depleted komatiite magma is modelled using the DMORB estimate of Gale *et al.* (2013), normalised to Lu in the Winnipegosis samples. Mixing trends between this melt and various enriched components are plotted in Figure 2.13. The effect of an enriched component in the mantle source is modelled as a vector towards EMORB (Gale *et al.*, 2013); subduction zone fluids are modelled as vectors towards high Sr (shallow subduction component) and Th (deep subduction component) at constant Nb/Yb (Pearce & Stern, 2006); and contamination by local continental crust is modelled as mixing with Superior Craton tonalites from borehole RP92-5. The observation that Sr, Th and Nb are significantly elevated relative to depleted MORB (Figure 2.13a) rules out subduction zone fluids as the enriching component, as these should increase non-conservative elements such as Sr and Th without significantly increasing Nb (Pearce & Stern, 2006).

Although on a Th/Yb against Nb/Yb plot (Figure 2.13b) the Winnipegosis samples lie on the boundary of the MORB-OIB array of (Pearce, 2008), there is no purely 'oceanic' (i.e., mantle derived) component that can cause such large and variable enrichments in both Th and Nb, and still plot within the MORB-OIB array. Slight enrichments in Th/Nb compared to DMORB are therefore interpreted as being caused by continental crustal contamination. Figure 2.13c shows that mixing the Lu-normalised DMORB composition with 1 – 3 % Superior craton tonalite results in a trace element pattern that closely approximates those of Winnipegosis Komatiite samples.

Effect of crustal contamination

Even for a mixture containing 3% assimilated continental crust, less than 10% of the total budget of elements more compatible than Hf would be supplied from assimilated continental crust, hence variable amounts of assimilation of these elements at any stage of the magmatic system should have a negligible effect on olivine control lines. By contrast, 21 – 45 % of Nb in the final, assimilated melt would arise from the small amount (1 – 3% respectively) of assimilated continental crust. As such, even small variations in the amount of continental crust assimilated as magmatism progressed could cause significant variations in the final Nb content of the magma, leading to the observed scatter in regressions of Nb against MgO. This interpretation is supported by the observation that samples from different parts of the lava pile in RP1A lie on different trends of Nb against MgO (Figure 2.3). The increase in Nb content up-section is consistent with an increasing Nb contribution from crustal contaminants as magmatism progressed.

By contrast, if the variation in Nb contents is to be interpreted as reflecting mantle source effects, this would require both that the Winnipegosis mantle source contained an enriched component with similar incompatible element concentrations to continental crust, and that the relative contribution of this enriched component increased as melting progressed. This seems at odds with the observation that maximum olivine Mg# appears to increase up-section (Figure 2.7), which hints at an increase in the level of depletion or degree of melting of the mantle source as melting progressed.

In summary, a small but variable amount of crustal contamination can explain both the scatter about olivine control lines observed for strongly incompatible but fluid immobile elements such as Nb and Th, and the flat trace element patterns of Winnipegosis samples. A combination of crustal contamination and mobility during

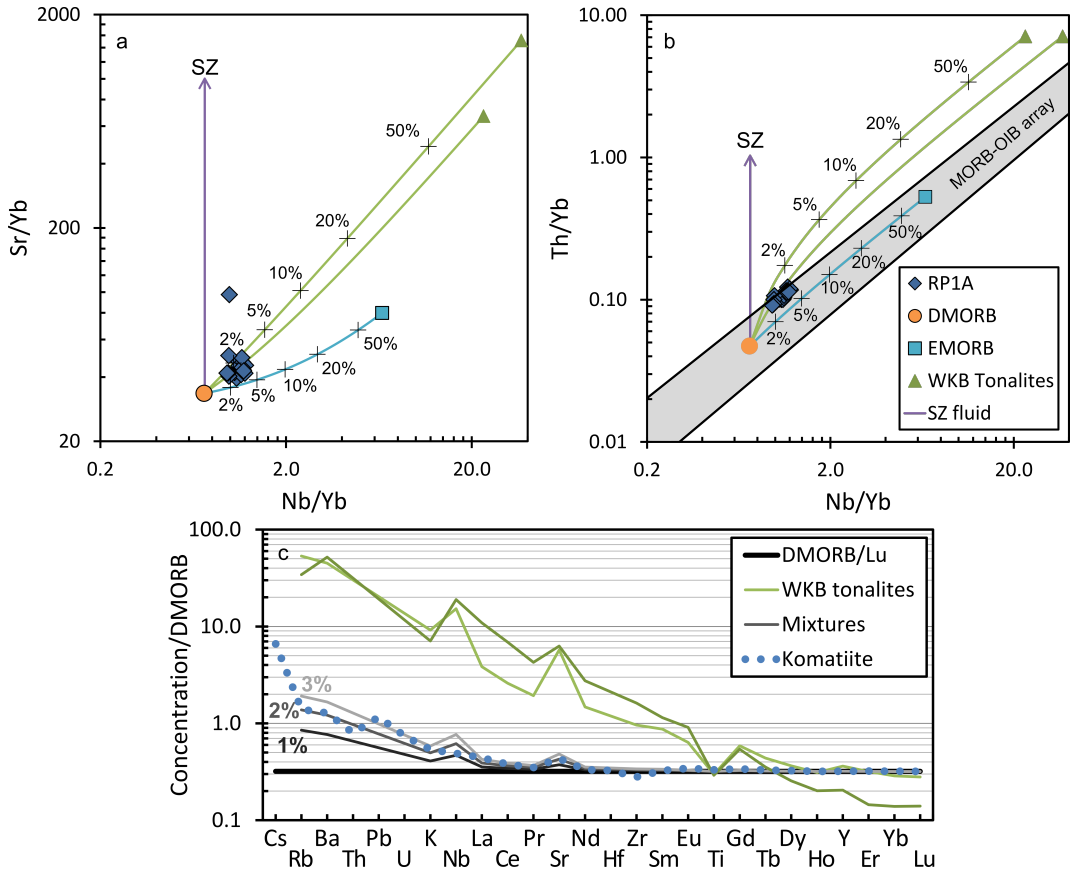

Figure 2.13: Models of contamination of a DMORB like melt with subduction zone fluids, enriched mantle sources, and continental crust. Tonalite data (green symbols and lines) from the GSC database; as Th was not measured for these samples, the median Th/Yb from Superior Craton Archaean tonalites (Whalen *et al.*, 2002) was used. a) Sr/Yb against Nb/Yb plot modified from Pearce & Stern (2006); Sr is used instead of Ba as it shows far less scatter due to mobility during metamorphism. Only RP1A samples are shown as metamorphism has variably enriched Sr in most RP12 samples. b) Th/Yb against Nb/Yb plot (Pearce, 2008). Crosses and percentages indicate amount of contaminant in mixture. c) DMORB (Gale *et al.*, 2013) normalised trace element patterns. Dotted blue line is the trace element pattern for RP1A-87, a sample with MgO content close to the calculated parental melt (Section 2.5.3). Solid black line is DMORB of Gale *et al.* (2013) normalised to Lu in RP1A-87. Grey lines show mixtures of DMORB-like melt mixed with 1, 2, and 3% tonalite.

metamorphism may be invoked to explain the large scatter in strongly incompatible fluid mobile elements such as Ba, Rb, Cs, and Pb.

2.5.3 Winnipegosis Komatiite parental melt MgO content

Olivine-liquid Fe-Mg exchange

Olivine-liquid Fe-Mg exchange is used to ascertain the parental liquid MgO content of the Winnipegosis Komatiites (e.g., Nisbet *et al.*, 1993). To use this method, an appropriate exchange coefficient must be selected (exchange coefficient, $K_{D,Fe2+-Mg}^{ol-liq} = (FeO/MgO)^{ol} / (FeO/MgO)^{liq}$, hereafter K_D), and the approximate $Fe^{2+}/\Sigma Fe$ of the magmas must be known. As K_D varies with liquid MgO (Herzberg & O'Hara, 2002), an olivine K_D of 0.345 is chosen, determined for bulk compositions similar to those of the Winnipegosis (Matzen *et al.*, 2011). Determining the appropriate $Fe^{2+}/\Sigma Fe$ is more challenging; below three independent methods are used to arrive at an estimate.

Chromite-liquid equilibrium

Firstly, the the $Fe^{2+}/\Sigma Fe$ of liquids in equilibrium with chromite can be calculated from the chromite Fe^{2+}/Fe^{3+} (Maurel & Maurel, 1982; Larsen & Pedersen, 2000). However, the Fe^{2+}/Fe^{3+} of the chromites must first be screened for the effects of sub-solidus equilibration with their host olivines. This is attempted using the spinel-olivine Fe-Mg exchange thermometer of Ballhaus *et al.* (1991). Temperatures significantly below magmatic temperatures are interpreted to indicate sub-solidus Fe-Mg exchange between chromite and their host olivines, which could affect the Fe^{2+}/Fe^{3+} of the chromites.

Fe^{2+}/Fe^{3+} ratios (calculated stoichiometrically; Droop, 1987) in the chromites range between 2.31 and 5.20, which, using the relationship of Maurel & Maurel (1982) indicates an apparent range in $Fe^{2+}/\Sigma Fe$ of their equilibrium liquids between 0.90 and 0.96 respectively. However, these equilibrium $Fe^{2+}/\Sigma Fe$ correlate negatively with the equilibration temperature of the olivine-chromite pairs (Figure 2.14), indicating that chromites which underwent sub-solidus equilibration with their host olivines gained Fe^{2+}. This, in turn, causes the liquid $Fe^{2+}/\Sigma Fe$ to be overestimated. A single olivine-chromite pair (RP1A-111_ol-chr_4) records an identical temperature from both the Al-in-olivine thermometer (1391 ± 9 °C), and the Fe-Mg exchange thermometer (1398 ± 27 °C), indicating that the portion analysed did not undergo subsolidus exchange of Fe with its host olivine. This chromite yields a liquid $Fe^{2+}/\Sigma Fe$ of 0.903 using the equation of Maurel & Maurel (1982). Alternatively, the liquid $Fe^{2+}/\Sigma Fe$ at magmatic temperatures can be calculated by regressing the data in Figure 2.14 to the temperature most of the chromites crystallised at (∼1400 °C from Al-in-olivine temperatures). This

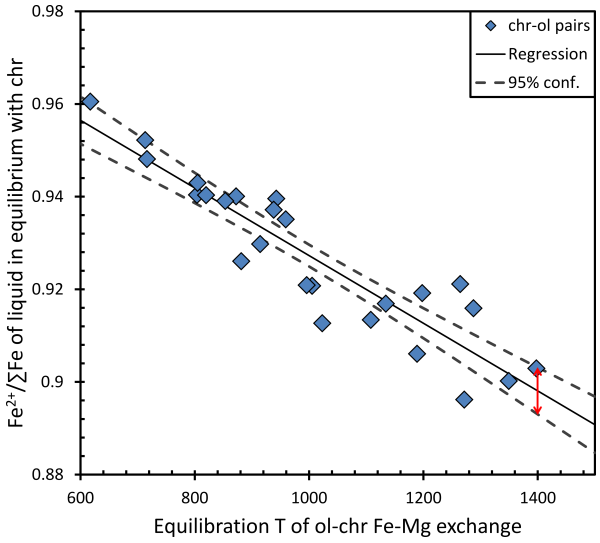

Figure 2.14: $Fe^{2+}/\Sigma Fe$ of liquids in equilibrium with chromite (Maurel & Maurel, 1982), plotted as a function of the Fe-Mg exchange thermometer (Ballhaus *et al.*, 1991) equilibration temperature. The higher $Fe^{2+}/\Sigma Fe$ at lower equilibration temperatures indicates that chromites which underwent extensive sub-solidus exchange with their olivine hosts gained Fe^{2+} through the interaction. 95% confidence limits about the regression indicate a liquid $Fe^{2+}/\Sigma Fe$ of 0.898 ± 0.005 at ∼1400 °C (red arrows).

gives a liquid $Fe^{2+}/\Sigma Fe$ of 0.898 ± 0.005, identical within error to the $Fe^{2+}/\Sigma Fe$ calculated from the undisturbed chromite. The chromite data therefore indicates a liquid $Fe^{2+}/\Sigma Fe$ at the time of chromite crystallisation of ∼0.90.

Vanadium-Scandium partitioning

Average V/Sc ratios of 6.0 ± 0.3 (1σ absolute) are consistent with an oxygen fugacity of the primary melt (i.e. as it segregated from the source region) approximately 1 $\log_{10}$ unit below the Quartz-Fayalite-Magnetite buffer (f_{O_2} = QFM – 1) if melting predominantly occurred in the spinel field, and an f_{O_2} of ∼QFM – 3 if melting occurred in the garnet stability field (Lee *et al.*, 2005). The pressures of melting assumed for these melting models by Lee *et al.* (2005) are 1.5 GPa (∼45 km) and 3 GPa (∼90 km) respectively. To obtain these f_{O_2} a melt fraction of 20% is assumed, the highest degree of melting the V-Sc system was calibrated for. Though estimates of melt fractions for komatiites are typically higher than this (e.g., Arndt *et al.*, 2008), isopleths of constant f_{O_2} relative to the QFM buffer are almost parallel for this range of V/Sc ratios at high melt fractions, and so extrapolating to higher melt fractions should not significantly affect f_{O_2} estimates. No significant correlation of V/Sc with MgO is observed for

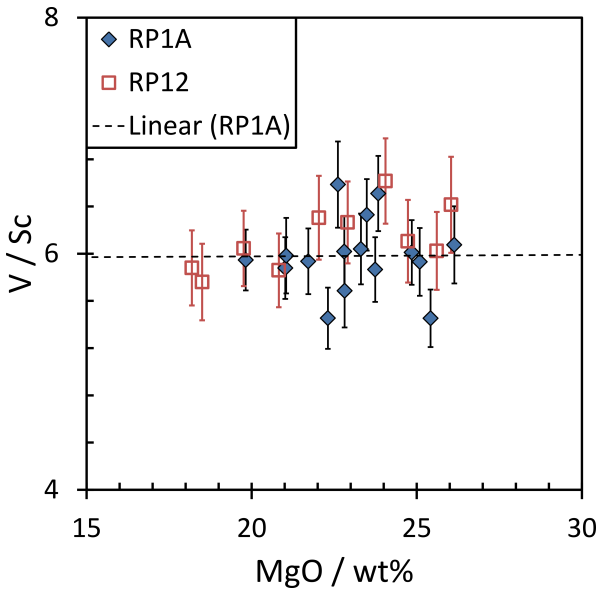

Figure 2.15: V/Sc of Winnipegosis komatiite samples from the RP1A and RP12 boreholes, plotted as a function of MgO. Dashed line shows a regression of RP1A samples. No significant correlation is observed between V/Sc and MgO.

Winnipegosis komatiites (Figure 2.15), and the total range of V/Sc in the rocks remains small compared to the variations of V/Sc generated due to varying f_{O_2}.

Equation 7 of Kress & Carmichael (1991) is used to calculate $Fe^{2+}/\Sigma Fe$ in the melts from these estimates of the relative oxygen fugacity, which additionally requires knowledge of the pressure, temperature and composition of the melts, and the absolute oxygen fugacity of QFM under the appropriate conditions.

The komatiites are assumed to have a temperature of ∼1500 °C at the surface (see Section 2.5.4), but note that the calculated $Fe^{2+}/\Sigma Fe$ is almost independent of temperature; reducing the assumed temperature to 1200 °C or increasing it to 1800 °C affects calculated $Fe^{2+}/\Sigma Fe$ by ≤ 0.01. These temperatures are extrapolated to the depths of melting assumed for garnet and spinel facies melting in the Lee *et al.* (2005) V/Sc melting models along an adiabat of 1 °C/km (Mckenzie & Bickle, 1988). However, the pressure assumed does not strongly affect calculated $Fe^{2+}/\Sigma Fe$ for a given f_{O_2} relative to QFM. For example, increasing the pressure assumed for garnet facies melting from 3 GPa to 6 GPa only affects $Fe^{2+}/\Sigma Fe$ by ∼0.001. The average of the $Fe^{2+}/\Sigma Fe$ calculated from all measured major element compositions is presented here, but the entire compositional range of the Winnipegosis Komatiites (between 26 and 10 wt% MgO) causes a range in $Fe^{2+}/\Sigma Fe$ of < 0.01 when other conditions are fixed. In

Table 2.5: Results of $Fe^{2+}/\Sigma Fe$ calculations based on V/Sc partitioning (Lee *et al.*, 2005). $Fe^{2+}/\Sigma Fe$ and 1σ absolute uncertainties given are the average and standard deviation of results for all measured major element compositions.

Melting region	*P (GPa)*	*Rel. f_{O_2}*	*T (°C)*	*Abs. $log_{10}(f_{O_2})$*	*av. $Fe^{2+}/\Sigma Fe$*	*1σ abs.*
Spinel Field	0 (surface)	QFM – 1	1500	–6.40	0.953	0.002
Spinel Field	1.5 (source)	QFM – 1	1545	–5.28	0.961	0.001
Garnet Field	0 (surface)	QFM – 3	1500	–8.40	0.980	0.001
Garnet Field	3 (source)	QFM – 3	1590	–6.20	0.985	0.001

general, bulk rock compositions with the lowest MgO give lower $Fe^{2+}/\Sigma Fe$, primarily due to their higher Na_2O and CaO contents. Finally, QFM is extrapolated to the temperatures and pressures of the source region using the calibration of Ballhaus *et al.* (1991), modified from O'Neill (1987), to calculate the absolute f_{O_2} of QFM – 1 and QFM – 3 indicated by V/Sc partitioning.

Assuming that the melt behaves as a completely closed system en-route to the surface, and that Fe is the only major element with multiple valence states, the $Fe^{2+}/\Sigma Fe$ must be the same as in the source region to preserve charge balance. This results in an $Fe^{2+}/\Sigma Fe$ of 0.961 for melting in the spinel stability field, and 0.985 for melting in the garnet stability field. If instead it is assumed that the melts are buffered to remain at constant f_{O_2} relative to QFM Kress & Carmichael (1991) $Fe^{2+}/\Sigma Fe$ at the surface is expected to be 0.953 if melting occurred in the spinel stability field, and 0.980 if melting occurred in the garnet stability field. The results of these calculations are presented in Table 2.5.

As can be seen from the discussion above, the largest uncertainty on the calculated $Fe^{2+}/\Sigma Fe$ is whether melting is assumed to have occurred in the spinel or garnet facies, which has a strong effect on the f_{O_2} calculated from V/Sc partitioning. However, these f_{O_2} estimates are necessarily approximate due to the presence of other elements, such as Cr, which can occupy multiple valence states, and may represent an upper bound if the assumptions that the magma behaves as a closed/buffered system are violated. This is especially likely if, as suggested in Section 2.5.2, the komatiites assimilated a small amount of continental crust. This assimilated continental crust is likely to be more oxidised than the komatiites, leading to a reduction in $Fe^{2+}/\Sigma Fe$ as crust is assimilated.

Preferred $Fe^{2+}/\Sigma Fe$

Finally, it is noted that the best fit of olivine Fe-Mg partitioning to Al-in-olivine temperatures (Figure 2.6 and Section 2.5.4) appears to be for $Fe^{2+}/\Sigma Fe \approx 0.9$, though the 'resolution' of this comparison is poor due to uncertainties in the Al-in-olivine temperatures.

A value of $Fe^{2+}/\Sigma Fe = 0.90$ is chosen for the calculations below, calculated from chromite Fe^{2+}/Fe^{3+}, as this provides the best constrained estimate of $Fe^{2+}/\Sigma Fe$ at the time of komatiite crystallisation, and is identical to previous estimates of komatiite $Fe^{2+}/\Sigma Fe$ (Berry *et al.*, 2008). This may represent a lower bound on the $Fe^{2+}/\Sigma Fe$ at the liquidus if olivine crystallisation consumed Fe^{2+} in the melt before chromite began to crystallise (Section 2.5.4). By contrast, V/Sc partitioning calculates the average f_{O_2} at the point the komatiites separated from their source, and provides an upper bound on $Fe^{2+}/\Sigma Fe$ of $\sim 0.95 - 0.98$.

Parental liquid MgO

Using $K_D = 0.345$ and $Fe^{2+}/\Sigma Fe = 0.90$, the highest Mg# olivine (Mg# = 0.923) crystallised from a liquid containing 23.6 wt% MgO and 11.3 wt% FeO_t. The largest uncertainties on this parental melt composition arise from the $Fe^{2+}/\Sigma Fe$ ratio of the melt and uncertainties in the maximum Mg# measured in olivine. If the upper bound $Fe^{2+}/\Sigma Fe$ values calculated from V/Sc partitioning are used, the parental melt MgO is elevated to 24.8 wt% for melting in the spinel field, and 25.6 wt% for melting in the garnet field. An uncertainty of ± 0.005 in the maximum Mg# of 0.923 results in calculated MgO ranging from 22.1 to 25.2 wt%; because this error is dominated by systematic differences between analytical sessions (Section B.4), it cannot be reduced by multiple measurements of the same olivine. However, the parental liquid MgO is believed to be more robust than indicated by this, as 6 olivine grains analysed for this thesis had Mg# > 0.92 (out of a total of 183 randomly selected olivines), and 9 olivine grains in the GSC database have Mg# > 0.92 (n = 160 olivine cores). The similar proportion of olivine analyses with Mg# > 0.92 measured in different labs robustly indicates the presence of olivines with Mg# > 0.92.

The calculated parental liquid MgO of 23.6 wt%, which lies well within the range of Winnipegosis bulk rock compositions, confirms that these rocks are komatiites (Arndt & Brooks, 1980). The presence of olivine spinifex in at least three flows in borehole RP12 (Section 1.4.2) means the Winnipegosis rocks also satisfy the more stringent komatiite

definition of Kerr & Arndt (2001). Supporting this interpretation is the fact that the median MgO, over a large number of samples covering two ∼250 m thick sections of lava is 22.4 wt% MgO, with an average estimated olivine phenocryst content of 17 vol%; these samples certainly do not represent small volume eruptions of a highly olivine-charged picrite. Finally, the composition of chill margins from the GSC database show a range of MgO between 19.6 wt% and 23.4 wt% (17 chill samples with < 1 wt% CO_2). Correcting for petrographically-estimated olivine phenocryst contents of 5 – 20 vol%, the residual liquids at the time of eruption were komatiite or basaltic komatiite, with olivine-corrected MgO approximately in the range 14.1 – 20.3 wt%.

2.5.4 Thermal evolution of Winnipegosis Komatiite melts

Liquidus temperature

The relationship of Matzen *et al.* (2011) is used to equate the parental melt MgO content of 23.6 wt% MgO to a liquidus temperature of 1501 ± 32 °C for the Winnipegosis Komatiite parental melt (2σ uncertainty calculated allowing ± 0.005 uncertainty in olivine Mg#). Use of the Primelt3 software (Herzberg & Asimow, 2015) corroborates this high liquidus temperature independent of measured olivine compositions. A liquidus temperature of 1492 ± 20 °C at a parental melt MgO of 23.2 ± 0.7 wt% (2σ of all bulk rock compositions that did not experience clinopyroxene fractionation) is calculated for batch melting. Calculations assuming accumulated fractional melting failed as the Winnipegosis compositions are too low in CaO to have been produced by fractional melting of fertile peridotite.

This liquidus temperature is ∼100 °C lower than upper-end estimates of the liquidus temperatures of Archaean komatiites (Nisbet *et al.*, 1993; Robin-Popieul *et al.*, 2012; Sossi *et al.*, 2016). However, it is similar to, or even lower than temperatures suggested for some Phanerozoic magmas, such as unerupted komatiitic magmas from the Etendeka LIP (Thompson & Gibson, 2000), West Greenland picrites (Larsen & Pedersen, 2000), and Tortugal Suite picrites (Trela *et al.*, 2017).

This calculation of the liquidus temperature can be more generally extended to a relationship between Mg# of olivine and temperature. The FeO/MgO of an olivine is related to its Mg# according to:

$$\left(\frac{FeO}{MgO}\right)_{ol} = \frac{m_{FeO}}{m_{MgO}}\left(\frac{1}{Mg\#} - 1\right) \tag{2.1}$$

where FeO and MgO are in wt%, and m signifies molar mass. This is related to the FeO/MgO of a liquid in equilibrium with the olivine by the exchange coefficient, K_D:

$$\left(\frac{FeO}{MgO}\right)_{liq} = \frac{\left(\frac{FeO}{MgO}\right)_{ol}}{K_D} = \frac{m_{FeO}}{K_D * m_{MgO}}\left(\frac{1}{Mg\#} - 1\right) \tag{2.2}$$

The intersection of this FeO/MgO with the relationship of bulk rock FeO against MgO gives the composition of the liquid the olivine crystallised from, assuming the bulk rock FeO and MgO contents provide a reasonable approximation of the liquid line of descent (LLD), and the $Fe^{2+}/\Sigma Fe$ remains roughly constant during crystallisation (see discussion below). The liquid MgO in equilibrium with olivine at a given Mg# is therefore:

$$MgO_{liq} = \frac{b}{\frac{m_{FeO}}{K_D * m_{MgO}}\left(\frac{1}{Mg\#} - 1\right) - a} \tag{2.3}$$

where a and b are the gradient and intercept of a straight line regression of bulk rock FeO against MgO ($FeO = a * MgO + b$) at a given $Fe^{2+}/\Sigma Fe$. Using the Matzen *et al.* (2011) linear relationship between MgO and temperature gives the dependence of temperature (T) on olivine Mg# and bulk rock FeO against MgO:

$$T = \frac{19.2 * b}{\frac{m_{FeO}}{K_D * m_{MgO}}\left(\frac{1}{Mg\#} - 1\right) - a} + 1048 \tag{2.4}$$

Though the bulk rock FeO against MgO relationship observed for the Winnipegosis Komatiites does not represent an LLD (Section 2.5.5), maximum deviations of 0.4 wt% FeO from a 'worst case' perfectly fractional crystallisation trend affect temperatures by a smaller amount than uncertainties in Mg# of olivine or the $Fe^{2+}/\Sigma Fe$ of the liquids. Therefore, the assumption that bulk rock FeO against MgO represents the liquid line of descent should not significantly affect temperatures calculated using equation 2.4.

The ratio of $Fe^{2+}/\Sigma Fe$ is unlikely to remain constant during olivine and chromite crystallisation, as Fe^{2+} is consumed by olivine crystallisation and both Fe^{2+} and Fe^{3+} are incorporated into chromite. However, no correction is applied for the preferential incorporation of FeO in olivine compared to Fe_2O_3 (Robin-Popieul *et al.*, 2012) for two reasons. Firstly, making such a correction affects all FeO values by < 0.5 wt%, with the size of the effect smallest (< 0.1 wt%) on samples close to the parental liquid com-

position. As such, the assumption of constant $Fe^{2+}/\Sigma Fe$ is also unlikely to significantly affect temperatures calculated using equation 2.4. Secondly, the variation of $Fe^{2+}/\Sigma Fe$ after chromite begins to crystallise at ∼20 wt% MgO is unknown (see below). Due to the inferred re-mixing of olivine and chromite phenocrysts shortly before or during eruption, it is not possible from the data to determine the exact proportion of chromite and olivine crystallising at any given MgO once chromite begins to crystallise; only the average proportions in the mixture are known.

Temperature against Mg# curves for the preferred value of $Fe^{2+}/\Sigma Fe = 0.90$, as well as upper bounds calculated using $Fe^{2+}/\Sigma Fe$ from V/Sc partitioning, are shown in Figure 2.6. These curves are calculated using constant $K_D = 0.345$ (Matzen *et al.*, 2011), as K_D is expected to vary by less than ∼0.02 over the range of MgO considered (14 wt% < MgO < 26 wt%; Herzberg & O'Hara, 2002). Use of the MgO dependent K_D parameterisation of Herzberg & O'Hara (2002) leads to 7 – 13 °C higher temperatures, but almost parallel curves, due to a weak variation of K_D at high liquid MgO. All temperatures are estimated assuming the olivine crystallised at close to zero pressure. Crystallisation at depth would increase the temperature relative to the 1 atm. liquidus temperatures. Allowing for scatter of data and possible systematic errors, the Al-in-olivine temperatures are an excellent match to those predicted by anhydrous olivine Fe-Mg partitioning for $Fe^{2+}/\Sigma Fe$ ∼0.90, confirming the high liquidus temperatures calculated above.

Hydrous komatiites?

Recently, Sobolev *et al.* (2016) revived the idea that some Archaean komatiites may originate from a hydrous transition zone source (Kawamoto *et al.*, 1996). For comparison, Figure 2.6 also shows a curve for $Fe^{2+}/\Sigma Fe = 0.90$, with a ∼60 °C depression of the liquidus predicted for 0.5 wt% H_2O (Falloon & Danyushevsky, 2000). This predicts temperatures that are too low to be consistent with the majority of Al-in-olivine temperatures. As the Al-in-olivine thermometer is not influenced by magmatic H_2O content or f_{O_2} (Coogan *et al.*, 2014), this suggests the Winnipegosis magmas are nominally anhydrous, and did not arise from a hydrous source. This interpretation is supported by the MORB-like trace element patterns and low Ce content of the komatiites, which predict ∼0.04 – 0.1 wt% H_2O in the parental melt for a H_2O/Ce of 100 – 250 respectively (Dixon *et al.*, 2002).

Cooling and crystallisation history

Using the comparison between the Al-in-olivine thermometer and olivine Fe-Mg partitioning, the cooling history of the Winnipegosis magmas can be reconstructed (Figure 2.16). Liquidus olivine crystallised from a melt containing 23.6 wt% MgO at a temperature of 1501 ± 32 °C. Olivine was the sole crystallising phase over an interval between 1501 °C and ∼1424 °C, the highest Al-in-olivine temperature recorded by coexisting olivine and chromite in all three samples studied. The spread in temperature of the first olivine-chromite pairs to crystallise from each sample is small, but absolute uncertainties of ± 25 °C arising from the calibration of the Al-in-olivine thermometer are likely to be larger than this spread. It is therefore inferred that the olivine-chromite cotectic was reached at 1424 ± 25 °C, from a liquid MgO of 19.6 ± 1.3 wt%. If the first crystallisation of chromite is calculated instead from the highest average Mg# measured for olivine enclosing chromite (Mg# = 0.911), an indistinguishable (within uncertainty) temperature of 1440 ± 24 °C, or liquid MgO of 20.4 ± 1.3 wt% is obtained.

Olivine and chromite continued to crystallise until at least 1321 ± 25 °C (14.2 ± 1.3 wt% MgO, calculated from Al-in-olivine temperature), or 1328 ± 13 °C (14.6 ± 0.7 wt% MgO, calculated from Fe-Mg partitioning) in RP1A-99, the least MgO rich sample for which Al-in-olivine temperatures were obtained. However, there is no evidence of such low temperatures in RP1A-8 and RP1A-111, both of which had higher bulk rock MgO. This liquid MgO content, from which the lowest temperature olivine and chromite pair crystallised, is similar to the lowest MgO estimated for a chill margin after olivine phenocryst subtraction (∼14.1 wt%). Thus, 1321 ± 25 °C may provide an approximation to the lowest temperature at which Winnipegosis Komatiites erupted. After eruption the growth of olivine phenocrysts effectively ceased, and olivine crystallisation continued only as skeletal overgrowths on existing phenocrysts, and crystallisation of hopper and dendritic chain olivine in the groundmass (Section 1.4.1). As pyroxene dendrites are always interstitial to olivine dendrites, and by analogy to the experiments of Faure & Tissandier (2014), it is inferred that pyroxene crystallisation did not commence until the temperature had fallen considerably and olivine dendrite growth had ceased (Section 1.7.1).

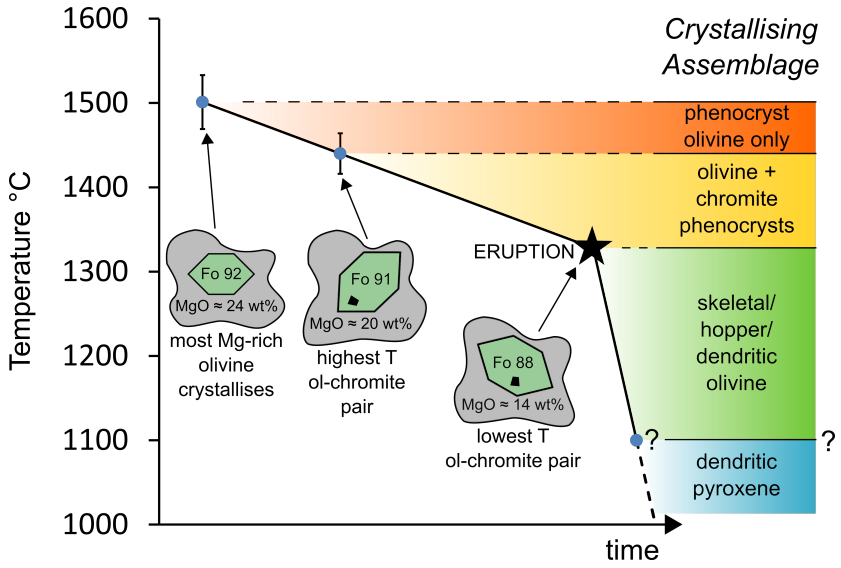

Figure 2.16: Schematic cooling history of the Winnipegosis Komatiites, showing crystallising assemblage at different temperatures. Temperatures of significant events are arranged assuming monotonic cooling of a single batch of magma. Straight lines are not intended to indicate linear cooling, as the cooling rate is unconstrained, but the break in slope separates slow cooling during phenocryst growth from rapid cooling and growth of dendritic forms after eruption. All temperatures and errors are derived from Fe-Mg partitioning for consistency. Dark grey indicates melt, green polygons indicate olivine, black polygons indicate chromite.

2.5.5 Bulk rock compositions are not liquid compositions – the role of mixing

The inference that chromite did not begin to crystallise until liquid MgO content reached < 21.7 wt% has profound implications for the understanding of bulk rock geochemical trends. If the bulk rock compositions are interpreted as a liquid line of descent (LLD), then Cr_2O_3 would be expected to increase with falling MgO until ~20 wt% MgO was reached, before falling once chromite began to crystallise. Instead, Cr_2O_3 is positively correlated with MgO for all samples. This positive correlation, and by extension all other olivine control lines, is best understood as a mixing line between a residual melt and a phenocryst mixture of olivine and chromite. Due to the largely constant volume proportion of phenocrysts throughout each flow, this mixing likely occurred shortly before, or during, magma eruption. Solid-liquid mixing can also explain why plots of FeO, MnO, and Ni against MgO are closely approximated by straight lines (Figures 2.3, 2.4), whereas the LLD for each of these elements should be curved as the crystallising olivine becomes progressively rich in FeO and MnO, and depleted in Ni. Mixing is

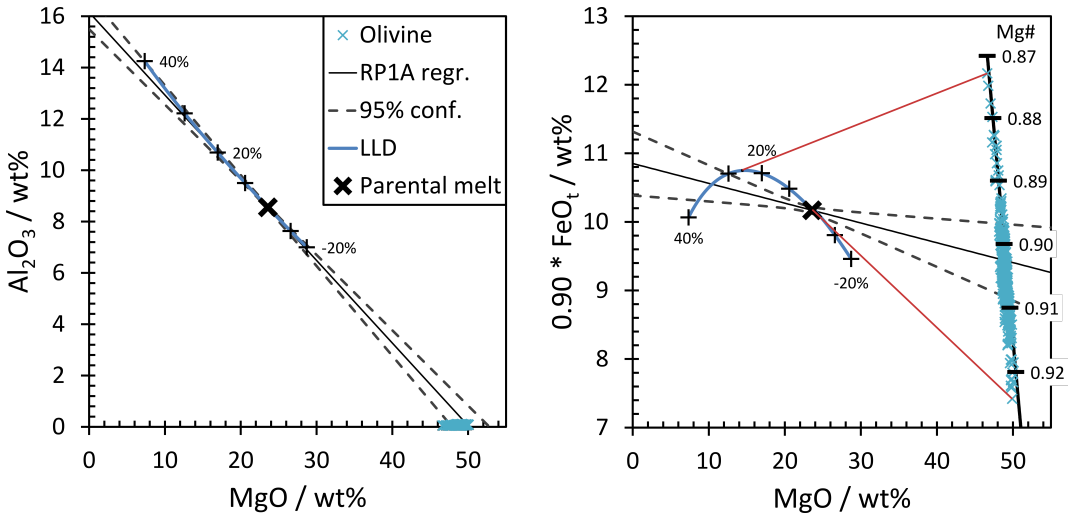

Figure 2.17: Comparison of regressions of bulk rock compositions to calculated LLDs. Bulk rock data omitted for clarity, see Figure 2.3. Crosses are 10 wt% increments of olivine removed from parental magma by fractional crystallisation, negative percentages correspond to olivine addition. Tick marks indicate Mg# of olivine. Red tie lines link highest and lowest Mg# olivines with their respective equilibrium liquids; these are tangential to the LLD.

also evidenced by the wide range of olivine compositions in each sample, which do not correlate with bulk rock MgO (Figure 2.7).

The liquid line of descent (LLD) for the Winnipegosis Komatiites is modelled through incremental addition and subtraction of olivine (Albarede, 1992; Larsen & Pedersen, 2000) from a parental melt composition defined by the intersection of bulk-rock element regressions against MgO with 23.6 wt% MgO (Figure 2.17). At each step, the composition of olivine in equilibrium with the melt is calculated (assuming fixed $Fe^{2+}/\Sigma Fe = 0.90$ and constant K_d of 0.345), and added or removed from the melt composition; this corresponds to fractional crystallisation. For simplicity, olivine was assumed to contain only SiO_2, MgO and FeO, and chromite was ignored due to its volumetrically small contribution and uncertainty in the ratio of olivine to chromite crystallising at a given temperature.

For incompatible elements such as Al_2O_3, LLDs are indistinguishable from the observed mixing lines, as their relationships with MgO are insensitive to the exact Mg# of olivine being added or subtracted (Francis, 1985). However, as the FeO/MgO ratio of an olivine depends on the FeO/MgO ratio of the liquid from which it crystallised, the predicted LLD in FeO – MgO space deviates more strongly from the observed bulk rock compositions. Despite this, the FeO predicted for the LLD never varies from the regression of bulk rock compositions by > 0.4 wt% FeO over the range of

bulk rock MgO observed in the Winnipegosis Komatiites (10 – 26 wt% MgO). This has a smaller effect on parental melt compositions and liquidus temperatures than the range of $Fe^{2+}/\Sigma Fe$ calculated or the uncertainty in the Mg# of the most magnesian olivine. The largest deviation from the LLD will occur in Cr_2O_3 against MgO due to the extremely strong dependence of bulk rock Cr_2O_3 on volumetrically small addition or subtraction of chromite.

2.5.6 Al-undepleted Winnipegosis Komatiites

Winnipegosis Komatiites have slightly sub-chondritic Al_2O_3/TiO_2 (17.2 ± 0.2, 1σ absolute), and slightly supra-chondritic Gd/Yb (Figure 2.18), placing them between average Al-depleted ($Al_2O_3/TiO_2 \approx 11$) and Al-undepleted komatiite ($Al_2O_3/TiO_2 \approx 20$; Nesbitt *et al.*, 1979). Olivine-corrected molar $[Al_2O_3]$ and $[TiO_2]$ values of 0.191 and 0.0142, respectively, identifies them as Al-undepleted komatiites according to the classification of Hanski *et al.* (2001). In terms of trace element patterns (Figure 2.5), Winnipegosis Komatiites are quite similar to other Al-undepleted komatiites (e.g., Alexo; Lahaye & Arndt, 1996) showing a generally incompatible element-depleted trend. Their slight HREE depletion relative to the MREEs is somewhat unusual for an Al-undepleted komatiite, but parallels the slight HREE depletion observed in Gorgona 'G1' komatiites Revillon *et al.* (2000). Contents of ~46.3 wt% SiO_2 calculated for the parental melt at 23.6 wt% MgO place the Winnipegosis komatiites in the low SiO_2 group of Parman & Grove (2005), similar to Munro komatiites and with a distinctly lower SiO_2 at a given MgO than Barberton komatiites.

2.6 Tectonic interpretation

2.6.1 The WKB as a part of the Circum-Superior Belt

The 1870.3 ± 7.1 Ma age of the Winnipegosis Komatiite Belt (Section 2.4.3) is identical, within uncertainty, to the youngest mafic and ultramafic bodies previously dated in the Circum-Superior Belt, both in the adjacent Thompson Nickel Belt and more than 2000 km away in the New Quebec Orogen (Heaman *et al.*, 2009; Ciborowski *et al.*, 2017). The Winnipegosis Komatiites also share many petrological features with other igneous rocks of the CSB: mafic/ultramafic rocks are abundant; depleted, MORB-like compositions are widespread (Heaman *et al.*, 2009); and magmatic olivine with

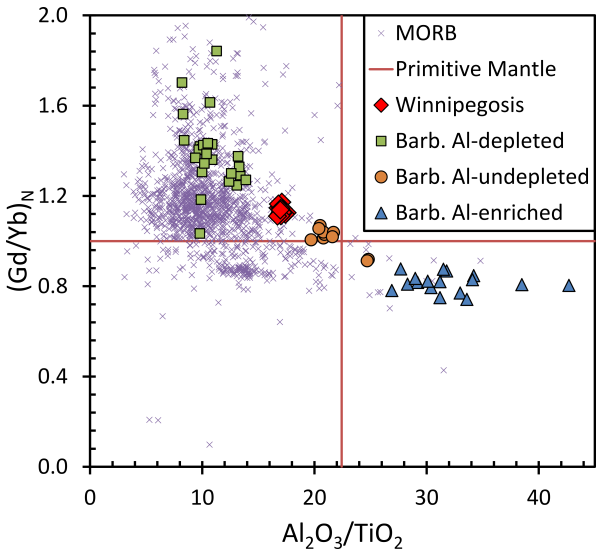

Figure 2.18: Chondrite normalised Gd/Yb ratios, $(Gd/Yb)_N$, plotted as a function of Al_2O_3/TiO_2. Winnipegosis Komatiites are compared to Al-depleted, Al-undepleted, and Al-enriched komatiites from Barberton (Robin-Popieul *et al.*, 2012), a global database of fresh MORB (www.earthchem.org/petdb; accessed Dec. 2012), and the primitive mantle values of Hofmann (1988). MORB are likely shifted towards lower Al_2O_3/TiO_2 due to plagioclase fractionation, but $(Gd/Yb)_N$ should remain representative of their parental melts.

high Mg# ($\geq$ 0.92), indicative of high temperature melts, is present, as has been reported from other regions of the CSB (Arndt *et al.*, 1987). Therefore, the tectonic interpretation of the Winnipegosis Komatiites cannot take place in isolation, and should be considered as a segment of the wider CSB.

2.6.2 Formation model

A model for the formation of the Winnipegosis Komatiites must satisfy the following geochemical evidence outlined in this chapter:

1. Formation of high MgO, high liquidus temperature parental magmas with no evidence of significant depression of the liquidus due to the presence of water.

2. Low absolute trace element abundances, approximately twice that of primitive mantle.

3. Generally depleted trace element signatures indicating a DMORB-like source.

4. Evidence of crustal contamination.

The following geological and geochronological evidence, outlined in Chapter 1, is also considered to be important:

5. The unconformable relationship of the WKB over Superior craton tonalites.
6. The transition from tholeiitic basalt to komatiite up-section within the WKB.
7. The transition in sedimentation style from a short interval of conglomerates and sandstones at the base of the WKB to carbonates and shales at higher stratigraphic levels (Burnham *et al.*, 2009; McGregor, 2011).
8. Formation in a convergent margin setting (Section 1.2; Corrigan *et al.*, 2009; Heaman *et al.*, 2009).
9. Age identical, within uncertainty, to both pericratonic arc magmatism in the Snow Lake Arc (Percival *et al.*, 2005), and mafic – ultramafic magmatism in the Circum-Superior Belt (Heaman *et al.*, 2009).

Emplacement of Winnipegosis Komatiites over rifted Superior Craton crust

As the Winnipegosis Komatiites were sourced from mantle similar to the DMORB source, high degrees of melting – combined with little crystal fractionation before eruption – are required to explain the low concentrations of incompatible elements. This is consistent with the high calculated liquidus temperatures. However, the Winnipegosis Komatiites were emplaced upon continental crust (points 4 and 5 above), as previously recognised for many Archaean komatiites and greenstone belts (Bickle *et al.*, 1994; Pearce, 2008). This observation rules out oceanic settings where high degrees of melting are observed such as mid-ocean ridges, and plume-generated oceanic plateaux. Instead, it is suggested that the high degrees of melting necessary to produce the Winnipegosis Komatiites are best explained by their emplacement within an evolving rift, near the Superior Craton margin. A rift setting is also consistent with points 6 and 7; the progression of volcanism from tholeiitic basalt to komatiite up section could represent increasing mantle melting as rifting progressed, and the style of sedimentation is consistent with a rift environment.

Thermal anomaly or ambient mantle?

Whether or not the Winnipegosis Komatiites can be generated from ambient mantle or require thermally anomalous mantle depends critically on the potential temperature of

the mantle during the Palaeoproterozoic. Traditional models of secular mantle cooling (e.g., Davies, 1999) suggest that Palaeoproterozoic mantle potential temperatures (T_p) may not have been much higher than today, with $T_p \approx 1300$ °C at 1.9 Ga relative to a modern MORB $T_p = 1220$ °C ($\Delta T \approx 80$ °C). In this case a thermal anomaly is clearly required to produce Winnipegosis magmas with a liquidus temperature of 1501 °C. By contrast, Herzberg *et al.* (2010) argue that the Proterozoic ambient mantle was capable of producing primary melts with 18 – 24 wt% MgO, with ambient T_p as high as 1600 °C at ∼1.9 Ga (relative to a modern MORB T_p of 1350 ± 50 °C, $\Delta T \approx 250$ °C). However, all of the highest temperature estimates ($T_p > 1500$ °C) for Proterozoic magmas examined by Herzberg *et al.* (2010) are for samples from the Cape Smith Belt, part of the larger Circum-Superior Belt. As the Circum-Superior Belt has previously been interpreted as a plume-derived LIP (Ernst & Bleeker, 2010; Minifie *et al.*, 2013), the evidence for high T_p estimates in ambient Proterozoic mantle is equivocal.

Excluding samples from the Cape Smith Belt, the highest T_p suggested for the Proterozoic by Herzberg *et al.* (2010) is ∼1490 °C for the 2056 Ma Lapland basalts. Given the inevitable temperature drops due to the latent heat of fusion and decompression during ascent, ambient mantle of $T_p = 1490$ °C cannot produce the Winnipegosis Komatiites. Calculations using Primelt3 software Herzberg & Asimow (2015) indicate mantle T_p of 1644 ± 33 °C (2σ of all bulk rock compositions that did not experience clinopyroxene fractionation) for Winnipegosis compositions. As such, the formation of the Winnipegosis Komatiites likely requires thermally anomalous mantle, regardless of the model of mantle thermal history used. This is supported by the observation that the MgO content of the Winnipegosis Komatiites is substantially higher than the average MgO content of mafic rocks during the Palaeoproterozoic, which was similar to the present day at < 10 wt% MgO (Keller & Schoene, 2012).

A model for the Winnipegosis Komatiites and Circum-Superior Belt

The requirement of above ambient mantle temperatures to generate the Winnipegosis Komatiites allows several models of Circum-Superior Belt formation, which generate high degrees of melting but do not predict elevated mantle temperatures (Heaman *et al.*, 2009, and references therein), to be ruled out. Instead, the formation of the WKB and the wider CSB are best explained as a mantle plume derived LIP (Ernst & Bleeker, 2010; Minifie *et al.*, 2013).

In addition to generating above ambient mantle temperatures and high degrees

of melting, a plume origin is consistent with the relatively short time span (1885 – 1870 Ma) of the majority of CSB magmatism (Heaman *et al.*, 2009). Within the WKB, erosion of the underlying Superior Craton tonalites can also be understood as occurring during a period of plume-driven uplift, followed by extensive volcanism and deposition of sediments occurring as rifting continued.

However, a number of other features of the CSB require refinement of a simple plume model. Despite the relatively tight age range for the majority of CSB mafic/ultramafic magmatism, the revised age of 1870.3 ± 7.1 Ma for the WKB extends the range of mean ages for ∼1.9 Ga CSB magmatism to ∼30 Myrs, with no evidence for a progressive migration of the magmatism over time (Heaman *et al.*, 2009). The distribution of magmatism along ∼3000 km of continental margin also appears at odds with the expectation of approximately equant plume heads (Campbell & Griffiths, 1990).

It is suggested that these inconsistencies can be resolved by a 'focussed' plume model (Figure 2.19), in which an upwelling plume is deflected to the margins of the Superior Craton by the underlying thick cratonic lithosphere (Thompson & Gibson, 1991; Sleep *et al.*, 2002; Minifie *et al.*, 2013), and interacts with a series of pre-existing rifts around the Superior margin. The presence of pre-existing rifts in the CSB, either due to back arc rifting or pull apart basins formed by oblique convergence (Skulski & Wares, 1993), might be expected due to convergence and closure of the Manikewan Ocean along the northern and western margins of the Superior Craton (Section 1.2; Corrigan *et al.*, 2009). This is especially clear for the WKB, which formed contemporaneously with, and inboard of, the pericratonic Snow Lake Arc (Percival *et al.*, 2005), and therefore plausibly formed over lithosphere thinned in a back arc setting.

The presence of rifts around the Superior margin would have generated a steep lithospheric gradient between the centre of the craton and its margins, focussing the plume head and leading to the observed distribution of magmatism around the craton margins. This type of lithospheric control on the distribution of komatiitic magmatism has previously been suggested for Archaean komatiites of the Yilgarn craton (Mole *et al.*, 2014), and similar plume models in convergent margin settings have been envisaged for the modern Yellowstone plume (Kincaid *et al.*, 2013). Pre-existing rifts can also explain the large, ∼30 Myr spread in magmatic ages. In this model, magmatism in back arc or pull apart rifts accounts for the earliest ∼1900 Ma magmatism (Heaman *et al.*, 2009), with the arrival of a plume causing a large outpouring of high temperature magmatism at 1885 – 1870 Ma.

This model differs from previous plume models for the CSB in that the plume is

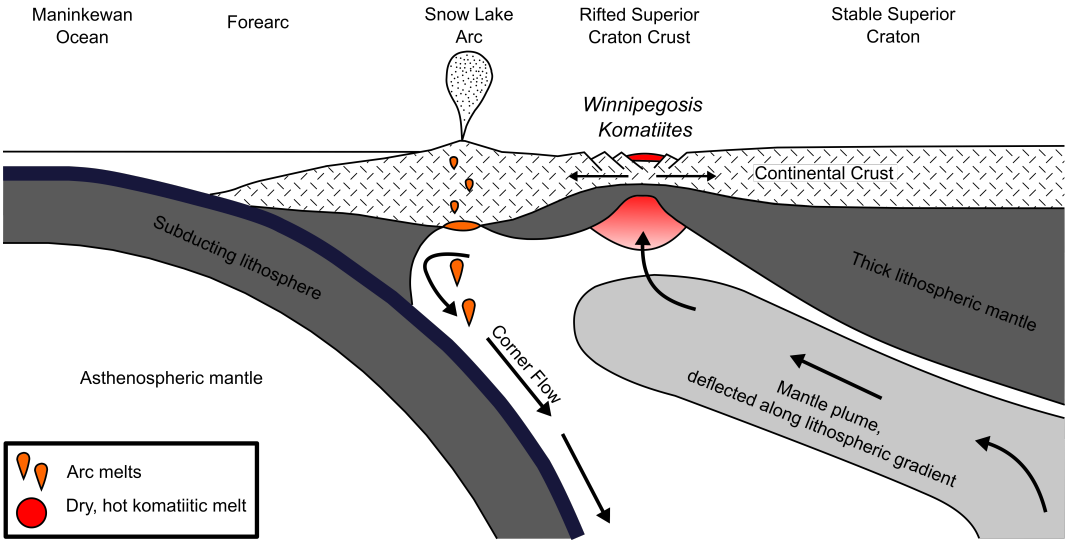

Figure 2.19: Schematic diagram illustrating a possible environment of formation for the Winnipegosis Komatiites. Thermally anomalous mantle generated by a mantle plume is deflected towards the margins of the Superior craton by a strong lithospheric gradient between the thick lithosphere of the Superior craton and back arc rifting along its margins.

envisaged to have impinged beneath the Superior craton, before being deflected by the local lithospheric architecture towards the margins, rather than impinging outboard of the northern margin of the Superior craton (Ernst & Bleeker, 2010). Decompression and therefore melting would have been limited beneath the thick Superior Craton lithosphere, though plume impingement may have triggered the generation of numerous carbonatite complexes and mafic dykes in the interior of the Superior Craton at ∼1.88 Ga (Rukhlov & Bell, 2010; Minifie *et al.*, 2013). This model is also consistent with evidence from the adjacent Thompson Nickel Belt, in which the formation of calc-alkaline granitoids at ∼1.89 Ga in a continental arc or back arc environment, preceded major ultramafic magmatism at ∼1.88 Ga (Hulbert *et al.*, 2005; Zwanzig, 2005).

2.7 Conclusions

The Winnipegosis Komatiites formed at 1870.3 ± 7.1 Ma as part of the Circum-Superior Belt LIP. Winnipegosis Komatiite parental melts contained ∼24 wt% MgO, which, along with the presence of spinifex layers and a median MgO of 22.4 wt% over > 250 m thickness of flows, confirms that these lavas are Proterozoic komatiites. The komatiites crystallised only olivine from 1501 °C to approximately 1424 °C, and then a mixture of olivine + chromite phenocrysts until eruption at approximately 1321 °C. Olivine and

chromite phenocrysts were entrained and variably mixed with residual melts shortly before and/or during eruption. Bulk rock compositions represent mixing lines between these phenocryst phases rather than the liquid line of descent.

The coincidence of Al-in-olivine temperatures with temperatures calculated from olivine Fe-Mg partitioning requires that the mantle source of the Winnipegosis Komatiites was nominally dry. This is supported by trace element patterns, which indicate a DMORB like, dry, parental melt. This melt was subsequently contaminated by small amounts of assimilated Superior craton continental crust, through which the Winnipegosis magmas erupted. Low absolute abundances of trace elements are consistent with high calculated liquidus temperatures, indicating high degrees of mantle melting. In the context of the broader Circum-Superior Belt, it is suggested the Winnipegosis Komatiites were generated by a mantle plume that was deflected towards the margins of the Superior craton by strong gradients in lithospheric thickness. The interpretation of the Circum-Superior Belt as a plume derived LIP casts doubt on ambient mantle potential temperatures as high as 1600 °C during the Proterozoic (Herzberg *et al.*, 2010).

Chapter 3

PGE systematics of the ∼1.9 Ga Winnipegosis Komatiites: Implications for Pt and Pd behaviour during high degree melting and mixing of the late veneer

Chapter Summary

The use of komatiites to understand the Platinum Group Element (PGE) systematics of the mantle throughout Earth's history critically depends on the understanding of how PGEs are fractionated between komatiite and source during their formation. Current consensus suggests that the PGEs are dominantly controlled by sulphide during mantle melting, and that Pt and Pd in particular should behave incompatibly following sulphide exhaustion. In this chapter, PGE concentrations and Re-Os isotopic data are presented for the ∼1.9 Ga Winnipegosis Komatiite, along with detailed modelling to test our understanding of PGE fractionation during the formation of komatiite and to evaluate the use of komatiite PGE concentrations as tracers of mantle PGEs through time. Whole rock Re-Os isotopic data define an isochron age of 1865 ± 40 Ma, identical to previously obtained U-Pb zircon ages for mafic rocks from the same belt. The isochron indicates an initial γ^{187}Os of – 0.2 ± 1.4, within error of chondritic evolution. PGE systematics in most Winnipegosis Komatiite samples were controlled by primary magmatic phases and were unaltered by crustal contamination and metamorphism. Elevated Ru and Os/Ir in one sample is best explained by the presence of rare grains of laurite, (Ru,Os,Ir)S_2. Correcting for magmatic fractionation, Winnipegosis parental melts contained 7.0 ± 0.8 ppb Pt and 7.2 ± 0.7 ppb Pd at an MgO content 23.6 ± 1.6 wt%. These values are > 60% lower than predicted by geochemical modelling of melting of a mantle source with primitive upper mantle-like PGE contents, using reasonable assumptions of melting conditions and melt

fraction. This discrepancy cannot be explained by melting of a source depleted in PGEs. The hypothesis that Pt and Pd in fact behave compatibly following sulphide exhaustion is tested by calculating parental melt compositions for a number of well-preserved komatiites and picrites. The parental melt compositions show a robust positive correlation between Mg# and both Pt and Pd, providing evidence that both elements exhibit some compatibility during high degree melting and are not exhausted from mantle residues until extreme melt fractions are reached, well beyond sulphide exhaustion. It is suggested that the residual silicate assemblage exerts an important control on komatiite PGE concentrations, and that much of the variability in komatiite PGEs through Earth history can be explained by variations in their degree of melting rather than source variations. Employing an empirical correction for differences in degrees of melting, it is demonstrated that the PGE contents of komatiite sources attained present day concentrations by at least 3.2 Ga. Though Al-depleted Palaeoarchaean komatiites still show low Pt and Pd even after this correction, this can potentially be explained by retention of these elements in a majoritic garnet residue without invoking sluggish mixing of late veneer.

3.1 Introduction

Komatiites have long been used to study the chemical state of the Earth's mantle (e.g., Bickle *et al.*, 1976). As large degree, high temperature mantle melts (Green, 1975; Nesbitt & Sun, 1976), they have the potential to provide representative chemical samples of the convecting mantle at their time of eruption (Puchtel *et al.*, 2004). In recent years, a number of studies have measured the platinum group element (PGE) contents of komatiites in an effort to reconstruct the PGE systematics of the convecting mantle throughout Earth history (Puchtel & Humayun, 2000; Maier *et al.*, 2003; Puchtel *et al.*, 2004, 2007, 2009b). Temporal variations in komatiite PGE abundances have been interpreted to result from slow mixing of PGE-rich late veneer materials into the mantle (Maier *et al.*, 2009; Fiorentini *et al.*, 2011), though both the presence and interpretation of these trends have been disputed (Puchtel *et al.*, 2014, 2016a).

The use of komatiites to assess mantle PGE abundances carries a number of benefits. Through their extrusion onto the Earth's surface, komatiites avoid persistent problems of mantle metasomatism, and cycles of depletion and refertilisation that plague the

interpretation of PGE data from direct mantle samples (Seyler *et al.*, 2007; Pearson *et al.*, 2014). Furthermore, large degree melts provide an 'average' over a much greater volume of mantle than point samples. However, as with the use of any mantle melt to infer source characteristics, great care must be taken to account for the fractionation of various elements during mantle melting and subsequent processes en-route to, and following emplacement at, the Earth's surface. Understanding how PGEs are fractionated between source and komatiite is therefore critical to using komatiite PGE abundances to estimate mantle PGE concentrations.

Due to the extremely chalcophile nature of the PGEs (e.g., Mungall & Brenan, 2014), a consensus has arisen that interaction with sulphide liquids provides the dominant control on PGE fractionation during mantle melting. This leads to an "all or nothing" behaviour during mantle melting (Barnes *et al.*, 2015); the presence of even minute quantities of residual sulphide in the source produces melts strongly depleted in PGEs, whereas melts produced after sulphide exhaustion in the source contain orders of magnitude higher PGE contents. This understanding underpins the use of komatiites to estimate mantle PGE concentrations. As the 'Platinum PGEs' (PPGEs; Pt and Pd) and Re are thought to behave incompatibly in the absence of sulphide (Barnes *et al.*, 1985), these elements are predicted to be quantitatively removed into mantle melts, providing the melt fraction exceeds the point at which sulphide is exhausted in the source. Observations from modern mantle rocks suggest this occurs after 12 – 15% melt extraction (Luguet *et al.*, 2003), whereas geochemical models typically suggest ~17 – 25% melting is required (e.g., Rehkämper *et al.*, 1999). The PPGE and Re contents of high degree (> 25% melting of the mantle) parental melts are therefore expected to depend only on their degree of melting and source composition, hence, komatiite compositions have been used to interpret secular variations in mantle PGE contents using only minor corrections for post-eruptive fractional crystallisation and the degree of mantle melting (Maier *et al.*, 2009; Fiorentini *et al.*, 2011; Puchtel *et al.*, 2004, 2016a). Clearly, this approach to constraining temporal variations in mantle PGE contents is critically dependent on our understanding of PGE partitioning behaviour.

In this chapter, PGE concentrations and Re-Os isotopic data for the well preserved Palaeoproterozoic Winnipegosis Komatiites is presented. These data provide an opportunity to test our understanding of komatiite-source PGE fractionations and supplies additional komatiite PGE data for the poorly represented Proterozoic aeon. Geochemical modelling is used to explore how PGEs are expected to fractionate between high degree melts and their sources, based on the current state of knowledge of PGE par-

titioning, and these models are tested against PGE data from the Winnipegosis komatiites and literature data for komatiites and picrites. Finally, temporal trends in komatiite PGE abundances are examined, and the implications for mixing of the late veneer into komatiite sources are discussed.

3.2 Background and samples

Background on the geological setting and age of the Winnipegosis Komatiite belt can be found in Chapter 1. The well preserved Winnipegosis Komatiites overlie voluminous tholeiitic basalts (Section 1.2), and were derived from high MgO, nominally dry primary melts with 23.6 ± 1.6 wt% MgO and ≤ 0.1 wt% H_2O, with high liquidus temperatures of ∼1500 ± 30 °C (Chapter 2). Their trace element systematics are consistent with derivation from a depleted source, subsequently contaminated by ∼1 – 3% continental crust. The majority of the komatiites erupted as massive, olivine-phyric flows, though differentiated flows containing olivine spinifex are also observed.

The 13 komatiite samples selected for this study cover a large stratigraphic range from borehole RP1A. The metamorphic grade is sub-greenschist (Section 1.4.3), with approximately one third of samples retaining ≥ 70% fresh olivine phenocrysts. Most incompatible elements, with the exception of the LILEs, show no evidence for remobilisation during metamorphism, though some immobile, incompatible elements such as Nb, Th, and the LREEs were affected by variable but minor crustal assimilation. Fresh bulk samples were selected on the basis of their low CO_2 and H_2O contents (Section 1.6.1), in order to avoid carbonate and serpentine veins not visible in the 2D plane of corresponding thin sections. All of the samples are from massive flows, as borehole RP1A did not intersect differentiated flows. Significant net accumulation of olivine and chromite phenocrysts within these samples is ruled out on the basis of measured MgO contents being similar to the calculated primary melt composition, and the petrographically observed low abundance of phenocrysts.

3.3 Analytical methods

Major, trace, and transition element data discussed in this chapter is presented in Chapter 2.

Platinum Group Elements and Re were analysed using isotope dilution techniques.

Approximately 1 g of whole rock powder and an appropriate amount of a spike, isotopically enriched in ^{99}Ru, ^{106}Pd, ^{185}Re, ^{190}Os, ^{191}Ir, and ^{194}Pt, were weighed precisely and added to 30 ml quartz glass vials. Inverse aqua regia composed of ∼2 ml concentrated HCl and ∼5 ml concentrated HNO_3 was added to the vials. The vials were closed with a semi-permeable Teflon seal and heated to 290 °C at a confining pressure of ∼130 bar for 16 hours in a high pressure asher (HPA), to digest PGE bearing phases and equilibrate the spikes and samples. Os was separated using $CHCl_3$ solvent extraction, back extracted into HBr (Cohen & Waters, 1996), and purified by micro-distillation (Birck *et al.*, 1997). Following Os extraction, the aqua regia was dried before converting Re and the other PGEs to chloride form by drying repeatedly in HCl. Matrix separation was achieved using anion exchange chromatography modified from Pearson & Woodland (2000).

Os isotopes and abundances were measured using negative thermal ionisation mass spectrometry (N-TIMS), on a Thermo Fisher Triton Plus at the Arctic Resources Geochemistry Laboratory at the University of Alberta. Measurements were undertaken by peak hopping on a secondary electron multiplier, with mass fractionation corrected to $^{192}Os/^{188}Os = 3.082614$. Accuracy and precision of the Os isotope analyses was assessed through repeated measurements of the DrOsS standard, which yielded $^{187}Os/^{188}Os = 0.16083 \pm 0.00023$ (2σ, n = 19), or a repeatability under measurement conditions (repeatability) of ∼1.4‰. This mean $^{187}Os/^{188}Os$ overlaps with the accepted value of 0.160924 ± 0.00004 (Luguet *et al.*, 2008) within 2 standard deviations; these data are therefore considered accurate at this level of precision.

PGE and Re abundances were measured on an Element 2 ICP-MS at the Arctic Resources Geochemistry Laboratory. Mass fractionation was corrected externally using synthetic 1 ppb PGE standards. The mass fractionation corrected measured isotopic composition of these standards were repeatable to ∼0.4% for Re, ∼0.6% for Ru, and ∼0.8% for Pd, Ir and Pt (2σ relative). These values represent the maximum precision on an individual isotopic measurement. One total procedural blank was measured for every five samples, yielding average blanks that constitute $< 0.5\%$ of the total concentrations analysed (Table 3.1). Accuracy of the PGE abundance measurements (including Os) was monitored through repeated analyses of the OKUM komatiite Reference Material. The data shows good agreement with previously published data, though 2σ repeatabilities are generally poor relative to expected analytical precision (Table 3.1). This discrepancy is attributed this discrepancy to nugget effects in the ∼1 g samples and/or slight variations in degree of spike-sample equilibration during HPA digestion.

Table 3.1: PGE and Re data for blanks, OKUM standard, and Winnipegosis komatiites. Average OKUM komatiite PGE and Re data from this study is compared to previous work. HPA-ID = High Pressure Asher-Isotope Dilution. NiS-FA = Nickel Sulphur-Fire Assay. Concentrations are given in ppb, except blanks, which are in units of pg. Uncertainties are quoted as 2σ of multiple measurements for blank and OKUM data, and 2σ uncertainties estimated from an in house data reduction scheme for Winnipegosis data. Outlier samples are marked with an asterisk. Os data was not obtained for RP1A-153; Ru data was not obtained for RP1A-53, RP1A-141, and RP1A-153.

	Method	*Os*	*Ir*	*Ru*	*Pt*	*Pd*	*Re*
Procedural Blank							
This study (pg; n = 3)	HPA-ID	1.0 ± 0.7	1.7 ± 1.5	< 12.6	3.0 ± 3.2	0.2 ± 0.2	1.0 ± 0.7
OKUM data							
This study (n = 3)	HPA-ID	0.80 ± 0.17	0.91 ± 0.13	4.51 ± 0.08	11.26 ± 1.05	11.21 ± 0.55	0.48 ± 0.04
repeatability (2σ rel.)		21%	14%	2%	9%	5%	9%
(Geo Labs, 2001)	NiS-FA		0.99 ± 0.14	4.25 ± 0.60	11.00 ± 0.60	11.70 ± 0.50	
(Barnes & Fiorentini, 2008)	NiS-FA		1.05 ± 0.14	4.20 ± 1.00	11.60 ± 0.60	11.80 ± 0.60	
(Maier *et al.*, 2009)	NiS-FA	0.83 ± 0.12	1.00 ± 0.12	4.29 ± 0.62	10.40 ± 0.68	11.43 ± 1.64	
(Savard *et al.*, 2010)	NiS-FA	0.98 ± 0.68	1.00 ± 0.26	4.33 ± 1.06	11.00 ± 0.58	11.35 ± 1.58	
Sample	*MgO*	*Os*	*Ir*	*Ru*	*Pt*	*Pd*	*Re*
Winnipegosis data							
RP1A-8	26.14	0.984 ± 0.005	0.835 ± 0.018	4.64 ± 0.15	6.07 ± 0.14	6.24 ± 0.13	0.445 ± 0.009
RP1A-15	22.81	0.937 ± 0.005	0.769 ± 0.017	4.12 ± 0.13	6.91 ± 0.16	7.09 ± 0.15	0.517 ± 0.011
RP1A-53	22.97	1.287 ± 0.007	1.026 ± 0.032		7.09 ± 0.17	7.51 ± 0.16	0.528 ± 0.014
RP1A-65	23.83	0.942 ± 0.005	0.805 ± 0.018	4.20 ± 0.11	7.44 ± 0.17	7.08 ± 0.15	0.552 ± 0.012
RP1A-87	24.04	0.855 ± 0.005	0.715 ± 0.016	3.98 ± 0.17	6.73 ± 0.15	7.03 ± 0.15	0.532 ± 0.011
RP1A-95*	19.82	1.273 ± 0.007	0.877 ± 0.019	6.84 ± 0.24	7.42 ± 0.17	7.52 ± 0.16	0.592 ± 0.012
RP1A-99*	23.31	1.021 ± 0.005	0.845 ± 0.018	4.37 ± 0.21	5.63 ± 0.13	5.21 ± 0.11	5.998 ± 0.154
RP1A-101	25.09	1.108 ± 0.006	0.865 ± 0.019	3.96 ± 0.15	6.13 ± 0.14	6.46 ± 0.14	0.496 ± 0.010
RP1A-111	25.42	1.110 ± 0.006	0.928 ± 0.020	4.17 ± 0.15	6.56 ± 0.15	6.65 ± 0.14	0.521 ± 0.011
RP1A-120	16.79	0.871 ± 0.005	0.745 ± 0.016	2.75 ± 0.16	9.60 ± 0.22	9.23 ± 0.20	0.703 ± 0.015
RP1A-141	25.05	1.633 ± 0.009	1.347 ± 0.038		6.99 ± 0.17	7.24 ± 0.16	0.473 ± 0.012
RP1A-148	21.05	0.980 ± 0.005	0.800 ± 0.017	3.59 ± 0.24	7.48 ± 0.17	7.59 ± 0.16	0.553 ± 0.012
RP1A-153	22.12		1.131 ± 0.033		7.76 ± 0.19	7.96 ± 0.18	0.586 ± 0.015

3.4 Results

3.4.1 PGE and Re Data

PGE abundance data are presented in Table 3.1. The Iridium PGEs (IPGEs; Os, Ir, Ru) show positive trends against MgO for Winnipegosis Komatiites (Figure 3.1). Ru shows a strong positive correlation, whereas Os and Ir (not shown) form widely scattered trends against MgO, towards lower Os and Ir at low MgO contents. Despite these scattered trends, Os and Ir contents are strongly correlated. As MgO and Cr are also positively correlated (Section 2.4.1), Ru also correlates positively with Cr (not shown). By contrast, the PPGEs and Re show tight negative correlations with MgO. Two samples (RP1A-95 and RP1A-99) form exceptions to several of these general trends. RP1A-95 is the only sample that lies off the Os-Ir correlation, having high Os relative to Ir, and also has a Ru content that lies above the Ru-MgO correlation. RP1A-99 had a high Re content of 6.0 ppb, and low Pd and Pt contents relative to other samples with similar MgO. Chondrite normalised PGE patterns (Figure 3.2) are fractionated with $4.2 \leq (Pd/Ir)_N \leq 9.6$, and $(Pd/Pt)_N > 1$ for all samples.

3.4.2 Re-Os Isotopic Data

Re-Os isotopic data are presented in Table 3.2. The Winnipegosis Komatiite whole rock data are well correlated on a ^{187}Re-^{187}Os isochron (Figure 3.3), defining an age of 1865 ± 40 Ma with low scatter (MSWD = 0.91). This age is identical, within error, to the 1870 ± 7 Ma U-Pb zircon age obtained from mafic rocks elsewhere in the WKB (Section 2.4.3). The initial $^{187}Os/^{188}Os$ of 0.1160 ± 0.0016 corresponds to a γOs of – 0.2 ± 1.4 at 1870 ± 7 Ma, where γOs is the percentage deviation of the initial $^{187}Os/^{188}Os$ from a mantle evolution line defined by the $^{187}Os/^{188}Os$ of Primitive Upper Mantle (PUM; Meisel *et al.*, 2001a) and assuming mantle Re/Os identical to O-chondrite (Walker *et al.*, 2002). The initial $^{187}Os/^{188}Os$ of Winnipegosis komatiites is therefore consistent with a time integrated Re/Os within error of chondritic evolution, as observed for the majority of Archaean and Proterozoic komatiites (Puchtel *et al.*, 2016a).

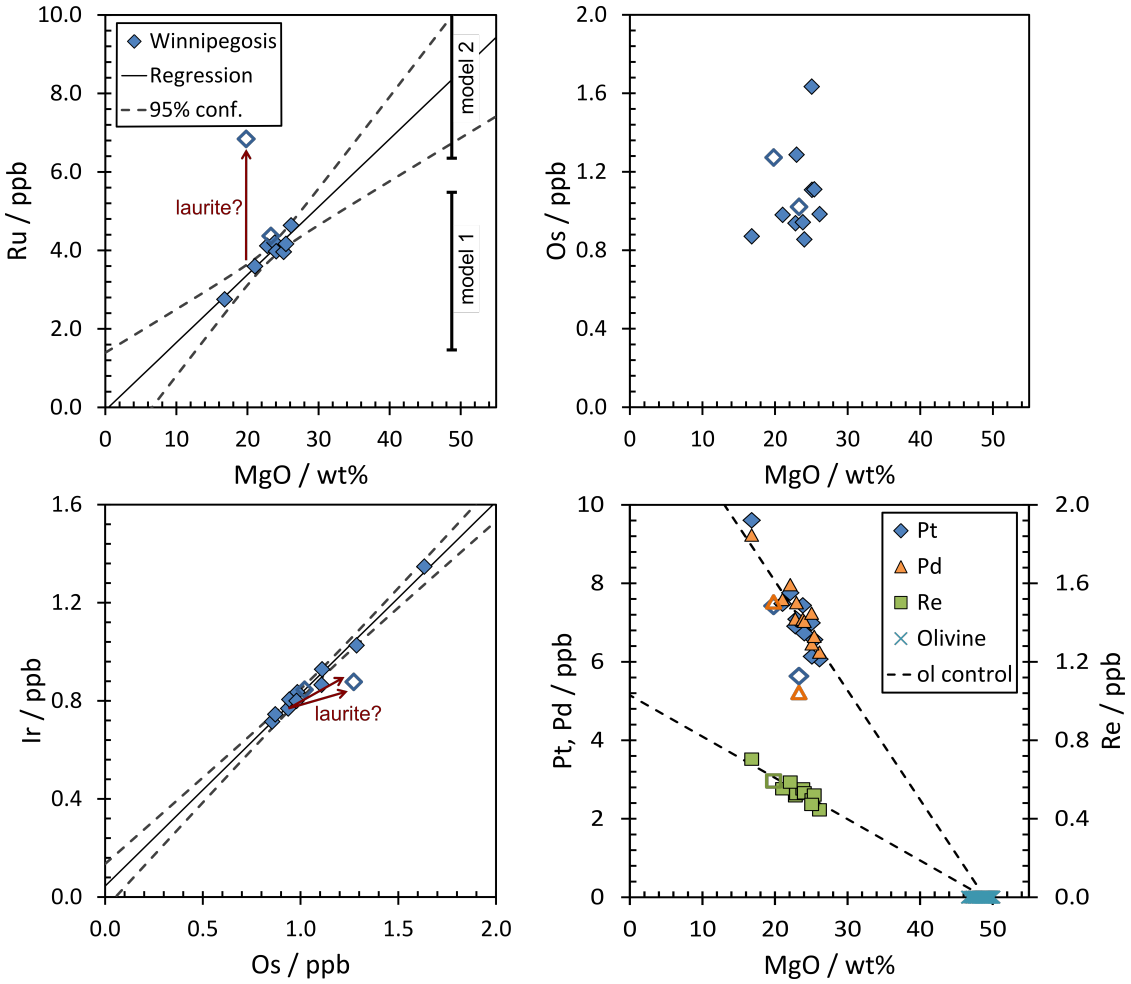

Figure 3.1: PGE and Re data for Winnipegosis Komatiites. Data are plotted as filled symbols except 'outlier' samples RP1A-95 and RP1A-99, which are plotted as open symbols. Solid, thin black lines in Ru-MgO and Ir-Os plots are linear regressions excluding outlier data, dashed grey curves are 95% confidence limits about these regressions. Red arrows show the effect of laurite addition (Section 3.5.2). Thick black bars in Ru-MgO plot are mixture models discussed in Section 5.2. Olivine MgO range (Chapter 2) is plotted assuming negligible contents of Pt, Pd, and Re in olivine. Dashed black olivine (ol) control lines are drawn through median olivine and median bulk rock sample composition (excluding outliers) in Pt-, Pd-, and Re-MgO space. Ol control lines for Pt and Pd are indistinguishable and not plotted separately. Note Re is plotted on secondary vertical axis.

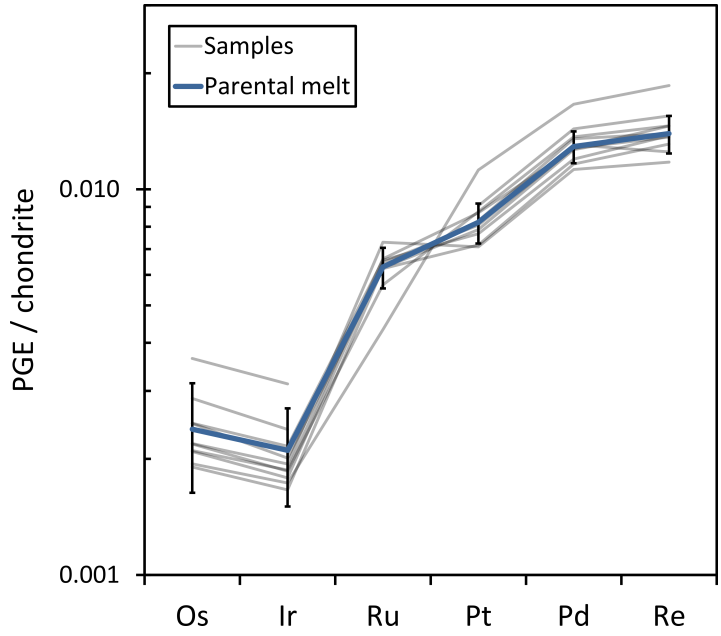

Figure 3.2: PGE + Re patterns for Winnipegosis Komatiite samples (thin grey lines; excluding outliers RP1A-95 and RP1A-99) and estimated parental melt composition (thick blue line with black bars showing 95% confidence limits; Section 3.5.3), normalised to average CI1 chondrite (Horan *et al.*, 2003). Some lines are broken as Ru was not measured for all samples.

Table 3.2: Re-Os isotopic data for Winnipegosis komatiite samples. 2σ absolute uncertainties are estimated using an in house data reduction scheme. $^{187}Re/^{188}Os$ and $^{187}Os/^{188}Os$ errors are correlated due to a shared denominator, ρ is the error correlation coefficient.

Sample number	$^{187}Re/^{188}Os$	2σ	$^{187}Os/^{188}Os$	2σ	ρ
RP1A-8	2.195	0.037	0.18580	0.00027	0.039
RP1A-15	2.683	0.046	0.20167	0.00021	0.034
RP1A-53	1.989	0.048	0.17859	0.00024	0.023
RP1A-65	2.850	0.048	0.20524	0.00024	0.032
RP1A-87	3.029	0.052	0.21135	0.00029	0.034
RP1A-95	2.259	0.038	0.18652	0.00015	0.037
RP1A-99	28.51	0.65	0.18272	0.00017	0.027
RP1A-101	2.172	0.037	0.18415	0.00028	0.033
RP1A-111	2.278	0.039	0.18748	0.00018	0.037
RP1A-120	3.947	0.067	0.24163	0.00028	0.035
RP1A-141	1.401	0.030	0.16069	0.00023	0.025
RP1A-148	2.743	0.048	0.20258	0.00016	0.036

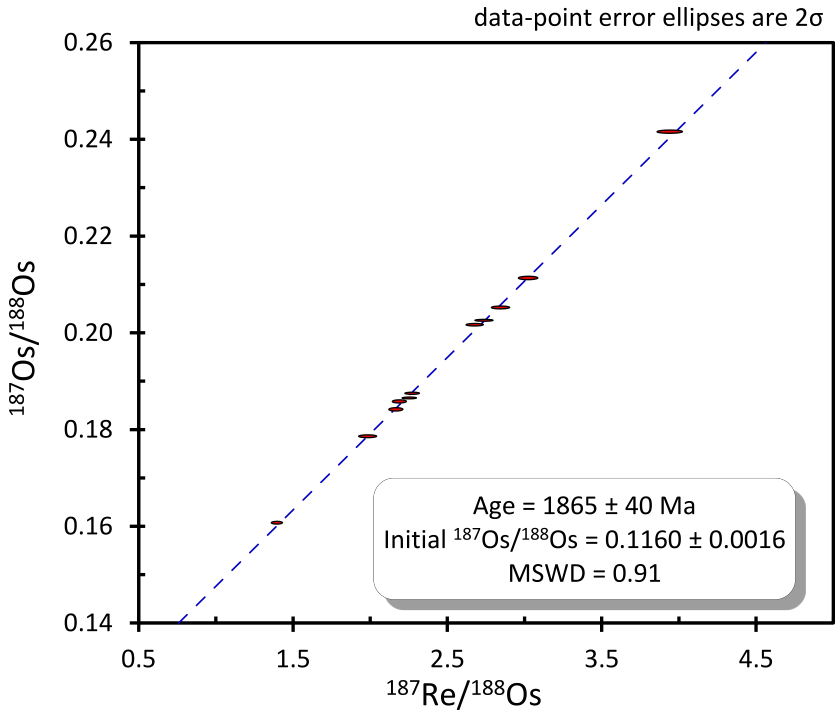

Figure 3.3: 'Model 1' Re-Os isochron for Winnipegosis Komatiites generated using Isoplot 4.11 (Ludwig, 2012) and the Re decay constant of Smoliar *et al.* (1996). The high Re sample RP1A-99 does not fall on the isochron and was excluded. Os data was not obtained for sample RP1A-153.

3.5 Discussion

3.5.1 Effect of sulphide segregation or crustal contamination?

Winnipegosis Komatiites are S-undersaturated, with a median S content of 428 ppm (n = 150; GSC Database) for unmineralised samples from borehole RP1A, compared to a sulphur concentration at sulphide saturation of ~2500 ppm (Mavrogenes & O'Neill, 1999). It is therefore unlikely that PGE contents of bulk rock Winnipegosis komatiites were modified by sulphide segregation (e.g., Barnes & Picard, 1993), as the magmas would not have reached sulphide saturation before extensive crystallisation.

The tight adherence of the PPGEs and Re to olivine control lines (Figure 3.1) is consistent with these elements being unaffected by the 1 – 3% crustal assimilation and subsequent sub-greenschist metamorphism that caused scattered highly incompatible lithophile element systematics (Sections 1.4.3, 2.5.2). The lack of correlation of PPGEs and Re against Th (Figure 3.4), a fluid immobile proxy for continental crustal contam-

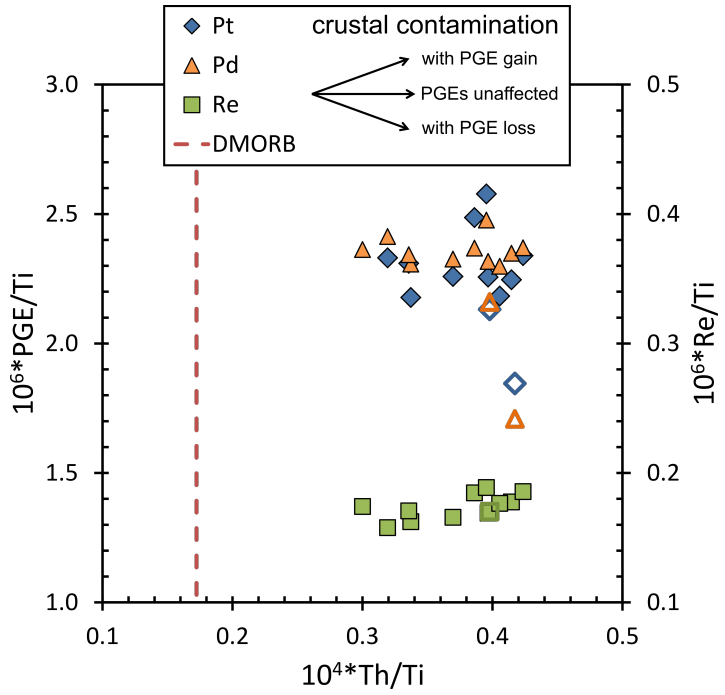

Figure 3.4: Winnipegosis Komatiite PPGE and Re data plotted against Th, a proxy for crustal contamination. Data are normalised to the incompatible element Ti to correct for olivine fractionation. The lack of correlation indicates there was no significant PPGE and Re loss or gain during crustal assimilation. Open symbols indicate outliers (Section 3.4.1).

ination (Lesher *et al.*, 2001), further confirms that there was no significant PPGE or Re gain through continental crust assimilation, or loss through interaction with crustal sulphide. The close agreement between Re-Os and U-Pb ages, chondritic initial Os isotope ratios, and linear relationship between Os and Ir in Winnipegosis Komatiites, rule out significant modification of the IPGEs by crustal assimilation.

3.5.2 Controls on PGE Variations

Os and Ir

Given the documented accuracy and precision of the PGE measurements, and concentrations in the Winnipegosis Komatiites that are well above procedural blank levels, the large scatter in Os and Ir data at a given MgO can be attributed to a 'nugget effect' (Meisel *et al.*, 2001b), i.e., the whole rock budget of these elements is dominated by small grains highly enriched in these elements. The broad positive correlation between MgO and Os suggests that these PGE-rich nuggets crystallised early and were con-

centrated in samples with higher proportions of olivine. Constant Ir/Os ratios across the majority of samples (Figure 3.1) indicate that the composition of these nuggets remained identical, and is consistent with a single Os-Ir bearing phase, such as an Os-Ir alloy (Barnes & Fiorentini, 2008; Kamenetsky *et al.*, 2015). The gradient of the Os-Ir correlation (0.78) implies a composition of $Os_{0.56}Ir_{0.44}$ for these alloys. If Os and Ir also partition significantly into the phenocryst phases olivine and chromite (Barnes & Fiorentini, 2008; Pagé *et al.*, 2012), constant Ir/Os ratios between samples with varying nugget contributions require that Os and Ir partitioned into these major phases in the same ratio ($Os_{0.56}Ir_{0.44}$) as the alloys.

Ru

The tight trend of Ru against MgO shown by most samples is interpreted as indicative of control primarily by major phases; any Ru contained in trace phases likely forms a minor part of the whole rock budget as no appreciable nugget effect is observed. The major and minor element compositions of Winnipegosis Komatiites are well explained by mixing variable amounts of residual melt with a mixture of phenocrysts comprising ~98.9% olivine and 1.1 ± 0.1% chromite (by mass; Section 2.5.1). In Figure 3.1, mixing between these three phases, assuming no Ru present in the residual melt, using median MgO values for Winnipegosis olivine and chromite (Chapter 2), and literature data for Ru in komatiitic olivine and chromite (Puchtel *et al.*, 2004, 2016a; Pagé *et al.*, 2012). 'Model 1' shows the range of compositions possible for mixing 98.9% olivine and 1.1% chromite, across the range of chromite Ru concentrations reported in the literature (147 – 456 ppb), assuming no significant Ru present in olivine (Pagé *et al.*, 2012). This model produces phenocryst mixture compositions with too little Ru to account for the Ru-MgO trend; for chromite to be the only significant Ru bearing phase in the Winnipegosis komatiites Ru concentrations of 696 – 837 ppb (95% confidence intervals) are required to intersect the trend, higher than previously reported in the literature. Model 2 shows the range of compositions possible for the same mixture, but assuming 4.9 ppb Ru in olivine (Puchtel *et al.*, 2016a). This intersects the Ru-MgO trend without requiring unusually high Ru contents. This indicates that the Ru budget of the Winnipegosis Komatiites is most likely controlled by both phenocryst olivine and chromite.

Pt, Pd, and Re

Negative correlations of Pt, Pd, and Re against MgO lie on trends consistent with olivine control lines. These elements were therefore incompatible in olivine and chromite during komatiite crystallisation and were concentrated into the residual melt, as observed in other komatiite suites (Walker *et al.*, 1988; Puchtel *et al.*, 2004). Volatile degassing of Re (Lassiter, 2003) is ruled out on the basis of consistent Re trends between samples from different depths within flows.

Outlier Samples – the effects of 'nuggets'

Sample RP1A-99 has extremely high Re, but low Pt and Pd compared to other samples. This sample is excluded from calculations of parental melt composition (Section 3.5.3), as petrographical observations identified a hydrous vein containing rare, ∼20 μm sulphide grains (Section 1.4.3), which are not observed in any other sample analysed in this study. It is likely that the PGEs in the sample were remobilised during sub-greenschist metamorphism.

Sample RP1A-95 lies 3.49 ± 0.28 ppb Ru above the Ru-MgO trend, at a significantly higher Os/Ir, without deviating from lithophile element (Chapter 2) or PPGE and Re trends. Similar anomalously high Ru has been measured in some Barberton komatiites (Puchtel *et al.*, 2014). This can be explained by RP1A-95 having experienced addition of a nugget phase, highly enriched in IPGEs; it is speculated that this phase is laurite – $(Ru,Os,Ir)S_2$. This mineral is commonly observed in high temperature, sulphur undersaturated melts and contains IPGEs in the proportions Ru > Os > Ir (Stockman & Hlava, 1984; González-Jiménez *et al.*, 2009; Kamenetsky *et al.*, 2015). Assuming laurite compositions between 38 and 56 wt% Ru (González-Jiménez *et al.*, 2009), the elevated Ru in the ∼1 g sample of RP1A-95 analysed can be explained by the inclusion of 6.5 – 9.4 ng of laurite, which corresponds to a grain of ∼13 μm diameter (assuming a single spherical grain, density ∼7 g/cm^3; Bowles *et al.*, 1983). Addition of laurite of this composition would cause deviation from Ir-Os trend along a vector with Ir/Os between 0.23 and 0.45 (Figure 3.1). As the abundance of this IPGE enriched nugget phase cannot be constrained from identification in a single sample, RP1A-95 is excluded from calculations of parental magma PGE composition (Section 3.5.3). However, it should be noted that Os, Ir, and particularly Ru abundances estimated for the parental magma may represent lower bounds.

3.5.3 Parental Magma PGE Composition

The majority of PGE and Re data for the Winnipegosis Komatiites can be explained by mixing between magmatic minerals (olivine, chromite, Os-Ir alloys) and a residual melt (Section 3.5.2), allowing a parental melt PGE composition to be confidently calculated for the komatiites. The PPGEs and Ru show strong correlations with MgO, and are interpolated along their respective linear regressions to the parental melt MgO content. Uncertainties are estimated from 95% confidence limits about these regressions at 23.6 ± 1.6 wt% MgO (Section 2.5.3). By contrast, Os and Ir are highly scattered, and their mean values and 95% confidence limits about these means are instead used to estimate the parental magma composition. This yields a parental melt composition with 1.1 ± 0.3 ppb Os, 0.91 ± 0.26 ppb Ir, 4.0 ± 0.5 ppb Ru, 7.0 ± 0.8 ppb Pt, 7.2 ± 0.7 ppb Pd, and 0.53 ± 0.06 ppb Re (Figure 3.2). Relative uncertainties on this composition are ∼10% for Ru, Pt, Pd and Re, and ∼30% for Os and Ir, though as previously noted, IPGE concentrations may represent lower bounds.

3.6 Modelling the PGE Content of Winnipegosis Komatiites

In order to relate this parental melt composition to the PGE content of the Winnipegosis Komatiite mantle source, it is essential to understand the controls that melting processes exert on the fractionation of PGEs between source and melt. Geochemical modelling of PGE behaviour during mantle melting (Mungall & Brenan, 2014) is therefore used in an attempt to reproduce the PGE contents calculated for the Winnipegosis parental magmas. Central to this modelling is the question: given the current state of knowledge of PGE partitioning during mantle melting, can the PGE contents of Winnipegosis Komatiites be reproduced under reasonable melting conditions?

Modelling PGE behaviour during mantle melting is complex due to their chalcophile and siderophile behaviour and their concentration in trace phases (Lorand & Luguet, 2015). In relatively fertile mantle rocks, PGEs are expected to be concentrated in base metal sulphides (Lorand & Alard, 2001), but for melting past sulphide exhaustion, the IPGEs and Pt may form alloys (Pearson *et al.*, 2004; Luguet *et al.*, 2007). The model of Mungall & Brenan (2014) takes these complexities into account by partitioning the PGEs between silicate minerals, a silicate melt, sulphide melt (where S concentrations in the restite exceed sulphide saturation), and alloys (where PGE contents in the silicate melt exceed alloy saturation) as a function of pressure, temperature, and oxygen and

sulphur fugacity, using the best available partition coefficients for the PGEs. Mantle potential temperature, T_p, is controlled by the pressure of melt initiation (assuming a KLB-1 fertile peridotite source). Oxygen fugacity (f_{O_2}) and initial S content in the source are variables. Melting is modelled in a series of increments, with 0.1% melt 'extracted' each step from a 1.1% batch silicate melt in equilibrium with the residual assemblage; this corresponds to critical melting (Maaløe, 1982), intermediate between batch and fractional melting. These incremental melts are pooled assuming a columnar melting regime. Though this is slightly different to batch melting proposed for some komatiites (e.g., Sossi *et al.*, 2016), pooled critical melts should closely resemble batch melts (Plank & Langmuir, 1992), particularly for komatiites which have melted past sulphide exhaustion in their mantle source.

A potential pitfall of applying this model to komatiite formation is that silicate-sulphide partition coefficients and alloy solubilities for the PGEs have only been determined at low (atmospheric) pressure, rather than the high pressures frequently inferred for komatiite formation (Nesbitt *et al.*, 1979; Ohtani, 1984; Arndt *et al.*, 2008). However, as the sulphide solubility model used has been calibrated to 9 GPa (Mavrogenes & O'Neill, 1999), and sulphide-silicate partition coefficients for the PGEs are generally very high ($\gg 10^3$, with the exception of Re), the results of the model should not be significantly affected by uncertainties in these partition coefficients, provided these partition coefficients remain high at pressures relevant to komatiite formation. The validity of this assumption is discussed in detail in Section 3.6.4. Though a pressure effect on alloy solubility cannot be ruled out at this stage, the effect is likely to be minor compared to the extremely strong dependence of alloy solubility on f_{O_2} (Mungall & Brenan, 2014).

3.6.1 Single Stage Melting of a Fertile Source

As many models for komatiite formation invoke large degree melting of a relatively fertile (or 'primitive') mantle source (e.g., Arndt *et al.*, 2008; Robin-Popieul *et al.*, 2012; Sossi *et al.*, 2016), this is a good starting point for modelling of the Winnipegosis Komatiite PGE contents. The initial source composition is assumed to be fertile KLB-1 with an S content of 185 ppm (Mungall & Brenan, 2014). A range of possible source PGE contents are used for modelling: PUM of Becker *et al.* (2006), median orogenic peridotite of Barnes *et al.* (2015), and Archaean Convecting Mantle (ACM) of Aulbach *et al.* (2015). As PGEs are not extensively depleted from the source until near sulphide

exhaustion, the results of this model broadly apply to sources that have undergone low levels of depletion (e.g., < 8%, see Section 3.6.3), though slightly higher melt PGE concentrations are produced due to a reduced 'dilution' effect from the earliest formed, PGE-poor melts. Likewise, varying the assumed initial sulphur content of the source affects the melt fraction at which sulphide exhaustion occurs, and therefore the PGE concentrations at low melt fractions, but does not qualitatively change the results of the model.

Primelt3 software (Herzberg & Asimow, 2015) indicates an average T_p of 1644 °C for formation of Winnipegosis Komatiites by batch melting of fertile peridotite (Section 2.6.2). Propagating uncertainties from both compositional variability of the komatiites and accuracy of Primelt3 calculations gives $T_p = 1644 \pm 53$ °C (2σ). This corresponds to a depth of melting initiation of 4.6 GPa, or ~150 km, in the Mungall & Brenan (2014) model. V/Sc partitioning for melting in the spinel field (Lee *et al.*, 2005) provides a likely lower bound on the f_{O_2} of Winnipegosis Komatiites of 1 $\log_{10}$ unit below QFM (QFM – 1; Section 2.5.3). The f_{O_2} of QFM – 3 predicted for melting in the garnet stability field is considered to be unreasonably low, as it is considerably lower than previous estimates of komatiite oxygen fugacity (e.g., Berry *et al.*, 2008), and it is difficult to envisage oxidation of the Winnipegosis magma by nearly four $\log_{10}$ f_{O_2} units between its genesis in the mantle and crystallisation of chromite phenocrysts. An upper bound is provided by Fe^{2+}/Fe^{3+} of chromites (Maurel & Maurel, 1982; Larsen & Pedersen, 2000), which suggest an $Fe^{2+}/\Sigma Fe$ of 0.90 at ~1400 °C (Section 2.5.3), corresponding to an f_{O_2} of QFM + 0.75 (Kress & Carmichael, 1991). Finally, the Primelt3 calculations provide approximate constraints on the degree of melting: 34 ± 6% (2σ) from FeO/MgO, and 36 ± 4% calculated using the Olivine-Anorthite-Quartz projection with a harzburgite residuum (Herzberg & Asimow, 2015). Using these approximate constraints, melt PGE contents are modelled as a function of melt fraction for aggregated critical melts (Figure 3.5). These are compared to the calculated Winnipegosis parental melt compositions (Section 3.5.3) at the widest possible 2σ range of melt fractions calculated by Primelt3 (28 – 40%).

Some first-order results of the model have been described previously (Mungall & Brenan, 2014) but are relevant here. Due to the chalcophile nature of the PGEs, early melts formed in equilibrium with sulphide in the restite have very low PGE concentrations; PGEs are quantitatively retained in the mantle source until sulphide exhaustion is reached (after ~8 – 11% aggregate melting under these conditions). At this point, the PPGEs and Re behave incompatibly and are effectively depleted in the

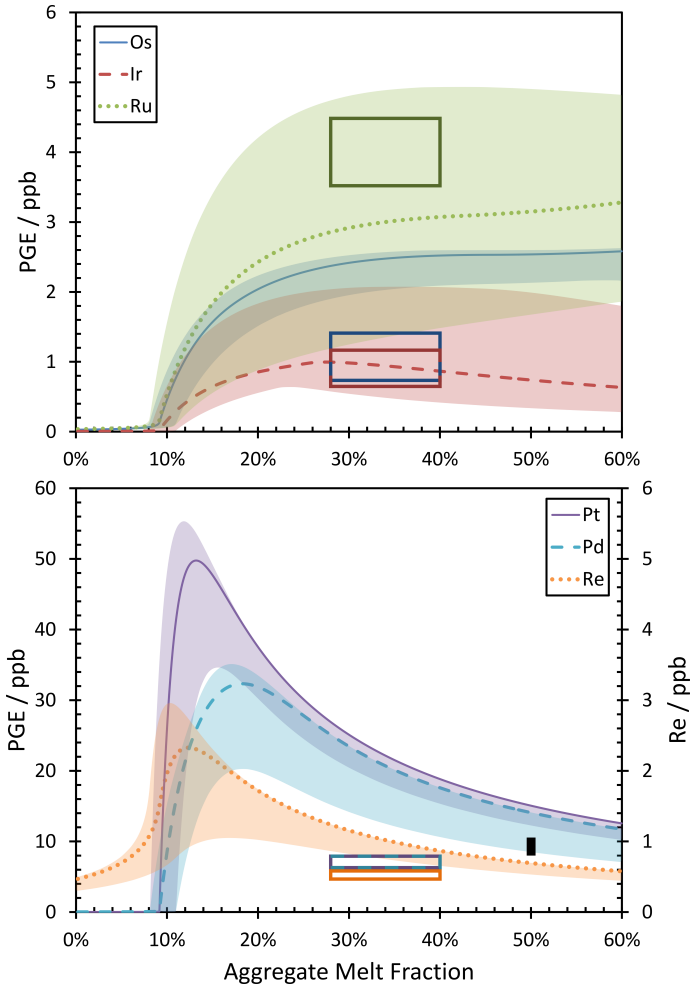

Figure 3.5: Modelled PGE concentrations as a function of aggregate melt fraction (maximum degree of melt extracted from source rock in the melt column). Opaque curves are for melting at T_p = 1644 °C, f_{O_2} = QFM, and a PUM initial source composition (Becker *et al.*, 2006). Transparent shaded regions show range of compositions that can be produced between 1591 < T_p < 1697 °C, QFM – 1 < f_{O_2} < QFM + 0.75, and varying initial source PGE concentrations between PUM, median orogenic peridotite (Barnes *et al.*, 2015) and Archaean Convecting Mantle (Aulbach *et al.*, 2015). The upper boundaries of these shaded areas correspond to higher initial source PGE contents, and hotter, more oxidising conditions, which promote earlier sulphide exhaustion. The lower boundaries represent cooler, more reducing conditions, with lower initial source PGE contents. At high degrees of melting (> 30%) the PPGE concentrations for different melting conditions converge; once PPGEs are exhausted from the source they only depend on the initial composition and extent of melting. Parental melt compositions for Winnipegosis Komatiites at estimated melt fractions of 28 – 40% are delineated by coloured boxes, with dashed lines where concentrations for different elements overlap. Black bar indicates calculated parental melt Pt and Pd contents for Pyke's Hill komatiites at an estimated melt fraction of ~50% for comparison (Section 3.6.4). Note secondary axis for Re.

source by approximately 20% melting. Pt alloy is not predicted to be stable under the high temperatures required for komatiite formation due the higher absolute f_{O_2} along a given oxygen buffer (e.g., QFM) at higher temperatures. In contrast, the more compatible IPGEs are partitioned more evenly between the silicate melt and restite after sulphide exhaustion, and are partially retained or even concentrated (in the case of Ir) in the source at extreme melt fractions. The inflection point in Ir concentration at a melt fraction of ∼26% corresponds to Ir alloy saturation.

The large range in predicted IPGE concentrations at a given melt fraction (Figure 3.5) is largely generated by uncertainties in the f_{O_2} of the Winnipegosis komatiites (QFM – 1 < f_{O_2} < QFM + 0.75), with higher f_{O_2} increasing alloy solubility. Increased temperatures also produce a similar effect due to the increase in absolute f_{O_2} with temperature, though this is minor in comparison. Higher f_{O_2} and temperature also promote sulphide exhaustion (Ding & Dasgupta, 2017), leading to increased contents of both IPGEs and PPGEs at lower degrees of melting. By contrast, at melt fractions of greater than about 20%, the PPGEs and Re are predicted to be completely independent of f_{O_2} and temperature due to their incompatible behaviour in the absence of sulphide, and depend only on the initial source composition and aggregate melt fraction. The PPGE concentration of the melt can then be approximated by:

$$[PPGE]_{melt} = \frac{[PPGE]_{source}}{F}, \tag{3.1}$$

where square brackets denote concentration, and F is the melt fraction.

A number of features of these models fail to reproduce the PGE contents of the Winnipegosis parental magma. Though Ir and Ru contents can be well matched within the range of melting conditions considered, the Os/Ir ratio of the model melts is much too high, except at the upper end of the f_{O_2} and T_p range, at which point Os and Ir concentrations are both considerably higher than observed. This high Os/Ir ratio may arise from uncertainties in the alloy solubility and olivine partition coefficients of Os, which are currently poorly constrained (Brenan *et al.*, 2005). Perhaps the most striking discrepancy in this modelling is that the PPGE contents of the model melts are considerably higher than those of the Winnipegosis Komatiites for any reasonable melt fraction and source composition, ranging from ∼27 ppb Pt and ∼25 ppb Pd, to ∼15 ppb Pt and ∼11 ppb Pd.

A comparison to Archaean komatiites demonstrates that these lower than predicted Pt and Pd concentrations in Winnipegosis Komatiites are not just a feature of the

Mungall & Brenan (2014) model. Winnipegosis Komatiites formed from a cooler source and likely a smaller aggregate degree of melting than their Archaean counterparts (Section 2.5.4), though still well beyond sulphide exhaustion. Therefore, for any single stage melting model in which Pt and Pd behave incompatibly following sulphide exhaustion, they are predicted to have higher Pt and Pd contents than typical Archaean komatiites due to less 'dilution' by continued addition of Pt- and Pd-poor melt. In contrast, Winnipegosis komatiites contain lower Pt contents than typical Neoarchaean komatiites, which contain 8 – 12 ppb Pt (Maier *et al.*, 2009). Possible solutions to the discrepancies between the model predictions and Winnipegosis data are discussed below.

3.6.2 Low PGE concentrations in the Winnipegosis mantle source?

One possibility is that low PGE concentrations in the Winnipegosis komatiites reflect low PGE concentrations in the Winnipegosis source, either due to the source only receiving a partial late veneer component, due to sluggish mantle mixing (Maier *et al.*, 2009), or the presence of low-PGE recycled oceanic crustal components (Sobolev *et al.*, 2007).

To reproduce the calculated parental melt compositions under the conditions outlined in Section 3.6.1, the Winnipegosis Komatiite source mantle would require Pt contents of 26 – 40% of PUM, and Pd contents of 29 – 38% of PUM. A source with only a partial late veneer component seems unlikely on the basis that this requires the preservation of a large volume of this very low-PGE mantle for ∼2 Ga since accretion. Furthermore, as the late veneer is required to be broadly chondritic to explain Earth's mantle PGE abundances (Chou, 1978), a source this depleted in Pt and Pd cannot explain the Ru and Ir concentrations in Winnipegosis Komatiites, which are accurately reproduced by the modelling.

Similarly, as oceanic crust and its metamorphosed equivalents is depleted in both PPGEs and IPGEs (Peucker-Ehrenbrink *et al.*, 2003; Dale *et al.*, 2009), the presence of a $> 60\%$ recycled oceanic crust in the Winnipegosis Komatiite source cannot simultaneously satisfy the IPGE and PPGE concentrations of the parental melt. Additionally, such a large contribution from recycled components would likely be distinguishable in major and trace element concentrations of Winnipegosis bulk rocks and olivines (Sobolev *et al.*, 2007; Maier *et al.*, 2009), and is not compatible with the chondritic initial Os composition of Winnipegosis Komatiites due to the high average Re/Os ratio

of oceanic crust (Peucker-Ehrenbrink *et al.*, 2003).

3.6.3 Two stage melting

One scenario that could potentially generate lower PPGEs in Winnipegosis komatiites without producing depleted IPGEs is prior depletion of their source by a previous stage of melt extraction. Due to the expected incompatibility of the PPGEs in the absence of sulphide, melting just beyond sulphide exhaustion should rapidly deplete the PPGEs without strongly affecting the compatible IPGEs. Two-stage melting is simulated using the model of Mungall & Brenan (2014), beginning with a fertile mantle source with the same PGE and S concentrations as described for the single stage model above, and modelling the extraction of melt fractions between 0 and 20%. This represents the first stage of melting or depletion of fertile mantle. Melt fractions beyond 20% were not considered as by this point the model predicts that PPGEs should have been quantitatively removed from the source, and so re-melting of this source could not generate melts with Winnipegosis PGE systematics. The second stage of melting was then modelled by assuming complete extraction of the remaining PPGEs in the residue into a melt. This approach is valid for second stage melts that form well beyond sulphide exhaustion (> 20% melting) providing the PPGEs behave incompatibly following sulphide exhaustion. The PPGE concentrations in the second stage melt can therefore be calculated using:

$$[PPGE]_{melt} = \frac{[PPGE]_{source}}{F_2 - F_1}, \tag{3.2}$$

where square brackets denote concentrations, $[PPGE]_{source}$ is the PPGE concentration in the source following prior depletion, F_1 is the degree of first stage melting (0 – 20%), and F_2 is the final degree of melt extraction after both stages of melting, taken as the total degree of melting calculated for the Winnipegosis komatiites by Primelt3 (28 – 40%).

Two different scenarios are examined. In the first, a fertile mantle source was depleted by extraction of melt at low, MORB-like temperatures ($T_p \approx 1400$ °C). This is intended to represent source depletion by melting that could potentially produce the tholeiitic basalts that underlie the Winnipegosis Komatiites in the Winnipegosis Komatiite Belt (Section 1.2), if these basalts were produced before impingement of the plume that formed the Circum Superior Belt. In the second, the source is depleted at the higher potential temperatures calculated for formation of the Winnipegosis Komatiites

themselves (T_p = 1644 ± 53 °C), representing early melt removal from the ascending plume that generated the komatiites. The Pd and Pt contents, and Pd/Pt ratio, of second stage melts are plotted in Figure 3.6 as a function of the degree of first stage melting (F_1).

This modelling supports the previous assertion that the single stage melting calculations are qualitatively unchanged by small degrees of prior depletion which do not exhaust sulphide in the source. The sharp inflection points on the Pt and Pd concentration plots (Figure 3.6) correspond to the degree of prior melting at which sulphide is exhausted, between 8 – 14% melt extraction depending on the exact T_p and f_{O_2}. For degrees of melting lower than this, the only effect prior depletion has on the second stage melts is to increase their PPGE contents, as the high PPGE melts formed immediately after sulphide exhaustion are less diluted by PPGE poor melt produced prior to sulphide exhaustion.

By contrast, if the first stage of melting progresses beyond sulphide exhaustion, the Pt and Pd concentrations remaining in the source rapidly diminish. This leads to a drop in the PPGE contents of the second stage melts, and either the Pt or Pd concentrations of the Winnipegosis parental melt can be generated from melting of a source that has previously undergone ∼10 – 20% melt extraction, depending on the exact conditions under which the first stage melt was extracted. However, after sulphide exhaustion, the Pd/Pt ratios of residues are predicted to diverge strongly from that of the original mantle source. For prior melting at low (MORB-like) temperatures and correspondingly low pressures, Pd is predicted to be less compatible than Pt, and the Pd/Pt ratios falls. However, as a monovalent element with a slightly smaller cation size than Na, Pd is predicted to be increasingly compatible in opx at high pressures (Aulbach *et al.*, 2015). As such, the model predicts that for melting at high T and P, Pd should be depleted less rapidly in the source after sulphide exhaustion, and so the source is driven to high Pd/Pt. Remelting of this source will then impart this fractionated Pd/Pt ratio to second stage melts. As the chondrite normalised Pd/Pt ratio of Winnipegosis parental melts, $(Pd/Pt)_N$ = 1.57 ± 0.24 (2σ), is identical to that of PUM, $(Pd/Pt)_N$ = 1.44 (Becker *et al.*, 2006), the Pt and Pd contents of the Winnipegosis parental melt cannot be simultaneously modelled if the first stage of melting occurs at 1400 °C or 1644 ± 53 °C.

However, due to this predicted variation of Pd compatibility with pressure, there exists the possibility that melting temperatures and pressures intermediate between the two endmember models can deplete the PPGEs with fractionating Pt from Pd.

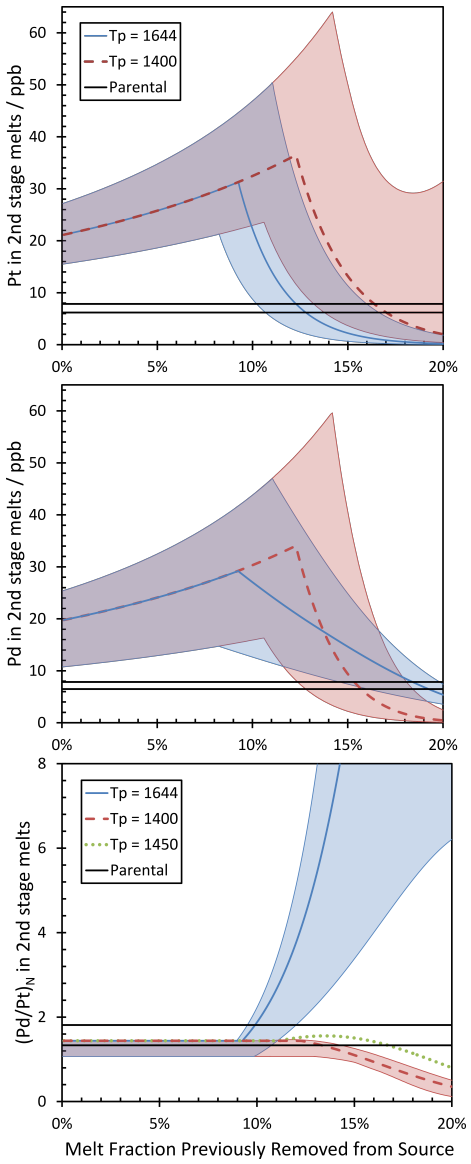

Figure 3.6: Modelled PGE concentrations in a second stage melt (melting of a previously depleted mantle source) formed by 28 – 40% melting, as a function of melt fraction removed during the first stage of melting. Thick opaque and dashed curves are for melting at f_{O_2} = QFM, and a PUM initial source composition (Becker *et al.*, 2006), at varying T_p indicated in the legend. Transparent shaded regions bordered by thin curves show range of compositions that can be produced between $1591 < T_p < 1697$ °C, QFM – 1 < f_{O_2} < QFM + 0.75 (blue), and QFM – 1 < f_{O_2} < QFM + 0.75 at fixed T_p of 1400 °C (red), both with a range of initial source PGE concentrations described in Section 3.6.1. Black bars show the 2σ range of Pt and Pd concentrations, and Pd/Pt calculated for Winnipegosis parental melts. In general, higher PPGE contents in the second stage melt are promoted by lower temperatures, f_{O_2}, and extent of melting during the first stage depletion.

Figure 3.6 also shows how the Pd/Pt ratio of a second stage melt varies following prior melting at 1450 °C and QFM. Under these conditions, it is theoretically possible to deplete the PPGEs while maintaining Pd/Pt ratios within the possible range for Winnipegosis parental melts. Nonetheless, this possibility is rejected on the grounds that natural mantle sample which have experienced large degrees of PPGE depletion invariably show absolute concentrations of Pt > Pd (Lorand *et al.*, 1999; Pearson *et al.*, 2004). This suggests that if Pd is in fact compatible in opx at high pressures, then Pt is also likely to be compatible in a silicate phase (Section 3.6.5).

In summary, though the (Mungall & Brenan, 2014) model does allow the PPGE concentrations of Winnipegosis Komatiites to be reproduced by two-stage melting under very specific conditions, it is unlikely that the Winnipegosis Komatiites could have been produced from a source depleted beyond sulphide exhaustion while maintaining PUM-like Pd/Pt ratios. Two-stage melting as a means of generating low PPGE contents in melts produced beyond sulphide exhaustion also appears particularly unlikely given the correlation between parental melt Mg# and PPGE concentrations observed in Section 3.6.4; paradoxically, this would require the lowest degree melts to have formed from the most depleted sources.

3.6.4 Compatibility of PPGEs during high degree mantle melting

Lower than predicted Pt and Pd concentrations in the Winnipegosis komatiites cannot be explained by melting of a PGE-poor source, or remelting of a source previously depleted in Pt and Pd through melt extraction. The possibility that the PPGEs were not fully exhausted in the Winnipegosis mantle source during melting is therefore considered, i.e., Pt and Pd behave more compatibly than currently thought after sulphide exhaustion.

Compilation of komatiite and picrite parental melts

To test this hypothesis, major element and PGE data was compiled from literature sources for a number of komatiites and picrites generated by high degrees of melting (beyond sulphide exhaustion in the source). For each suite, parental melt MgO, FeO, Mg#, Pt, Pd, TiO_2, and Al_2O_3/TiO_2 were calculated (Summarised in Table 3.3). Unlike previous studies which have used large databases of PGE data (e.g., Maier *et al.*, 2009; Fiorentini *et al.*, 2011), this compilation focusses on a smaller number of well-studied localities which either retain primary igneous olivine or for which primary melt

MgO has been previously estimated. Only localities for which PPGE data could be described by primary igneous differentiation trends (mostly olivine control lines) were considered.

Where olivine is preserved, parental melt MgO, FeO and Mg# were calculated using olivine-melt Fe-Mg exchange (Roeder & Emslie, 1970; Nisbet *et al.*, 1993), using K_D = 0.345 (Matzen *et al.*, 2011), $Fe^{2+}/\Sigma Fe$ = 0.90 (Section 2.5.3; Berry *et al.*, 2008). Errors were estimated by propagating an error in Mg# of ± 0.005 (2σ) to account for systematic differences between EPMA calibration in different sessions or labs (Section B.4). Where olivine was not preserved, previous estimates of parental MgO were used, and parental melt FeO contents and Mg# were estimated from correlations between FeO and MgO with $Fe^{2+}/\Sigma Fe$ = 0.90. Arbitrary errors of ± 3 wt% MgO were assigned to account for analytical errors, possible metamorphic effects, and differences in methods of calculating MgO between studies.

Parental melt Pt, Pd, and TiO_2 were calculated from regressions of these elements against MgO to the parental melt MgO. As all three of these elements are normally incompatible during crystallisation of high degree melts, addition or subtraction of olivine will closely approximate the liquid line of descent (Section 2.5.5; Francis, 1985), and so olivine control lines can be used to estimate parental melt compositions. Errors were conservatively estimated by calculating 95% confidence limits about the regression from the residual standard deviation and the student's t value, and calculating the range of values at these limits at the parental melt MgO ± 2σ. Use of 95% confidence limits means that scattered data or sample suites with few PGE analyses produce large errors in estimated parental melt composition. Parental melt Al_2O_3/TiO_2 was calculated by taking averages for all samples in each suite.

Table 3.3: Summary of calculated parental melt compositions from the komatiite and picrite compilation. A full list of references can be found in Table C.1. Estimated uncertainties are given as ± 2σ for age, melt Mg#, MgO, and Al_2O_3/TiO_2, and as the range in 95% confidence limits at the parental melt MgO ± 2σ for Pt, Pd, and TiO_2.

			Calculated parental melt compositions					
Location	*Age (Ma)*	*Max Ol Mg#*	*Melt Mg#*	*MgO (wt%)*	*Al_2O_3/TiO_2*	*Pt (ppb)*	*Pd (ppb)*	*TiO_2 (wt%)*
Mauna Kea	∼0	0.884	0.72 ± 0.01	15.5 ± 0.8	5.3 ± 0.3	1.3 ± 0.7	1.6 ± 0.9	2.10 ± 0.11
Hualalai	∼0	0.890	0.74 ± 0.01	14.4 ± 0.9	6.5 ± 0.2	2.0 ± 0.9	2.1 ± 1.2	1.77 ± 0.12
Loihi	∼0	0.894	0.74 ± 0.01	17.7 ± 0.9	4.8 ± 0.3	6.9 ± 1.9		2.07 ± 0.38
Kilauea	∼0	0.899	0.75 ± 0.01	16.8 ± 0.7	5.3 ± 0.3	2.1 ± 0.6	2.4 ± 1.4	1.98 ± 0.15
Mauna Loa	∼0	0.903	0.76 ± 0.01	18.5 ± 1.1	6.4 ± 0.4	2.5 ± 0.9	1.5 ± 1.1	1.60 ± 0.21
Gorgona G1	89 ± 1	0.915	0.79 ± 0.01	21.2 ± 1.3	19.1 ± 3.9		11.4 ± 2.1	0.61 ± 0.04
Gorgona G2	89 ± 1	0.915	0.79 ± 0.01	19.7 ± 1.3	26.2 ± 3.4	14.2 ± 6.3		0.41 ± 0.04
Winnipegosis	1870 ± 7	0.923	0.81 ± 0.01	23.6 ± 1.6	17.1 ± 0.2	7.0 ± 0.8	7.2 ± 0.7	0.50 ± 0.03
W. Greenland	62 ± 1	0.928	0.82 ± 0.01	25.3 ± 2.0	10.4 ± 1.9	8.4 ± 1.8	6.7 ± 2.3	0.97 ± 0.10
Emeishan	259 ± 3	0.928	0.82 ± 0.01	25.1 ± 1.3	8.1 ± 4.2	7.4 ± 1.3		0.96 ± 0.10
Schapenburg	3550 ± 87	-	0.82 ± 0.01	∼ 27	9.1 ± 0.5	3.6 ± 0.6	3.1 ± 0.7	0.47 ± 0.07
Komati Fm	3484 ± 38	0.929	0.82 ± 0.02	28.0 ± 2.6	10.1 ± 0.3	5.2 ± 0.8	5.1 ± 0.7	0.41 ± 0.05
Kostomuksha	2795 ± 40	-	0.82 ± 0.02	∼ 27	17.0 ± 0.5	10.6 ± 1.4	10.6 ± 1.6	0.45 ± 0.07
Coonterunah	3505 ± 15	-	0.82 ± 0.02	∼ 23	22.3 ± 1.6	3.8 ± 1.3	4.3 ± 3.9	0.36 ± 0.22
Belingwe	2689 ± 16	0.936	0.83 ± 0.01	28.4 ± 1.9	19.8 ± 0.3	8.0 ± 1.0	7.6 ± 0.7	0.31 ± 0.03
Volotsk	2850 ± 84	-	0.83 ± 0.02	∼ 27	23.7 ± 1.3	10.9 ± 1.9	10.6 ± 2.6	0.30 ± 0.04
Alexo	2733 ± 20	0.938	0.84 ± 0.01	28.7 ± 1.9	20.6 ± 0.4	9.7 ± 1.1	9.9 ± 1.1	0.34 ± 0.03
Regal	∼3200	-	0.84 ± 0.02	∼ 27	10.9 ± 1.8	6.9 ± 3.1	6.0 ± 3.6	0.38 ± 0.03
Pyke's Hill 1	2733 ± 20	0.944	0.85 ± 0.01	30.1 ± 1.9	20.3 ± 0.2	9.1 ± 0.8	9.4 ± 0.9	0.33 ± 0.03
Pyke's Hill 2	2733 ± 20	0.944	0.85 ± 0.01	30.7 ± 1.8	20.6 ± 0.3	9.7 ± 0.8	9.3 ± 0.9	0.31 ± 0.03
Weltevreden	3263 ± 12	0.950	0.87 ± 0.01	30.8 ± 2.4	29.3 ± 0.6	9.0 ± 1.1	7.0 ± 0.9	0.19 ± 0.02

Compilation results

Parental melt Mg# was used as a proxy for the melt fraction, as this broadly increases with extent of melting, and unlike parental melt MgO, does not significantly increase with pressure of melting (e.g., Herzberg & O'Hara, 2002). For incompatible PPGE behaviour after sulphide exhaustion, parental melt PPGE contents are expected to fall as melting progresses and the Mg# increases. However, excluding the Gorgona komatiites and picrites from Loihi, Hawaii, which appear to have formed from PPGE/IPGE enriched sources (see below), both Pt and Pd concentrations in calculated parental melts correlate positively with parental melt Mg# (Figure 3.7), with R^2 values of 0.66 and 0.59 respectively (statistically significant at the 95% level for n = 18 and n = 17 respectively). Archaean komatiites such as the Weltevreden and Abitibi komatiites, with the highest parental melt Mg#s have the highest PPGE contents whereas the lowest Mg# picrites from Hawaii have the lowest PPGE contents. Parental melt PPGE contents also negatively correlate with parental melt TiO_2 contents (Figure 3.8). This behaviour indicates that Pt and Pd cannot be strongly incompatible during high degree mantle melting following sulphide exhaustion, and must be partially retained in the mantle source even at very high degrees of melting.

Limited compatibility of the PPGEs after sulphide exhaustion readily explains the low PPGE contents of Winnipegosis komatiites. Winnipegosis komatiites contain lower PPGE concentrations than predicted by the (Mungall & Brenan, 2014) model because Pt and Pd were not rapidly exhausted in the source following sulphide exhaustion. They contain lower PPGE concentrations than many Archaean komatiites because they were formed by lower degrees of melting. Winnipegosis PPGE concentrations (7.0 ± 0.8 ppb Pt, 7.2 ± 0.7 ppb Pd at Mg# 0.81) are within error of both the 60 Ma West Greenland picrites (8.4 ± 1.8 ppb Pt, 6.7 ± 2.3 ppb Pd) and ∼2.7 Ga Belingwe komatiites (8.0 ± 1.0 ppb Pt, 7.6 ± 0.7 ppb Pd), which formed from melts with similar parental melt Mg#s of 0.82 and 0.83 respectively.

Gorgona and Loihi – high PPGE/IPGE sources?

The only two suites that lie significantly above the trend in parental melt PPGEs against Mg# (Figure 3.7) are Gorgona komatiites (Brügmann *et al.*, 1987; Brandon *et al.*, 2003) and picrites from Loihi, Hawaii (Ireland *et al.*, 2009). A possible explanation for this is that parental melt Mg#s and MgO contents for these lavas were underestimated; as the PPGEs are generally negatively correlated with MgO, any such underestimation

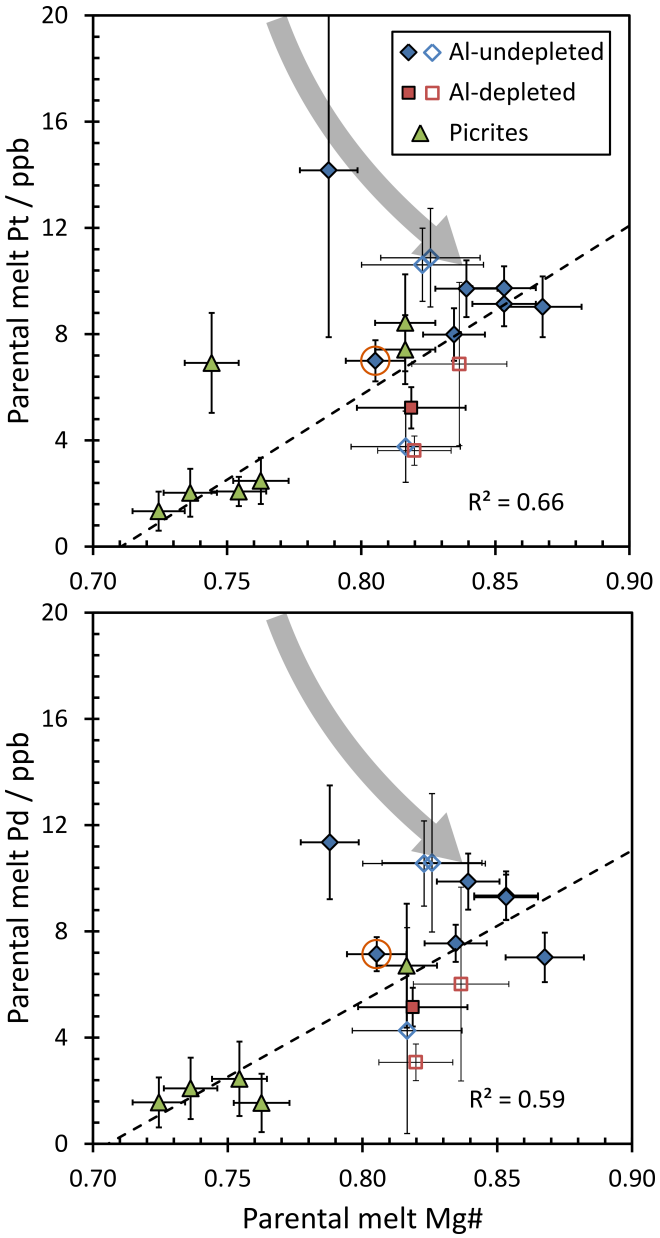

Figure 3.7: Parental melt Pt and Pd contents plotted as a function of parental melt Mg# for a wide range of komatiites and picrites. Closed symbols represent localities where fresh olivine was preserved, and parental melt Mg# and MgO could be calculated from olivine-melt Fe-Mg partitioning. Open symbols are localities where olivine was not preserved and previous estimates of parental melt MgO were used. Winnipegosis komatiite data are highlighted with orange circles. Dashed lines are linear regressions through the data (excluding Gorgona and Loihi) with the given R^2 values representing statistically significant positive correlations at the 95% level for n = 18 (Pt) and n = 17 (Pd) samples. Grey arrows show schematic trend expected for incompatible Pt and Pd behaviour following sulphide exhaustion in the source (Figure 3.5).

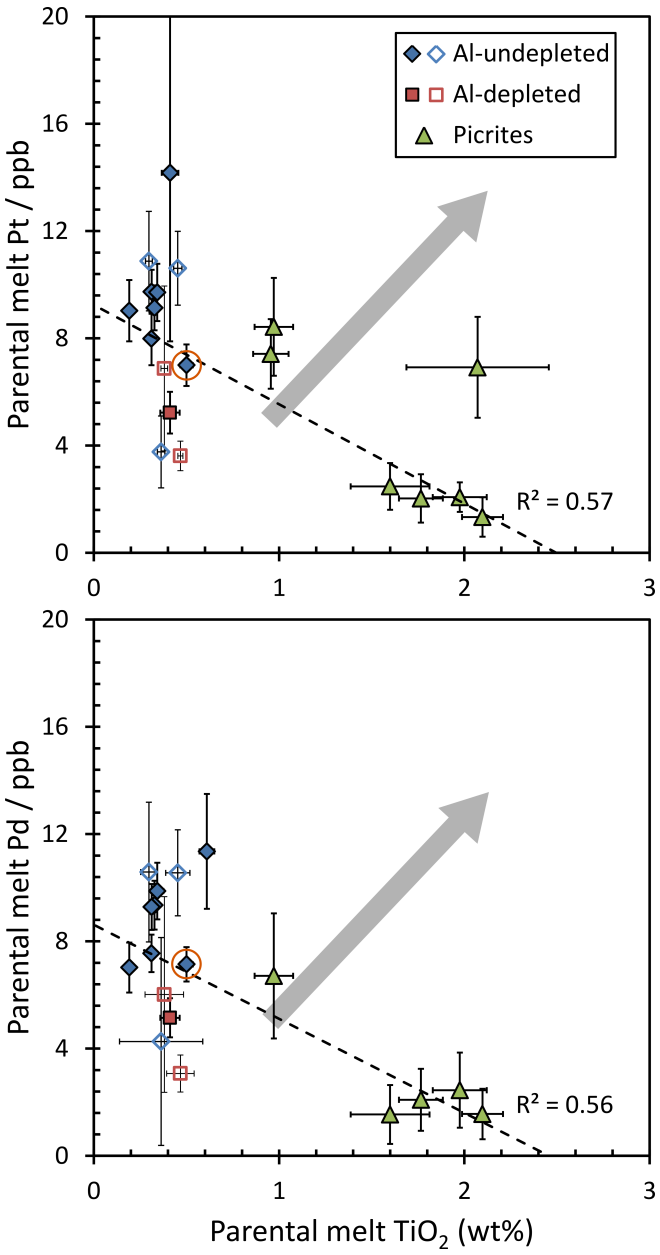

Figure 3.8: Parental melt Pt and Pd contents plotted as a function of parental melt TiO_2 for a wide range of komatiites and picrites. Symbols as in Figure 3.7, Winnipegosis komatiite data are again highlighted with orange circles. Dashed lines are linear regressions through the data (excluding Gorgona and Loihi). Grey arrows schematically show the expected trend for incompatible Pt and Pd behaviour following sulphide exhaustion in the source; for incompatible behaviour Pt and Pd should correlate positively with the incompatible element Ti. The observed trend is perpendicular to this prediction.

would shift the data almost perpendicularly to the observed trend towards higher PPGE contents and lower Mg#. However, this is considered unlikely for these localities; the highest Mg# olivines from Loihi are comparable to other Hawaiian picrites, and a wide range of studies have identified relatively low parental melt MgO contents of 17 – 20% for Gorgona komatiites (Revillon *et al.*, 2000; Kamenetsky *et al.*, 2010), similar to the values calculated here (Table 3.3). Instead, these rocks are suggested to have formed from unusual, PPGE enriched sources. Loihi picrites contain far higher Re and PPGE contents, and lower IPGE contents than other Hawaiian picrites (Ireland *et al.*, 2009), and though complete PGE datasets are lacking for Gorgona samples, their high $^{186}Os/^{188}Os$ ratios indicate a source with a long term enrichment in Pt relative to Os (Brandon *et al.*, 2003).

3.6.5 Mantle residue PPGE hosts after sulphide exhaustion

Mild compatibility of the PPGEs during mantle melting has previously been suggested based on systematically decreasing PPGE/Ti from komatiites, through komatiitic basalts, to basalts in Archaean greenstone belts (Barnes *et al.*, 2015). Barnes *et al.* (2015) explained this by lower degree accumulated melts having a higher proportion of PGE-poor melt derived from S-saturated, deeper parts of the melting column (Rehkämper *et al.*, 1999; Momme *et al.*, 2006). However, if PPGEs are incompatible in the absence of sulphide, then melts from the sulphide exhausted parts of the melting column should also be PPGE poor, leading to a peak in PPGE contents for melts that just reach sulphide exhaustion in the uppermost part of the melting column (Section 3.6.1; Mungall & Brenan, 2014). This model is therefore rejected, and alternative PPGE hosts that could explain their apparent compatibility in high degree melts are considered below.

One possibility is that PPGE bearing sulphides might be physically shielded from interaction with silicate liquids during the formation of high degree melts, for example as inclusions within residual olivine. However, evidence from natural mantle samples suggests that sulphides included within primary mantle minerals tend to be enriched in IPGEs, whereas the PPGEs are concentrated in interstitial sulphides (Alard *et al.*, 2000) which would not be 'shielded' during mantle melting.

Alternatively, given their highly siderophile nature, PPGEs might be retained in the source regions of high degree melts if these if these melts sample regions of the mantle saturated in Fe metal. Theoretical and experimental evidence indicates that the upper

mantle may become saturated in Fe metal at ∼250 km depth (Ballhaus, 1995; Rohrbach *et al.*, 2007), and native Fe has been observed in sub-lithospheric diamond inclusions (Smith *et al.*, 2016). However, these depths of metal saturation are likely too great to explain PPGE depletions observed in the Winnipegosis komatiites, which likely formed at depths < 150 km (Section 3.6.1).

Finally, PPGEs might in fact moderately compatible in some mantle silicate minerals following sulphide exhaustion. As a monovalent element with a slightly smaller cation size than Na, Pd has previously been suggested to be similarly or more compatible than Na in orthopyroxene at high pressure (Aulbach *et al.*, 2015). Furthermore, mineral-melt partition coefficients as high as ∼2 have previously been measured for Pd in olivine, orthopyroxene, and clinopyroxene (Sweeney *et al.*, 1995), though these were measured for a carbonatite melt. It is speculated that both Pd and Pt are mildly compatible in orthopyroxene at high pressure, providing a means to explain the difference in PPGE content between the highest degree Archaean komatiite melts, and lower degree melts such as the Winnipegosis komatiites and Phanerozoic picrites. In this model (Figure 3.9), Archaean komatiites with the highest degrees of melting (F ∼50%), such as the Weltevreden and Abitibi komatiites, segregated from a dunitic residue (Walter, 1998; Herzberg, 2004) in which the PPGEs were not compatible, and contain the highest PPGE contents. By contrast, lower degree melts (F < 50%) segregated from a harzburgitic residue did not fully extract the PPGEs from their source regions due to partial retention in orthopyroxene, and so have lower PPGE contents. This interpretation is consistent with studies of natural mantle samples, which only approach complete PPGE loss at extreme depletions of > 40% melt extraction (Pearson *et al.*, 2004) in samples with olivine Mg# consistent with melting to orthopyroxene exhaustion (Bernstein *et al.*, 2007).

3.7 Implications for the timing of late veneer mixing

This interpretation of PPGE behaviour during high degree mantle melting has profound implications for the use of komatiite PPGEs to trace input and mixing of the late veneer into the mantle. For example, many of the Palaeoarchaean komatiites and komatiitic basalts studied by Maier *et al.* (2009) had relatively low MgO contents, such as the Apex basalt (all samples MgO < 18 wt%), Euro basalt (most samples MgO < 15 wt%), and Coonterunah komatiites (parental melt MgO ∼23 wt%; Sossi *et al.*, 2016).

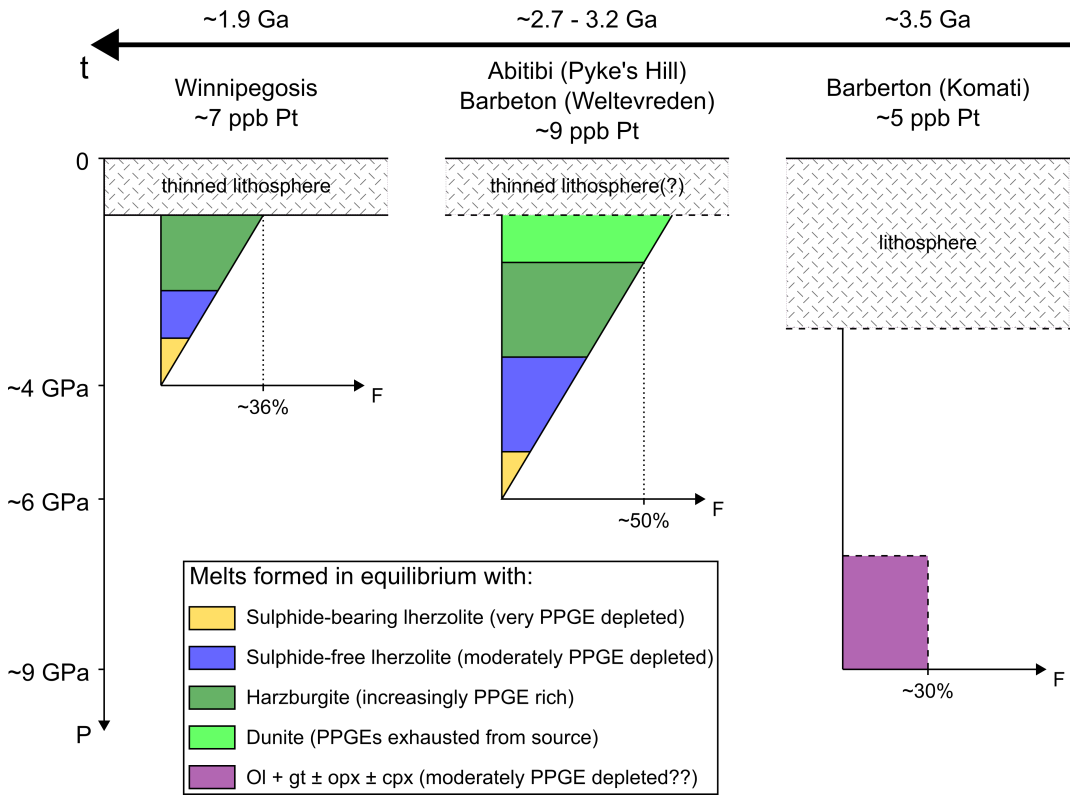

Figure 3.9: Schematic melt columns for komatiites showing different melt PPGE contents along with the mineralogical evolution of their evolving mantle sources during progressive melt extraction. Residual assemblages at a given melt fraction and pressure are from Walter (1998). Aggregate melt fraction, F, calculated using Primelt3 for the Winnipegosis komatiite (Section 3.6.1; Herzberg & Asimow, 2015), estimated for Pyke's Hill and Weltevreden assuming they melted beyond orthopyroxene exhaustion at ~50% melting (Walter, 1998), and taken from previous estimates for the Komati formation (Sossi *et al.*, 2016; Arndt *et al.*, 2008).

In systems where PPGEs are strongly incompatible after sulphide exhaustion, the low PPGE contents of these magmas can only be interpreted as arising from a PGE depleted mantle source. However, if PPGEs are mildly compatible in orthopyroxene, their low PPGE contents, used as primary evidence for a low PGE early mantle (Maier *et al.*, 2009), may simply reflect the lack of orthopyroxene exhaustion in their mantle sources.

Because the extent of mantle melting is clearly a critical factor in determining PPGE concentrations in melts, an attempt is made to reconstruct a 'best estimate' for the PPGE contents of komatiites and picrites through time using an empirical correction for the degree of melting. The percentage difference in Pt contents between calculated and predicted parental melts at a given Mg# (ΔPt) from the regression of Pt against Mg# (Figure 3.7), is plotted as a function of age in Figure 3.10.

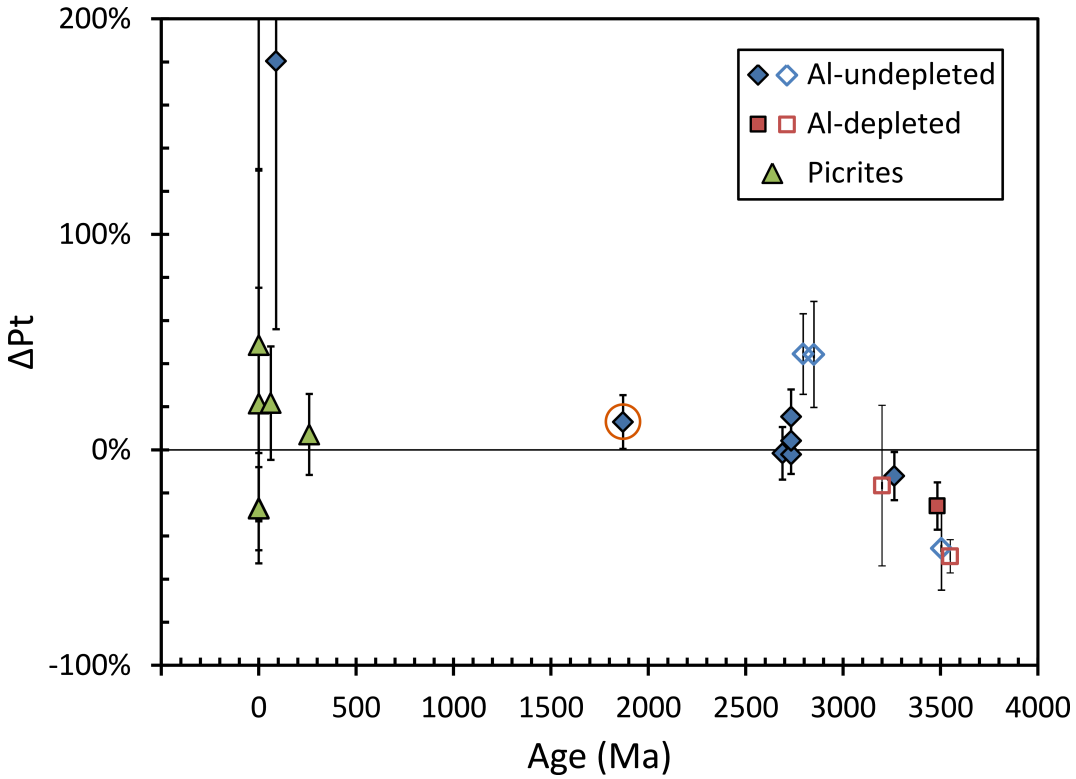

Figure 3.10: Percentage difference between Pt contents calculated for parental melts and those empirically predicted from a regression of parental melt Pt against Mg# (Figure 3.7), plotted as a function of age. Negative ΔPt values indicate melts with lower Pt contents than would be predicted for their Mg#, and positive values have higher Pt contents than predicted. Symbols as in Figure 3.7.

Most komatiites and picrites fall within error of the Pt against Mg# correlation, suggesting differences in their PPGE contents can be entirely explained by different degrees of melting. There are, however, a few notable exceptions. Neoarchaean komatiites for which parental melt MgO contents were estimated by previous authors fall to higher Pt contents than would be predicted from the Pt – Mg# regression. This likely reflects uncertainties in calculated MgO contents; as Pt negatively correlates with MgO during komatiite crystallisation, any underestimation of the parental melt MgO results in both a shift towards lower Mg# and higher Pt contents. A ~3 wt% underestimation of MgO by previous authors (Puchtel *et al.*, 2005, 2007) relative to these calculations is sufficient to explain this deviation. This appears reasonable given that parental melt MgO contents estimated here for Pyke's Hill komatiites (~30 – 31 wt%, Table 3.3) are similarly elevated compared to those estimated by the same authors (~28 wt%; Puchtel *et al.*, 2004).

Parental melt Pt concentrations of 5.2 ppb and 3.6 ppb Pt, respectively, at parental melt Mg#s of ∼0.82 are calculated for ∼3.5 Ga komatiites of the Komati formation and Schapenburg greenstone remnant (Puchtel *et al.*, 2009b, 2014). These Pt contents are ∼30% and ∼50% lower, respectively, than other komatiites with comparable parental melt Mg#s. Their low PPGE contents therefore cannot be explained by lower relative degrees of melting alone. Previous studies have attributed their low PPGE contents to survival of mantle heterogeneities produced during magma ocean crystallisation (Puchtel *et al.*, 2009b), or slow mixing of PGE-rich late veneer materials into komatiite sources (Maier *et al.*, 2009). An alternative explanation based on differences in melting conditions is presented here, which does not require unusual source PGE contents. A number of authors have attributed the low Al_2O_3/TiO_2 of Barberton komatiites at high melt fractions to high pressure melting, leaving residues containing majoritic garnet (Nesbitt *et al.*, 1979; Arndt *et al.*, 2008; Robin-Popieul *et al.*, 2012). It is suggested that the PPGEs may be moderately compatible in these residues comprising olivine + garnet ± orthopyroxene ± clinopyroxene (Walter, 1998), leading to low PPGE contents in the Barberton and Schapenburg komatiites (Figure 3.9). The compilation of komatiite and picrite parental melt compositions appears to show positive trends in PPGE contents against Al_2O_3/TiO_2 (Figure 3.11), which could potentially indicate increased compatibility of the PPGEs with pressure. However, this trend may be in part generated by the tendency of komatiites and particularly picrites with low Al_2O_3/TiO_2 to have lower Mg#s, so this interpretation remains tentative. Regardless of the interpretation of the low PPGE contents of ∼3.5 Ga komatiites, the ∼3.3 – 3.2 Ga Weltevreden and Regal komatiites have Pt contents within error of Neoarchaean komatiites, providing a minimum age on the completion of mixing of late veneer materials into the komatiite source.

3.8 Conclusions

PGE systematics in most Winnipegosis komatiite samples were undisturbed by crustal assimilation and metamorphism, and are controlled by the primary magmatic phases olivine, chromite, residual melt, and Os-Ir alloy. One sample shows evidence of a Ru-rich phase with elevated Os/Ir, interpreted as evidence for laurite – $(Ru,Os,Ir)S_2$ – in this sample. Winnipegosis parental melts contained 1.1 ± 0.3 ppb Os, 0.91 ± 0.26 ppb Ir, 4.0 ± 0.5 ppb Ru, 7.0 ± 0.8 ppb Pt, 7.2 ± 0.7 ppb Pd, and 0.53 ± 0.06 ppb Re.

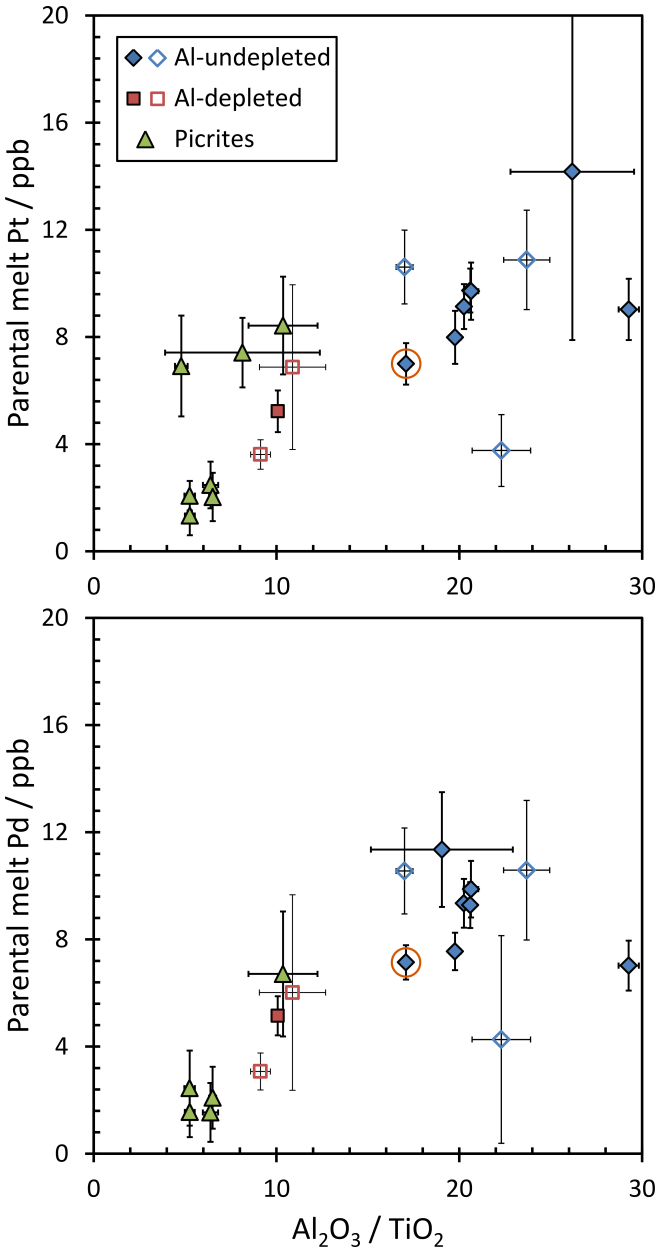

Figure 3.11: Parental melt Pt and Pd contents plotted as a function of average Al_2O_3/TiO_2 from the komatiite picrite compilation (Section 3.6.4). Symbols as in Figure 3.7. The apparent positive trends towards increasing PPGE contents at increasing Al_2O_3/TiO_2 may indicate an increase in PPGE compatibility with average pressure of melting. However, this trend may be in part generated by the generally lower melt fractions calculated for Al-depleted komatiites and picrites, which also have very low Al_2O_3/TiO_2.

Modelling of mantle melting reproduces the Ru and Ir contents of Winnipegosis komatiites well, but Winnipegosis Pt and Pd contents are $> 60\%$ lower than predicted by geochemical modelling using reasonable assumptions of melting conditions, melt fraction and source composition. These low Pt and Pd contents cannot be explained by melting of a source depleted in PGEs. A compilation of major element and PGE data from well preserved komatiites and picrites suggests that Pt and Pd in fact behave more compatibly after sulphide exhaustion during high degree mantle melting than predicted based on the current state of knowledge of PGE partitioning, and it is suggested that residual silicate mineral assemblages may exert an important control on the PGE contents of high degree melts. Applying an empirical correction for the degree of melting allows almost all of the komatiite and picrite PGE variability in the compilation to be explained by melting of a source with the same PGE contents, implying that the PGE contents of the Earth's mantle remain unchanged since $\sim$3.2 Ga. Al-depleted Palaeoarchaean komatiites form an exception, showing low Pt and Pd contents even after correcting for their degree of melting. Though PGE depleted sources cannot be ruled out at this stage, these low PPGE contents may also be explained by exceptionally high pressure melting and retention of Pt and Pd in a majoritic garnet residue.

Chapter 4
Plumbing system of a Proterozoic Greenstone Belt

Chapter Summary

The rock type most commonly associated with komatiite throughout Earth history is tholeiitic basalt. However, despite this well-known association, the link between komatiite and basalt formation remains unclear. Two models have been suggested: that tholeiitic basalts represent the products of extensive fractional crystallisation of komatiite, or that basalts are formed by lower degrees of melting than komatiites in the cooler portions of a zoned plume. This chapter presents major and trace element data for basalts and dunites from the Palaeoproterozoic Winnipegosis Komatiite Belt (WKB), which are combined with previously obtained data for komatiites from the same belt to explore the link between komatiite and basalt formation. The dunites are olivine + chromite adcumulates that were pervasively serpentinised during metamorphism, which caused a decrease in MgO contents and increase in Al_2O_3 contents in some samples. However, FeO was undisturbed during metamorphism, suggesting that their highly magnesian compositions that overlap komatiitic olivine represent derivation from a komatiitic magma. Tholeiitic basalts comprise a greenschist facies mineral assemblage but have generally unremarkable geochemical characteristics for ∼1.9 Ga basalts, with the exception of high FeO contents. REE patterns are similar to Winnipegosis komatiites, although absolute concentrations are higher by a factor of ∼2.5, and the basalts show slightly elevated LREE/MREE compared to the komatiites. The ability of thermodynamic modelling with MELTS software to reproduce komatiite liquid lines of descent (LLD) is evaluated by comparison to the crystallisation sequence and mineral compositions observed for Winnipegosis komatiites. With minor caveats, MELTS is able to successfully reproduce the LLD. This modelling is extended to higher pressures to simulate crystallisation of komatiitic melt in

an upper crustal magma chamber. All major and rare-earth element characteristics of the tholeiitic basalts can be reproduced by ∼60% crystallisation of a Winnipegosis komatiite-like parental melt at pressures of ∼1.5 – 2 kb at oxygen fugacities between QFM – 1 and QFM, respectively. Although it is difficult to explicitly rule out formation of the basalts from a lower degree parental melt, all geochemical and geological evidence is consistent with their derivation from a komatiitic melt, and the presence of a large komatiite-derived dunite body in the WKB provides evidence of extensive fractionation of komatiite in the upper crust. Uniform basalt compositions are likely the result of a density minimum in the evolving komatiitic melt between clinopyroxene and plagioclase saturation, and efficient extraction of melt from a mixture containing ∼60% crystals. Other komatiite localities, such as Gorgona Island, contain basalts and komatiites with similar geochemical characteristics, and show abundant evidence of upper crustal fractionation of komatiitic magmas. Hence, this model of tholeiitic basalt formation from extensive komatiite fractionation may be more broadly applicable.

4.1 Introduction

The most common igneous rock type associated with komatiites are tholeiitic basalts, which dominate most komatiite-bearing volcanic sequences (Storey *et al.*, 1991; Bickle *et al.*, 1994; Arndt *et al.*, 2008; Campbell & Davies, 2017). Following the discovery of komatiites (Viljoen & Viljoen, 1969b,a), the relationship between komatiites and associated tholeiitic basalts was an important question in komatiite research, with two main models suggested. Tholeiitic basalts might represent the product of extensive fractional crystallisation of komatiitic parental melts (Arndt *et al.*, 1977; Arndt & Nisbet, 1982). Alternatively, komatiites and tholeiites might be derived from different parental melts with tholeiites formed through much lower degrees of mantle melting (Nesbitt & Sun, 1976; Sun & Nesbitt, 1978; Stamatelopoulou-Seymour *et al.*, 1983). Distinguishing between these models was hampered by the common presence of a compositional gap between komatiitic and tholeiitic compositions.

Despite this early debate, recent authors have tended to favour komatiites deriving from the hottest central portion of an ascending mantle plume, and tholeiites deriving from the cooler margins (Campbell *et al.*, 1989; Rollinson, 1999; Kerr, 2005; Manikyamba *et al.*, 2008). However, the former model has never been explicitly dis-

proven, and certain localities show evidence of a continuous spectrum of fractionated melts between komatiite and tholeiitic basalt (Arndt *et al.*, 1977).

The Winnipegosis Komatiite Belt (WKB) is an ideal location to test the relationship between basalts and komatiites. Both komatiitic and basaltic volcanism are abundant, and the Winnipegosis komatiites are very well preserved, providing a high fidelity geochemical record. Additionally, the presence of large bodies of ultramafic cumulates suggests the possibility of extensive komatiite fractionation in the upper crust. This chapter presents new major element data for basalts and dunites from the WKB. These are combined with previously obtained data for Winnipegosis komatiites and data from the GSC database to test the hypothesis that the basalts formed through extensive crystallisation of a komatiitic parental magma. Thermodynamic modelling of komatiite crystallisation is undertaken using Rhyolite-MELTS software (Gualda *et al.*, 2012; Ghiorso & Gualda, 2015), and the results of the models are compared to well constrained observations of komatiite crystallisation (Chapter 2). The modelling indicates that fractional crystallisation of komatiitic parental melts is a viable mechanism for producing tholeiitic basalts, and geological constraints indicate it was most likely in operation during formation of the WKB.

4.2 Background and Samples

4.2.1 Igneous rocks in the WKB

A description of the general geological background and regional tectonics at the time of Winnipegosis Komatiite Belt (WKB) formation, along with detailed petrographical descriptions of komatiites, basalts, and dunites from the belt, can be found in Chapter 1. Relative proportions of the different igneous rock types found in the WKB are difficult to establish due to the lack of surface exposure, and because borehole locations were chosen based on their geophysically identified Ni-Cu potential (McGregor, 2011), thus providing a biased record of the WKB stratigraphy. However, basaltic rocks are a significant component of the belt, with eruptive basalt sequences and/or gabbros intersected in 11 of the 27 boreholes drilled. By comparison, komatiites were intersected in ten of the 27 boreholes drilled. Basalts are frequently interlayered with siltstones, argillites, and dolomitic rocks, and are generally not intersected in komatiite-dominated boreholes, though thin layers of gabbro are described in some komatiite-dominated cores (McGregor, 2011). Estimates of the total stratigraphic thickness of basalt preserved

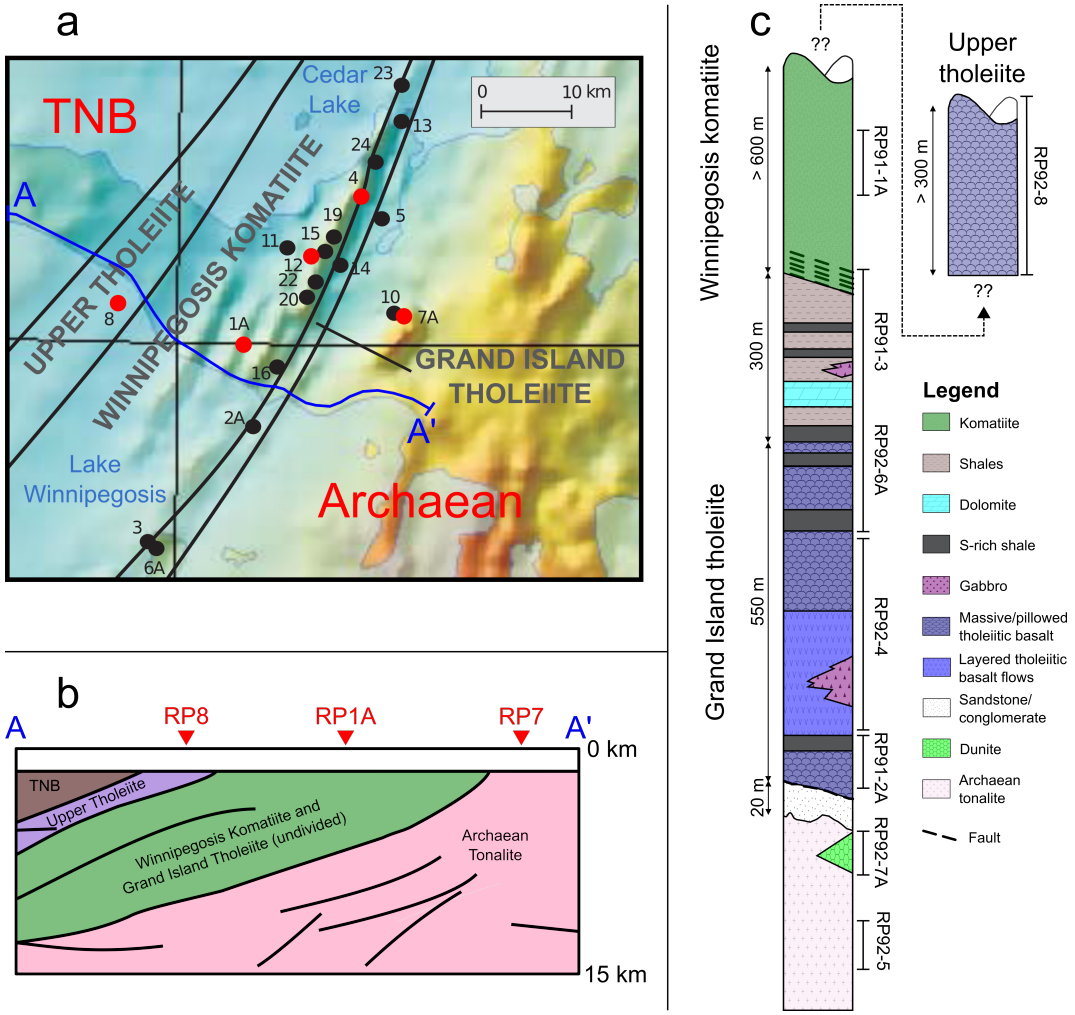

Figure 4.1: a) Aeromagnetic map of the central portion of the Winnipegosis Komatiite Belt, modified from McGregor (2011). Red and yellows indicate magnetic highs, including linear magnetic highs of WKB volcanics and rounded magnetic high of RP7 dunite body, blue indicates magnetic lows. Black lines divide tectono-stratigraphic units. 'TNB' = Thompson Nickel Belt. b) Seismic-reflection interpretation of Lithoprobe line 3b modified from Lucas *et al.* (1996) along blue line between A and A' in Figure 4.1a. Approximate positions of boreholes RP1A, RP7, and RP8 are projected along strike onto line. c) Reconstructed stratigraphy of the Winnipegosis Komatiite Belt, modified from Figure 1.3, with Upper tholeiite thickness based on section intersected by borehole RP8 (McGregor, 2011). Dashed connection between Winnipegosis komatiite and Upper tholeiites reflects their uncertain stratigraphic relationship.

in the WKB range between 550 m (Figure 4.1c; Hulbert *et al.*, 1994) and < 1 km (McGregor, 2011). This is comparable to estimates of the total komatiite thickness in the WKB, which range between > 600 m (Figure 4.1; Hulbert *et al.*, 1994) and < 1 km (McGregor, 2011).

By contrast, dunitic rocks were identified more rarely during WKB drilling, with only a single large intrusive dunite body intersected by boreholes RP7 and RP10. This body was identified from a ∼5 ×2.5 km ellipse-shaped magnetic high, found ∼5 km East of the supracrustal rocks of the WKB, and has a thickness of > 600 m in borehole RP10. A number of smaller peridotite-dunite bodies were also identified within the Winnipegosis stratigraphic sequence, including a ∼300 m thick intrusive peridotite-gabbro section in borehole RP18 (McGregor, 2011). However, it is not clear from core logging descriptions whether many of the smaller peridotite-dunite bodies represent intrusive rocks or komatiitic cumulates, especially given their frequent association with spinifex-textured komatiites.

4.2.2 Sample Selection

Despite the widespread occurrence of basaltic rocks in the WKB, the only samples available for this study were from borehole RP8. The RP8 metabasalts (referred to as the RP8 basalts for simplicity) are the only example of rocks from the 'Upper Tholeiite' suite of the WKB, and their relationship to the rest of the WKB is uncertain, either representing a stratigraphically distinct unit or a thrust repetition of the structurally lower 'Grand Island Tholeiite' suite (Section 1.2.1; Burnham *et al.*, 2009; McGregor, 2011). However, previous studies have noted the geochemical similarity of these rocks to the Grand Island Tholeiite (unpublished Cominco report, 1992; Burnham *et al.*, 2009; McGregor, 2011), and so the RP8 rocks are taken as an example of the style of basaltic magmatism in the WKB. In addition to existing major element data in the GSC database, six samples were selected for major element reanalysis, one of which was measured in triplicate. Although the depths of sampling location in RP8 are unknown, samples were chosen over a wide relative depth range in borehole RP8 (assuming sample number increases with depth, as for other boreholes; Section 1.3). The RP8 basalts do not preserve any primary minerals or textures, and are pervasively altered to a homogeneous greenschist mineral assemblage of actinolite, hornblende, epidote, quartz, sphene, with minor chlorite and opaque oxides (Section 1.4.5).

Seven dunitic samples from borehole RP7 were selected for major element reanalysis in this study. These were chosen to cover the entire depth range sampled in the borehole, and are supplemented with data from the GSC database. Dunites from borehole RP7 are altered to a sub-greenschist (Jolly, 1982) metamorphic assemblage of serpentine, brucite, and magnetite, with no primary olivine preserved. Igneous chromite is retained,

but overgrown by metamorphic magnetite. Remnants of a cumulate mesh texture are faintly outlined by thin bands of magnetite (Section 1.4.4).

Komatiite bulk rock major element data measured by XRF, and in-situ major element data measured by EPMA, is taken from Chapter 2. Additional clinopyroxene major element data from the komatiites, measured by EPMA, is described below. Data was obtained from one random olivine spinifex sample and one acicular pyroxene sample from differentiated flow 'A' (RP12-306.1 and RP12-307.3, respectively; Section 1.4.2), two 'type 1' massive flow sample (RP1A-18, RP1A-111), a sample with textures transitional between 'type 1' and 'type 2' samples (RP1A-8), and a 'type 2' massive flow sample (RP1A-99; Section 1.4.1).

4.3 Methods

4.3.1 Bulk rock major and minor elements

Whole rock major and minor element geochemistry was measured by X-Ray Fluorescence (XRF), using the same techniques as for the komatiite whole rock analyses described in Section 2.3.1 (Mertzman, 2000). Eight replicates of the harzburgite certified reference material, MUH-1, were analysed in two different analytical sessions to assess the accuracy and repeatability of the analyses for compositions similar to the RP7 dunites (Table 4.1). SiO_2, MgO, Al_2O_3, Cr, and the loss on ignition (LOI) were repeatable to a precision of $< 2\%$ (1σ relative); FeO_t, MnO, and CaO had repeatabilities of $< 5\%$; Na_2O and V had repeatabilities of $< 15\%$; while TiO_2, K_2O, and P_2O_5, present in very low quantities in MUH-1, had poor repeatabilities ranging between $\sim$20 and 44%. All elements except for TiO_2 and P_2O_5 overlap with the certified 95% confidence limits (IAG, 2015) within two standard deviations, and are considered accurate at the level of precision of the measurements. Due to the inaccuracy and low precision of TiO_2 and P_2O_5, the extremely low precision of K_2O data, and given the geochemical similarity of MUH-1 and the RP7 dunites, TiO_2, K_2O, and P_2O_5 data from the RP7 dunites measured using this method are likely to be imprecise and/or inaccurate, and will not be used quantitatively in this study. As for the OKUM standard (Section 2.3.1), Ni data for MUH-1 was not repeatable using this method.

Despite overlapping certified reference values, FeO_t and MnO show low precision relative to other major elements and their precision measured in the OKUM standard (Section 2.3.1). This apparently low precision arises from a systematic offset in FeO_t

Table 4.1: Bulk rock major and minor element data measured by XRF for the MUH-1 certified reference material. 'Average MUH-1' data ± 2 standard deviations (2σ abs., n = 8) from this study are compared to the OKUM certified values ('OKUM cert') and 95% confidence limits (IAG, 2015). Data for oxides, V, and Cr was renormalised to 100% totals on an anhydrous basis, with FeO_t calculated assuming all Fe is present as FeO. LOI was not renormalised. Raw totals are given as an indication of data quality. Repeatability under measurement conditions for each element is shown as 1 relative standard deviation of the data. 'LOI' = loss on ignition.

	Average MUH-1	2σ abs.	MUH cert.	95% conf.	Repeatability (1σ rel.)
SiO_2 *(wt%)*	44.66	1.08	45.28	0.19	1.2%
TiO_2	0.023	0.009	0.0386	0.0029	20.5%
Al_2O_3	1.506	0.031	1.4958	0.0213	1.0%
FeO_t	9.06	0.83	8.67	0.05	4.6%
MnO	0.139	0.011	0.1322	0.0016	4.1%
MgO	43.06	0.44	42.89	0.18	0.5%
CaO	1.439	0.092	1.360	0.011	3.2%
Na_2O	0.095	0.015	0.117	0.011	7.6%
K_2O	0.014	0.013	0.013	0.003	44.3%
P_2O_5	0.0037	0.0019	0.0084	0.0025	25.3%
Total	99.07	0.28	99.42		0.1%
LOI	9.15	0.33	9.38	0.10	1.8%
V (ppm)	39	10	46	4	13.2%
Cr	2940	86	3039	123	1.5%

and MnO data measured from different analytical sessions, with data from the second analytical session showing a significant offset from the certified values for MUH, and greater scatter (Figure 4.2). The reason for this is unclear, as the same calibration was used for both sets of analyses (Stan Mertzman, personal communication, 2017). However, the data from each session are relatively tightly grouped, and so a correction can be applied to the data from the second analytical session to account for the mismatch between the measured and certified analytical values. All data from the RP7 dunites were analysed in the second analytical session; FeO_t and MnO data for these samples are corrected by multiplying by correction factors of 0.9093 and 0.9096 respectively, where the correction factors are calculated as the ratio of the certified concentration in MUH-1 to the measured concentration in three replicates of MUH-1 measured in the second analytical session. Repeatabilities of 2.5% and 2.8% (1σ relative) for FeO_t and MnO respectively are assigned based on three MUH-1 replicates from the second analytical session, though it should be noted that this does not include systematic errors potentially introduced by applying this correction.

No basalt certified reference material was measured with the RP8 basalt samples, though these were measured in the same analytical session as the RP1A and RP12 ko-

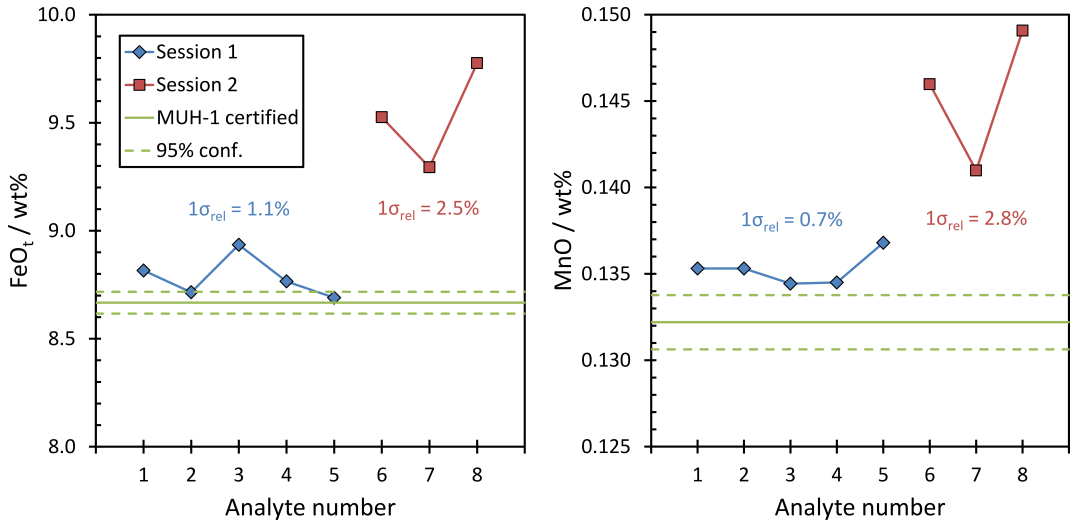

Figure 4.2: FeO_t and MnO data measured for the MUH-1 certified reference material during two analytical sessions, compared to the certified average MUH-1 value and 95% confidence limits about this average (95% conf.). Data for both FeO_t and MnO from the second analytical session is systematically high relative to both the certified value, and data from the first analytical session.

matiites, during which ten aliquots of the OKUM standard were analysed and showed good precision and accuracy (Section 2.3.1). Precision of the basalt analyses was assessed by measuring the sample RP8-7 in triplicate. Average values and 2σ uncertainties for the three analyses are given in Table 4.3. Data for most elements showed repeatabilities of $< 2\%$ (1σ relative); with the exception of MgO, P_2O_5, and the LOI, which had repeatabilities $< 5\%$; and Cr, which had a repeatability of $\sim 7\%$.

4.3.2 Rare-Earth Element (REE) data

In addition to new bulk rock data, RP8 basalt REE data measured by solution ICP-MS from the GSC database are presented in Section 4.4.2. Quality of the GSC data was assessed in Section 1.5 by comparison to new data collected for this thesis from the same samples. Although no new basalt REE data has been collected, the GSC REE data for RP1A and RP12 komatiites generally showed a good agreement to new ICP-MS data presented in Section 2.4.1. Though the GSC data is of low precision in comparison to the new data, it is likely to be sufficiently precise and accurate to determine approximate absolute REE concentrations and the shape of REE patterns.

4.3.3 Clinopyroxene EPMA Analyses

Clinopyroxene analyses for massive komatiite samples from borehole RP1A and differentiated komatiite samples from borehole RP12 were carried out by Electron Probe Micro-Analysis (EPMA) on a a JEOL 8900R electron microprobe at the University of Alberta using the 'routine' methods described in Section 2.3.2. Spots were analysed for 30 seconds on peak for most elements, at a beam current of 20 nA and an accelerating voltage of 20 kV. Primary standards used are listed in Table B.1. Due to the micron-scale size of some of the clinopyroxene dendrites (particularly the smallest 'type 2' sample dendrites), there was a risk of the EPMA interaction volume partially sampling devitrified glass interstitial to the pyroxene dendrites. The data was therefore screened to exclude samples which contained more than 2 Si cations per formula unit (2 Si cations per 6 oxygen anions), as these are not consistent with stoichiometric pyroxene compositions and may represent additional Si sampled from the interstitial glass. The data was additionally screened to exclude points with totals > 101 wt% or < 99 wt%.

4.4 Results

4.4.1 RP7 dunite

Dunites from borehole RP7 are highly magnesian, with anhydrous MgO contents between 46 – 49 wt% (Figure 4.3, Table 4.2). They contain low concentrations of elements incompatible in olivine such as Al_2O_3 and CaO. LOI are consistently > 13 wt%, which reflect high H_2O contents in the metamorphic mineral assemblage. Their bulk rock compositions fall close to an array of modelled olivine compositions on a plot of FeO_t against MgO, and within the range of Mg# sampled from the RP1A komatiites (Section 2.4.2). However, the majority of samples fall slightly off this array, towards lower MgO concentrations. The dunites also form loose negative correlations towards high Al_2O_3 concentrations at lower MgO contents, and higher Al_2O_3 with decreasing loss on ignition (LOI). The relationship between MgO and Cr_2O_3 is scattered, with Cr_2O_3 contents up to $\sim$1 wt%.

Table 4.2: Bulk rock major and minor element data for dunites from borehole RP7. Data normalisation as in Table 4.1.

Rock type	RP7-1 Dunite	RP7-3 Dunite	RP7-4 Dunite	RP7-7 Dunite	RP7-9 Dunite	RP7-11 Dunite	RP7-16 Dunite
SiO_2 (wt%)	40.94	41.16	39.91	40.75	41.24	40.57	41.91
TiO_2	0.03	0.03	0.03	0.02	0.02	0.02	0.06
Al_2O_3	1.13	0.95	0.83	1.18	0.86	0.91	1.62
FeO_t	9.62	9.24	10.74	9.15	8.45	9.16	9.52
MnO	0.06	0.10	0.12	0.21	0.18	0.17	0.16
MgO	47.66	47.79	48.09	48.46	48.94	48.90	46.43
CaO	0.33	0.58	0.10	0.08	0.19	0.12	0.14
Na_2O	0.15	0.14	0.16	0.11	0.10	0.11	0.10
K_2O	0.07	0.01	0.01	0.03	0.02	0.02	0.03
P_2O_5	0.01	0.01	0.01	0.01	0.01	0.01	0.01
Total	98.87	98.70	98.84	98.91	98.61	98.79	98.74
LOI	14.86	15.43	15.33	15.32	15.82	15.46	13.65
V (ppm)	19	27	24	13	33	25	39
Cr	5323	6728	6936	5480	6616	5789	5613

4.4.2 RP8 basalts

As noted in Section 1.6.2, basalts from borehole RP8 show a limited compositional range (Table 4.3). Compositionally, they share a number of similarities to typical MORBs (Gale *et al.*, 2013), with ∼50 wt% SiO_2, ∼7.5 wt% MgO, ∼14 wt% Al_2O_3, and ∼10 wt% CaO. However, FeO_t contents of ∼13 wt% are distinctly elevated relative to MORB (average $FeO_t \approx 10$ wt%), but well within the range of Phanerozoic Continental Flood Basalts (CFBs; e.g., Lightfoot *et al.*, 1990; Wooden *et al.*, 1993; Lange, 2002). TiO_2 contents of ∼1.25 wt% are low compared to MORB compositions, but also lie within the range of Phanerozoic CFBs (Lightfoot *et al.*, 1990; Wooden *et al.*, 1993). Na_2O data show considerable scatter but average contents of ∼2.5 wt% are close to the average for ∼1.9 Ga basalts (Keller & Schoene, 2012).

Rare-earth element patterns for two RP8 samples (Table 4.3, Figure 4.4) show similar 'hump shaped' patterns to Winnipegosis Komatiite samples (Section 2.4.1), with modest depletions in both the heavy and light REEs (HREEs and LREEs) relative to the middle REEs (MREEs). REE concentrations fall around approximately $6 * PUM$, but are consistently ∼2.5 times higher than estimated REE contents for the Winnipegosis Komatiite parental melt (Section 4.6.1).

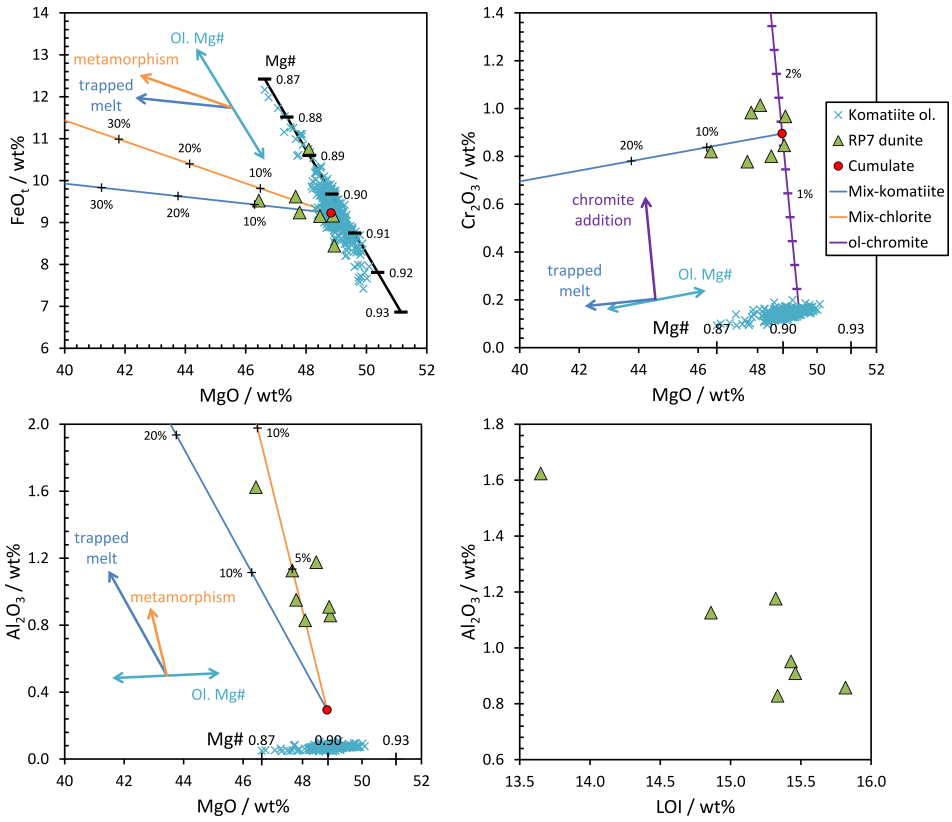

Figure 4.3: Variations of major elements in the RP7 dunites. Dunite data are compared to model olivine compositions with Mg# between 0.87 and 0.93 (black line and thick bars, calculated stoichiometrically assuming 1 wt% minor element content), and compositions of olivines measured from the RP1A komatiites. Coloured lines show mixing trends between average Winnipegosis komatiite chromite and olivine ('ol-chromite'), and between the assumed accumulating assemblage composition ('Cumulate') and both Winnipegosis komatiite parental melt ('Mix-komatiite') and an Mg-rich chlorite ('Mix-chlorite'), intended to represent the effect of trapped interstitial melt and metamorphism, respectively (Section 4.5). Black crosses with percentages indicate the amount of trapped melt or chlorite in mixture. Coloured arrows are vectors representing the geochemical effects of various processes.

4.4.3 Clinopyroxene chemistry

Winnipegosis komatiite clinopyroxenes show compositional variations based on their size and habit. Large phenocrysts from the acicular pyroxene sample, RP12-307.3, are augitic in composition, Mg-rich and Ca-poor compared to dendritic clinopyroxenes (Table 4.4, Figure 4.5). The olivine spinifex sample RP12-306.1 contains the coarsest dendrites. These range in composition from augites to diopsides, along a trend of increasing Ca and decreasing Mg at approximately constant Fe. Dendritic pyroxenes from the massive flows are diopsides or augites with very high Ca. There is a slight

Table 4.3: Bulk rock major, minor and rare-earth element data for basalts from borehole RP8. Major and minor elements (above line) were measured by XRF, REE data (below line) are from the GSC database. Data normalisation as in Table 4.1. Average values and 2σ (absolute) uncertainties are given for major and minor element data from sample RP8, which was measured in triplicate.

Rock type	RP8-1 Basalt	RP8-3 Basalt	RP8-5 Basalt	RP8-9 Basalt	RP8-10 Basalt	RP8-7 av. Basalt	RP8-7 2σ
SiO_2 *(wt%)*	51.03	51.29	50.33	50.43	49.53	50.50	1.59
TiO_2	1.24	1.22	1.22	1.21	1.26	1.27	0.03
Al_2O_3	13.89	13.87	14.13	14.06	14.35	13.93	0.47
FeO_t	13.14	12.92	13.06	13.22	13.73	13.36	0.28
MnO	0.18	0.19	0.19	0.19	0.22	0.20	0.01
MgO	7.52	7.58	7.62	7.75	7.87	7.41	0.39
CaO	10.48	10.81	10.55	10.17	10.26	10.36	0.38
Na_2O	2.29	1.93	2.58	2.56	2.41	2.68	0.09
K_2O	0.14	0.10	0.22	0.32	0.28	0.18	0.01
P_2O_2	0.09	0.09	0.09	0.09	0.09	0.09	0.01
Total	99.71	99.88	100.07	99.94	99.38	99.88	0.23
LOI	2.17	2.07	2.02	2.13	2.08	2.03	0.19
V (ppm)	362	342	357	362	427	369	17
Cr	179	158	171	183	215	163	23
La				13.9	14.3		
Ce				15.7	15.8		
Pr				16.2	16.2		
Nd				17.7	17.7		
Sm				17.6	18.2		
Eu				17.8	19.5		
Gd				18.1	18.6		
Tb				17.5	17.5		
Dy				16.7	17.1		
Ho				16.1	16.5		
Er				15.6	16.3		
Yb				15.5	16.1		
Lu				15.0	15.9		

trend towards decreasing Mg/Fe with decreasing clinopyroxene dendrite size, from the coarsest grained type 1 sample (RP1A-111), through the transitional type 1/2 sample (RP1A-8) towards the finest grained type 2 samples (RP1A-18, RP1A-99). Al contents and the percentage of the tetrahedral site occupied by Al (% Al_z) generally increase with decreasing grain size. This likely results from metastable pyroxene growth at high cooling rates (Faure & Tissandier, 2014), with the highest Al contents in fine grained type 2 dendrites resulting from the highest degree of undercooling, and lower Al contents in the RP12-307.3 phenocrysts resulting from growth closer to equilibrium conditions.

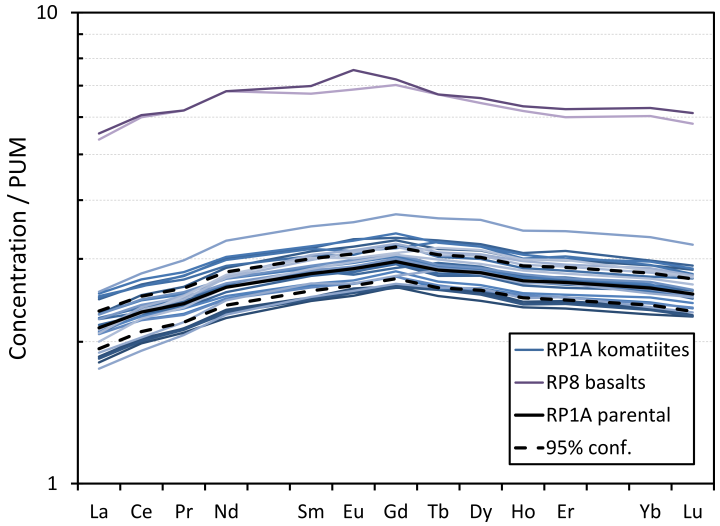

Figure 4.4: REE patterns for the RP8 basalts, normalised to PUM (Hofmann, 1988), are compared to individual REE patterns for massive komatiites from borehole RP1A and the calculated komatiite parental melt composition with 95% confidence limits (Section 4.6.1).

Table 4.4: Representative Winnipegosis komatiite clinopyroxene (cpx) compositions, analysed by EPMA. 'Type' = petrographical types described in Section 1.4. 'Aci. px' = acicular pyroxene sample, 'Ol spin.' = random olivine spinifex. Wo, En, and Fs are the relative proportions of wollastonite ($Ca_2Si_2O_6$), enstatite ($Mg_2Si_2O_6$), and ferrosilite ($Fe_2Si_2O_6$), respectively. % Al_z is the stoichiometrically calculated percentage of the tetrahedral site occupied by Al.

Sample	RP12-307.3	RP12-306	RP1A-111	RP1A-8	RP1A-18	RP1A-99
grain	cpx7	cpx10	cpx9	cpx8	cpx15	cpx3
Type	Aci. px	Ol spin.	Type 1	Type 1/2	Type 2	Type 2
SiO_2 *(wt%)*	52.75	48.23	48.85	47.57	45.55	46.00
TiO_2	0.29	0.65	0.69	0.78	1.15	0.91
Al_2O_3	3.17	7.51	6.69	9.11	9.91	9.65
Cr_2O_3	0.47	0.25	0.29	0.20	0.12	0.12
MnO	0.21	0.21	0.17	0.19	0.18	0.29
FeO	7.40	10.74	7.73	9.17	10.36	13.32
NiO	0.04	0.02	0.02	0.01	0.02	0.00
MgO	20.75	14.82	13.77	13.01	10.03	10.14
CaO	15.43	17.23	21.43	19.86	21.67	18.89
Na_2O	0.13	0.20	0.24	0.25	0.27	0.35
K_2O	0.00	0.00	0.00	0.00	0.00	0.03
P_2O_5	0.01	0.05	0.02	0.04	0.03	0.06
Total	100.66	99.93	99.89	100.20	99.29	99.76
Mg#	0.833	0.711	0.761	0.717	0.633	0.576
Wo $(Ca_2Si_2O_6)$	0.308	0.373	0.460	0.440	0.496	0.435
En $(Mg_2Si_2O_6)$	0.576	0.446	0.411	0.401	0.319	0.325
Fs $(Fe_2Si_2O_6)$	0.115	0.181	0.129	0.159	0.185	0.240
% Al_z	5.1%	10.7%	9.6%	12.0%	13.9%	12.9%

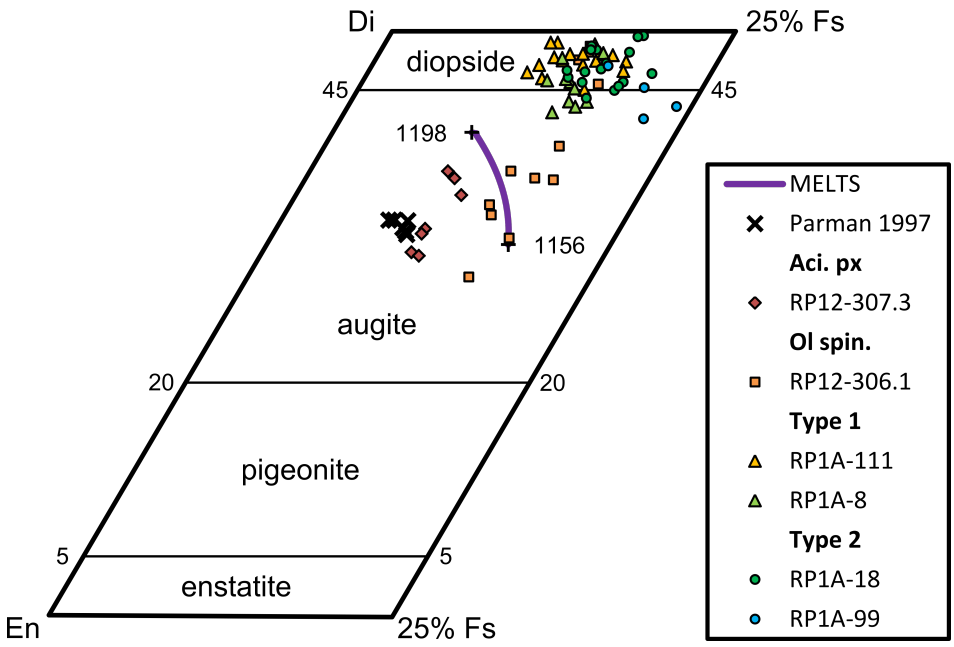

Figure 4.5: Compositions of clinopyroxenes from massive Winnipegosis Komatiite samples from borehole RP1A, and differentiated komatiite samples from borehole RP12. Data are plotted on a section of the pyroxene quadrilateral (Morimoto *et al.*, 1988), with vertices at diopside (Di; $CaMgSi_2O_6$), enstatite (En; $Mg_2Si_2O_6$), and at 25% ferrosilite (Fs; $Fe_2Si_2O_6$ along the enstatite-ferrosilite and diopside-hedenbergite boundaries. Data are subdivided by sample (symbol colour) and petrographical type (symbol shape), and compared to compositions predicted by MELTS ('MELTS'; modelled with an f_{O_2} of QFM and pressure of 1 bar) and experimental pyroxenes of Parman *et al.* (1997), crystallised from a similar bulk rock composition under anhydrous conditions. Crosses with labels indicate temperatures of pyroxene saturation (1198 °C) and lowest temperature pyroxene before MELTS predicts saturation of low Ca pyroxene (1156 °C).

4.5 Discussion – relationship between dunites and komatiites

The highly magnesian nature of the RP7 dunites, and their compositional similarity to olivine compositions measured in Winnipegosis Komatiite samples, suggests that the dunites may represent cumulates of komatiitic olivine and chromite. However, care must be taken with this interpretation as the RP7 dunites have been metamorphosed and do not represent pristine cumulates. Below, compositional variations in RP7 dunite samples are investigated with a view to understanding how they relate to the komatiites, and how their compositions might have been modified during metamorphism.

4.5.1 Accumulating mineral assemblage

Variations in the composition of accumulating olivine are predicted to form a negative trend in a plot of FeO against MgO (Figure 4.3). This can explain some of the compositional variability in the RP7 samples. For example, sample RP7-4 (48.1 wt% MgO, 10.7 wt% FeO_t) and sample RP7-11 (48.9 wt% MgO, 9.2 wt% FeO_t) both fall within the field of measured komatiitic olivine compositions, with the higher FeO_t of RP7-4 attributable to the accumulation of olivine with a lower average Mg#. The FeO contents of the dunites preclude average accumulating olivine compositions with Mg# much greater than ∼0.91, or much lower than ∼0.89, unless FeO was mobile during metamorphism.

However, RP7 samples also show trends towards decreasing MgO and increasing Al_2O_3 at near constant FeO, which cannot be explained by variations in olivine composition. These trends also cannot be explained by differences in chromite chemistry, or in the relative proportions of chromite and olivine in the dunites due to the small modal proportion of chromite in the dunites (see below). Two possible explanations for this trend are explored below. Firstly, the presence of trapped interstitial melt between accumulating olivine grains could lower the MgO and increase the incompatible element contents of the bulk cumulate. Secondly, this trend could represent a metamorphic effect, due to leaching of MgO by a metamorphic fluid and/or effective dilution of MgO in a rock by a net addition of metamorphic minerals with lower MgO contents than the original bulk rock.

To model these two possibilities, the composition of the primary cumulate assemblage must first be chosen. Due to the similarities in dunite bulk rock compositions to Winnipegosis Komatiite olivine, and lack of unaltered primary minerals in the dunites, the composition of primary olivine and chromite in the dunite is assumed to be the same as those found in the komatiites. The relative proportions of olivine and chromite in the accumulating mixture can then be calculated by comparison to a mixing line between these compositions on a plot of Cr_2O_3 against MgO (Figure 4.3). RP7 samples show a scattered relationship in Cr_2O_3 against MgO, which can be explained by variations in the proportion of chromite in the accumulating mixture between ∼1.2 and ∼1.8 wt% chromite. For the purposes of modelling, the igneous cumulate assemblage is assumed to comprise 98.5 wt% average Winnipegosis komatiite olivine (Mg# = 0.907) and 1.5 wt% average Winnipegosis komatiite chromite, plotted as 'Cumulate' in Figure 4.3.

4.5.2 Effects of trapped interstitial melt and metamorphism

The compositional effect of trapped interstitial melt on dunite compositions is modelled (Figure 4.3) as mixing between the assumed cumulate assemblage, and the Winnipegosis komatiite parental melt composition (Section 2.5.3). The MgO, FeO, and Cr_2O_3 contents of the RP7 samples can be reproduced by inclusion of ∼10 wt% trapped komatiitic melt in a cumulate pile with slight variations in olivine Mg# and proportion of chromite in the mixtures. However, in Al_2O_3-MgO space the dunite samples fall on a trend steeper than that predicted for addition of komatiitic melt, and would require inclusion of ∼17 wt% trapped melt to reproduce the Al_2O_3 contents of sample RP7-16 (1.6 wt% Al_2O_3). Accumulation of much higher Mg# olivine could be invoked to fit the trapped melt mixing model to the Al_2O_3-MgO trend in dunite data, but this is not compatible with the observed FeO-MgO data. The presence of trapped komatiitic melt alone cannot therefore simultaneously explain the trends in dunite FeO and Al_2O_3 against MgO. Assumption of a basaltic composition for interstitial melt, such as that of the RP8 basalts, produces trends along almost identical vectors (not shown in Figure 4.3 for clarity), and so also fails to explain the steep trend in dunite Al_2O_3-MgO data.

Possible metamorphic effects are modelled by mixing between the same accumulating assemblage composition, and high-Mg chlorite – $(Mg_{3.75}Fe_{1.25})Si_3Al_2O_{10}(OH)_8$. This produces mixing lines along vectors that can match both the FeO-MgO and Al_2O_3-MgO trends in the dunite data (Figure 4.3). Furthermore, the amount of chlorite required to match both the MgO and Al_2O_3 contents of the lowest MgO, highest Al_2O_3 sample (RP7-16) is similar, at 10 wt% and 8 wt% chlorite addition respectively.

Increases in the modal chlorite proportion may also explain the trend towards higher Al_2O_3 and lower H_2O contents near the base of borehole RP7 (Section 1.6.2), and the negative correlation between Al_2O_3 and LOI (Figure 4.3). The observed metamorphic assemblage comprises serpentine, brucite, and magnetite (Sections 1.4.4, 4.2.2). Chlorite and serpentine both contain ∼13 wt% H_2O (Deer *et al.*, 1992), and chlorite has high Al_2O_3 contents, whereas brucite contains ∼30 wt% H_2O and does not contain stoichiometric Al_2O_3. It is therefore speculated that chlorite contents increase at the expense of brucite with an increase in metamorphic grade towards the base of borehole RP7, causing an increase in Al_2O_3 and decrease in bulk rock H_2O. The source of the Al_2O_3 required to form chlorite is not clear from these data. Though dunite compositions no longer reflect primary igneous trends, the presence of small amounts of interstitial melt prior to metamorphism cannot be ruled out definitively. All of the RP7 dunites

have Al_2O_3 contents > 0.8 wt%, which if sourced from trapped interstitial melt would correspond ∼6 wt% melt in the primary cumulate. Alternatively, the Al_2O_3 may have been introduced by metamorphic fluids from external sources. In either case, the RP7 dunites likely represent metamorphosed olivine and chromite adcumulates.

4.5.3 RP7 dunites are metamorphosed komatiitic cumulates

The trends in RP7 dunite data described above and in Section 1.6.2 can be attributed to two processes. Coupled increases in FeO with decreasing MgO reflect variations in the composition of olivine accumulating, whereas coupled Al_2O_3 increases with decreases in MgO and LOI likely reflect increasing metamorphic grade. Despite the evidence of metamorphic control on dunite compositions, no evidence of FeO-loss or gain during metamorphism was found. As such, RP7 bulk rock compositions that lie close to olivine compositions in FeO-MgO space are likely broadly representative of the average composition of accumulating olivine that formed them. These compositions can therefore be used to calculate the approximate composition of the liquids that they formed from.

Assuming a similar bulk rock FeO – MgO relationship and $Fe^{2+}/\Sigma Fe$ as for the komatiites (Section 2.5.3), the most Fe-rich dunite sample (RP7-4), which has a composition close to that of olivine with an Mg# of 0.89, would be in equilibrium with a liquid with ∼16 wt% MgO. The most Fe-poor sample (RP7-9), with a composition similar to olivine with an Mg# of 0.91, would be in equilibrium with a liquid with ∼20 wt% MgO. If the liquid composition is assumed to have a higher FeO content, more similar to the RP8 basalts, even higher MgO contents are calculated. It is therefore highly likely that komatiitic melts (with > 18 wt% MgO) were required to form the RP7 dunites.

4.6 Relationship between basalts and komatiites

The similarity of REE patterns between the RP8 basalts and Winnipegosis komatiites (Figure 4.4) suggests a possible genetic link between the two suites. This could reflect formation of the basalts through extensive crystallisation of a komatiitic parental melt, or both volcanic suites being sourced from a similar mantle source which experienced different degrees of melting (Arndt & Nesbitt, 1982). These possibilities are examined by first testing the hypothesis that fractional crystallisation of a parental melt similar to the Winnipegosis Komatiites could generate melts that match both the major element

composition (Section 4.6.3) and REE systematics (Section 4.6.4) of the RP8 basalts.

4.6.1 MELTS modelling of komatiite crystallisation

Modelling of limited degrees of crystallisation within komatiitic rocks is relatively simple due to the dominant control of olivine (Section 2.5). By contrast, modelling the extensive, > 50 % crystallisation required to form a basalt from a komatiitic parent melt is complicated by the likelihood of saturation in other major phases, such as plagioclase and pyroxene, and requires prediction of the composition of these phases, at what point they become saturated in the melt, and their relative abundances. To undertake this modelling, Rhyolite-MELTS software v1.2 (Gualda *et al.*, 2012; Ghiorso & Gualda, 2015) is used, which supercedes previous MELTS software for modelling crystallisation of magmas in the pressure range 0 – 2 GPa. Rhyolite-MELTS (referred to simply as 'MELTS' below), and other variants of MELTS software, have shown success in reproducing many features of crystallisation of a number of magma compositions, including MORBs (e.g., Ghiorso, 1997; Asimow *et al.*, 2004; Asimow & Longhi, 2004), Martian basalts (Balta & McSween, 2013), and rhyolites (Gualda *et al.*, 2012). However, the reliability of MELTS software in predicting komatiitic crystallisation trends has not yet been established, and an attempt is first made to evaluate whether MELTS can successfully reproduce characteristics of Winnipegosis Komatiite crystallisation established in Section 2.5. The limited but well constrained fractionation trends in Winnipegosis komatiites provide a robust test of the accuracy of MELTS models before modelling a more extensive fractionation trend from komatiite to basalt.

Parental melt composition

The komatiite parental melt composition for this modelling is calculated as in Sections 2.5.5 and 3.5.3, by interpolating the regressions of various elements against MgO for RP1A komatiites to the parental melt MgO content of $\pm$ 1.6 wt% (Section 2.5.3). Uncertainties are calculated as the maximum and minimum values of the 95% confidence intervals about the regression lines in the interval 23.6 $\pm$ 1.6 wt% MgO. For elements with tight regression lines against MgO (Section 2.4.1), these uncertainties are dominated by the $\pm$ 1.6 wt% uncertainty in MgO, leading to similar relative uncertainties and errors in parental melt composition that are correlated with MgO along olivine control lines. Parental melt compositions are summarised in Table 4.5, REE concentrations are plotted in Figure 4.4, and major element compositions are indicated in

Table 4.5: Bulk rock major, minor, and rare-earth element composition calculated for the parental melt to RP1A komatiites. See text for details on calculations. Major element composition is renormalised with all Fe as FeO, including 0.1 wt% H_2O. REE concentrations are not renormalised.

Oxide	Parental melt	95% conf.	*Element*	Parental melt	95% conf.
SiO_2	46.01	0.41	*La*	1.32	0.12
TiO_2	0.50	0.03	*Ce*	3.70	0.32
Al_2O_3	8.50	0.57	*Pr*	0.58	0.05
Cr_2O_3	0.32	0.03	*Nd*	3.11	0.25
FeO_t	11.23	0.03	*Sm*	1.08	0.08
MnO	0.18	0.00	*Eu*	0.42	0.03
MgO	23.46	1.64	*Gd*	1.52	0.12
NiO	0.140	0.015	*Tb*	0.27	0.02
CoO	0.013	0.001	*Dy*	1.79	0.14
CaO	8.27	0.52	*Ho*	0.38	0.03
Na_2O	1.18	0.10	*Er*	1.11	0.09
K_2O	0.070	0.020	*Yb*	1.08	0.08
P_2O_5	0.037	0.002	*Lu*	0.16	0.01
H_2O	0.10	N/A			

Figures 4.6, 4.8, and 4.10.

This method should provide good estimates of the parental melt composition for strongly incompatible elements, such as TiO_2 and Al_2O_3, as the mixing lines between the phenocryst assemblage of olivine + chromite and residual melt, defined by the komatiite bulk rock compositions, closely approximate the liquid line of descent (LLD; Section 2.5.5). Komatiite LREEs show some evidence of scatter due to small amounts of crustal assimilation (Section 2.5.2); use of the same contamination modelling as in Section 2.5.2 suggests 10 – 25% of La present in the komatiitic melt after crustal assimilation would arise from 1 – 3 wt%, respectively, of assimilated continental crust. Heavier REEs are expected to be less affected, with crustal contamination contributing $< 5\%$ of the final budget of REEs heavier than Nd, even for the maximum calculated crustal assimilation of 3 wt%. These interpolations should therefore provide good approximations to the komatiite parent melt before contamination for the MREEs and HREEs, though LREEs are overestimated relative to the parental melt before contamination. As for the LREEs, concentrations of strongly incompatible elements (e.g., K_2O) are likely overestimated.

In contrast, elements compatible, or mildly incompatible in olivine, such as FeO, SiO_2, MnO, Ni, and Co are predicted to have curved LLDs due to variations in the composition of olivine during crystallisation. As a result, their bulk rock trends against

MgO do not follow the komatiite LLD. However, the projections of these mixing lines to the parental melt MgO may still provide a reasonable estimate of the parental melt concentrations for these elements, providing there was no net loss of olivine and no net change in the composition of the olivine (e.g. loss of Mg-rich olivine and gain of Fe-rich olivine; Larsen & Pedersen, 2000) before the melt-phenocryst mixing process occurred. The calculated parental melt content of 23.6 ± 1.6 wt% MgO lies within error of average bulk rock MgO content (22.2 ± 2.2 wt%; Section 2.4.1), suggesting no significant net loss of olivine phenocrysts. Establishing that there was no net change in olivine chemistry is more difficult, as bulk rock MgO is more sensitive to the net amount of olivine addition/subtraction than the olivine composition. Using the simple olivine crystallisation model from Section 2.5.5, and the petrographically observed average ∼17 vol% olivine phenocrysts across the entire RP1A section, the average composition of olivine calculated to crystallise from the komatiite parental melt has an Mg# of 0.901. This calculated average olivine composition is used as high Mg# olivine is probably over-represented in measured olivine core compositions (Section 2.4.2). The extrapolated regression of RP1A bulk rock FeO against MgO passes very close to, and within error of, this composition (Figure 2.17). Therefore, the average composition of olivines in the komatiites is identical to the average composition predicted to have crystallised from the calculated parental melt. Therefore, this method of calculating Winnipegosis komatiite parental melt compositions is applicable even to elements compatible or mildly incompatible in olivine.

The exception to this is Cr_2O_3, as chromite exerts a significant control on its whole rock budget. The method described above is only valid if there was no fractionation between olivine and chromite, i.e., no preferential incorporation of either phase into the erupted mixture, when the phenocrysts and melt were finally mixed. It is unclear whether or not this criterion was met, and it should be noted that Cr_2O_3 contents calculated for the parental melt are necessarily approximate.

Modelling conditions

MELTS crystallisation models for the Winnipegosis komatiite were run at a fixed pressure of 1 bar, from a temperature above the liquidus (1550 °C), to approximately 1000 °C in 1 °C temperature steps, by which point the majority (> 90 wt%) of the liquid had crystallised. Though crystallisation of olivine and chromite phenocrysts is believed to have predominantly occurred before komatiite eruption (Section 2.5.4), low (atmo-

spheric) pressure crystallisation is assumed as a starting point for the modelling. Due to uncertainties in the oxygen fugacity of the komatiites, several models were run, with initial f_{O_2} varying from QFM – 1 to QFM + 1 (Sections 2.5.3, 3.6.1). Models were run under both fixed and freely varying f_{O_2} conditions. The parental melt composition was assumed to contain 0.1 wt% H_2O, the maximum value calculated assuming fixed H_2O/Ce (Section 2.5.4; Dixon *et al.*, 2002). However, results of the models were indistinguishable from those using an anhydrous composition. During the modelling, it was found that removal of small mass increments of minerals, particularly chromite, led to a large over-estimation of their abundances and an associated gain in total mass during crystallisation. As such, all models were run with the parental melt wt% composition scaled to a mass of 10,000 g.

4.6.2 Komatiite MELTS crystallisation results

Crystallisation sequence

All of the MELTS models run were consistent with the petrographically observed crystallisation sequence for the Winnipegosis Komatiites, of olivine + chromite, followed by clinopyroxene and rarely plagioclase (Section 1.7.1). Although the relative crystallisation order of olivine and chromite could not be established petrographically, both a comparison of Al-in-olivine and olivine Fe-Mg temperatures (Section 2.5.4), and the observation that olivines with chromite inclusions tend to have lower Mg# than those without, suggest that olivine was the liquidus phase for Winnipegosis komatiites. Most of the MELTS models predict olivine as the liquidus phase, but the stability of spinel is predicted to increase with increasing f_{O_2}, and spinel was predicted to be the liquidus phase in the most oxidising model, with an f_{O_2} of QFM + 1. Although clinopyroxene was predicted to crystallise before plagioclase in all models, the temperature gap between clinopyroxene and plagioclase saturation is predicted to fall with decreasing f_{O_2}.

Liquidus temperature and olivine compositions

The temperature of olivine saturation varied from 1498 °C at QFM + 1, to 1508 °C at QFM – 1, in extremely good agreement with the olivine liquidus temperature of 1501 ± 32 °C calculated from Fe-Mg olivine-melt partitioning (Section 2.5.4). Despite this agreement, liquidus olivine compositions are substantially more magnesian than

observed in Winnipegosis Komatiites, varying from an Mg# of 0.944 at QFM + 1 to Mg# 0.932 at QFM – 1. This mismatch is a result of a previously documented underestimation of the olivine-liquid Fe-Mg exchange coefficient (K_D) by MELTS (Balta & McSween, 2013), with higher Mg#s predicted under more oxidising conditions due to both lower $Fe^{2+}/\Sigma Fe$ in the melt, and MELTS predicting lower K_D values at higher f_{O_2} (Figure 4.6a). The effect of this K_D underestimation on the LLD is investigated by comparing the LLDs predicted by MELTS to those calculated using incremental olivine subtraction from the same parental melt composition (Section 2.5.5; Albarede, 1992; Larsen & Pedersen, 2000) and K_D values from experimental studies (Herzberg & O'Hara, 2002; Matzen *et al.*, 2011). Although the olivine subtraction calculations do not include the effect of chromite crystallisation, MELTS models run without permitting spinel crystallisation indicate this should have a effect of <0.1 wt% FeO_t on the FeO-MgO LLD, due to the small proportion of chromite in the crystallising assemblage. LLDs predicted by MELTS have systematically high FeO_t contents relative to those calculated using experimentally derived K_D values, with an increasing mismatch in FeO_t as crystallisation progresses. However, this has a relatively small effect on the LLD, with FeO_t overestimated by a maximum of $\sim$ 1 wt% FeO_t after 35 wt% olivine crystallisation under the most oxidising conditions modelled (Figure 4.6b).

Chromite

Chromite saturation temperatures in the MELTS models vary from 1457 °C at QFM – 1 to 1512 °C at QFM + 1. These temperatures are higher than the highest Al-in-olivine temperatures (1424 ± 25 °C; Section 2.5.4) obtained for co-crystallisation of olivine and chromite, which could be explained by an overestimation of spinel stability by MELTS (Balta & McSween, 2013). However, it is also possible that higher temperature chromites were simply not sampled as part of the 25 successful Al-in-olivine analyses. The relative proportions of chromite in the crystallising assemblage (chromite + olivine) predicted by MELTS is shown in Figure 4.7a. MELTS overestimates chromite crystallisation relative to the average proportions of olivine and chromite phenocrysts calculated from Winnipegosis komatiite mixing lines (1.1 ± 0.1 wt% chromite; Section 2.5.1) under all modelled conditions, suggesting that high chromite saturation temperatures are likely an artefact of the MELTS modelling, rather a failure to analyse high temperature chromite during Al-in-olivine analyses.

Chromite compositions predicted by MELTS in the temperature range 1350 °C <

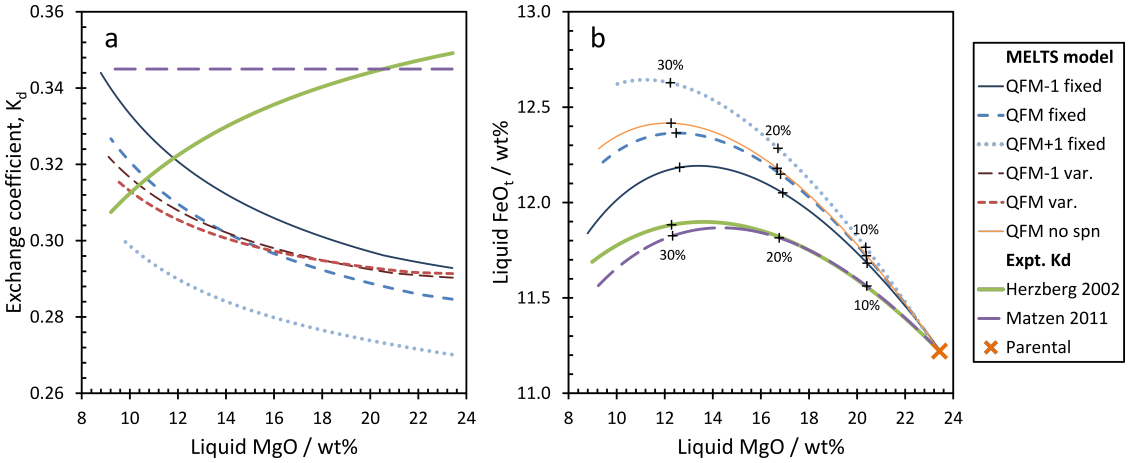

Figure 4.6: a) Olivine-liquid Fe-Mg exchange coefficient, K_D, as a function of liquid MgO. Values predicted by MELTS with initial f_{O_2} ranging between QFM – 1 and QFM + 1, under fixed f_{O_2} ('fixed') and freely varying f_{O_2} ('var.'), are compared to previously published K_D values derived from experiments (Herzberg & O'Hara, 2002; Matzen *et al.*, 2011). MELTS underestimates K_D, particularly at high MgO. b) Comparison of the FeO-MgO LLD predicted by MELTS, with LLDs calculated using incremental olivine subtraction from the same parental melt composition, and experimentally derived K_D values. Tick marks and percentages indicate wt% of liquid that has crystallised. MELTS LLDs end at the temperature step immediately before cpx saturation ($\sim$ 1200 °C, $\sim$35 – 37 wt% of liquid crystallised); LLDs calculated by olivine subtraction end at $\sim$36 wt% liquid crystallised. LLDs for MELTS models with varying f_{O_2} (not shown) fall within the range defined by the fixed f_{O_2} models. The underestimation of K_D by MELTS leads to increasing errors in liquid FeO content as crystallisation progresses. 'QFM no spn' = MELTS model with spinel crystallisation suppressed.

T < 1500 °C have similar Cr#s (Cr# = Cr/(Cr + Al)) to Winnipegosis chromites used for Al-in-olivine analyses (Figure 4.7b). However, similar to the predicted olivines compositions, they show elevated Mg# (Mg# = Mg/(Mg + Fe^{2+})) relative to all measured compositions. Although some chromites are likely to have gained Fe^{2+} during low temperature equilibration with their host olivine (Section 2.5.3), the MELTS chromite Mg#s are high even relative to chromite from an olivine-chromite pair which showed magmatic Al-in-olivine and Fe-Mg equilibration temperatures of $\sim$1400 °C (RP1A-111_ol-chr_4), and had not undergone low temperature Fe gain. Despite these errors in estimated Mg#, this is expected to have no appreciable effect on the LLDs for MgO and FeO as chromite forms a negligible proportion of the bulk rock FeO and MgO budget.

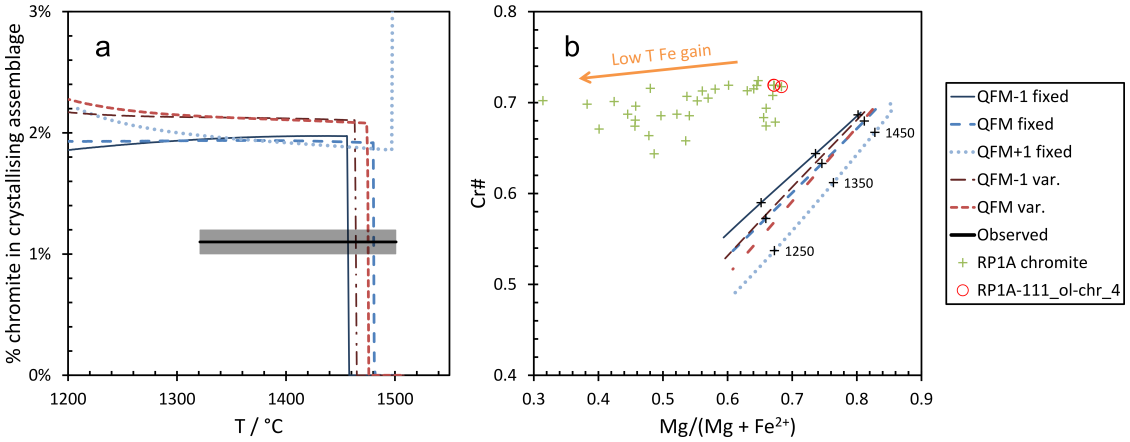

Figure 4.7: a) Proportion of chromite in the crystallising olivine + chromite mixture predicted by MELTS as a function of temperature, compared to an average of 1.1 ± 0.1 wt% chromite (Section 2.5.1) in phenocryst assemblage in temperature interval ~1501 – 1321 °C (liquidus to estimated eruption temperature), derived from komatiite bulk rock data ('Observed'). b) Comparison of chromite compositions predicted by MELTS as a function of temperature, to chromites included in olivine analysed from Winnipegosis komatiite samples ('RP1A chromite'). Chromite which had not gained Fe^{2+} during low temperature equilibration is highlighted ('RP1A-111_ol-chr_4').

Why does MELTS overestimate chromite stability?

Due to the overestimation of chromite crystallising, it might be expected that Cr_2O_3 would fall too rapidly in the MELTS calculations relative to the true LLD. However, a comparison of the MELTS Cr_2O_3-MgO LLD to experimentally derived Cr solubilities (Figure 4.8a) shows that MELTS provides a good approximation to the expected LLD. This is perhaps to be expected as a number of experimental studies of Cr solubilities in mafic and ultramafic compositions (Murck & Campbell, 1986; Barnes, 1986; Roeder & Reynolds, 1991) were included in the original MELTS calibration dataset (Ghiorso & Sack, 1995).

The combination of overestimated chromite stability but correct Cr_2O_3-MgO LLDs can be reconciled by the fact that MELTS does not take into account incorporation of Cr_2O_3 into olivine. Despite low Cr_2O_3 contents in olivine, it's volumetric dominance means that it accounts for approximately 32% of the Cr_2O_3 budget in the calculated phenocryst mixture of 98.9 wt% olivine and 1.1 wt% chromite. The lack of Cr_2O_3 in MELTS olivines results in the MELTS liquid composition evolving more steeply in Cr_2O_3-MgO space than would be expected for crystallisation of observed olivine compositions (Figure 4.8a). This has two main effects on the MELTS model: 1) the Cr

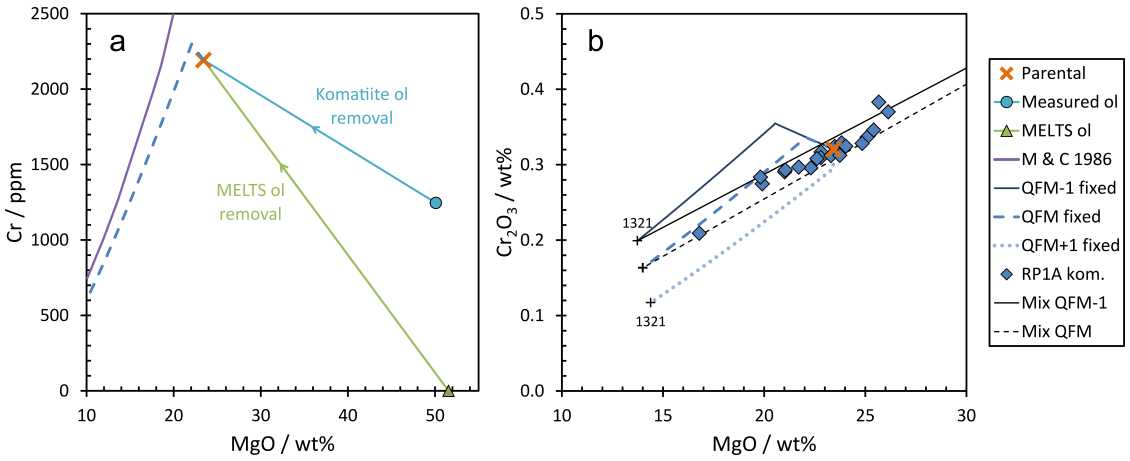

Figure 4.8: a) Comparison of the Cr-MgO LLD predicted by MELTS to experimentally derived Cr solubility of Murck & Campbell (1986), using the best fit curve of Barnes (1998). Compositions of measured highest Mg# olivine ('measured ol') and liquidus olivine predicted by MELTS ('MELTS ol') are shown, with tie lines to parental melt and arrows indicating direction melt composition would evolve through removal of these olivines. Lack of Cr in MELTS olivine causes a steeper LLD, and Cr solubility is reached after less olivine crystallisation (at higher temperatures). b) Cr_2O_3-MgO LLDs predicted by MELTS, compared to bulk rock data from borehole RP1A. The bulk rock data approximately falls along mixing lines ('Mix QFM-1', 'Mix QFM') between the MELTS LLDs at the estimated eruption temperature (1321 °C; Section 2.5.4), and the composition of the olivine + chromite phenocryst assemblage calculated for the komatiites.

solubility surface is reached after a smaller interval of crystallisation, leading to higher temperatures of chromite saturation; 2) more chromite crystallisation is required for the liquid composition to adhere to the predicted Cr solubility surface, causing an overestimation in the proportion of chromite crystallising. However, the LLD is not affected by these problems, and the MELTS calculated LLD can plausibly generate the observed bulk rock mixing lines (Figure 4.8b; Section 2.5.5).

Clinopyroxene

Clinopyroxene crystallisation is predicted to commence between 1202 and 1193 °C, with the slightly lower temperatures favoured by lower f_{O_2}. MELTS predicts that olivine crystallisation effectively ceases at the onset of clinopyroxene crystallisation, which is consistent with the petrographical observation that olivine never terminates on clinopyroxene (Sections 1.7.1, 2.5.4). In all models, the first clinopyroxene to crystallise is a high Ca augite, and its predicted composition varies insignificantly with modelled f_{O_2}; MgO, CaO, and FeO_t are all roughly constant at ∼17 wt%, ∼20 wt%, and ∼7 wt%,

respectively. Pyroxene compositions are then predicted to evolve, broadly, towards lower CaO and higher FeO_t at roughly constant MgO, until saturation of a second, low Ca pyroxene at 1167 – 1145 °C.

This predicted composition cannot be compared to pyroxenes in the massive komatiite flows, or olivine spinifex zones of differentiated flows, as the dendritic nature of these pyroxenes indicates they did not grow under equilibrium conditions. However, pyroxene phenocrysts from the acicular pyroxene zone of differentiated flow A ('Aci. px', sample RP12-307.3; Figure 4.5) have habits indicative of conditions closer to equilibrium (Section 1.4.2), and compositions close to experimental augites grown under anhydrous equilibrium conditions (Parman *et al.*, 1997). MELTS predicted compositions fall close to the compositions of the acicular pyroxene phenocrysts, although MELTS compositions are higher in CaO and lower in MgO than the observed phenocrysts, which have MgO and CaO contents of ∼18 – 20 and 15 – 18 wt% respectively (Figure 4.5). Therefore, following clinopyroxene saturation, the LLD predicted by MELTS will be too steep in MgO-CaO space compared to an LLD generated by removal of the observed phenocrysts, i.e. CaO will fall by too much over a given interval of decreasing MgO. However, errors introduced due to these differences in clinopyroxene composition are likely to be small compared to the differences in the CaO-MgO LLD arising from the varying temperature of clinopyroxene saturation with pressure (Section 4.6.3).

Plagioclase

Plagioclase was predicted to saturate at ∼1192 °C in all 1 b crystallisation models, showing no dependence on f_{O_2}. The first plagioclase to saturate in all models was Ca rich, with molar anorthite (An) contents of ∼80%, and molar albite contents are predicted to increase at the expense of An with continued crystallisation. No plagioclase phenocrysts were observed in Winnipegosis komatiites against which to assess the MELTS predicted plagioclase compositions. However, the predicted compositions are similar to granular plagioclase compositions in coarse spinifex-textured komatiite from Gorgona Island (up to An_{83}; Echeverria, 1980), and so the MELTS predicted plagioclase compositions appear plausible.

4.6.3 Modelling the major element composition of RP8 basalts

To summarise, MELTS appears able to adequately model the low pressure komatiite LLD from the liquidus temperature to ∼1200 °C to a good degree of precision, with two

main caveats. Firstly, FeO_t in the MELTS liquid is likely to be overestimated by up to ∼1 wt% at the onset of clinopyroxene saturation, due to errors in the MELTS predicted olivine-melt Fe-Mg exchange coefficient. Secondly, the prediction of clinopyroxene with higher CaO contents, and lower MgO contents than observed may cause the LLD to evolve along a trajectory that is too steep in CaO-MgO space, causing slightly underestimated CaO at a given MgO after clinopyroxene saturation. With these caveats in mind, MELTS is used to model the formation of the RP8 basalts through fractional crystallisation of the RP1A komatiitic parental melt. Though the effects of metamorphism on the basalt compositions have not been established due to a lack of pristine samples or primary minerals, the modelling below investigates whether the observed compositions can be explained by igneous processes alone before invoking metamorphic processes. As noted previously (Section 4.4.2), there is a very limited compositional range in RP8 basalts, which contributes to the difficulty of discerning between igneous or metamorphic trends in these rocks. The reasons behind such restricted compositional variations will be revisited in Section 4.7.

Effect of pressure

Extensive crystallisation of a komatiitic melt to a basalt would likely require the presence of a magma chamber at depth, and so the effect of different crystallisation pressures on the LLD must be considered. MELTS models run with freely varying f_{O_2} starting from QFM show olivine saturation temperatures increasing by approximately 8 °C per kb, from 1505 °C at 1 b to 1534 °C at 4 kb. However, olivine compositions are almost constant between models and so this is expected to have no significant effect on the LLD. Chromite saturation temperatures are also predicted to increase with depth, and between 3 and 4 kb spinel becomes the liquidus phase. Again, this is not expected to significantly affect the LLD for most elements except Cr_2O_3.

The main effect of crystallisation pressure on the LLD predicted by MELTS is a difference in the relative onset of clinopyroxene and plagioclase crystallisation. Increased pressures cause both pyroxene and plagioclase to saturate at higher temperatures, but the effect is greater for pyroxene, leading to a larger temperature gap between pyroxene and plagioclase saturation at higher temperatures. This predicted temperature gap increases from 8 °C at a pressure of 1 b (clinopyroxene saturation at 1201 °C, plagioclase saturation at 1193 °C) to 51 °C at a pressure of 4 kb (clinopyroxene saturation at 1275 °C, plagioclase saturation at 1224 °C). This is manifested in the LLD as a larger gap in

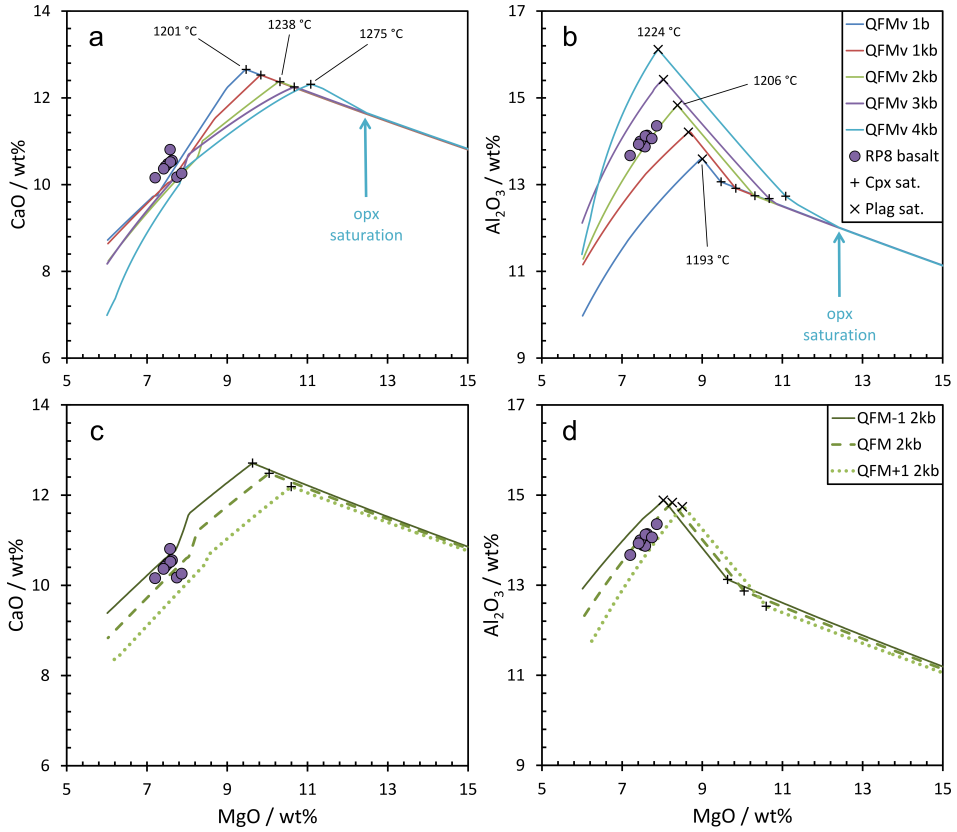

Figure 4.9: MELTS predicted LLDs for CaO and Al_2O_3 as a function of MgO, compared to RP8 basalt bulk rock compositions. a), b) Variation in predicted LLDs with pressure of crystallisation varying from 1 b to 4 kb. f_{O_2} was initially set to QFM at the liquidus but allowed to vary during crystallisation ('QFMv'). Compositions at clinopyroxene saturation ('Cpx sat.') indicated in both figures, with temperatures of at 1 b, 2 kb, and 4 kb indicated in *a*. Compositions and temperatures at plagioclase saturation ('Plag sat') are indicated in *b*. Higher pressures lead to a larger gap in temperature and MgO between clinopyroxene and plagioclase saturation, causing greater Al_2O_3 enrichment in the melt. Orthopyroxene (opx) saturation in the 4 kb model is indicated. c), d) Variation in the predicted LLD with f_{O_2} at a fixed pressure of 2 kb. Oxygen fugacity was fixed during crystallisation to maintain constant f_{O_2} differences. Lower f_{O_2} also promotes greater Al_2O_3 enrichment in the melt by delaying both clinopyroxene and plagioclase saturation to lower MgO.

MgO between CaO beginning to fall and Al_2O_3 rising more rapidly (upon clinopyroxene saturation), and Al_2O_3 beginning to fall (upon plagioclase saturation; Figure 4.9a, b). Notably, this causes maximum Al_2O_3 enrichment in the evolving melt to increase with pressure.

The best fit to the basalt Al_2O_3-MgO data for crystallisation of the komatiitic parent with initial f_{O_2} of QFM is for a pressure of ~2 kb. However, this is not a unique solution due to a trade-off with modelled f_{O_2}; at lower f_{O_2}, clinopyroxene crystallises at

lower MgO (Figure 4.9c, d). This causes the same degree of Al_2O_3 enrichment at lower crystallisation pressures, with a 1 log unit decrease in f_{O_2} having approximately the same effect as a 0.5 kb increase in pressure. Uncertainties in the parental melt Al_2O_3 composition of 8.49 ± 0.57 wt% might be expected to have a similar effect. However, uncertainties in Al_2O_3 and many other elements in the komatiites are strongly correlated with MgO uncertainties along the olivine control lines used to estimate the parental melt composition (Section 4.6.1). Uncertainties in the parental melt composition therefore largely move the parental melt composition along olivine control lines, leading to almost identical LLDs (not shown), though the amount of fractional crystallisation required to produce basaltic MgO contents does vary.

CaO contents in the basalts are slightly underestimated in the variable f_{O_2} models (Figure 4.9a, b). This may be explained by the overestimated CaO/MgO in the MELTS clinopyroxene compositions, or by the evolution of the modelled melts to higher f_{O_2} with crystallisation (from QFM at the liquidus to ∼QFM + 0.5 at basaltic compositions), which causes earlier clinopyroxene saturation. However, it is also possible that CaO was mobile during metamorphism, considering the higher metamorphic grade of RP8 basalts compared to the komatiites (Section 1.4).

Major element composition of RP8 basalts can be generated by extensive crystallisation of a komatiite parental magma

By adjusting the pressure and f_{O_2} conditions, almost all major elements in the basalts can be matched by 56 – 62 wt% crystallisation (depending on the exact starting composition) of a parental melt with the same composition as the RP1A komatiite parental melt (Figure 4.10).

The exceptions to this are FeO_t, which is overestimated due to the errors in K_D outlined in Section 4.6.2, and SiO_2, which is systematically underestimated by 2 – 4 wt% for conditions that can replicate the other major elements. Basalt FeO_t data can be matched by accounting for a ∼1 wt% overestimation of FeO_t by the MELTS models (Section 4.6.2, Figure 4.10). However, MELTS predicted igneous mineral assemblage at basaltic compositions (dominated by clinopyroxene and plagioclase) cannot account for the enrichment in SiO_2 observed in the RP8 basalts, or the steep trend in SiO_2 data against MgO. Estimated 2σ uncertainties for basalt SiO_2 measurements of ± 1.6 wt% (Section 4.3.1) are insufficient to explain this discrepancy.

Three possibilities are considered to explain the elevated SiO_2 relative to modelled

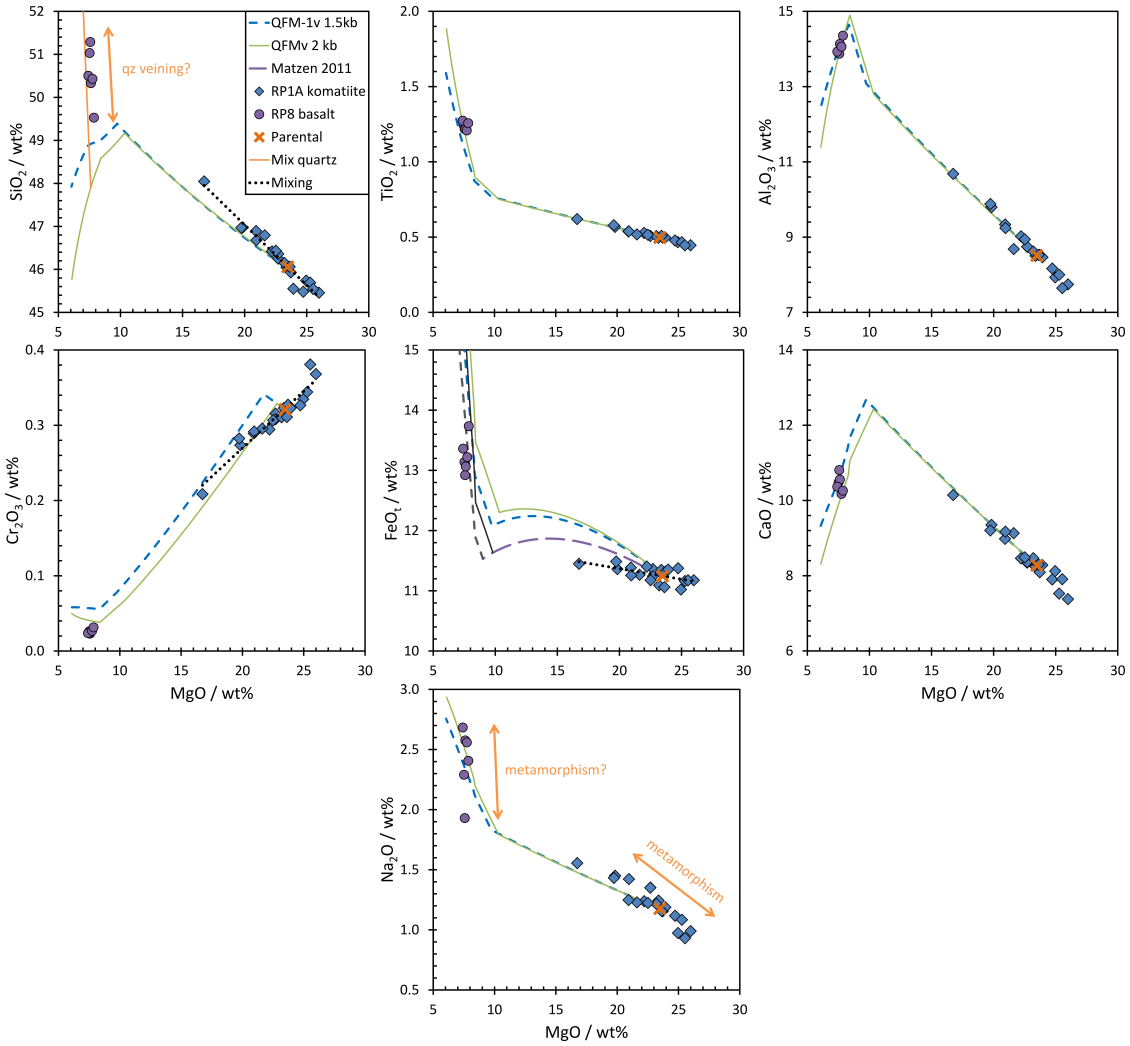

Figure 4.10: MELTS predicted LLDs for initial f_{O_2} = QFM – 1 and pressure = 1.5 kb ('QFM-1v 1.5kb'), and initial f_{O_2} = QFM and pressure = 2 kb ('QFMv 2kb'), compared to RP1A komatiite and RP8 basalt data. f_{O_2} was allowed to vary in both models. LLDs show an excellent match to basalt compositions for all major elements with the exception of FeO_t and SiO_2. Komatiite bulk rock data follow mixing trends between the phenocryst assemblage and residual melt, which are oblique to the LLD for elements compatible or mildly incompatible in olivine or chromite ('Mixing'). Na_2O follows trends oblique to the LLD for both the basalts and komatiites, likely due to metamorphism (arrows). However, the komatiite LLDs still pass through the centre of the range of basalt compositions. SiO_2 plot shows a mixing line from the MELTS LLDs at the average RP8 basalt MgO content (7.6 wt%) to quartz. FeO_t plot also shows the LLD calculated using the Matzen *et al.* (2011) olivine-melt K_D value as MELTS underestimates K_D leading to overestimated FeO_t contents in the melt (Section 4.6.2). Plausible LLDs accounting for this FeO_t overestimation are calculated by subtracting 1 wt% FeO_t from the MELTS predictions after their intersection with the Matzen *et al.* (2011) LLD (grey lines).

compositions. Firstly, the komatiitic parental melt could have been further crustally contaminated by SiO_2-rich material during crystallisation, beyond the ∼2% crustal contamination inferred for Winnipegosis komatiites used to calculate the parental melt composition. Secondly, SiO_2 may have been elevated during metamorphic processes, such as intrusion of petrographically observed quartz-carbonate veins (Section 1.4.5). Thirdly, high SiO_2 may indicate that the basalts were derived from a different parental melt to the komatiites (Aitken & Echeverría, 1984). The first two of these possibilities should be distinguishable using the REE systematics of the basalts and komatiites, as potential crustal contaminants such as the tonalitic compositions invoked to explain the incompatible element systematics of the komatiites (Section 2.5.2) should be elevated in LREEs. The third will be discussed in detail in Section 4.6.5.

4.6.4 Modelling the REE composition of RP8 basalts

Minimum degree of fractional crystallisation

The minimum degree of fractional crystallisation required to generate the REE abundances in the RP8 basalts from crystallisation of komatiite parental melt can be estimated by assuming perfectly incompatible behaviour of the REEs during crystallisation. From mass balance, the mass fraction, f of crystallisation required is

$$f = 1 - \frac{[REE]_{parent}}{[REE]_{basalt}}, \tag{4.1}$$

where square brackets indicate concentration and the crystallising solid is assumed to have a REE concentration of zero. If REEs are at all partitioned into the fractionating solids, this calculation underestimates the amount of crystallisation required.

This calculation broadly suggests that the REE abundances in both basalt samples can be explained by at least 52 – 65 wt% crystallisation of a melt with the calculated komatiite parental melt composition (Figure 4.11). However, the basalts show higher LREE/HREE ratios than the calculated komatiite parental melt, leading to higher estimated percentages of fractional crystallisation from the LREEs. For the basalts to have formed by crystallisation of the komatiite parental melt, this requires that HREE were more compatible during crystallisation, or that LREE were added, for example, through additional crustal contamination. Additionally, elevated Eu relative to other REEs in sample RP8-10 cannot be explained solely by concentration of the REEs during crystallisation of the komatiite parental melt, and may require igneous

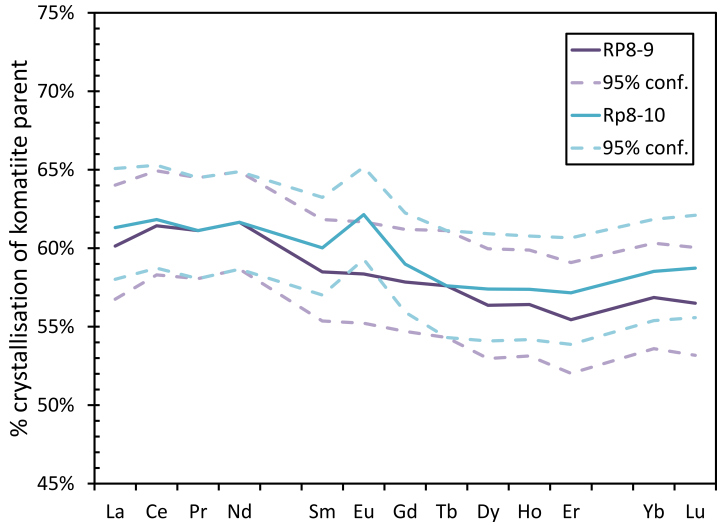

Figure 4.11: Minimum degree of fractional crystallisation required to generate REE abundances of RP8 basalts from a komatiitic parent melt, including uncertainties from 95% confidence limits about parental melt composition, calculated using equation 4.1.

plagioclase accumulation (Weill & Drake, 1973) or Eu mobility during metamorphism (Bau, 1991).

REE partitioning model

To address these complexities, a REE partitioning model is attached to the outputs of the two MELTS crystallisation models above that successfully reproduce the major element compositions of the RP8 basalts. At each 1 °C temperature increment, REEs are partitioned between the liquid and the solids fractionated in that step. Chromite mineral/liquid REE partition coefficients ($D_{REE}^{min-liq}$, hereafter 'D') are assumed to be zero due to its minor mass and lack of partition coefficients for natural compositions, though experiments on synthetic compositions suggest D is low (Nagasawa *et al.*, 1980). Augite and pigeonite D are calculated as a function of clinopyroxene Wo content, after Mckay *et al.* (1986). Plagioclase Ds are taken from QFM, 1200 °C experimental runs of Aigner-Torres *et al.* (2007), to match the approximate temperature and oxygen fugacity of plagioclase crystallisation in the MELTS models. Olivine Ds are calculated using the lattice strain model of Sun & Liang (2013), which incorporates pressure, temperature, olivine Fo content, and melt Al content.

The 2 kb QFM model is able to reproduce all of the REE concentrations in the RP8 basalts within parental melt composition uncertainties, with the exception of elevated

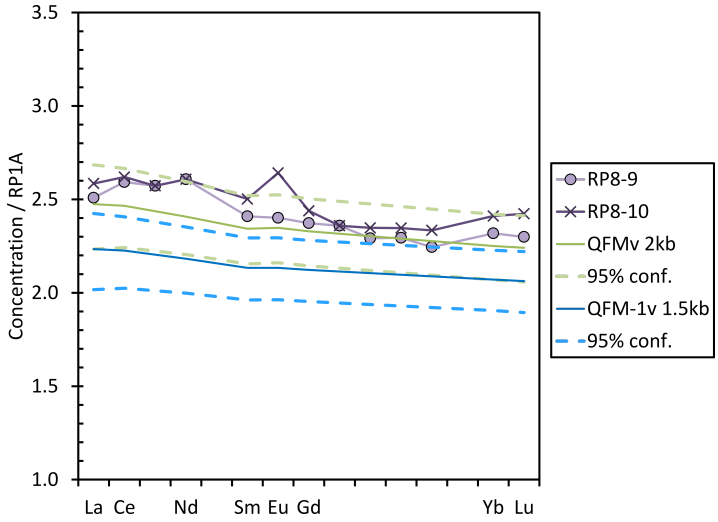

Figure 4.12: MELTS models (as in Figure 4.10) of REE concentrations resulting from crystallisation of a komatiite parental melt to 7.6 wt% MgO, compared to data from RP8 basalts. All data are normalised to the average calculated komatiite parental melt composition. Dashed lines indicate REE patterns generated from same crystallisation model, but using the upper and lower 95% confidence limits about the average parental melt composition. Only REEs labelled on the x axis were modelled.

Eu in sample RP8-10, through fractional crystallisation of the komatiite parental melt to the MgO content of RP8 basalts (7.6 wt%; Figure 4.12). The 1.5 kb QFM – 1 model predicts REE concentrations that are slightly too low to match the observed basalt REE contents, as a lower total mass of crystals fractionated is required to reach 7.6 wt% MgO in this model. However, both models reproduce the slight enrichment of LREE/HREE compared to the komatiite parental magma as the HREEs are more compatible in olivine and augite than the LREEs. The contribution, in particular from augite, dwarfs that of plagioclase, in which the LREEs are more compatible than the HREEs, leading to a net HREE depletion during fractional crystallisation to form a basalt. Plagioclase REE concentrations are too low to explain Eu anomalies in sample RP8-10 without a large accumulation of plagioclase, which can be ruled out as RP8-10 has a similar major element composition to the rest of the basalts.

4.6.5 Formation of the RP8 basalts

The fact that the REE systematics of the RP8 basalts can be entirely explained by fractional crystallisation processes rules out the possibility that high SiO_2 contents in the RP8 basalts are due to further crustal contamination of an RP1A komatiite-

like parental melt, as even small levels of crustal assimilation should further raise the LREE/HREE ratio in the crystallising melt.

To summarise, almost all analysed aspects of the RP8 basalt geochemistry can be explained by ~60% fractional crystallisation of a komatiite with the composition of the RP1A komatiite parental melt, with a best fit MELTS pressure of crystallisation of ~2 kb, and f_{O_2} of ~QFM. The only exceptions to this are high SiO_2 and Eu contents, and steep slopes in SiO_2 against MgO. These are best explained in this model by metamorphic effects such as fluid flow (Bau, 1991) and quartz veining (Figure 4.10, Section 1.4.5) during metamorphism. It is stressed here that these best fit pressures and oxygen fugacities are not precisely constrained, as the success of the MELTS model in predicting the LLD at non-atmospheric pressures could not be evaluated. However, the underlying reasons for the variations in LLD (reduced plagioclase stability compared to clinopyroxene at higher pressure) and approximate f_{O_2} both appear geologically reasonable.

Could RP8 basalts have formed by lower degree melting of a similar mantle source?

An alternative explanation for the similarity in REE patterns between RP8 basalts and the RP1A komatiites is that the basalts formed from a similarly depleted mantle source which experienced a lower degree of melting. This can be envisioned as the basalts forming through passive rifting before or after plume impingement generated the komatiites (e.g. in a back arc basin; Section 2.6), forming in the cooler edges of a plume spreading beneath the lithosphere (spatial variations in plume temperature, e.g., Campbell *et al.*, 1989), or forming during a cooler pulse of plume activity (temporal variations in plume temperature, e.g., White *et al.*, 1995). These scenarios could generate a picritic or high Mg-basalt parental melt, which then fractionated to form the RP8 basalts.

Distinguishing whether the RP8 basalts formed from fractional crystallisation of a komatiite or a lower melt fraction primary melt, is difficult for a number of reasons. The RP8 basalts lack of primary minerals, and show evidence of metamorphic disturbance of some elements, such as Na_2O, which can be used to indicate depths and extents of melting (Klein & Langmuir, 1987). Furthermore, the modelling in Section 4.6.3 shows that a wide range of basalt compositions (particularly Al_2O_3 and CaO contents) can be produced from the same primary melt depending on the pressure and f_{O_2} of crystallisation. Finally, for many incompatible elements (e.g. the TiO_2), there is a trade

off between increasing degree of mantle melting, which decreases their concentrations in the parental melt, and an increasing degree of fractional crystallisation required to reach basaltic compositions.

In theory, the possibility that the basalts formed from lower degrees of melting can be examined on the basis of their FeO_t-MgO and SiO_2-MgO relationships. FeO in melts formed by adiabatic decompression increases with mantle potential temperature and associated depth of melting initiation (e.g., Klein & Langmuir, 1987), and while MgO also increases (Herzberg & O'Hara, 2002), FeO-MgO LLDs that are essentially flat during olivine fractionation maintain the FeO offsets inherited from the parental melt until clinopyroxene and/or plagioclase saturation is reached. By contrast, SiO_2 is expected to decrease with mantle potential temperature and associated depth of melting initiation (e.g., Asimow & Longhi, 2004; Lee *et al.*, 2009).

Formation from a lower degree melt was considered a possible explanation for the elevated SiO_2 of the RP8 basalts relative to modelled komatiite crystallisation (Section 4.6.3), as the basalts have similar SiO_2 contents to modern MORBs (Section 4.4.2, Figure 4.13). However, fractional crystallisation of a lower degree melt cannot explain the steep trend in SiO_2 against MgO observed for the RP8 basalts, as the major crystallising phases at an MgO content relevant to basalt formation (olivine, clinopyroxene, plagioclase) all have similar SiO_2 contents to the melt, leading to fractionation trends that are relatively flat in SiO_2-MgO space. It is therefore likely that the steep SiO_2-MgO trends require metamorphic alteration regardless of the inferred SiO_2 content of the parental melt.

By contrast, FeO_t contents of the RP8 basalts are distinctly elevated compared to modern MORBs (Section 2.4.1; Figure 4.13), consistent with higher mantle potential temperatures and pressures of melting. Though this rules out a modern MORB-like parental melt for the RP8 basalts, a number of factors limit the 'resolution' of this relationship with regards to temperature and extent of melting, such as steep slopes in FeO_t against MgO for basaltic compositions, and differences in plagioclase and clinopyroxene saturation driven by variations in pressure of crystallisation. Therefore, although extremely high mantle potential temperatures (T_p) in the Proterozoic have previously been ruled out (Section 2.6.2; Herzberg & Asimow, 2015), it remains unclear whether ambient mantle potential temperatures ∼0 – 70 °C (Keller & Schoene, 2018), or ∼80 °C (Davies, 1999) higher than modern ambient mantle are able to generate melts with the high Fe contents of the RP8 basalts through passive rifting. Similarly, it is unlikely that crystallisation of a picritic melt with lower initial MgO than the RP1A komati-

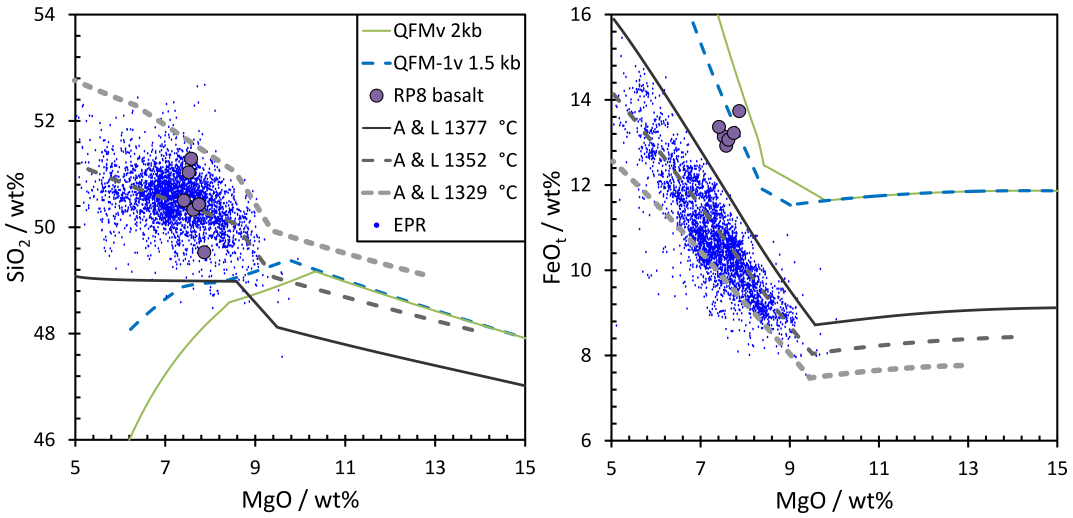

Figure 4.13: FeO_t and SiO_2 against MgO plots for RP8 basalts, compared to modern MORB and modelled LLDs for komatiite parental melt and MORBs. Komatiite LLDs ('QFMv 2kb' and 'QFM-1v 1.5kb') for FeO_t are composite LLDs generated using the Matzen *et al.* (2011) olivine-melt K_D value and MELTS LLDs corrected for MELTS overestimation of FeO (grey curves in Figure 4.10). SiO_2 LLDs are unaltered MELTS outputs. East Pacific Rise ('EPR') modern MORB data and pMELTS modelled MORB LLDs are from (Asimow & Longhi, 2004, 'A & L'). LLDs are labelled with modelled mantle potential temperature.

ites formed from a slightly cooler portion of the plume can be distinguished using this method.

4.7 Plumbing system of the Winnipegosis Komatiite Belt

Ultimately, crystallisation of a primary melt formed through lower degrees of melting than the Winnipegosis komatiites, but higher degrees of melting than modern MORBs, cannot be rigorously ruled out based on geochemistry alone. Despite this, all available geochemical evidence is consistent with the formation of the RP8 basalts through extensive crystallisation of a komatiite parental melt, which also erupted relatively unfractionated in the same greenstone belt. No evidence was found of a possible lower degree parental melt, such as a picrite. It is concluded that the RP8 basalts most likely formed through ~60% crystallisation of a komatiitic parent melt, and subsequently experienced minor alteration during greenschist metamorphism.

This solution is also consistent with all the available geological constraints. Extensive fractionation of komatiitic magmas in the upper crust near the Winnipegosis Komatiite Belt supracrustal rocks is evidenced by the large dunite body intersected

by borehole RP7 (Section 4.5), and numerous gabbroic bodies intersected throughout the WKB (McGregor, 2011). Furthermore, the volume of the RP7 dunite body is at least ∼5 km × 2.5 km × 0.6 km (7.5 km^3), with an erosional upper contact. For the ∼60 wt% crystallisation a komatiitic precursor required to generate a basalt, a magma chamber of this size could process 12.5 km^3 of komatiitic melt, generating 5 km^3 of basalt. Though this alone may not be enough to generate all of the basalt in the WKB, the complete lack of surface exposure and small number of boreholes drilled in the WKB make it difficult to constrain how common magma chambers of this size might be. The RP7 dunite body at least demonstrates that magma chambers capable of producing large volumes of basalt were present in the upper crust at the time of WKB formation.

The approximate palaeo-depth of the RP7 dunite body is calculated for comparison with the best fit pressures identified from the MELTS modelling. Flow tops in the WKB consistently dip towards the West, consistent with seismic fabrics with dips of ∼20° to the West (Figure 4.1b; Lucas *et al.*, 1996), suggesting the entire belt was tilted westward during the Trans-Hudson Orogen. The RP7 dunite body occurs ∼5 km perpendicular to strike from the structurally lowest supracrustal rocks in the WKB, and approximately ∼16.5 km perpendicular to strike from borehole RP8 (Figure 4.1a). Assuming stratigraphic relationships in the WKB were broadly preserved through Trans-Hudson deformation, and a dip of ∼20°, the approximate depth of the RP7 dunite body was ∼1.7 km at the time of first supracrustal formation, or 5.6 km at the time of RP8 basalt eruption. For comparison, the MELTS best fit pressures of 1.5 – 2 kb, and an average crustal density of 2.88 gcm^{-3} in the WKB (Hosain & Bamburak, 2002), suggest that depths of 5.3 – 7.1 km are necessary for the basalts to have formed through differentiation of a komatiite. Therefore not only does the RP7 dunite body provide evidence of extensive fractionation of komatiitic magma in the WKB, but it could potentially represent a magma chamber in which differentiation to form the RP8 basalts occurred.

It is suggested that, rather than representing melts from different portions of a temperature-zoned plume (e.g., Campbell *et al.*, 1989), the different volcanic styles expressed in the Winnipegosis Komatiite Belt simply reflect differences in low pressure fractional crystallisation of a komatiitic parental melt. Where the melt was able to rapidly ascend to the surface, minimal fractionation occurred and komatiite flows were formed. If the magma stalled in an upper crustal magma chamber, it fractionated extensively to form basaltic flows and complementary ultramafic cumulates (Figure 4.14).

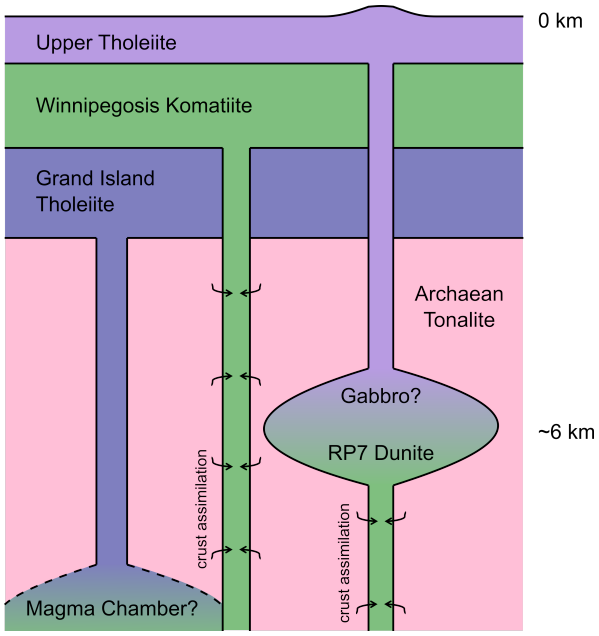

Figure 4.14: Schematic diagram of volcanism in the WKB. Komatiitic magma that rises rapidly to the surface forms komatiite flows, but if it stall in a magma chamber it differentiates to produce basaltic volcanism and ultramafic cumulates. Komatiitic magma experienced crustal assimilation during ascent (Section 2.5.2), but there is no evidence of additional crustal assimilation during fractionation of the komatiitic parental melt to form basalts (Section 4.6.5).

4.7.1 What caused eruption of homogeneous basalt?

Dunite compositions in borehole RP7 show only small variations in Fo content (from FeO-MgO relationships) and do not show systematic changes with depth (Sections 1.6.2, 4.4.1). As such, the RP7 dunite body is unlikely to have been generated by gradual fractional crystallisation of a single batch of komatiitic magma, and instead reflects episodes of magma recharge (e.g., Prægel & Holm, 2001). However, the compositions of RP8 basalts are extremely uniform. This begs the question, if the basalts are the products of extensive crystallisation of multiple batches komatiitic melt, what caused them to erupt with such a uniform composition?

Two previously suggested fluid dynamic models can potentially explain the uniform composition of RP8 basalts. Sparks & Huppert (1984) noted that removal of dense phases such as olivine and pyroxene decrease the density of a fractionating magma. However, removal of plagioclase, which is less dense than the magma, causes an increase in magma density, leading to a minimum in magma density immediately before plagioclase saturation. This presence of this density minimum means that magmas

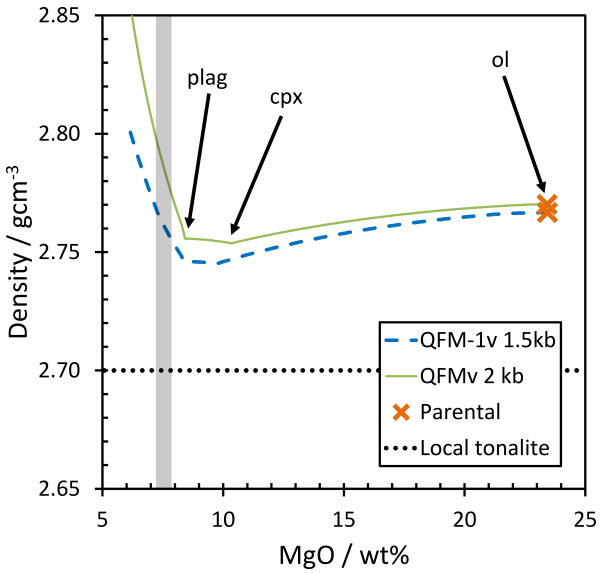

Figure 4.15: MELTS predicted densities during fractionation of a komatiite parent melt to produce basalt, for the two best fit models (QFM-1v 1.5 kb, QFMv 2 kb) from Section 4.6.3. Saturation of olivine ('ol'), clinopyroxene ('cpx'), and plagioclase ('plag') are indicated. MgO range of RP8 basalts is indicated by the grey band. Average density of local Archaean tonalite through which the WKB volcanics erupted (East of the WKB) is also shown, calculated from gravity profiles (Hosain & Bamburak, 2002).

which have fractionated plagioclase, and more primitive magmas injected at the base of the magma chamber should have similar densities, promoting mixing. This can cause the growth of a zone of constant melt composition in the magma chamber. MELTS predicted densities are consistent with this model, as a broad density minimum exists between clinopyroxene saturation at ∼10 wt% MgO and plagioclase saturation at ∼8 wt% MgO (Figure 4.15). This would allow production of a constant composition melt at ∼8 – 10 wt% MgO, which may have undergone additional fractionation upon ascent to the surface to generate RP8 basalts with ∼7.5 wt% MgO.

Secondly, Dufek & Bachmann (2010) suggested that crystal-liquid separation is most efficient in a mixture with between 50 – 70% crystals, as this crystal fraction shuts down chamber-wide convection, promoting compaction. Around 60% crystallisation of a komatiitic melt is required to generate RP8 basalt compositions, consistent with the window of predicted maximum melt segregation efficiency. The constant composition of RP8 basalts can therefore be attributed to magma homogenisation due to a density minimum, efficient segregation of basaltic magma from cumulates at ∼60% fractional crystallisation, or a combination of both of these processes.

4.8 Conclusions

The Winnipegosis Komatiite Belt (WKB) contains abundant evidence of basaltic and komatiitic volcanism, along with evidence of a large upper crustal magma chamber containing abundant dunite cumulates. Dunites are highly magnesian and compositionally similar to komatiitic olivine. They crystallised from komatiitic liquids and represent olivine adcumulates with minor chromite and <6 wt% interstitial melt. Basalts show an extremely restricted compositional range and REE patterns that are similar in shape to Winnipegosis komatiites, albeit with higher absolute concentrations and slightly elevated LREE/MREE.

MELTS modelling is used to investigate whether the RP8 basalts could have formed from extensive crystallisation of a komatiitic parental melt similar to the Winnipegosis komatiites. MELTS is able to successfully reproduce komatiite LLDs with the exception of FeO, which is overestimated due to errors in predicted olivine K_D, and CaO, which is likely underestimated due to MELTS overestimating CaO/MgO in clinopyroxene. The proportion of chromite is overestimated as MELTS does not take into account Cr_2O_3 in olivine, but this should not affect predicted LLDs.

Crystallisation of komatiitic magma at higher pressures leads to a greater degree of Al_2O_3 enrichment in evolved melts, due to an increasing temperature and compositional gap between clinopyroxene and plagioclase saturation. Differences in f_{O_2} can have a similar effect, with a 1 log unit decrease in f_{O_2} producing roughly the same Al_2O_3 enrichment as a 0.5 kb increase in pressure of crystallisation. This trade-off means there is no unique pressure-f_{O_2} solution to form a basalt through extensive fractionation of a komatiitic parental melt. However, almost all aspects of the major element chemistry of RP8 basalts can be matched by ~60% fractional crystallisation of a komatiite parent, in a magma chamber at pressures of 1.5 to 2 kb, at an oxygen fugacity of QFM – 1 to QFM, respectively. RP8 basalt REE patterns are best matched by crystallisation at 2 kb and an f_{O_2} of QFM.

The geochemical evidence that RP8 basalts formed from crystallisation of a parental melt similar to the Winnipegosis komatiites is well supported by geological evidence which suggests there was extensive crystallisation of komatiitic magma in the upper crust near the supracrustal rocks of the WKB. It is inferred that basalts in the WKB are not the product of melting in cooler portions of a plume (Campbell *et al.*, 1989), but instead the product of upper crustal crystallisation of komatiitic magmas (Arndt *et al.*,

1977). Where komatiitic parental melts were able to rapidly ascend to the surface, komatiite flows were formed. However, if the komatiitic melts stalled, they fractionated extensively to form basalts. Eruption of homogeneous basalts may have been promoted by a density minimum at the point of plagioclase saturation (Sparks & Huppert, 1984), and/or efficient segregation of basaltic melt from cumulates after 60% crystallisation (Dufek & Bachmann, 2010).

This demonstration that basaltic compositions can form from crystallisation of komatiitic magmas in upper crustal magma chambers contradicts the suggestion that komatiites represent a different geochemical 'lineage' to tholeiites (e.g., Arndt & Brooks, 1980). In the case of the WKB, komatiites are a high MgO extreme endmember of the tholeiitic lineage. This model of basalt formation may also apply to other komatiite-tholeiite sequences, such as the d-basalts and G2 komatiites on the island of Gorgona (Kerr, 2005). Gorgona d-basalts have similar REE patterns to the G2 komatiites, with the exception of minor LREE/MREE enrichment, and like the Winnipegosis Komatiite Belt, there is compelling evidence of crustal differentiation of ultramafic magmas in the form of abundant dunite and wehrlite. Notably, like the Winnipegosis RP8 basalts, Gorgona d-basalts are also relatively Fe enriched. Combined with previous observations that tholeiites derived from fractionation of komatiite in the Archaean Abitibi greenstone belt are also Fe-rich (Arndt *et al.*, 1977), it is suggested that high Fe contents in basalts with low overall trace element concentrations may be indicative of their derivation from high degree melts such as komatiites.

Conclusions

The Winnipegosis Komatiite Belt

The Winnipegosis komatiites are exceptionally well preserved Palaeoproterozoic komatiites that have received little previous attention in the scientific literature. They occur in the Winnipegosis Komatiite Belt (WKB), a greenstone belt dominated by basalt and komatiite with no surface exposure. The WKB comprises part of the Circum-Superior Belt large igneous province, which formed along a convergent margin during destruction of the Palaeoproterozoic Manikewan Ocean, and was metamorphosed during the ∼1.8 Ga Trans-Hudson Orogen. Komatiites, basalts, and dunites from boreholes drilled during mineral exploration of the WKB were available for study in this thesis, along with zircon separates from a coarse gabbroic unit.

The majority of Winnipegosis komatiites erupted as massive olivine-porphyritic flows, though a few flows differentiated to form spinifex and cumulate layers. All komatiite flows intersected by borehole RP1A, and most flows intersected by borehole RP12, are massive. These contain only olivine and chromite as phenocryst phases, which are relatively evenly distributed throughout the depth profile of each flow. The groundmass comprises serpentinised skeletal and dendritic olivine, dendritic and spherulitic clinopyroxene, and devitrified glass in all samples. However, groundmass textures very significantly within individual flows, interpreted to reflect differences in cooling rate or degree of undercooling at the time of groundmass crystallisation. Differentiated flows are only found in borehole RP12, and show a range of textural and compositional variations, including hopper olivine cumulates, pyroxene phenocryst bearing layers, and olivine spinifex. The presence of massive and differentiated flows in the same sequence without significant geochemical differences between flow morphologies is interpreted as reflecting how far flows travelled before ponding and solidification. Komatiites from borehole RP1A are very well preserved, having only experienced sub-greenschist facies metamorphism, and are primarily altered around hydrous and carbonate veins. Ko-

matiites from borehole RP12 are more altered, and show a greenschist facies mineral assemblage. Dunites from borehole RP7 are completely serpentinised, and retain only chromite as a primary igneous mineral; igneous textures are difficult to discern. Basalts from borehole RP8 comprise a greenschist mineral assemblage with primary minerals and textures completely overprinted during metamorphism.

A large database of previously unpublished geochemical data ('GSC database') was used to assess the effects of metamorphic alteration on the komatiites. Threshold values of > 0.3 wt% CO_2 and > 4 wt% H_2O were chosen to exclude samples most affected by carbonate and hydrous veins, respectively. This database was also used to construct geochemical depth profiles through the boreholes studied in this thesis. In general, the komatiites, basalts, and dunites have uniform geochemical compositions and do not show systematic trends with depth in each borehole. The largest geochemical anomalies are associated with carbonate veining in boreholes RP1A and RP12, and the formation of differentiated flows in borehole RP12.

Tectonic model for the formation of Winnipegosis komatiites

New U-Pb SHRIMP dating of mafic zircons from a gabbroic unit in the WKB yielded an age of 1870.3 ± 7.1 Ma, justifying the inclusion of the WKB within the Circum-Superior Belt. Bulk rock compositions of the komatiites are generally arrayed along olivine (+ chromite) control lines. However, some incompatible elements have also been affected by crustal contamination and subsequent mobility during metamorphism. Trace element patterns are consistent with derivation from depleted mantle, though crustal contamination slightly enriched the komatiites in highly incompatible elements. The komatiites are classed as Al-undepleted, though some of their characteristics are transitional between Al-depleted and Al-undepleted komatiites.

A combination of Al-in-olivine thermometry and olivine-melt Fe-Mg partitioning indicates that the komatiite parental melts were dry, consistent with their derivation from depleted mantle. Parental melts contained 23.6 ± 1.6 wt% MgO, and had a liquidus temperature of 1501 ± 32 °C. Derivation from liquids with > 18 wt% MgO, a median MgO of 22.4 wt% over > 250 m thickness of flows, low phenocryst contents, and the presence of olivine spinifex textures in borehole RP12, means the Winnipegosis samples meet the definition of komatiites *sensu stricto*. Winnipegosis komatiite liquidus temperatures are ∼100 °C cooler than the hottest Archaean komatiites, and significantly cooler than the hottest Phanerozoic picrites. However, they likely still require

anomalously hot mantle and high degrees of melting. A tectonic model is proposed to account for above ambient mantle potential temperatures, the distribution of Circum-Superior magmatism along ∼3000 km of continental margin, and the unconformable emplacement of the WKB onto continental crust. It is suggested that Winnipegosis komatiites and broader Circum-Superior Belt magmatism are derived from a mantle plume that was deflected towards the margins of the Superior craton by strong gradients in lithospheric thickness. This plume model for the Circum-Superior Belt is incompatible with previous suggestions of ambient mantle potential temperatures as high as 1600 °C during the Proterozoic (Herzberg *et al.*, 2010).

Crystallisation of Winnipegosis komatiites and the link between komatiites, basalts, and dunites

Winnipegosis komatiites crystallised olivine alone from ∼1501 °C to approximately ∼1424 °C, and then a mixture of olivine and chromite phenocrysts until their eruption at ∼1321 °C. Bulk rock olivine control lines do not represent the komatiite LLD, but instead the mixing of this olivine and chromite phenocryst mixture with residual melts shortly before and/or during eruption. After eruption, crystallisation in the massive flows was largely restricted to skeletal overgrowths on olivine phenocrysts, and the formation of dendritic olivine and pyroxene. Some differentiated flows also crystallised augite phenocrysts, and plagioclase is a rare groundmass phase where cooling rates were low. The ability of MELTS thermodynamics software to model low pressure komatiite crystallisation is tested against these observations. MELTS successfully reproduces this crystallisation sequence and, in general, is able to successfully reproduce komatiite LLDs. Notable exceptions are FeO, which is overestimated due to errors in predicted olivine K_D, and CaO, which is underestimated due to MELTS overestimating CaO/MgO in clinopyroxene. The proportion of chromite crystallising is overestimated as MELTS does not allow incorporation of Cr_2O_3 in olivine, which represents ∼ 32% of the Cr_2O_3 budget of the phenocryst mixture, but this does not affect predicted LLDs.

The MELTS modelling is extended to higher pressures to investigate whether basalts in the WKB could have formed from extensive crystallisation of a komatiitic parental melt similar to the Winnipegosis komatiites. These basalts have similar REE patterns to Winnipegosis komatiites, albeit with higher absolute concentrations and slightly elevated LREE/MREE. The main effect predicted for crystallisation at higher pressures is to increase the gap in temperature and MgO between clinopyroxene and plagioclase

saturation. This leads to a greater degree of Al_2O_3 enrichment at basaltic MgO contents. Variations in f_{O_2} are also predicted to affect the gap in MgO between clinopyroxene and plagioclase saturation, with a 1 log unit decrease in f_{O_2} having a similar effect to a 0.5 kb increase in pressure of crystallisation. Varying pressure and f_{O_2} allows almost all aspects of the major and rare-earth element chemistry of basalts from borehole RP8 to be matched by ∼60% fractional crystallisation of a Winnipegosis komatiite-like parental melt. Best fit pressures are 1.5 kb at an oxygen fugacity of QFM – 1, to 2 kb at an oxygen fugacity of QFM, suggesting crystallisation at depths of ∼5.3 – 7.1 km.

Though it is difficult to geochemically rule out the possibility that tholeiitic basalts in the WKB formed from a lower degree parental melt than the komatiites, there is abundant geological evidence of extensive fractionation of komatiitic melts in the upper crust. A large, highly magnesian dunite body in the WKB is interpreted as a magma chamber filled by komatiitic cumulates, and its estimated palaeo-depth of ∼5.6 km at the time of RP8 basalt eruption is consistent with best fit fractionation depths from thermodynamic modelling. It is suggested that basalts and komatiites in the WKB formed from similar parental melts which underwent different amounts of fractional crystallisation before eruption (Arndt *et al.*, 1977), rather than representing different degrees of melting in a zoned plume (Campbell *et al.*, 1989). Komatiitic melts that were able to rise rapidly to the surface formed komatiite flows, whereas those that stalled in upper crustal magma chambers fractionated extensively to form tholeiitic basalts. The uniform composition of tholeiitic basalts in the WKB likely reflects homogenisation of melts in magma chambers caused by a density minimum at the point of plagioclase saturation (Sparks & Huppert, 1984), and/or efficient segregation of magma from cumulates after 60% crystallisation (Dufek & Bachmann, 2010). The demonstration that basalts can form from extensive crystallisation of komatiite confirms that komatiites are a high MgO, extreme endmember to the tholeiitic series. It is suggested that this model of basalt formation may also apply to other komatiite-tholeiite sequences, such as those found on the island of Gorgona (Kerr, 2005).

Komatiite PGEs and late accretion

Winnipegosis komatiite Re-Os isotope data lie on an isochron with age 1865 ± 40 Ma and γOs of – 0.2 ± 1.4 at the U-Pb age of 1870 ± 7 Ma. Re-Os and U-Pb ages for the WKB overlap within error, suggesting a similar formation age for basalts and komatiites in the WKB and demonstrating that Re and Os were undisturbed during

metamorphism. PGE systematics in most Winnipegosis komatiite samples show control by the primary magmatic phases olivine, chromite, residual melt, and Os-Ir alloy. One sample shows evidence of a Ru-rich phase with elevated Os/Ir, which is interpreted as evidence for laurite – $(Ru,Os,Ir)S_2$. The Winnipegosis komatiite parental melt is calculated to contain 1.1 ± 0.3 ppb Os, 0.91 ± 0.26 ppb Ir, 4.0 ± 0.5 ppb Ru, 7.0 ± 0.8 ppb Pt, 7.2 ± 0.7 ppb Pd, and 0.53 ± 0.06 ppb Re. The Pt and Pd contents corrected to 25 wt% MgO are low compared to Neoarchaean komatiites (Maier *et al.*, 2009), and comparable to Palaeoarchaean komatiites (Puchtel *et al.*, 2014).

Modelling mantle melting using the model of Mungall & Brenan (2014) can reproduce the Ru and Ir contents of Winnipegosis komatiites well, but Winnipegosis Pt and Pd contents are > 60% lower than predicted by geochemical modelling under any reasonable assumptions of melting conditions, melt fraction and source composition. Low Pd and Pt contents cannot be explained by melting of a source depleted in PGEs, and are unlikely to represent re-melting of a previously depleted source.

According to the current state of knowledge of PGE partitioning, Pt and Pd should be highly incompatible after sulphide exhaustion. Therefore, once sulphide exhaustion is reached in a komatiite mantle source, the PPGEs should be rapidly depleted, and further melting should cause a decrease in komatiite PPGE contents. A compilation of major element and PGE data from well preserved komatiites and picrites finds no evidence of this predicted decrease in PPGE concentrations with increasing degree of melting. Instead, there is a broad increase in Pd and Pt contents with indicators of degree of melting, suggesting Pt and Pd may be more compatible during high degree mantle melting than currently understood. It is speculated that the residual silicate mineral assemblage may exert an important control on the PGE contents of high degree melts. In this case, low PPGE concentrations in komatiites may reflect partial retention of PGEs in their mantle sources and differences in melting conditions, rather than evidence of low-PGE mantle generated by uneven late accretion (Maier *et al.*, 2009) and/or magma ocean differentiation (Puchtel *et al.*, 2014).

Further Work

The well preserved nature and unusual Proterozoic age of the Winnipegosis komatiites permits a number of avenues for further work that might not be possible with more altered typical Archaean komatiites, and may help provide insights into the temporal evolution of komatiite mantle sources. Suggestions for further work include:

- Measurement of trace, rare-earth, and platinum group elements in Winnipegosis olivine by ICP-MS. Much of the growing field of trace element analysis in olivine has been restricted to olivine which grew from lower temperature magmas with more enriched compositions (Foley *et al.*, 2013). However, most Archaean komatiites do not preserve sufficient fresh olivine to permit LA-ICP-MS analysis of trace elements with large laser spot sizes. These data could be used to test trace element partitioning models for olivine (Sun & Liang, 2013), determine the importance of olivine in bulk rock PGE budgets (Puchtel *et al.*, 2004; Pagé *et al.*, 2012), and investigate whether komatiites partition REEs in olivine differently to basalts (Arndt & Lesher, 1992).

- Measurement of the oxygen isotopes in Winnipegosis olivine by Secondary Ion Mass Spectroscopy (SIMS). Recent laser fluorination analyses of olivine from the Weltevreden komatiites has identified light oxygen isotope compositions, interpreted to reflect mantle heterogeneities generated in a Hadean magma ocean (Byerly *et al.*, 2017). However, the olivines analysed are small remnants in an extensively serpentinised komatiite, and are cut by numerous cracks. The abundance of fresh olivine in Winnipegosis komatiites, and smaller analytical spot size of SIMS compared to laser fluorination could allow a robust test of whether these anomalous oxygen isotopes reflect properties of the mantle source, or alteration of oxygen isotope compositions during metamorphism.

- Measurement of the lithophile isotope systematics (Lu-Hf, Sm-Nd, Rb-Sr, U-Pb) of Winnipegosis komatiites and associated basalts. These data could provide further constraints on the influence of crustal contamination on Winnipegosis trace element systematics (Chapter 2), and the relationship between tholeiitic basalts and komatiites in the WKB (Chapter 4). Conventional Lu-Hf and ^{147}Sm-^{143}Nd data could be used to provide additional constraints on how the depletion of komatiite sources has evolved throughout Earth history (Blichert-Toft & Puchtel, 2010), whereas the short lived ^{146}Sm-^{142}Nd system could be used to investigate whether early formed enriched and depleted reservoirs were able to survive into the Proterozoic (Rizo *et al.*, 2012).

- Analysis of the short lived ^{182}Hf-^{182}W systematics of Winnipegosis komatiites. Preliminary, unpublished work by Jingao Liu identified a positive ^{182}W anomaly in a single Winnipegosis komatiite sample. However, this sample was the most

altered sample analysed, and cut by a large carbonate vein. Less altered samples had insufficient W concentrations for analysis with the typical mass of sample powder used for W isotope analysis at the Arctic Resources Geochemistry Laboratory at the University of Alberta. Repeat analyses of less altered samples using larger total samples masses might allow a test of whether the ^{182}W anomaly was inherited from local Archaean basement during metamorphism, or is a primary feature of the Winnipegosis mantle source. If primary, the identification of ^{182}W anomalies in ∼1.9 Ga mantle would have significant implications for the preservation of early Earth mantle heterogeneities over geological timescales (Puchtel *et al.*, 2016a; Rizo *et al.*, 2016).

Bibliography

Aigner-Torres, M., Blundy, J., Ulmer, P., & Pettke, T. 2007. Laser Ablation ICPMS study of trace element partitioning between plagioclase and basaltic melts: An experimental approach. *Contributions to Mineralogy and Petrology*, **153**(6), 647–667.

Aitken, B. G., & Echeverría, L. M. 1984. Petrology and Geochemistry of Komatiites and Tholeiites from Gorgona-Island, Colombia. *Contributions to Mineralogy and Petrology*, **86**(1), 94–105.

Alard, O., Griffin, W. L., Lorand, J. P., Jackson, S. E., & O'Reilly, S. Y. 2000. Non-chondritic distribution of the highly siderophile elements in mantle sulphides. *Nature*, **407**(6806), 891–894.

Albarede, F. 1992. How deep do common basaltic magmas form and differentiate? *Journal of Geophysical Research*, **97**(B7), 10997.

Allegre, C. J. 1982. Genesis of Archaean komatiites in a wet ultramafic subducted plate. *Chap. 17, pages 495 – 500 of:* Arndt, N. T., & Nisbet, E. G. (eds), *Komatiites*. London: George Allen & Unwin.

Angerer, T., Kerrich, R., & Hagemann, S. G. 2013. Geochemistry of a komatiitic, boninitic, and tholeiitic basalt association in the Mesoarchean Koolyanobbing greenstone belt, Southern Cross Domain, Yilgarn craton: Implications for mantle sources and geodynamic setting of banded iron formation. *Precambrian Research*, **224**, 110–128.

Ansdell, K. M. 2005. Tectonic evolution of the Manitoba-Saskatchewan segment of the Paleoproterozoic Trans-Hudson Orogen, Canada. *Canadian Journal of Earth Sciences*, **42**(4), 741–759.

Ansdell, K. M., Lucas, S. B., Connors, K., & Stern, R. A. 1995. Kisseynew metasedimentary gneiss belt, Trans-Hudson orogen (Canada): back-arc origin and collisional inversion. *Geology*, **23**(11), 1039–1043.

Arndt, N., & Brooks, C. 1980. Komatiites. *Geology*, **8**, 155 – 156.

Arndt, N., Lesher, C. M., & Barnes, S. J. 2008. *Komatiite*. Cambridge: Cambridge University Press.

Arndt, N. T. 1982. Proterozoic spinifex-textured basalts of Gilmour Island, Hudson Bay. *Pages 137 – 142 of: Current Research, Part A, Geological Survey of Canada, Paper 82-1A*. Geological Survey of Canada.

Arndt, N. T. 1986. Differentiation of komatiite flows. *Journal of Petrology*, **27**(2), 279–301.

Arndt, N. T. 2003. Komatiites, kimberlites, and boninites. *Journal of Geophysical Research: Solid Earth*, **108**(B6), 1–11.

Arndt, N. T., & Fleet, M. E. 1979. Stable and metastable pyroxene crystallization in layered komatiite lava flows. *American Mineralogist*, **64**, 856–864.

Arndt, N. T., & Lesher, C. M. 1992. Fractionation of REEs by olivine and the origin of Kambalda komatiites, Western Australia. *Geochimica et Cosmochimica Acta*, **56**(12), 4191–4204.

Arndt, N. T., & Nesbitt, R. W. 1982. Geochemistry of Munro Township basalts. *Chap. 20, pages 309–330 of:* Arndt, N. T., & Nisbet, E. G. (eds), *Komatiites*. London: George Allen & Unwin.

Arndt, N. T., & Nisbet, E. G. 1982. What is a komatiite? *Chap. 2, pages 19 – 27 of:* Arndt, N. T., & Nisbet, E. G. (eds), *Komatiites*. London: George Allen & Unwin.

Arndt, N. T., Naldrett, A. J., & Pyke, D. R. 1977. Komatiitic and iron-rich tholeiitic lavas of munro township, Northeast Ontario. *Journal of Petrology*, **18**(2), 319–369.

Arndt, N. T., Brugmann, G. E., Lehnert, K., Chauvel, C., & Chappell, B. W. 1987. Geochemistry, petrogenesis and tectonic environment of Circum- Superior Belt basalts, Canada. Geological Society Special Publications No. 33. *Pages 133–145 of: Geochemistry and Mineralization of Proterozoic Volcanic Suites*. Blackwell Scientific Publications.

Arndt, N. T., Ginibre, C., Chauvel, C., Albarede, F., Cheadle, M., Herzberg, C., Jenner, G., & Lahaye, Y. 1998. Were komatiites wet? *Geology*, **26**(8), 739–742.

Asafov, E.V., Sobolev, A.V., Gurenko, A.A., Arndt, N.T., Batanova, V.G., Portnyagin, M.V., Garbe-Schonberg, D., & Krasheninnikov, S.P. 2017. Belingwe komatiites (2.7Ga) originate from a plume with moderate water content, as inferred from inclusions in olivine. *Chemical Geology*.

Asimow, P. D., & Longhi, J. 2004. The significance of multiple saturation points in the context of polybaric near-fractional melting. *Journal of Petrology*, **45**(12), 2349–2367.

Asimow, P. D., Dixon, J. E., & Langmuir, C. H. 2004. A hydrous melting and fractionation model for mid-ocean ridge basalts: Application to the Mid-Atlantic Ridge near the Azores. *Geochemistry, Geophysics, Geosystems*, **5**(1), 1–24.

Aulbach, S., Mungall, J. E., & Pearson, D. G. 2015. Distribution and processing of Highly Siderophile Elements in Cratonic Mantle Lithosphere. *Reviews in Mineralogy and Geochemistry*, **81**, 293 – 303.

Bailey, E. B., & McCalien, W. J. 1953. Serpentine lavas, the Ankara Melange and the Anatolian Thrust. *Transactions of the Royal Society of Edinburgh*, **62**(11), 403 – 442.

Baldwin, D. A., Syme, E. C., Zwanzig, H. V., Gordon, T. M., Hunt, P. A., & Stevens, R. D. 1987. U-Pb zircon ages from the Lynn Lake and Rusty Lake metavolcanic belts, Manitoba: two ages of Proterozoic magmatism. *Canadian Journal of Earth Sciences*, **24**(5), 1053–1063.

Ballhaus, C. 1995. Is the upper mantle metal-saturated? *Earth and Planetary Science Letters*, **132**(1-4), 75–86.

Ballhaus, C., Berry, R. F., & Green, D. H. 1991. High pressure experimental calibration of the olivine-orthopyroxene-spinel oxygen geobarometer: implications for the oxidation state of the upper mantle. *Contributions to Mineralogy and Petrology*, **107**(1), 27–40.

Balta, J. B., & McSween, H. Y. 2013. Application of the MELTS algorithm to martian compositions and implications for magma crystallization. *Journal of Geophysical Research E: Planets*, **118**(12), 2502–2519.

Baragar, W. R. A., & Scoates, R. F. J. 1981. The Circum-Superior Belt: A Proterozoic plate margin? *Chap. 12, pages 297 – 330 of:* Kroner, A. (ed), *Developments in Precambrian Geology*, vol. 4. Elsevier.

Barnes, S. J. 1986. The distribution of chromium among orthopyroxene, spinel and silicate liquid at atmospheric pressure. *Geochimica et Cosmochimica Acta*, **50**(9), 1889–1909.

Barnes, S. J. 1998. Chromite in Komatiites , 1. Magmatic Controls on Crystallization and Composition. *Journal of Petrology*, **39**(10), 1689–1720.

Barnes, S. J., & Fiorentini, M. L. 2008. Iridium, ruthenium and rhodium in komatiites: Evidence for iridium alloy saturation. *Chemical Geology*, **257**(1-2), 44–58.

Barnes, S.-J., & Often, M. 1990. Ti-rich komatiites from northern Norway. *Contributions to Mineralogy and Petrology*, **105**(1), 42–54.

Barnes, S. J., & Picard, C. P. 1993. The Behavior of Platinum-Group Elements during Partial Melting, Crystal Fractionation, and Sulfide Segregation - an Example from the Cape-Smith Fold Belt, Northern Quebec. *Geochimica et Cosmochimica Acta*, **57**(1), 79–87.

Barnes, S.-J., Naldrett, A. J., & Gorton, M. P. 1985. The origin of the fractionation of platinum-group elements in terrestrial magmas. *Chemical Geology*, **53**(3-4), 303–323.

Barnes, S. J., Hill, R. E. T., & Gole, M. J. 1988. The Perseverance ultramafic complex, Western Australia: The product of a komatiite lava river. *Journal of Petrology*, **29**(2), 305–331.

Barnes, S. J., Mungall, J. E., & Maier, W. D. 2015. Platinum group elements in mantle melts and mantle samples. *Lithos*, **232**, 395–417.

Batanova, V. G., Sobolev, A. V., & Kuzmin, D. V. 2015. Trace element analysis of olivine: High precision analytical method for JEOL JXA-8230 electron probe microanalyser. *Chemical Geology*, **419**, 149–157.

Bau, M. 1991. Rare-Earth Element Mobility During Hydrothermal and Metamorphic Fluid Rock Interaction and the Significance of the Oxidation-State of Europium. *Chemical Geology*, **93**(3-4), 219–230.

Becker, H., Horan, M. F., Walker, R. J., Gao, S., Lorand, J. P., & Rudnick, R. L. 2006. Highly siderophile element composition of the Earth's primitive upper mantle: Constraints from new data on peridotite massifs and xenoliths. *Geochimica et Cosmochimica Acta*, **70**(17), 4528–4550.

Bedard, J. H. 2017. Stagnant lids and mantle overturns: Implications for Archaean tectonics, magmagenesis, crustal growth, mantle evolution, and the start of plate tectonics. *Geoscience Frontiers*.

Bernstein, S., Kelemen, P. B., & Hanghøj, K. 2007. Consistent olivine Mg# in cratonic mantle reflects Archean mantle melting to the exhauston of orthopyroxene. *Geology*, **35**(5), 459–462.

Berry, A. J., Danyushevsky, L. V., O'Neill, H. St. C., Newville, M., & Sutton, S. R. 2008. Oxidation state of iron in komatiitic melt inclusions indicates hot Archaean mantle. *Nature*, **455**(7215), 960–963.

Bickle, M. J. 1982. The magnesium content of komatiitic liquids. *Chap. 27, pages 479 – 494 of:* Arndt, N. T., & Nisbet, E. G. (eds), *Komatiites*. London: George Allen & Unwin.

Bickle, M. J., Martin, A., & Nisbet, E. G. 1975. Basaltic and peridotitic komatiites and stromatolites above a basal unconformity in the Belingwe Greenstone Belt, Rhodesia. *Earth and Planetary Science Letters*, **27**, 155–162.

Bickle, M. J., Nisbet, E. G., & Martin, A. 1994. Archean Greenstone Belts Are Not Oceanic Crust. *The Journal of Geology*, **102**(2), 121–137.

Bickle, M.J., Hawkesworth, C.J., Martin, A., Nisbet, E.G., & O'Nions, R.K. 1976. Mantle composition derived from the chemistry of ultramafic lavas. *Nature*, **263**, 577 – 580.

Birck, J. L., Roy Barman, M.R., & Capmas, F. 1997. Re-Os Isotopic Measurements at the Femtomole Level in Natural Samples. *Geostandards Newsletter*, **20**(6), 19 – 27.

Blichert-Toft, J., & Puchtel, I. S. 2010. Depleted mantle sources through time: Evidence from {L}u-{H}f and {S}m-{N}d isotope systematics of {A}rchean komatiites. *Earth and Planetary Science Letters*, **297**(3-4), 598–606.

Bowen, N. L. 1927. The origin of ultra-basic and related rocks. *American Journal of Science*, **14**(80), 89 – 108.

Bowles, J. F. W., Atkin, D., Lambert, J. L. M., & Phillips, R. 1983. The chemistry, reflectance ,and cell size of the erlichmanite (OsS_2)-laurite (RuS_2) series. *Mineralogical Magazine*, **47**, 465 – 471.

Brandon, A. D., Walker, R. J., Puchtel, I. S., Becker, H., Humayun, M., & Revillon, S. 2003. ^{186}Os-^{187}Os systematics of Gorgona Island komatiites: implications for early growth of the inner core. *Earth and Planetary Science Letters*, **206**, 411–426.

Brenan, J. M., McDonough, W. F., & Ash, R. 2005. An experimental study of the solubility and partitioning of iridium, osmium and gold between olivine and silicate melt. *Earth and Planetary Science Letters*, **237**(3-4), 855–872.

Brooks, C., & Hart, S. R. 1974. On the Significance of Komatiite. *Geology*, **2**, 107–110.

Bruce, E. L. 1926. Geology of McArthur, Bartlett, Douglas and Geikie townships (Redstone River area), District of Timiskaming. *Pages 37–56 of: Ontario Department of Mines Annual Report 35 Part VI*. Toronto: Printers to the King's Most Excellent Majesty.

Brügmann, G. E., Arndt, N. T., Hofmann, A. W., & Tobschall, H. J. 1987. Noble metal abundances in komatiite suites from Alexo, Ontario and Gorgona Island, Colombia. *Geochimica et Cosmochimica Acta*, **51**(8), 2159–2169.

Burnham, O. M., Halden, N., Layton-Mathews, D., Lesher, C. M., Liwanag, J., Heaman, L., Hulbert, L., Machado, N., Michalak, D., Pacey, M., Peck, D. C., Potrel, A., Theyer, P., Toope, K., & Zwanzig, H. V. 2009. *CAMIRO Project 97E-02, Thompson Nickel Belt: final report March 2002, revised and updated 2003*. Tech. rept. Manitoba Geological Survey.

Byerly, B. L., Kareem, K., Bao, H., & Byerly, G. R. 2017. Early Earth mantle heterogeneity revealed by light oxygen isotopes of Archaean komatiites. *Nature Geoscience*, **10**(11), 871–875.

Cameron, W. E., Nisbet, E. G., & Dietrich, V. J. 1979. Boninites, komatiites and ophiolitic basalts. *Nature*, **280**, 550 – 553.

Campbell, I. H., & Davies, D. R. 2017. Raising the continental crust. *Earth and Planetary Science Letters*, **460**, 112–122.

Campbell, I. H., & Griffiths, R. W. 1990. Implications of mantle plume structure for the evolution of flood basalts. *Earth and Planetary Science Letters*, **99**, 79–93.

Campbell, I. H., & Griffiths, R. W. 2014. Did the formation of DPrime; cause the Archaean-Proterozoic transition? *Earth and Planetary Science Letters*, **388**, 1–8.

Campbell, I. H., Griffiths, R. W., & Hill, R. I. 1989. Melting in an Archaean mantle plume: heads it's basalts, tails it's komatiites. *Nature*, **342**, 189–92.

Cann, J. R. 1970. Rb, Sr, Y, Zr and Nb in some ocean floor basaltic rocks. *Earth and Planetary Science Letters*, **10**(1), 7–11.

Chou, C.-L. 1978. Fractionation of siderophile elements in the earth's upper mantle. *Pages 219 – 230 of: Procedings of the 9th Lunar and Planetary Science Conference.*

Ciborowski, T. J. R., Minifie, M. J., Kerr, A. C., Ernst, R. E., Baragar, B., & Millar, I. L. 2017. A mantle plume origin for the Palaeoproterozoic Circum-Superior Large Igneous Province. *Precambrian Research*, **294**, 189–213.

Cohen, A. S., & Waters, F. G. 1996. Separation of osmium from geological materials by solvent extraction for analysis by thermal ionisation mass spectrometry. *Analytica Chimica Acta*, **332**(2-3), 269–275.

Condie, K. C., & O'Neill, C. 2010. The Archean-Proterozoic boundary: 500 MY of tectonic transition in Earth history. *American Journal of Science*, **310**, 775–790.

Connolly, B. D., Puchtel, I. S., Walker, R. J., Arevalo, R., Piccoli, P. M., Byerly, G., Robin-Popieul, C. C. M., & Arndt, N. T. 2011. Highly siderophile element systematics of the 3.3Ga Weltevreden komatiites, South Africa: Implications for early Earth history. *Earth and Planetary Science Letters*, **311**(3-4), 253–263.

Coogan, L. A., Saunders, A. D., & Wilson, R. N. 2014. Aluminum-in-olivine thermometry of primitive basalts: Evidence of an anomalously hot mantle source for large igneous provinces. *Chemical Geology*, **368**(0), 1–10.

Corrigan, D. 2012. Paleoproterozoic crustal evolution and tectonic process: Insights from the Lithoprobe program in the Trans Hudson Orogen, Canada. *Chap. 4, pages 237 – 284 of:* Percival, J. A., Cook, F. A., & Clowes, R. M. (eds), *Special Paper 49. Tectonic styles in Canada: The Lithoprobe perspective.* Geological Association of Canada.

Corrigan, D., Pehrsson, S., Wodicka, N., & de Kemp, E. 2009. The Palaeoproterozoic Trans-Hudson Orogen: a prototype of modern accretionary processes. *Pages 457–479 of:* Murphy, J. B., Keppie, J. D., & Hynes, A. J. (eds), *Geological Society, London, Special Publications.* Special Publications, vol. 327, no. 327 (1). Geological Society, London.

Cox, M. G. C. 1983. Experimental Determination of X-ray Intensities. *Pages 125 – 146 of:* Scott, V. D., & Love, G. (eds), *Quantitative Electron-Probe Microanalysis.* Chichester: Ellis Horwood Limited.

Dale, C. W., Burton, K. W., Pearson, D. G., Gannoun, A., Alard, O., Argles, T. W., & Parkinson, I. J. 2009. Highly siderophile element behaviour accompanying subduction of oceanic crust: whole rock and mineral-scale insights from a high-pressure terrain. *Geochemistry, Geophysics, Geosystems*, **73**(5), 1394 – 1416.

Dann, J. C. 2000. The 3.5 Ga Komati Formation, Barberton Greenstone Belt, South Africa, Part I: New maps and magmatic architecture. *South African Journal of Geology*, **103**(1), 47–68.

David, J., Bailes, A. H., & Machado, N. 1996. Evolution of the Snow Lake portion of the Palaeoproterozoic Flin Flon and Kisseynew belts, Trans-Hudson Orogen, Manitoba, Canada. *Precambrian Research*, **80**(1-2), 107–124.

Davies, G. F. 1999. *Plates, Plumes and Mantle Convection*. Cambridge: Cambridge University Press.

de Wit, M. J. 1998. On Archean granites, greenstones, cratons and tectonics: does the evidence demand a verdict? *Precambrian Research*, **91**(1-2), 181–226.

de Wit, M. J., Hart, R. A., & Hart, R. J. 1987. The Jamestown Ophiolite Complex, Barberton mountain belt: a section through 3.5 Ga oceanic crust. *Journal of African Earth Sciences*, **6**(5), 681–730.

Deer, W. A., Howie, R. A., & Zussman, J. 1992. *An introduction to the rock forming minerals*. 2nd edition edn. Harlow: Pearson Education.

Ding, S., & Dasgupta, R. 2017. The fate of sulfide during decompression melting of peridotite – implications for sulfur inventory of the MORB-source depleted upper mantle. *Earth and Planetary Science Letters*, **459**(1), 183 – 195.

Dixon, J. E., Leist, L., Langmuir, C., & Schilling, J.-G. 2002. Recycled dehydrated lithosphere observed in plume-influenced mid-ocean-ridge basalt. *Nature*, **420**(6914), 385–389.

Donaldson, C. H. 1976. An Experimental Investigation of Olivine Morphology. *Contributions to Mineralogy and Petrology*, **57**, 187–213.

Donaldson, C. H. 1982. Spinifex-textured komatiites: a review of textures, compositions and layering. *Chap. 16, pages 213–244 of:* Arndt, N. T., & Nisbet, E. G. (eds), *Komatiites*. London: George Allen & Unwin.

Donaldson, J. A., & De Kemp, E. A. 1998. Archaean quartz arenites in the Canadian Shield: examples from the Superior and Churchill Provinces. *Sedimentary Geology*, **120**(1-4), 153–176.

Droop, G. T. R. 1987. A general equation for estimating Fe3+ concentrations in ferromagnesian silicates and oxides from microprobe analyses , using stoichiometric criteria. *Mineralogical Magazine*, **51**, 431 – 435.

Dufek, J., & Bachmann, O. 2010. Quantum magmatism: Magmatic compositional gaps generated by melt-crystal dynamics. *Geology*, **38**(8), 687–690.

Echeverria, L. M. 1980. Tertiary or Mesozoic komatiites from Gorgona Island, Colombia: Field relations and geochemistry. *Contributions to Mineralogy and Petrology*, **73**(3), 253–266.

Ernst, R., & Bleeker, W. 2010. Large igneous provinces (LIPs), giant dyke swarms, and mantle plumes: significance for breakup events within Canada and adjacent regions from 2.5 Ga to the Present. *Canadian Journal of Earth Sciences*, **47**(5), 695–739.

Evans, B. W., & Frost, B. R. 1975. Chrome-Spinel in Progressive Metamorphism - Preliminary Analysis. *Geochimica et Cosmochimica Acta*, **39**(6-7), 959–972.

Falloon, T. J., & Danyushevsky, L. V. 2000. Melting of Refractory Mantle at 1.5, 2 and 2.5 GPa under Anhydrous and H_2O-undersaturated Conditions: Implications for the Petrogenesis of High-Ca Boninites and the Influence of Subduction Components on Mantle Melting. *J. Petrol.*, **41**(2), 257–283.

Faure, F., & Tissandier, L. 2014. Contrasted Liquid Lines of Descent Revealed by Olivine-hosted Melt Inclusions and the External Magma. *Journal of Petrology*, **9**(0), 1779–1798.

Faure, F., Trolliard, G., Nicollet, C., & Montel, J.-M. 2003. A developmental model of olivine morphology as a function of the cooling rate and the degree of undercooling. *Contributions to Mineralogy and Petrology*, **145**(2), 251–263.

Faure, F., Arndt, N. I., & Libourel, G. 2006. Formation of spinifex texture in komatiites: An experimental study. *Journal of Petrology*, **47**(8), 1591–1610.

Fiorentini, M. L., Barnes, S. J., Maier, W. D., Burnham, O. M., & Heggie, G. 2011. Global Variability in the Platinum-group Element Contents of Komatiites. *Journal of Petrology*, **52**(1), 83–112.

Foley, S. F., Prelevic, D., Rehfeldt, T., & Jacob, D. E. 2013. Minor and trace elements in olivines as probes into early igneous and mantle melting processes. *Earth and Planetary Science Letters*, **363**, 181–191.

Francis, D. 1985. The Baffin Bay lavas and the value of picrites as analogues of primary magmas. *Contributions to Mineralogy and Petrology*, **89**(2-3), 144–154.

Furnes, H., de Wit, M., & Robins, B. 2013. A review of new interpretations of the tectonostratigraphy, geochemistry and evolution of the Onverwacht Suite, Barberton Greenstone Belt, South Africa. *Gondwana Research*, **23**(2), 403–428.

Gale, A., Dalton, C. A., Langmuir, C. H., Su, Y., & Schilling, J.-G. 2013. The mean composition of ocean ridge basalts. *Geochemistry, Geophysics, Geosystems*, **14**(3), 489–518.

Gansser, A., Dietrich, V. J., & Cameron, W. E. 1979. Paleogene komatiites from Gorgona Island. *Nature*, **278**, 545 – 546.

Garcia, M. O., Foss, D. J. P., West, H. B., & Mahoney, J. J. 1995. Geochemical and isotopic evolution of Loihi Volcano, Hawaii. *Journal of Petrology*, **36**(6), 1647–1674.

Geo Labs. 2001. *OKUM (Ontario Komatiite Ultramafic) Geo Lab's in-house reference material.* Tech. rept. Ontario Geological Survey, Sudbury, ON, Canada.

Ghiorso, M. S. 1997. Thermodynamic Models of Igneous processes. *Annual Reviews in Earth and Planetary Science*, **25**, 221 – 241.

Ghiorso, M. S., & Gualda, G. A.R. 2015. An H_2O-CO_2 mixed fluid saturation model compatible with rhyolite-MELTS. *Contributions to Mineralogy and Petrology*, **169**(6), 1–30.

Ghiorso, M. S., & Sack, R. O. 1995. Chemical masstransfer in magmaticprocesses IV. A revised and internally consistent thermodynamic model for the interpolation and extrapolation of liquid-solidequilibria in magmatic systems at elevated temperatures and pressures. *Contribution Mineralogy Petrology*, **119**, 197–212.

Goldstein, J., Newbury, D., Joy, D., Lyman, C., Echlin, P., Lifshin, E., Sawyer, L., & Michael, J. 2003. *Scanning Electron Microscopy and X-Ray Microanalysis.* 3rd edition edn. New York: Springer Science + Business.

Gole, M. J., Barnes, S. J., & Hill, R. E. T. 1990. Partial melting and recrystallization of Archeaan komatiites by residual heat from rapidly accumulated flows. *Contributions to Mineralogy and Petrology*, **105**(6), 704–714.

González-Jiménez, J. M., Gervilla, F., Proenza, J. A., Kerestedjian, T., Augé, T., & Bailly, L. 2009. Zoning of laurite (RuS_2)–erlichmanite (OsS_2): implications for the origin of PGM in ophiolite chromitites. *European Journal of Mineralogy*, **21**(2), 419–432.

Green, D. H. 1972. Archaean greenstone belts may include terrestrial equivalents of lunar maria? *Earth and Planetary Science Letters*, **15**, 263–270.

Green, D. H. 1975. Genesis of Archean peridotitic magmas and constraints on Archean geothermal gradients and tectonics. *Geology*, **3**(1), 15–18.

Green, D. H., Nicholls, I. A., Viljoen, M. J., & Viljoen, R. P. 1975. Experimental Demonstration of the Existence of Peridotitic Liquids in Earliest Archean Magmatism. *Geology*, **3**(1), 11–14.

Grove, T. L., & Parman, S. W. 2004. Thermal evolution of the {E}arth as recorded by komatiites. *Earth and Planetary Science Letters*, **219**(3-4), 173–187.

Gualda, G. A. R., Ghiorso, M. S., Lemons, R. V., & Carley, T. L. 2012. Rhyolite-MELTS: A modified calibration of MELTS optimized for silica-rich, fluid-bearing magmatic systems. *Journal of Petrology*, **53**(5), 875–890.

Gurenko, A. A., Kamenetsky, V. S., & Kerr, A. C. 2016. Oxygen isotopes and volatile contents of the Gorgona komatiites, Colombia: A confirmation of the deep mantle origin of H_2O. *Earth and Planetary Science Letters*, **454**, 154–165.

Gurriet, P. C. 1988. *Geochemistry of Hawaiian dredged lavas*. M.Phil. thesis, Massachussets Institute of Technology.

Hampel, F. R. 1974. The Influence Curve and its Role in Robust Estimation. *Journal of the American Statistical Association*, **69**(346), 383–393.

Hanski, E., Huhma, H., Rastas, P., & Kamenetsky, V. S. 2001. The Palaeoproterozoic Komatiite - Picrite Association of Finnish Lapland. *Journal of Petrology*, **42**(5), 855–876.

Hanski, E., Walker, R. J., Huhma, H., Polyakov, G. V., Balykin, P. A., Hoa, T. T., & Phuong, N. T. 2004. Origin of the Permian-Triassic komatiites, northwestern Vietnam. *Contributions to Mineralogy and Petrology*, **147**(4), 453–469.

Heaman, L. M., Machado, N., Krogh, T. E., & Weber, W. 1986. Precise U-Pb zircon ages for the Molson dyke swarm and the Fox River sill: Constraints for Early Proterozoic crustal evolution in northeastern Manitoba, Canada. *Contributions to Mineralogy and Petrology*, **94**(1), 82–89.

Heaman, L. M., Peck, D., & Toope, K. 2009. Timing and geochemistry of 1.88 Ga Molson Igneous Events, Manitoba: Insights into the formation of a craton-scale magmatic and metallogenic province. *Precambrian Research*, **172**(1-2), 143–162.

Herzberg, C. 2004. Geodynamic information in peridotite petrology. *Journal of Petrology*, **45**(12), 2507–2530.

Herzberg, C., & O'Hara, M. J. 2002. Plume-Associated Ultramafic Magmas of Phanerozoic Age. *Journal of Petrology*, **43**(10), 1857–1883.

Herzberg, C., Condie, K., & Korenaga, J. 2010. Thermal history of the Earth and its petrological expression. *Earth and Planetary Science Letters*, **292**(1-2), 79–88.

Herzberg, C. T., & Asimow, P. D. 2015. PRIMELT3 MEGA.XLSM software for primary magma calculation: Peridotite primary magma MgO contents from the liquidus to the solidus. *Geochemistry, Geophysics, Geosystems*, **16**, 563–578.

Hofmann, A. W. 1988. Chemical differentiation of the Earth: the relationship between mantle, continental crust, and oceanic crust. *Earth and Planetary Science Letters*, **90**(3), 297–314.

Hollings, P., & Ansdell, K. 2002. Paleoproterozoic arc magmatism imposed on an older backarc basin: Implications for the tectonic evolution of the Trans-Hudson orogen, Canada. *GSA Bulletin*, **114**(2), 153–168.

Hollings, P., Wyman, D., & Kerrich, R. 1999. Komatiite-basalt-rhyolite volcanic associations in Northern Superior Province greenstone belts: significance of plume-arc interaction in the generation of the proto continental Superior Province. *Lithos*, **46**(1), 137–161.

Hon, K., Kauahikaua, J., Denlinger, R., & Mackay, K. 1994. Emplacement and inflation of pahoehoe sheet flows: observations and measurements of active lava flows on Kilauea volcano, Hawaii. *Geological Society of America Bulletin*, **106**(3), 351–370.

Horan, M. F., Walker, R. J., Morgan, J. W., Grossman, J. N., & Rubin, A. E. 2003. Highly siderophile elements in chondrites. *Chemical Geology*, **196**, 5–20.

Hosain, I. T., & Bamburak, J. D. 2002. Interpretation of Thompson-type geophysical signatures (NTS 63B and 63F) and the possible cause of the Camperville gravity low (NTS 62N and 63C), West-central Manitoba. *Pages 117–130 of: Report of Activities 2002*. Manitoba Industry, Trade and Mines, Manitoba Geological Survey.

Hronsky, J. M. A., & Schodde, R. C. 2006. Nickel exploration history of the {Yilgarn Craton}: from the Nickel boom to today. *Society of Economic Geologists Special Publication*, **13**, 1–11.

Hulbert, L., Stern, R., Kyser, T. K., Pearson, J., Lesher, M., & Grinenko, L. 1994. The Winnipegosis komatiite belt, central Manitoba. *Page 21 of: Manitoba Mining and Minerals Convention 1994, Program and Abstracts*. Manitoba Energy and Mines.

Hulbert, L. J., Hamilton, M. A., Horan, M. F., & Scoates, R. F. J. 2005. U-Pb zircon and Re-Os isotope geochronology of mineralized ultramafic intrusions and associated nickel ores from the Thompson Nickel Belt, Manitoba, Canada. *Economic Geology*, **100**(1), 29–41.

Huppert, H. E., & Sparks, R. S. J. 1985. Komatiites I: Eruption and flow. *Journal of Petrology*, **26**(3), 694–725.

Huppert, H. E., Sparks, R. S. J., Turner, J. Stewart, & Arndt, N. T. 1984. Emplacement and cooling of komatiite lavas. *Nature*, **309**, 19–22.

Hynes, A., & Francis, D. M. 1982. A transect of the early Proterozoic Cape Smith foldbelt, New Quebec. *Tectonophysics*, **88**, 23–59.

IAG. 2015. *IAG Certified Reference Materials*. http://www.iageo.com/index.php/certified-reference-materials.html.

Ireland, T. J., Walker, R. J., & Garcia, M. O. 2009. Highly siderophile element and ^{187}Os isotope systematics of Hawaiian picrites: Implications for parental melt composition and source heterogeneity. *Chemical Geology*, **260**(1-2), 112–128.

JCGM. 2012. *JCGM 200:2012 International vocabulary of metrology – Basic and general concepts and associated terms (VIM).* Tech. rept. International Organization for Standardization, Geneva.

Jensen, L. S. 1982. Stratigraphy and petrogenesis of Archaean metavolcanic sequences, southwestern Abitibi Subprovince, Ontario. *Chap. 6, pages 65 – 87 of:* Ayers, L. D., Thurston, P. C., Card, K. D., & Weber, W. (eds), *Evolution of Archaean Supracrustal Sequences. Geological Association of Canada special paper; 28.* St John's: George Allen & Unwin.

Jolly, W. T. 1982. Progressive metamorphism of komatiites and related Archaean lavas of the Abitibi area, Canada. *Chap. 17, pages 247 – 266 of:* Arndt, N. T., & Nisbet, E. G. (eds), *Komatiites.* London: George Allen & Unwin.

Kamenetsky, V. S., Gurenko, A. A., & Kerr, A. C. 2010. Composition and temperature of komatiite melts from Gorgona Island, Colombia, constrained from olivine-hosted melt inclusions. *Geology*, **38**(11), 1003–1006.

Kamenetsky, V. S., Park, J. W., Mungall, J. E., Pushkarev, E. V., Ivanov, A. V., Kamenetsky, M. B., & Yaxley, G. M. 2015. Crystallization of platinum-group minerals from silicate melts: Evidence from Cr-spinel-hosted inclusions in volcanic rocks. *Geology*, **43**(10), 903–906.

Kawamoto, T., Hervig, R. L., & Holloway, J. R. 1996. Experimental evidence for a hydrous transition zone in the early Earth's mantle. *Earth and Planetary Science Letters*, **142**(3-4), 587–592.

Keays, R. R. 1982. Palladium and Iridium in komatiites and associated rocks: application to petrogenetic problems. *Chap. 25, pages 435 – 457 of:* Arndt, N. T., & Nisbet, E. G. (eds), *Komatiites.* London: George Allen & Unwin.

Keller, C. B., & Schoene, B. 2012. Statistical geochemistry reveals disruption in secular lithospheric evolution about 2.5 Gyr ago. *Nature*, **485**(7399), 490–493.

Keller, C. B., & Schoene, B. 2018. Plate tectonics and continental basalt geochemistry throughout Earth history. *Earth and Planetary Science Letters*, **481**, 290–304.

Kerr, A. C. 2005. La Isla de Gorgona, Colombia: A petrological enigma? *Lithos*, **84**(1-2), 77–101.

Kerr, A. C., & Arndt, N. T. 2001. A Note on the IUGS Reclassification of the High-Mg and Picritic Volcanic Rocks. *Journal of Petrology*, **42**(11), 2169–2171.

Kerr, A. C., Marriner, G. F., Arndt, N. T., Tarney, J., Nivia, A., Saunders, A. D., & Duncan, R. A. 1996. The petrogenesis of Gorgona komatiites, picrites and basalts: new field, petrographic and geochemical constraints. *Lithos*, **37**(2-3), 245–260.

Kerrich, R., Wyman, D. A., Fan, J., & Bleeker, W. 1998. Boninite series: Low Ti-tholeiite associations from the 2.7 Ga Abitibi greenstone belt. *Earth and Planetary Science Letters*, **164**(1-2), 303–316.

Kincaid, C., Druken, K. A., Griffiths, R. W., & Stegman, D. R. 2013. Bifurcation of the Yellowstone plume driven by subduction-induced mantle flow. *Nature Geoscience*, **6**(5), 395–399.

Kinzler, R. J., & Grove, T. L. 1985. Crystallization and differentiation of Archean komatiite lavas from northeast Ontario : phase equilibrium and kinetic studies. *American Mineralogist*, **70**, 40–51.

Klein, E. M., & Langmuir, C. H. 1987. Global correlation of ocean ridge basalt chemistry with axial depth and crustal thickness. *Journal of Geophysical Research*, **92**, 8089–8115.

Köhler, T. P., & Brey, G. P. 1990. Calcium exchange between olivine and clinopyroxene calibrated as a geothermobarometer for natural peridotites from 2 to 60 kb with applications. *Geochimica et Cosmochimica Acta*, **54**(9), 2375–2388.

Kress, V. C., & Carmichael, I. S. E. 1991. The compressibility of silicate liquids containing Fe_2O_3 and the effect of composition, temperature, oxygen fugacity and pressure on their redox states. *Contributions to Mineralogy and Petrology*, **108**(1-2), 82–92.

Lahaye, Y., & Arndt, N. T. 1996. Alteration of a Komatiite Flow from Alexo, Ontario, Canada. *Journal of Petrology*, **37**(6), 1261–1284.

Lajoie, J., & Gelinas, L. 1978. Emplacement of Archean peridotitic komatiites in La Motte township, Quebec. *Canadian Journal of Earth Sciences*, **15**(1973), 672–677.

Lange, R. A. 2002. Constraints on the preeruptive volatile concentrations in the Columbia River flood basalts. *Geology*, **30**(2), 179–182.

Larsen, L. M., & Pedersen, A. K. 2000. Processes in High-Mg, High-T Magmas: Evidence from Olivine, Chromite and Glass in Palaeogene Picrites from West Greenland. *Journal of Petrology*, **41**(7), 1071–1098.

Larsen, L. M., Pedersen, A. K., Tegner, C., Duncan, R. A., Hald, N., & Larsen, J. G. 2016. Age of Tertiary volcanic rocks on the West Greenland continental margin: volcanic evolution and event correlation to other parts of the North Atlantic Igneous Province. *Geological Magazine*, **153**(3), 487–511.

Lassiter, J. C. 2003. Rhenium volatility in subaerial lavas: Constraints from subaerial and submarine portions of the HSDP-2 Mauna Kea drillcore. *Earth and Planetary Science Letters*, **214**(1-2), 311–325.

Le Bas, M. J. 2000. IUGS reclassification of the high-Mg and picritic volcanic rocks. *Journal of Petrology*, **41**(10), 1467–1470.

Lee, C.-T. A., Leeman, W. P., Canil, D., & Li, Z.-X. A. 2005. Similar V/Sc Systematics in MORB and Arc Basalts: Implications for the Oxygen Fugacities of their Mantle Source Regions. *Journal of Petrology*, **46**(11), 2313–2336.

Lee, C. T. A., Luffi, P., Plank, T., Dalton, H., & Leeman, W. P. 2009. Constraints on the depths and temperatures of basaltic magma generation on Earth and other terrestrial planets using new thermobarometers for mafic magmas. *Earth and Planetary Science Letters*, **279**(1-2), 20–33.

Lesher, C. M. 2007. Ni-Cu-(PGE) deposits in the Raglan area, Cape Smith Belt, New Quebec. *Pages 351–386 of:* Goodfellow, W. D. (ed), *Mineral deposits of Canada: a synthesis of major deposit-types, district metallogeny, the evolution of geological provinces, and exploration methods.* Special Publication, no. 5. St. Johns, NL, Canada: Geological Association of Canada, Mineral Deposits Division.

Lesher, C. M., Burnham, O. M., Keays, R. R., Barnes, S. J., & Hulbert, L. 2001. Trace-element geochemistry and petrogenesis of barren and ore-associated komatiites. *Canadian Mineralogist*, **39**(2), 673–696.

Leys, C., Ley, C., Klein, O., Bernard, P., & Licata, L. 2013. Detecting outliers: Do not use standard deviation around the mean, use absolute deviation around the median. *Journal of Experimental Social Psychology*, **49**(4), 764–766.

Li, C., Tao, Y., Qi, L., & Ripley, E. M. 2012. Controls on PGE fractionation in the Emeishan picrites and basalts: Constraints from integrated lithophile-siderophile elements and Sr-Nd isotopes. *Geochimica et Cosmochimica Acta*, **90**, 12–32.

Lightfoot, P. C., Hawkesworth, C. J., Devey, C. W., Rogers, N. W., & Van Calsteren, P. W. C. 1990. Source and differentiation of Deccan trap lavas: Implications of geochemical and mineral chemical variations. *Journal of Petrology*, **31**(5), 1165–1200.

Llovet, X., Pinard, P. T., Donovan, J. J., & Salvat, F. 2012. Secondary fluorescence in electron probe microanalysis of material couples. *Journal of Physics D: Applied Physics*, **45**(22), 225301.

Lorand, J. P., & Alard, O. 2001. Platinum-group element abundances in the upper mantle: New constraints from in situ and whole-rock analyses of massif central xenoliths (France). *Geochimica et Cosmochimica Acta*, **65**(16), 2789–2806.

Lorand, J. P., & Luguet, A. 2015. Chalcophile and Siderophile Elements in Mantle Rocks: Trace Elements Controlled by Trace Minerals. *Reviews in Mineralogy and Geochemistry*, **81**, 441 – 488.

Lorand, J. P., Pattou, L., & Gros, M. 1999. Fractionation of Platinum-group Elements and Gold in the Upper Mantle: a Detailed Study in Pyrenean Orogenic Lherzolites. *Journal of Petrology*, **40**(6), 957–981.

Lowrey, J. R., Ivanic, T. J., Wyman, D. A., & Roberts, M. P. 2017. Platy pyroxene: new insights into spinifex texture. *Journal of Petrology*, egx069.

Lucas, S., White, D., Bleeker, W., Hajnal, Z., Lewry, J., & Weber, W. 1996. Crustal structure of the Superior Boundary zone (Thompson Belt) from new Lithoprobe seismic reflection data. *Pages 82 – 94 of: Trans-Hudson Orogen Transect, Lithoprobe Report, v. 55.* University of British Columbia.

Lucas, S. B., Green, A., Hajnal, Z., White, D. J., Lewry, J. F., Ashton, K., Weber, W., & Clowes, R. 1993. Deep seismic profile across a Proterozoic collision zone: surprises at depth. *Nature*, **363**, 339–342.

Ludwig, K. R. 2012. User 's Manual for Isoplot, v3.75, A Geochronological Toolkit for Microsoft Excel. *Berkeley Geochronology Center Special Publications*, 1–75.

Luguet, A., Lorand, J. P., & Seyler, M. 2003. Sulfide petrology and highly siderophile element geochemistry of abyssal peridotites: A coupled study of samples from the Kane Fracture Zone (45Â°W 23Â°20N, MARK area, Atlantic Ocean). *Geochimica et Cosmochimica Acta*, **67**(8), 1553–1570.

Luguet, A., Shirey, S. B., Lorand, J. P., Horan, M. F., & Carlson, R. W. 2007. Residual platinum-group minerals from highly depleted harzburgites of the Lherz massif (France) and their role in HSE fractionation of the mantle. *Geochimica et Cosmochimica Acta*, **71**(12), 3082–3097.

Luguet, A., Nowell, G. M., & Pearson, D. G. 2008. $^{184}Os/^{188}Os$ and $^{186}Os/^{188}Os$ measurements by Negative Thermal Ionisation Mass Spectrometry (N-TIMS): Effects of interfering element and mass fractionation corrections on data accuracy and precision. *Chemical Geology*, **248**(3-4), 342–362.

Maaløe, S. 1982. Geochemical aspects of permeability controlled partial melting and fractional crystallization. *Geochimica et Cosmochimica Acta*, **46**(1), 43–57.

Machado, N., Zwanzig, H., & Parent, M. 1999. U-Pb ages of plutonism, sedimentation, and metamorphism of the Paleoproterozoic Kisseynew metasedimentary belt, Trans-Hudson Orogen (Manitoba, Canada). *Canadian Journal of Earth Sciences*, **36**(11), 1829–1842.

Maier, W. D., Roelofse, F., & Barnes, S.-J. 2003. The Concentration of the Platinum-Group Elements in South African Komatiites: Implications for Mantle Sources, Melting Regime and PGE Fractionation during Crystallization. *Journal of Petrology*, **44**(10), 1787–1804.

Maier, W. D., Barnes, S. J., Campbell, I. H., Fiorentini, M. L., Peltonen, P., Barnes, S.-J., & Smithies, R. H. 2009. Progressive mixing of meteoritic veneer into the early Earth's deep mantle. *Nature*, **460**(7255), 620–623.

Manikyamba, C., Kerrich, R., Khanna, T. C., Keshav Krishna, A., & Satyanarayanan, M. 2008. Geochemical systematics of komatiite-tholeiite and adakitic-arc basalt associations: The role of a mantle plume and convergent margin in formation of the Sandur Superterrane, Dharwar craton, India. *Lithos*, **106**(1-2), 155–172.

Marsh, B. D. 1981. On the crystallinity, probability of occurrence, and rheology of lava and magma. *Contributions to Mineralogy and Petrology*, **78**(1), 85–98.

Matzen, A. K., Baker, M. B., Beckett, J. R., & Stolper, E. M. 2011. Fe-Mg Partitioning between Olivine and High-magnesian Melts and the Nature of Hawaiian Parental Liquids. *Journal of Petrology*, **52**(7-8), 1243–1263.

Maurel, C., & Maurel, P. 1982. Etude expérimentale de l'équilibre Fe2+-Fe3+ dans les spinelles chromifères et les liquides silicatés basiques coexistants 1 atm. *Comptes Rendus de l'Académie des Sciences*, **295**, 209 – 212.

Mavrogenes, J. A., & O'Neill, H. St. C. 1999. The relative effects of pressure, temperature and oxygen fugacity on the solubility of sulfide in mafic magmas. *Geochimica et Cosmochimica Acta*, **63**(7), 1173–1180.

McDonough, W. F., & Ireland, T. R. 1993. *Intraplate Origin of Komatiites Inferred From Trace-Elements in Glass Inclusions.*

McGregor, C. R. 2011. *Open File OF2011-1: GIS compilation of relogged sub-Phanerozoic Precambrian exploration drillcore from the Thompson Nickel Belt, eastern Flin Flon Belt and Winnipegosis Komatiite Belt (parts of NTS 63B, C, F, G, J, K).* Tech. rept. Manitoba Geological Survey.

Mckay, G., Wagstaff, J., & Yang, S. R. 1986. Clinopyroxene REE distribution coefficients for shergottites: The REE content of the Shergotty melt. *Geochimica et Cosmochimica Acta*, **50**(6), 927–937.

Mckenzie, D., & Bickle, M. J. 1988. The volume and composition of melt generated by extension of the lithosphere. *Journal of Petrology*, **29**(3), 625–679.

Meisel, T., Walker, R. J., Irving, A. J., & Lorand, J. P. 2001a. Osmium isotopic composition of mantle xenoliths: A global perspective. *Geochimica et Cosmochimica Acta*, **65**(8), 1311–1323.

Meisel, T., Moser, J., & Wegscheider, W. 2001b. Recognizing heterogeneous distribution of platinum group elements (PGE) in geological materials by means of the Re-Os isotope system. *Fresenius' Journal of Analytical Chemistry*, **370**(5), 566–572.

Mertzman, S. 2000. K-Ar results from the southern Oregon-northern California Cascade Range. *Oregon Geology*, **62**(4), 99–122.

Minifie, M. J., Kerr, A. C., Ernst, R. E., Hastie, A. R., Ciborowski, T. J. R., Desharnais, G., & Millar, I. L. 2013. The northern and southern sections of the western ca. 1880 Ma Circum-Superior Large Igneous Province, North America: The Pickle Crow dyke connection? *Lithos*, **174**(0), 217–235.

Mole, D. R., Fiorentini, M. L., Thebaud, N., Cassidy, K. F., McCuaig, T. C., Kirkland, C. L., Romano, S. S., Doublier, M. P., Belousova, E. A., Barnes, S. J., & Miller, J. 2014. Archean komatiite volcanism controlled by the evolution of early continents. *Proceedings of the National Academy of Sciences*, **111**(28), 10083–10088.

Momme, P., Tegner, C., Brooks, C. K., & Keays, R. R. 2006. Two melting regimes during Paleogene flood basalt generation in East Greenland: Combined REE and PGE modelling. *Contributions to Mineralogy and Petrology*, **151**(1), 88–100.

Morimoto, N., Fabries, J., Ferguson, A. K., Ginzburg, I. V., Ross, M., Seifert, F. A., Zussman, J., Aoki, K., & Gottardi, G. 1988. Nomenclature of pyroxenes. *Mineralogical Magazine*, **52**, 535 – 550.

Mungall, J., & Brenan, J. 2014. Partitioning of platinum-group elements and Au between sulfide liquid and basalt and the origins of mantle-crust fractionation of the chalcophile elements. *Geochimica et Cosmochimica Acta*, **125**, 265–289.

Murck, B. W., & Campbell, I. H. 1986. The effects of temperature, oxygen fugacity and melt composition on the behaviour of chromium in basic and ultrabasic melts. *Geochimica et Cosmochimica Acta*, **50**(9), 1871–1887.

Nagasawa, H., Schreiber, H. D., & Morris, R. V. 1980. Experimental mineral/liquid partition coefficients of the rare earth elements (REE), Sc and Sr for perovskite, spinel and melilite. *Earth and Planetary Science Letters*, **46**, 431–437.

Nesbitt, R. W., & Sun, S.-S. 1976. Geochemistry of Archaean spinifex-textured peridotites and magnesian and low-magnesian tholeiites. *Earth and Planetary Science Letters*, **31**, 433–453.

Nesbitt, R. W., Sun, S.-S., & Purvis, A. C. 1979. Komatiites: Geochemistry and Genesis. *Canadian Mineralogist*, **17**, 165 – 169.

Nesbitt, R.W. 1971. Skeletal crystal forms in the ultramafic rocks of the Yilgarn Block, Western Australia: evidence for an Archaean ultramafic liquid. *Geological Society of Australia Special Publication*, 331–348.

Nicklas, R. W., Puchtel, I. S., & Ash, R. D. 2018. Redox state of the Archean mantle: Evidence from V partitioning in 3.5–2.4 Ga komatiites. *Geochimica et Cosmochimica Acta*, **222**(Supplement C), 447 – 466.

Nisbet, E. G. 1982. The tectonic setting and petrogenesis of komatiites. *Chap. 29, pages 501–520 of:* Arndt, N. T., & Nisbet, E. G. (eds), *Komatiites*. London: George Allen & Unwin.

Nisbet, E. G., Cheadle, M. J., Arndt, Nicholas T., & Bickle, M. J. 1993. Constraining the potential temperature of the Archaean mantle: A review of the evidence from komatiites. *Lithos*, **30**(3-4), 291–307.

Norman, M. D., & Garcia, M. O. 1999. Primitive magmas and source characteristics of the Hawaiian plume: Petrology and geochemistry of shield picrites. *Earth and Planetary Science Letters*, **168**(1-2), 27–44.

Ohtani, E. 1984. Generation of komatiite magma and gravitational differentiation in the deep upper mantle. *Earth and Planetary Science Letters*, **67**(2), 261–272.

O'Neill, H. St. C. 1987. Quartz-fayalite-iron and quartz-fayalite-magnetite equilibria and the free energy of formation of fayalite (Fe_2SiO_4) and magnetite (Fe_3O_4). *American Mineralogist*, **72**(1-2), 67–75.

Ottley, C. J., Pearson, D. G., & Irvine, G. J. 2003. A routine method for the dissolution of geological samples for the analysis of REE and trace elements via ICP-MS. *Pages 221–230 of:* Holland, J. G., & Tanner, S. D. (eds), *Plasma Source Mass Spectrometry: Applications and Emerging Technologies*, vol. 3. Cambridge: The Royal Society of Chemistry.

Pagé, P., & Barnes, S.-J. 2009. Using Trace Elements in Chromites to Constrain the Origin of Podiform Chromitites in the Thetford Mines Ophiolite, Québec, Canada. *Economic Geology*, **104**(7), 997 LP – 1018.

Pagé, P., Barnes, S.-J., Bédard, J. H., & Zientek, M. L. 2012. In situ determination of Os, Ir, and Ru in chromites formed from komatiite, tholeiite and boninite magmas: Implications for chromite control of Os, Ir and Ru during partial melting and crystal fractionation. *Chemical Geology*, **302-303**, 3–15.

Parman, S. W., & Grove, T. L. 2005. Komatiites in the Plume Debate. *Geological Society Of America Special Papers*, **388**, 249–256.

Parman, S. W., Dann, J. C., Grove, T. L., & de Wit, M. J. 1997. Emplacement conditions of komatiite magmas from the 3.49 Ga Komati Formation, Barberton Greenstone Belt, South Africa. *Earth and Planetary Science Letters*, **150**, 303–323.

Parman, S. W., Grove, T. L., & Dann, J. C. 2001. The production of Barberton komatiites in an Archean Subduction Zone. *Geophysical Research Letters*, **28**(13), 2513–2516.

Parman, S. W., Grove, T. L., Dann, J. C., & de Wit, M. J. 2004. A subduction origin for komatiites and cratonic lithospheric mantle. *South African Journal of Geology*, **107**(1-2), 107–118.

Pearce, J. A. 2008. Geochemical fingerprinting of oceanic basalts with applications to ophiolite classification and the search for Archean oceanic crust. *Lithos*, **100**(1-4), 14–48.

Pearce, J. A., & Stern, R. J. 2006. Origin of Back-Arc Basin Magmas : Trace Element and Isotope Perspectives. *Pages 63 – 86 of: Geophysical Monograph Series, Volume 166. Back-Arc Spreading Systems: Geological, Biological, Chemical, and Physical Interactions.* American Geophysical Union.

Pearson, D. G., & Woodland, S. J. 2000. Solvent extraction/anion exchange separation and determination of PGEs (Os, Ir, Pt, Pd, Ru) and Re-Os isotopes in geological samples by isotope dilution ICP-MS. *Chemical Geology*, **165**(1-2), 87–107.

Pearson, D. G., Irvine, G. J., Ionov, D. A., Boyd, F. R., & Dreibus, G. E. 2004. Re-Os isotope systematics and platinum group element fractionation during mantle melt extraction: a study of massif and xenolith peridotite suites. *Chemical Geology*, **208**, 29–59.

Pearson, D. G., Canil, D., & Shirey, S. 2014. Mantle samples included in volcanic rocks: Xenoliths and diamonds. *Chap. 2.05, pages 171 – 275 of:* Holland, H. D., & Turekian, K. K. (eds), *Treatise in Geochemistry, Volume 2.*, 2nd edition edn. Elsevier.

Percival, J. A., Whalen, J. B., & Rayner, N. 2005. Pikwitonei-Snow Lake Manitoba transect (parts of NTS 63J, 63O and 63P), Trans-Hudson Orogen-Superior Margin Metallotect Project: new results and tectonic interpretation. *Pages 69–91 of: Report of Activities 2005, Manitoba Industry, Economic Development and Mines.* Manitoba Geological Survey.

Peucker-Ehrenbrink, B., Bach, W., Hart, S. R., Blusztajn, J. S., & Abbruzzese, T. 2003. Rhenium-osmium isotope systematics and platinum group element concentrations in oceanic crust from DSDP/ODP Sites 504 and 417/418. *Geochemistry, Geophysics, Geosystems*, **4**(7), 1–28.

Philibert, J. 1963. A method for calculating the absorption correction in electron probe microanalysis. *Pages 379–392 of:* Pattee, H. H., Cosslett, V. E., & Engstrom, A. (eds), *X-ray Optics and X-ray Microanalysis*. New York and London: Academic Press.

Philibert, J., & Tixier, R. 1968. Electron penetration and the atomic number correction in electron probe microanalysis. *Journal of Physics D: Applied Physics*, **1**(6), 685–694.

Plank, T., & Langmuir, C. H. 1992. Effects of the Melting Regime on the Composition of the Oceanic Crust. *Journal of Geophysical Research*, **97**(B13), 19749 – 19770.

Potts, P. J. 1992. *A Handbook of Silicate Rock Analysis*. Springer.

Prægel, N.-O., & Holm, P. M. 2001. Replenishment episodes and crustal assimilation in the development of an early Tertiary magma chamber, East Greenland: evidence from layered cumulates of the Kælvegletscher ultramafic complex, Kangerlussuaq. *Mineralogy and Petrology*, **73**(4), 279 – 304.

Puchtel, I., & Humayun, M. 2000. Platinum group elements in Kostomuksha komatiites and basalts: Implications for oceanic crust recycling and core-mantle interaction. *Geochimica et Cosmochimica Acta*, **64**(24), 4227–4242.

Puchtel, I. S., Haase, K. M., Hofmann, A. W., Chauvel, C., Kulikov, V. S., Garbe-Schönberg, C. D., & Nemchin, A. A. 1997. Petrology and geochemistry of crustally contaminated komatiitic basalts from the Vetreny Belt, southeastern Baltic Shield: Evidence for an early Proterozoic mantle plume beneath rifted Archean continental lithosphere. *Geochimica et Cosmochimica Acta*, **61**(6), 1205–1222.

Puchtel, I. S., Hofmann, A. W., Mezger, K., Jochum, K. P., Shchipansky, A. A., & Samsonov, A. V. 1998. Oceanic plateau model for continental crustal growth in the Archaean: A case study from the Kostomuksha greenstone belt, NW Baltic Shield. *Earth and Planetary Science Letters*, **155**(1-2), 57–74.

Puchtel, I. S., Brügmann, G. E., & Hofmann, A. W. 2001. ^{187}Os-enriched domain in an Archean mantle plume: Evidence from 2.8 Ga komatiites of the Kostomuksha Greenstone Belt, NW Baltic Shield. *Earth and Planetary Science Letters*, **186**(3-4), 513–526.

Puchtel, I. S., Humayun, M., Campbell, A. J., Sproule, R. A., & Lesher, C. M. 2004. Platinum group element geochemistry of komatiites from the Alexo and Pyke Hill areas, Ontario, Canada. *Geochimica et Cosmochimica Acta*, **68**(6), 1361–1383.

Puchtel, I. S., Brandon, A. D., Humayun, M., & Walker, R. J. 2005. Evidence for the early differentiation of the core from Pt-Re-Os isotope systematics of 2.8-Ga komatiites. *Earth and Planetary Science Letters*, **237**(1-2), 118–134.

Puchtel, I. S., Humayun, M., & Walker, R. J. 2007. Os-Pb-Nd isotope and highly siderophile and lithophile trace element systematics of komatiitic rocks from the Volotsk suite, SE Baltic Shield. *Precambrian Research*, **158**(1-2), 119–137.

Puchtel, I. S., Walker, R. J., Brandon, A. D., & Nisbet, E. G. 2009a. Pt-Re-Os and Sm-Nd isotope and HSE and REE systematics of the 2.7 Ga Belingwe and Abitibi komatiites. *Geochimica et Cosmochimica Acta*, **73**(20), 6367–6389.

Puchtel, I. S., Walker, R. J., Anhaeusser, C. R., & Gruau, G. 2009b. Re-Os isotope systematics and HSE abundances of the 3.5 Ga Schapenburg komatiites, South Africa: Hydrous melting or prolonged survival of primordial heterogeneities in the mantle? *Chemical Geology*, **262**(3-4), 391–405.

Puchtel, I. S., Blichert-Toft, J., Touboul, M., Walker, R. J., Byerly, G. R., Nisbet, E. G., & Anhaeusser, C. R. 2013. Insights into early Earth from Barberton komatiites: Evidence from lithophile isotope and trace element systematics. *Geochimica et Cosmochimica Acta*, **108**, 63–90.

Puchtel, I. S., Walker, R. J., Touboul, M., Nisbet, E. G., & Byerly, G. R. 2014. Insights into early Earth from the Pt-Re-Os isotope and highly siderophile element abundance systematics of Barberton komatiites. *Geochimica et Cosmochimica Acta*, **125**, 394–413.

Puchtel, I. S., Touboul, M., Blichert-Toft, J., Walker, R. J., Brandon, A. D., Nicklas, R. W., Kulikov, V. S., & Samsonov, A. V. 2016a. Lithophile and siderophile element systematics of Earth's mantle at the Archean-Proterozoic boundary: Evidence from 2.4 Ga komatiites. *Geochimica et Cosmochimica Acta*, **180**, 227–255.

Puchtel, I. S., Blichert-Toft, J., Touboul, M., Horan, M. F., & Walker, R. J. 2016b. The coupled ^{182}W-^{142}Nd record of early terrestrial mantle differentiation. *Geochemistry Geophysics Geosystems*, **17**, 2168–2193.

Pyke, D. R., Naldrett, A. J., & Eckstrand, O. R. 1973. Archean ultramafic flows in Munro Township, Ontario. *Bulletin of the Geological Society of America*, **84**(3), 955–978.

Reed, S. B. J. 1965. Characteristic fluorescence corrections in electron-probe microanalysis. *British Journal of Applied Physics*, **16**, 913 – 926.

Reed, S. J. B. 2000. Quantitative trace analysis by wavelength-dispersive EPMA. *Mikrochimica Acta*, **132**(2-4), 145–151.

Rehkämper, M., Halliday, A. N., Fitton, J. G., Lee, D. C., Wieneke, M., & Arndt, N. T. 1999. Ir, Ru, Pt, and Pd in basalts and komatiites: new constraints for the geochemical behavior of the platinum-group elements in the mantle. *Geochimica et Cosmochimica Acta*, **63**(22), 3915–3934.

Renner, R. 1989. *Cooling and Crystallisation of Komatiite Flows from Zimbabwe*. Ph.D. thesis, University of Cambridge.

Renner, R., Nisbet, E. G., Cheadle, M. J., Arndt, N. T., Bickle, M. J., & Cameron, W. E. 1994. Komatiite flows from the reliance formation, belingwe belt, Zimbabwe: I. petrography and mineralogy. *Journal of Petrology*, **35**(2), 361–400.

Revillon, S., Arndt, N. T., Chauvel, C., & Hallot, E. 2000. Geochemical Study of Ultramafic Volcanic and Plutonic Rocks from Gorgona Island, Colombia: the Plumbing System of an Oceanic Plateau. *Journal of Petrology*, **41**(7), 1127–1153.

Rhodes, J. M. 1996. Geochemical stratigraphy of lava flows sampled by the Hawaii Scientific Drilling Project. *Journal of Geophysical Research*, **101**(B5), 11729.

Rhodes, J. M., & Vollinger, M. J. 2004. Composition of basaltic lavas sampled by phase-2 of the Hawaii Scientific Drilling Project: Geochemical stratigraphy and magma types. *Geochemistry, Geophysics, Geosystems*, **5**(3).

Rizo, H., Boyet, M., Blichert-Toft, J., O'Neil, J., Rosing, M. T., & Paquette, J. L. 2012. The elusive Hadean enriched reservoir revealed by ^{142}Nd deficits in Isua Archaean rocks. *Nature*, **491**(7422), 96–100.

Rizo, H., Walker, R. J., Carlson, R. W., Horan, M. F., Mukhopadhyay, S., Manthos, V., Francis, D., & Jackson, M. G. 2016. Preservation of Earth-forming events in the tungsten isotopic composition of modern flood basalts. *Science*, **352**(6287), 809–812.

Robin-Popieul, C. C. M., Arndt, N. T., Chauvel, C., Byerly, G. R., Sobolev, A. V., & Wilson, A. 2012. A new model for Barberton komatiites: Deep critical melting with high melt retention. *Journal of Petrology*, **53**(11), 2191–2229.

Roeder, P. L., & Emslie, R. F. 1970. Olivine-liquid equilibrium. *Contributions to Mineralogy and Petrology*, **29**(4), 275–289.

Roeder, P. L., & Reynolds, I. 1991. Crystallization of chromite and chromium solubility in basaltic melts. *Journal of Petrology*, **32**(5), 909–934.

Rohrbach, A., Ballhaus, C., Golla-Schindler, U., Ulmer, P., Kamenetsky, V. S., & Kuzmin, D. V. 2007. Metal saturation in the upper mantle. *Nature*, **449**(7161), 456–458.

Rollinson, H. 1999. Petrology and geochemistry of metamorphosed komatiites and basalts from the Sula Mountains greenstone belt, Sierra Leone. *Contributions to Mineralogy and Petrology*, **134**, 86–101.

Rukhlov, A. S., & Bell, K. 2010. Geochronology of carbonatites from the canadian and baltic shields, and the canadian cordillera: Clues to mantle evolution. *Mineralogy and Petrology*, **98**(1-2), 11–54.

Saha, A., Manikyamba, C., Santosh, M., Ganguly, S., Khelen, A. C., & Subramanyam, K. S. V. 2015. Platinum Group Elements (PGE) geochemistry of komatiites and boninites from Dharwar Craton, India: Implications for mantle melting processes. *Journal of Asian Earth Sciences*, **105**, 300–319.

Salters, V. J. M., & Stracke, A. 2004. Composition of the depleted mantle. *Geochemistry, Geophysics, Geosystems*, **5**(5).

Savard, D., Barnes, S.-J., & Meisel, T. 2010. Comparison between nickel-sulfur fire assay te co-precipitation and isotope dilution with high-pressure asher acid digestion for the determination of platinum-group elements, rhenium and gold. *Geostandards and Geoanalytical Research*, **34**(3), 281–291.

Self, S., Thordarson, T., Keszthelyi, L., Walker, G. P. L., Hon, K., Murphy, M. T., Long, P., & Finnemore, S. 1996. A new model for the emplacement of Columbia River basalts as large, inflated pahoehoe lava flow fields. *Geophysical Research Letters*, **23**(19), 2689–2692.

Seyler, M., Lorand, J. P., Dick, H. J. B., & Drouin, M. 2007. Pervasive melt percolation reactions in ultra-depleted refractory harzburgites at the Mid-Atlantic Ridge, 15° 20'N: ODP Hole 1274A. *Contributions to Mineralogy and Petrology*, **153**(3), 303–319.

Shore, M., & Fowler, D. 1999. The origin of spinifex texture in komatiites. *Nature*, **397**, 691–694.

Silva, K. E., Cheadle, M. J., & Nisbet, E. G. 1997. The Origin of Bl Zones in Komatiite Flows. *Journal of Petrology*, **38**(11), 1565–1584.

Simkin, T., & Smith, J. V. 1970. Minor-element distribution in olivine. *The Journal of Geology*, **78**(3), 304 – 325.

Sinton, C. W., Duncan, R. A., Storey, M., Lewis, J., & Estrada, J. J. 1998. An oceanic flood basalt province within the Caribbean plate. *Earth and Planetary Science Letters*, **155**(3-4), 221–235.

Skulski, T., & Wares, R. P. 1993. Early Proterozoic (1.88 - 1.87 Ga) tholeitic magmatism in the New Quebec Orogen. *Canadian Journal of Earth Sciences*, **30**, 1505 – 1520.

Sleep, N. H., Ebinger, C. J., & Kendall, J.-M. 2002. Deflection of mantle plume material by cratonic keels. *Geological Society, London, Special Publications*, **199**(1), 135–150.

Smith, E. M., Shirey, S. B., Nestola, F., Bullock, E. S., Wang, J., Richardson, S. H., & Wang, W. 2016. Large gem diamonds from metallic liquid in Earth's deep mantle. *Science*, **354**(6318), 1403–1405.

Smithies, H. R., Champion, D. C., & Sun, S.-S. 2004. The case for Archaean boninites. *Contributions to Mineralogy and Petrology*, **147**(6), 705–721.

Smoliar, M. I., Walker, R. J., & Morgan, J. W. 1996. Re-Os ages of group IIA, IIIA, IVA, and IVB iron meteorites. *Science*, **271**(5252), 1099–1102.

Sobolev, A. V., Hofmann, A. W., Kuzmin, D. V., Yaxley, G. M., Arndt, N. T., Chung, S.-L., Danyushevsky, L. V., Elliott, T., Frey, F. A., Garcia, M. O., Gurenko, A. A., Kamenetsky, V. S., Kerr, A. C., Krivolutskaya, N. A., Matvienkov, V. V., Nikogosian, I. K., Rocholl, A., Sigurdsson, I. A., Sushchevskaya, N. M., & Teklay, M. 2007. The Amount of Recycled Crust in Sources of Mantle-Derived Melts. *Science*, **316**(5823), 412–417.

Sobolev, A. V., Asafov, E. V., Gurenko, A. A., Arndt, N. T., Batanova, V. G., Portnyagin, M. V., Garbe-Schönberg, D., & Krasheninnikov, S. P. 2016. Komatiites reveal a hydrous Archaean deep-mantle reservoir. *Nature*, **531**(7596), 628–632.

Sossi, P. A., Eggins, S. M., Nesbitt, R. W., Nebel, O., Hergt, J. M., Campbell, I. H., O'Neill, H. St. C., Van Kranendonk, M., & Rhodri Davies, D. 2016. Petrogenesis and geochemistry of Archean Komatiites. *Journal of Petrology*, **57**(1), 147–184.

Sparks, R. S. J., & Huppert, H. E. 1984. Density changes during the fractional crystallization of basaltic magmas: fluid dynamic implications. *Contributions to Mineralogy and Petrology*, **85**(3), 300–309.

Stamatelopoulou-Seymour, K., Francis, D., & Ludden, J. 1983. The Petrogenesis of the Lac Guyer Komatiites and Basalts and the Nature of the Komatiite-Komatiitic Basalt Compositional Gap. *Contributions to Mineralogy and Petrology*, **84**, 6–14.

Stauffer, M. R. 1984. Manikewan: An Early Proterozoic Ocean in Central Canada, its Igneous History and Orogenic Closure. *Precambrian Research*, **25**, 257–281.

Stockman, H. W., & Hlava, P. F. 1984. Platinum-group minerals in alpine chromitites from southwestern Oregon. *Economic Geology*, **79**(3), 491–508.

Stone, W. E., Deloule, E., Larson, M. S., & Lesher, C. M. 1997. Evidence for hydrous high-MgO melts in the Precambrian. *Geology*, **25**(2), 143–146.

Storey, M., Mahoney, J. J., Kroenke, L. W., & Saunders, A. D. 1991. Are oceanic plateau sites of komatiites formation. *Geology*, **19**, 376–379.

Sun, C., & Liang, Y. 2013. The importance of crystal chemistry on REE partitioning between mantle minerals (garnet, clinopyroxene, orthopyroxene, and olivine) and basaltic melts. *Chemical Geology*, **358**, 23–36.

Sun, S.-S. 1982. Chemical composition and origin of the earth' s primitive mantle. *Geochimica et Cosmochimica Acta*, **46**(1), 179–192.

Sun, S.-S., & McDonough, W. F. 1989. Chemical and isotopic systematics of oceanic basalts: implications for mantle composition and processes. *Geological Society, London, Special Publications*, **42**(1), 313–345.

Sun, S.-S., & Nesbitt, R. W. 1978. Petrogenesis of Archaean ultrabasic and basic volcanics: Evidence from rare earth elements. *Contributions to Mineralogy and Petrology*, **65**(3), 301–325.

Sweeney, R. J., Prozesky, V., & Przyblowicz, W. 1995. Selected trace and minor element partitioning between peridotite. *Geochimica et Cosmochimica Acta*, **59**(18), 3671–3683.

Thompson, R. N., & Gibson, S. A. 1991. Subcontinental mantle plumes, hotspots and pre-existing thinspots. *Journal of the Geological Society*, **148**, 973–977.

Thompson, R. N., & Gibson, S. A. 2000. Transient high temperatures in mantle plume heads inferred from magnesian olivines in Phanerozoic picrites. *Nature*, **407**, 502 – 506.

Trela, J., Gazel, E., Sobolev, A. V., Moore, L., Bizimis, M., Jicha, B., & Batanova, V. G. 2017. The hottest lavas of the Phanerozoic and the survival of deep Archaean reservoirs. *Nature Geosci*, **10**(6), 451–456.

Turner, J. S., Huppert, H. E., & Sparks, R. S. J. 1986. Komatiites II: Experimental and Theoretical Investigations of Post-emplacement Cooling and Crystallization. *Journal of Petrology*, **27**(2), 397–437.

Van Kranendonk, M. J., Hugh Smithies, R., Hickman, A. H., & Champion, D. C. 2007. Review: Secular tectonic evolution of Archean continental crust: interplay between horizontal and vertical processes in the formation of the Pilbara Craton, Australia. *Terra Nova*, **19**(1), 1–38.

Viljoen, M. J., & Viljoen, R. P. 1969a. Evidence for the existence of a mobile extrusive peridotitic magma from the Komati Formation of the Onvernacht Group. *Geological Survey of South Africa, Special Publication*, **21**, 87 – 112.

Viljoen, M. J., & Viljoen, R. P. 1969b. The geology and geochemistry of the lower ultramafic unit of the Onverwacht group and a proposed new class of igneous rocks. *Geological Survey of South Africa, Special Publication*, **21**, 55–85.

Walker, R. J., Shirey, S. B., & Stecher, O. 1988. Comparative Re-Os, Sm-Nd and Rb-Sr isotope and trace element systematics for Archean komatiite flows from Munro Township, Abitibi Belt, Ontario. *Earth and Planetary Science Letters*, **87**(1-2), 1–12.

Walker, R. J., Storey, M., Kerr, A. C., Tarney, J., & Arndt, N. T. 1999. Implication of ^{187}Os isotopic heterogeneities in a mantle plume: Evidence from Gorgona Island and Curacao. *Geochimica et Cosmochimica Acta*, **63**(5), 713–728.

Walker, R. J., Horan, M. F., Morgan, J. W., Becker, H., Grossman, J. N., & Rubin, A. E. 2002. Comparative ^{187}Re-^{187}Os systematics of chondrites: Implications regarding early solar system processes. *Geochimica et Cosmochimica Acta*, **66**(23), 4187– 4201.

Walter, M. J. 1998. Melting of garnet peridotite and the origin of komatiite and depleted lithosphere. *Journal of Petrology*, **39**(1), 29–60.

Wan, Z., Coogan, L. A., & Canil, D. 2008. Experimental calibration of aluminum partitioning between olivine and spinel as a geothermometer. *American Mineralogist*, **93**(7), 1142–1147.

Wang, X., Griffin, W. L., Chen, J., Huang, P., & Li, X. 2011. U and Th contents and Th/U ratios of zircon in felsic and mafic magmatic rocks: Improved zircon-melt distribution coefficients. *Acta Geologica Sinica*, **85**(1), 164 – 174.

Waterton, P., Pearson, D. G., Kjarsgaard, B., Hulbert, L., Locock, A., Parman, S. W., & Davis, B. 2017. Age, Origin, and Thermal Evolution of the ultra-fresh ∼1.9 Ga Winnipegosis Komatiites, Manitoba, Canada. *Lithos*, **268-271**, 114–130.

Weill, D. F., & Drake, M. J. 1973. Europium Anomaly in Plagioclase Feldspar: Experimental Results and Semiquantitative Model. *Science*, **180**(4090), 1059–1060.

Weller, O. M., & St-Onge, M. R. 2017. Record of modern-style plate tectonics in the Palaeoproterozoic Trans-Hudson orogen. *Nature Geosci*, **10**(4), 305–311.

Whalen, J. B., Percival, J. A., McNicoll, V. J., & Longstaffe, F. J. 2002. A mainly crustal origin for tonalitic granitoid rocks, Superior Province, Canada: Implications for late archean tectonomagmatic processes. *Journal of Petrology*, **43**(8), 1551–1570.

White, D. J., Lucas, S. B., Bleeker, W., Hajnal, Z., Lewry, J. F., & Zwanzig, H. V. 2002. Suture-zone geometry along an irregular Paleoproterozoic margin: The Superior Boundary Zone, Manitoba, Canada. *Geology*, **30**(8), 735–738.

White, R. S., Bown, J. W., & Smallwood, J. R. 1995. The temperature of the Iceland plume and origin of outward-propagating V-shaped ridges. *Journal of the Geological Society*, **152**(6), 1039–1045.

Wilson, A. H., Versfeld, J. A., & Hunter, D. R. 1989. Emplacement, crystallization and alteration of spinifex-textured komatiitic basalt flows in the Archaean Nondweni greenstone belt, southern Kaapvaal Craton, South Africa. *Contributions to Mineralogy and Petrology*, **101**(3), 301–317.

Wilson, J. F., Bickle, M. J., Hawkesworth, C. J., Martin, A., Nisbet, E. G., & Orpen, J. L. 1978. Granite-greenstone terrains of the Rhodesian Archaean craton. *Group*, **271**, 23 – 27.

Wooden, J. L., Czamanske, G. K., Fedorenko, V. A., Arndt, N. T., Chauvel, C., Bouse, R. M., King, B. S. W., K., R. J., & Siems, D. F. 1993. Isotopic and trace-element constraints on mantle and crustal contributions to Siberian continental flood basalts, Noril'sk area, Siberia. *Geochimica et Cosmochimica Acta*, **57**(15), 3677–3704.

Woodland, Sarah J. 1999. *Development of ICP-MS isotope dilution pre-concentration techniques for determination of platinum group elements in volcanic rocks*. Ph.D. thesis, University of Durham.

Wyman, D., & Hollings, P. 1998. Long-lived mantle-plume influence on an Archean protocontinent: geochemical evidence from the 3 Ga Lumby Lake greenstone belt, Ontario, Canada. *Geology*, **26**(8), 719–722.

Wyman, D. A. 1999. A 2.7 Ga depleted tholeiite suite: Evidence of plume-arc interaction in the Abitibi Greenstone Belt, Canada. *Precambrian Research*, **97**(1-2), 27–42.

Zhou, M.-F., & Kerrich, R. 1992. Morphology and Composition of Chromite in Komatiites from the Belingwe Greenstone Belt, Zimbabwe. *Canadian Mineralogist*, **30**, 303–317.

Zhou, M.-F., Malpas, J., Song, X. Y., Robinson, P. T., Sun, M., Kennedy, A. K., Lesher, C. M., & Keays, R. R. 2002. A temporal link between the Emeishan large igneous province (SW China) and the end-Guadalupian mass extinction. *Earth and Planetary Science Letters*, **196**(3-4), 113–122.

Zwanzig, H. V. 2005. Geochemistry, Sm-Nd isotope data and age constraints of the Bah Lake assemblage, Thompson Nickel Belt and Kisseynew Domain margin: relation to Thompson-type ultramafic bodies and a tectonic model (NTS 63J, O and P). *Pages 40–53 of: Report of Activities 2005, Manitoba Industry, Economic Development and Mines*. Manitoba Geological Survey.

Appendices

Appendix A

List of available samples

Table A.1: Full list of samples available from the Winnipegosis Komatiite belt for this thesis. 'Cont.' denotes powders that may have become contaminated during storage at the Geological Survey of Canada. Rock types: 'Mass. K.' = massive komatiite, 'Min. K.' = mineralised komatiite, 'Serp. dun.' = serpentinised dunite, 'D.K.' = differentiated komatiite. Subtypes within differentiated komatiite flows: 'ol spin.' = olivine spinifex, 'chill' = chilled margin, 'aci. px' = acicular pyroxene zone, 'hopper' = hopper olivine cumulates, 'px. spin.' = pyroxene spinifex, 'c.' = cumulate.

			Rock Powders		Thin Sections	
Sample #	*Rock Type*	*Samples*	*Clean*	*Cont.*	*Covered*	*Polished*
RP1A-1	Mass. K.	1	1	-	1	1
RP1A-2	Mass. K.	1	1	-	1	-
RP1A-4	Mass. K.	2	1	-	1	1
RP1A-5	Mass. K.	1	1	-	1	1
RP1A-7	Mass. K.	1	1	-	4	-
RP1A-8	Mass. K.	1	1	-	1	1
RP1A-9	Mass. K.	1	1	-	1	-
RP1A-10	Mass. K.	1	-	1	4	1
RP1A-11	Mass. K.	1	1	-	1	-
RP1A-12	Mass. K.	1	1	-	1	1
RP1A-13	Mass. K.	2	1	-	1	-
RP1A-14	Mass. K.	2	1	-	1	-
RP1A-15	Mass. K.	2	1	-	1	2
RP1A-16	Mass. K.	2	1	-	1	2
RP1A-17	Mass. K.	1	1	-	4	1
RP1A-18	Mass. K.	1	1	-	1	1
RP1A-19	Mass. K.	1	1	-	1	-
RP1A-20	Mass. K.	1	1	-	1	-
RP1A-21	Mass. K.	1	1	-	1	1
RP1A-22	Mass. K.	2	1	-	1	-
RP1A-23	Mass. K.	1	1	-	1	-

Table A.1: continued

			Rock Powders		Thin Sections	
Sample #	*Rock Type*	*Samples*	*Clean*	*Cont.*	*Covered*	*Polished*
RP1A-24	Mass. K.	1	-	1	4	1
RP1A-25	Mass. K.	1	1	-	1	-
RP1A-26	Mass. K.	2	1	-	1	1
RP1A-27	Mass. K.	1	1	-	1	1
RP1A-28	Mass. K.	1	1	-	1	-
RP1A-29	Mass. K.	2	1	-	1	-
RP1A-30	Mass. K.	1	1	-	1	1
RP1A-31	Mass. K.	1	1	-	1	-
RP1A-32	Mass. K.	1	1	-	1	-
RP1A-33	Mass. K.	1	1	-	1	-
RP1A-34	Min. K.	1	1	-	1	1
RP1A-35	Mass. K.	2	1	-	1	-
RP1A-36	Mass. K.	1	1	-	1	-
RP1A-37	Mass. K.	1	1	-	1	-
RP1A-38	Mass. K.	1	2	-	1	1
RP1A-39	Mass. K.	2	1	-	1	-
RP1A-40	Mass. K.	2	-	1	1	-
RP1A-41	Mass. K.	2	1	-	1	-
RP1A-42	Min. K.	1	1	-	1	-
RP1A-43	Mass. K.	1	-	1	1	-
RP1A-44	Mass. K.	2	1	-	1	1
RP1A-45	Mass. K.	2	1	-	1	1
RP1A-46	Mass. K.	1	1	-	1	1
RP1A-47A	Mass. K.	1	1	-	1	-
RP1A-47B	Mass. K.	1	1	-	-	-
RP1A-48	Mass. K.	1	1	-	1	1
RP1A-49	Mass. K.	-	2	1	1	1
RP1A-50	Mass. K.	1	1	-	1	-
RP1A-51	Mass. K.	1	1	-	1	-
RP1A-52	Mass. K.	2	-	1	1	-
RP1A-53	Mass. K.	2	1	1	1	1
RP1A-54	Mass. K.	2	1	-	1	1
RP1A-55	Mass. K.	2	1	-	1	1
RP1A-56	Mass. K.	2	2	-	1	1
RP1A-57	Mass. K.	1	1	-	1	-
RP1A-58	Mass. K.	2	1	-	1	-
RP1A-59	Mass. K.	2	1	-	1	-
RP1A-60	Mass. K.	1	1	-	1	-

Table A.1: continued

			Rock Powders		Thin Sections	
Sample #	*Rock Type*	*Samples*	*Clean*	*Cont.*	*Covered*	*Polished*
RP1A-61	Mass. K.	1	1	-	2	-
RP1A-62	Mass. K.	1	-	1	1	1
RP1A-63	Mass. K.	2	-	1	1	1
RP1A-64	Mass. K.	2	1	-	2	-
RP1A-65	Mass. K.	1	1	-	1	-
RP1A-66	Mass. K.	-	3	-	1	1
RP1A-67	Mass. K.	-	3	-	1	1
RP1A-68	Mass. K.	2	1	-	1	2
RP1A-69	Mass. K.	1	1	-	1	1
RP1A-70	Mass. K.	1	1	-	1	-
RP1A-71	Mass. K.	1	1	-	1	-
RP1A-72	Mass. K.	1	-	1	1	-
RP1A-73	Mass. K.	1	1	-	1	-
RP1A-75	Mass. K.	1	1	-	1	1
RP1A-76	Mass. K.	1	1	-	1	-
RP1A-77	Mass. K.	-	3	-	1	-
RP1A-78	Mass. K.	1	1	-	1	-
RP1A-79	Mass. K.	2	1	-	1	1
RP1A-80	Mass. K.	1	1	-	1	-
RP1A-81	Mass. K.	1	1	-	1	1
RP1A-82	Mass. K.	1	1	-	1	-
RP1A-83	Mass. K.	1	1	-	1	1
RP1A-85	Mass. K.	1	1	-	1	1
RP1A-86	Mass. K.	1	1	-	1	-
RP1A-87	Mass. K.	2	1	-	1	1
RP1A-88	Mass. K.	1	-	1	1	1
RP1A-89	Mass. K.	1	-	-	1	-
RP1A-90	Mass. K.	-	2	1	1	-
RP1A-91	Mass. K.	1	1	-	1	1
RP1A-92	Mass. K.	1	1	-	4	-
RP1A-93	Mass. K.	1	1	-	1	-
RP1A-94	Mass. K.	1	1	-	1	-
RP1A-95	Mass. K.	1	1	-	1	-
RP1A-96	Mass. K.	1	1	-	1	-
RP1A-97	Mass. K.	1	1	-	1	-
RP1A-98	Mass. K.	1	1	-	1	-
RP1A-99	Mass. K.	1	2	-	1	1
RP1A-100	Mass. K.	1	1	-	1	1

Table A.1: continued

			Rock Powders		Thin Sections	
Sample #	*Rock Type*	*Samples*	*Clean*	*Cont.*	*Covered*	*Polished*
RP1A-101	Mass. K.	1	1	-	1	-
RP1A-102	Mass. K.	1	1	-	1	1
RP1A-103	Mass. K.	2	1	-	1	1
RP1A-104	Mass. K.	1	2	-	1	-
RP1A-105	Mass. K.	1	1	-	1	1
RP1A-106	Mass. K.	1	1	-	1	-
RP1A-107	Mass. K.	1	1	-	1	1
RP1A-108	Mass. K.	1	-	1	1	-
RP1A-109	Mass. K.	1	-	1	1	-
RP1A-110	Mass. K.	1	1	-	1	1
RP1A-111	Mass. K.	1	1	1	4	1
RP1A-112	Mass. K.	1	1	1	2	-
RP1A-113	Mass. K.	1	2	-	1	1
RP1A-114	Mass. K.	1	1	-	1	-
RP1A-115	Mass. K.	1	1	-	1	-
RP1A-116	Mass. K.	1	1	-	1	-
RP1A-117	Mass. K.	1	1	-	1	-
RP1A-118	Mass. K.	1	1	1	1	1
RP1A-119	Mass. K.	1	1	-	1	-
RP1A-120	Mass. K.	1	1	-	1	-
RP1A-121	Mass. K.	1	1	-	1	1
RP1A-122	Mass. K.	1	1	-	1	-
RP1A-123	Mass. K.	1	1	-	1	-
RP1A-124	Mass. K.	1	1	-	1	-
RP1A-125	Mass. K.	1	1	-	1	-
RP1A-126	Mass. K.	1	1	-	1	-
RP1A-127	Mass. K.	1	1	-	1	1
RP1A-128	Mass. K.	2	1	-	1	1
RP1A-129	Mass. K.	2	1	-	-	-
RP1A-130	Mass. K.	2	-	-	1	1
RP1A-131	Mass. K.	1	1	-	1	-
RP1A-132	Mass. K.	2	1	-	1	2
RP1A-15-133A	Min. K.	1	1	-	3	-
RP1A-133-B	Min. K.	1	-	-	1	-
RP1A-133-1C1	Min. K.	1	1	-	1	-
RP1A-133-2C	Min. K.	1	1	-	2	-
RP1A-133-1D	Min. K.	1	-	-	4	-
RP1A-133E	Min. K.	1	-	-	2	-

Table A.1: continued

			Rock Powders		Thin Sections	
Sample #	*Rock Type*	*Samples*	*Clean*	*Cont.*	*Covered*	*Polished*
RP1A-134	Mass. K.	-	1	-	1	-
RP1A-135	Mass. K.	1	1	-	1	-
RP1A-136	Mass. K.	1	1	-	1	-
RP1A-137	Mass. K.	2	-	-	1	-
RP1A-138	Mass. K.	1	1	-	1	1
RP1A-139	Mass. K.	2	1	-	1	1
RP1A-140	Mass. K.	2	1	-	1	1
RP1A-141	Mass. K.	-	1	1	1	-
RP1A-142	Mass. K.	2	-	1	1	2
RP1A-143	Mass. K.	1	1	-	1	-
RP1A-144	Mass. K.	2	1	-	1	-
RP1A-145	Mass. K.	2	-	-	1	1
RP1A-146	Mass. K.	1	1	-	1	-
RP1A-147	Mass. K.	1	1	-	1	1
RP1A-148	Mass. K.	2	1	-	1	1
RP1A-149	Mass. K.	1	-	2	1	1
RP1A-150	Mass. K.	2	1	-	1	1
RP1A-151	Mass. K.	2	1	-	1	-
RP1A-152	Mass. K.	1	1	-	1	-
RP1A-153	Mass. K.	1	1	-	1	1
RP1A-154	Mass. K.	2	1	-	1	-
RP1A-516.78	Min. K.	2	-	-	-	-
RP7-1	Serp. dun.	1	1	-	-	-
RP7-2	Serp. dun.	1	-	-	-	-
RP7-3	Serp. dun.	1	1	-	-	-
RP7-4	Serp. dun.	1	1	-	-	-
RP7-5	Serp. dun.	1	1	-	-	-
RP7-6	Serp. dun.	1	1	-	-	-
RP7-7	Serp. dun.	1	1	-	-	-
RP7-8	Serp. dun.	2	1	-	-	-
RP7-9	Serp. dun.	1	1	-	-	-
RP7-10	Serp. dun.	1	1	-	1	-
RP7-11	Serp. dun.	1	1	-	-	-
RP7-12	Serp. dun.	1	1	-	-	-
RP7-13	Serp. dun.	1	1	-	-	-
RP7-14	Serp. dun.	1	1	-	1	-
RP7-15	Serp. dun.	1	1	-	-	-
RP7-16	Serp. dun.	1	2	-	-	-

Table A.1: continued

			Rock Powders		Thin Sections	
Sample #	*Rock Type*	*Samples*	*Clean*	*Cont.*	*Covered*	*Polished*
RP8-1	Metabasalt	1	1	-	1	-
RP8-2	Metabasalt	2	1	-	1	-
RP8-3	Metabasalt	2	1	-	1	-
RP8-4	Metabasalt	-	1	1	1	-
RP8-5	Metabasalt	2	1	-	1	1
RP8-6	Metabasalt	2	1	-	1	-
RP8-7	Metabasalt	2	1	-	1	-
RP8-8	Metabasalt	2	-	1	1	-
RP8-9	Metabasalt	2	1	-	1	-
RP8-10	Metabasalt	2	2	-	1	-
RP8-562.8	Metabasalt	1	-	-	-	-
RP12-272.1	Mass. K.	1	1	1	1	-
RP12-282.5	D.K. (ol spin.)	1	1	1	-	1
RP12-284.4	Mass. K.	1	1	1	1	-
RP12-284.6	Mass. K.	1	1	1	1	-
RP12-304.8A	D.K. (chill)	1	1	1	1	-
RP12-304.8B	D.K. (chill)	1	1	1	1	-
RP12-305.3	D.K. (ol spin.)	1	1	1	-	2
RP12-306.1	D.K. (ol spin.)	1	1	1	-	1
RP12-306.8	D.K.	-	1	1	-	-
RP12-307.3	D.K. (aci. px)	1	1	1	-	1
RP12-308.3	D.K. (aci. px)	1	1	1	-	1
RP12-311.5	D.K. (hopper)	1	1	1	1	-
RP12-326	D.K. (ol spin.)	1	1	1	1	-
RP12-335.4	Mass. K.	-	-	1	1	-
RP12-347.3	Min. K.	1	-	-	-	1
RP12-350.7	Mass. K.	1	1	1	1	-
RP12-353	Mass. K.	1	1	1	1	-
RP12-355.3	Mass. K.	1	1	1	2	-
RP12-355.4	Mass. K.	1	1	-	-	-
RP12-356	Mass. K.	1	1	1	1	-
RP12-356.6	Min. K.	1	-	-	-	1
RP12-357.2	Mass. K.	1	-	2	1	-
RP12-357.6	Mass. K.	1	1	1	1	-
RP12-359.45	Mass. K.	1	1	1	1	-
RP12-360.3	Mass. K.	1	1	1	1	-
RP12-360.8	Mass. K.	1	1	1	1	-
RP12-362.3	Mass. K.	1	1	1	1	-

Table A.1: continued

			Rock Powders		Thin Sections	
Sample #	*Rock Type*	*Samples*	*Clean*	*Cont.*	*Covered*	*Polished*
RP12-364	Mass. K.	1	1	1	1	-
RP12-365.8	Mass. K.	1	1	1	1	-
RP12-371.4	Mass. K.	1	1	1	1	-
RP12-372.4	Mass. K.	1	1	1	1	-
RP12-373.9	Mass. K.	1	1	-	1	-
RP12-374.8	Mass. K.	1	-	1	1	-
RP12-375.9	Mass. K.	1	1	1	1	-
RP12-376.8	Mass. K.	1	1	1	1	-
RP12-377.67	Mass. K.	-	1	1	-	-
RP12-377.8	Mass. K.	1	1	1	1	-
RP12-379.2	Mass. K.	1	1	1	1	-
RP12-379.8	Mass. K.	-	1	-	-	-
RP12-383.7	Mass. K.	1	-	1	1	-
RP12-385.7	Mass. K.	-	1	-	-	-
RP12-387.5A	Mass. K.	1	-	-	-	1
RP12-387.5B	Mass. K.	-	-	-	-	1
RP12-390.1	Mass. K.	1	1	1	1	-
RP12-394	Mass. K.	1	1	1	1	-
RP12-398.3	Mass. K.	1	1	-	1	-
RP12-404.3	Mass. K.	1	1	1	1	-
RP12-415.1	Mass. K.	1	1	1	1	-
RP12-419.4	Mass. K.	1	1	1	1	-
RP12-420	Mass. K.	1	-	-	-	-
RP12-423.85	Min. K.	-	-	-	-	1
RP12-424.22A	Min. K.	-	-	-	-	-
RP12-424.22B	Min. K.	-	-	-	-	1
RP12-426.7	D.K. (px spin.)	1	1	1	-	1
RP12-428.5	D.K. (c)	1	1	1	1	-
RP12-429.8	D.K. (c)	1	-	-	1	-
RP12-429.9	D.K. (c)	-	1	1	-	-
RP12-433.6	D.K. (c)	1	1	1	1	-
RP12-434.55	D.K. (c)	1	1	1	1	-
RP12-435.7	D.K. (c)	1	1	1	1	-
RP12-436.80	Mass. K.	-	-	-	-	1
RP12-438.8	Mass. K.	1	1	1	1	-
RP12-440.9	Mass. K.	1	1	1	1	-
RP12-446.1	Mass. K.	1	1	1	1	-
RP12-446.3	Mass. K.	1	-	-	-	-

Table A.1: continued

			Rock Powders		Thin Sections	
Sample #	*Rock Type*	*Samples*	*Clean*	*Cont.*	*Covered*	*Polished*
RP12-451	Mass. K.	1	-	-	-	-
RP12-451.6	Mass. K.	1	1	1	1	-
RP12-453	Mass. K.	1	1	1	1	-
RP12-454	Mass. K.	1	1	1	1	-
RP12-457.3	Mass. K.	1	1	1	1	-
RP12-459.35A	Mass. K.	1	-	-	-	2
RP12-459.35B	Mass. K.	-	-	-	-	1
RP12-459.38C	Mass. K.	-	-	-	-	1
RP12-460.85	D.K. (ol spin.)	1	1	1	1	-
RP12-464.3	Mass. K.	1	-	2	1	-
RP12-468.6	Mass. K.	1	-	-	-	-
RP12-480.05	Mass. K.	-	-	-	-	1
RP12-481.2	Mass. K.	1	1	1	1	-
RP12-486.45	Mass. K.	1	1	1	2	-
RP12-490.6	Mass. K.	1	1	1	1	-

Appendix B
High precision EPMA methods

B.1 EPMA Measurement Conditions and Standardisation

Trace elements in olivine were measured during two analytical sessions one month apart, with almost identical measurement conditions used in each session. To generate a high enough signal to noise ratio, and to measure the background with sufficient precision to allow for quantification of trace elements by EPMA, high beam currents and long counting times are required (Reed, 2000). However, the beam current chosen for analysis must be limited to avoid detector saturation. On the JEOL 8900R Superprobe used, the detector shows significant saturation effects at approximately 65,000 cps, so a cut off of ∼50,000 cps is used to keep analyses well within the linear range of the detector. An optimal beam current of 100 nA was selected for analyses; this gave signals of ∼45,000 cps on Cr in chromite, and ∼40,000 cps on Si and ∼33,000 cps on Mg in olivine.

As EPMA standards generally contain high concentrations of their elements of interest, the standardisation could not be run at such high beam currents without saturating the detector. Standards were mostly run at 50 nA, except for Ni, Co, Mn (when measured on an Mn-Cu alloy), and Na, which were measured at 20 nA. Ni, Co, and Mn had to be measured at this lower beam current to avoid saturating the detector with the high signal generated by the pure metal wires, whereas Na was standardised at 20 nA to minimise Na mobilisation in albite. Integral mode was used to avoid errors caused by shifts in the SCA settings as a result of changes in beam current between the standards and the samples. All standards were run using a focussed beam, with the exception of Na, which was measured with a 10 μm beam width to minimise the effects of Na mobilisation.

Possible interferences on the trace elements of interest were investigated. The magnitude of a 5th-order Ni Kα peak close to the Al Kα peak was checked by scanning

across the Al position with a 50 nA beam on a pure Ni wire standard. No signal was detectable above background, and so this interference should have no effect on Al measurements in olivine containing even relatively high Ni concentrations of 3000 ppm. A 2nd-order Ni Kα peak that can interfere with the lower background measurement for Ca was avoided during the first analytical session by placing the lower background 4 mm below the peak. Due to discrepancies in the Ca values measured by EPMA in this study and by other methods (see below), during the second analytical session the lower background was measured 2 mm below the peak, in an attempt to rule out curvature of the background as a possible cause of these discrepancies. The 2nd-order Ni Kα peak was then removed using pulse height analysis. A large interference from the Fe Kβ peak overlaps with Co Kα. This could not be removed using pulse height analysis due to the similarities in X-ray energy, and so an overlap correction was made using the measured Fe signal. The magnitude of the overlap correction was determined by measuring the net signal detected on the Co peak while analysing a pure Fe wire at 20 nA.

Two sided backgrounds were found to be essential to reproducing the concentrations of trace elements in the standards used, as at signals very close to the background level, the curvature of the background has a strong effect on the net signal measured. A summary of the standards used, standardisation currents, and background positions for each element is given in Table B.1.

Long counting times were required for the precise measurement of Al in olivine. As such, many of the counting times for other elements could be increased without affecting the overall measurement time. The measurement times and channels for all elements are presented in Figure B.1. Al can be measured on either the TAP or TAPJ crystals, but TAPJ was preferred for its approximately 20% better sensitivity for Al. All data were reduced using a ZAF procedure (Philibert, 1963; Reed, 1965; Philibert & Tixier, 1968).

B.2 EPMA Trace Element Accuracy, Repeatability and Limits of Determination

Average values measured by EPMA for the in house SC-BK and SC/KA standards, are compared to existing data for these standards in Table B.2, along with the average limits of quantification for each oxide measured. Before averaging, the trace element

Table B.1: Measurement conditions of standards and background positions. Metal wire standards are reported as elemental wt%, all other standards are reported as oxide wt%. The use of Spessartine or Mn-Cu alloy as the Mn standard was found to have no effect on the measured concentrations of Mn. 'bkgd' = background position.

Oxide or Element	*Standard*	*wt% Oxide or Element*	*Current (nA)*	*Lower bkgd (mm)*	*Upper bkgd (mm)*
TiO_2	rutile	100	50	2	2
Na_2O	Albite-VA	11.52	50	6	3
K_2O	Sanidine-MAD	16.21	50	2	2
SiO_2	Fo93	40.85	50	N/A	3
FeO	Fayalite-CB1	66.94	50	5	5
Cr_2O_3	Cr_2O_3-CB1	99.546	50	1.9	3
MgO	Fo93	51.63	50	N/A	2
CaO	diopside	25.73	50	4 / 2	2
Al_2O_3	Frank Smith-CB1	21.75	50	2.6	2
MnO	SpessartineSK	25.06	50	6	1.5
Mn	Mn-Cu alloy	80.2	20	6	1.5
P_2O_5	apatite	40.87	50	4	2
Ni	Ni wire-CB1	100	20	1.5	1.5
Co	Co metal	100	20	6	3

data were checked for outliers using a Median Absolute Deviation (MAD) test (Hampel, 1974; Leys *et al.*, 2013), a robust outlier test. A relative high (but arbitrary) threshold was set, where only values $>5 * \text{MAD}$ from the median were considered outliers (equivalent to $\sim 3.4\sigma$ from the mean for Gaussian distributed data) as it is expected that measured trace element concentrations would be Poisson rather than Gaussian distributed for signals close to the background levels. Limits of determination (LOD, 6 standard deviations above the background, or approximately the smallest signal that can be quantitatively measured; Potts, 1992) were calculated using a modified version of equation 9.25 of Goldstein *et al.* (2003):

$$LOD = \frac{6 * \sqrt{N^B_{sam}} * C_{std}}{N^P_{std} - N^B_{std}}, \tag{B.1}$$

where N^P_{std} and N^B_{std} are the total counts on peak and background of the standard respectively, and N^B_{sam} are the total counts on the sample background. As the LOD is proportional to the square-root of the background, these limits of quantification vary between measurements. However, the background count rate was found to be extremely stable for each phase measured (olivine or chromite), both within an analytical session and between the two analytical sessions. For example the average LOD for measurements of Al_2O_3 in the SC-BK standard was 0.00376 ± 0.00005 wt% (n = 41, across

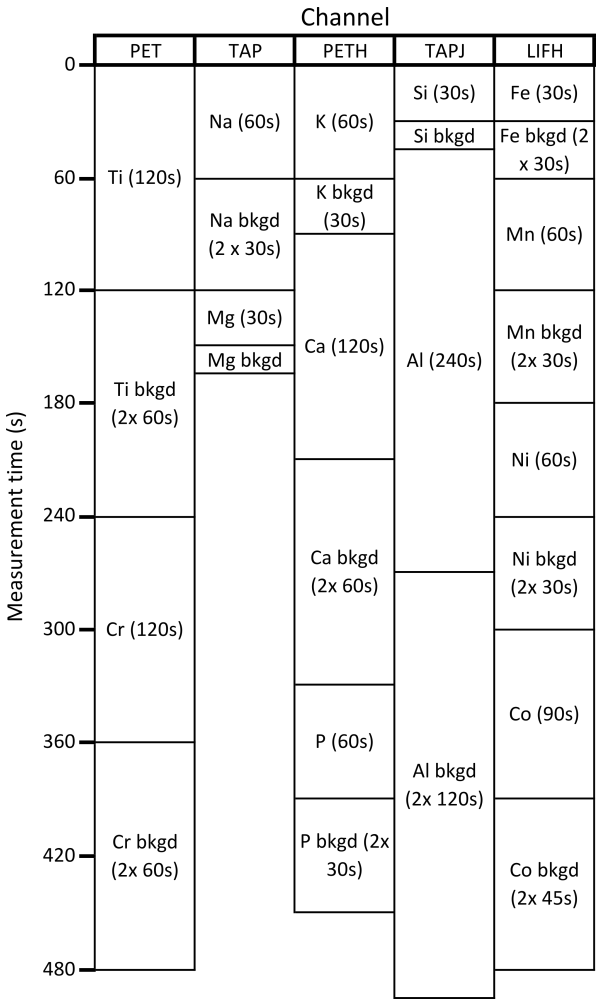

Figure B.1: Measurement times and channels for high precision EPMA data. During the second trace element analytical session, K_2O was no longer measured, so the Ca peak measurement was extended to 180 s and the background times were extended to $2 * 90$ s.

both analytical sessions). As such, only the average LODs for all high precision olivine analyses are given in Table B.2.

The constancy of the background signal can be attributed to the background mainly being generated by *Bremsstrahlung* radiation, as this is controlled by the major element composition of the sample, which is relatively constant for each phase. These remarkably steady backgrounds suggest that it may be possible to make quantitative measurements at even lower concentrations than investigated in this study, even without the use of extremely high beam currents (Batanova *et al.*, 2015), provided long-enough peak and background measurement times are possible, and that the background is sufficiently well characterised around the element of interest.

Table B.2: Measured average compositions, theoretical precisions and LODs for the two olivine standards used in this study. SC-BK and SC-KA EPMA data are averages and standard deviations of 41 and 15 spots, respectively, following outlier filtering using a median absolute deviation (MAD) test. Oxide data are given as wt%, trace element data in ppm. 'NQ' = not quantifiable, concentrations below limit of determination.

[1]LA-ICP-MS measurements of SC-BK made at the Geological Survey of Canada (n = 32).
[2]Instrumental Neutron Activation Analysis (INAA) data for Cr, Mn, Co, Ni in SC/KA (Gerhard Brey, personal communication, 2015).
[3]Isotope Dilution (ID) measurements of Ca in SC/KA from Köhler & Brey (1990).

	SC-BK EPMA	*1σ*	*SC-BK LA-ICP-MS*[1]	*1σ*	*SC/KA EPMA*	*1σ*	*SC/KA INAA,ID*	*1σ*	*Average LOD*
SiO_2	40.49	0.31			40.42	0.59			0.0104
TiO_2	NQ				NQ				0.0079
Al_2O_3	0.0146	0.0011			0.0169	0.0010			0.0039
Cr_2O_3	0.0221	0.0025			0.0159	0.0024			0.0105
MnO	0.1360	0.0023			0.1427	0.0030			0.0085
FeO	9.37	0.08			10.21	0.09			0.0118
CoO	0.0150	0.0018			0.0160	0.0011			0.0066
NiO	0.3867	0.0047			0.3658	0.0038			0.0088
MgO	49.88	0.36			48.61	0.73			0.0154
CaO	0.0778	0.0013			0.0773	0.0015			0.0034
Na_2O	NQ				NQ				0.0112
K_2O	NQ				NQ				0.0043
P_2O_5	NQ				NQ				0.0097
Total	100.44	0.57			99.98	0.61			
Mg#	0.9047	0.0013			0.8946	0.0022			
Al	77.5	5.9	80.4	2.3	89.7	5.2			
Cr	151.5	16.9	154.9	1.5	108.5	16.1	110.0	4.4	(INAA)[2]
Mn	1053.3	17.6	1065.7	7.3	1104.9	22.9	1065	32	(INAA)[2]
Co	117.6	14.2	139.2	1.1	126.1	8.9	143.0	5.7	(INAA)[2]
Ni	3038.5	37.2	3024.9	26.7	2874.6	30.2	2950	148	(INAA)[2]
Ca	555.9	9.3	456.7	6.8	552.2	10.5	524	4	(ID)[3]

All trace elements measured above the LOD for both standards, with the exception of Ca, agree with the pre-existing data within two standard deviations, demonstrating the accuracy of the high precision EPMA trace element data. The use of a plagioclase calibration standard for Al rather than Frank Smith pyrope increases the average Al concentration by ∼4.5%, which is smaller than both the precision on the EPMA measurements and the effect of using Si or Mg as an internal standard in the LA-ICP-MS data.

Ca measured by EPMA was systematically high in both olivine standards relative to values determined using other methods (although the measured Ca concentration fell within 3 standard deviations of the isotope dilution concentration for Ca in SC/KA).

This systematic offset was not affected by changes to the background position described in Appendix B.1, and systematically high Ca concentrations in these standards are currently unexplained. Though Co data agrees within 2 standard deviations with the previously measured data, it appears to be slightly low in both standards. This may be the result of uncertainties in the Fe overlap correction, which was conducted at 20 nA on a pure Fe wire, and thus represents quite different conditions to the 100 nA measurements in olivine. It may be difficult in general to obtain high precision Co data in olivines, due to the large interference produced by the Fe Kβ peak; careful and possibly repeated measurements of the magnitude of overlap correction are suggested for future work.

B.3 Expected precision of Winnipegosis Al-in-olivine analyses

The repeatability of trace elements measurements in both standards was variable, with elements with higher concentrations or longer counting times generally showing better repeatabilities. These are reported as one relative standard deviation (1σ relative) of the repeated analyses in Table B.3, with lower standard deviations corresponding to better repeatabilities or higher precision. However, as the Winnipegosis Komatiite olivines investigated in this study contain much higher concentrations of trace elements than the San Carlos olivine standards used, the repeatabilities of these standard measurements are likely to underestimate the precision of sample measurements. Theoretical precisions can be calculated for olivines with different trace element concentrations following the formula of Cox (1983):

$$\sigma_{rel} = \frac{\sqrt{\frac{N^P_{sam}}{(t^P_{sam})^2} + \frac{N^B_{sam}}{(t^B_{sam})^2}}}{\frac{N^P_{sam}}{t^P_{sam}} - \frac{N^B_{sam}}{t^B_{sam}}}, \tag{B.2}$$

where σ_{rel} is the relative standard deviation, and t^P_{sam} and t^B_{sam} are the total measurement times on peak and background, respectively (the sum of both background measurement times is used for a two sided background measurement). This theoretical precision assumes that errors only arise from Poisson distributed counting errors. Hence, it represents the best possible precision for a given measurement, as it ignores all other possible sources of error such as detector deadtime or calibration errors. There-

Table B.3: Measurement repeatabilities and theoretical precisions of trace elements in the SC-BK and SC/KA olivine standards.

	SC-BK		SC/KA	
Element	*Measured Repeatability*	*Theoretical Precision*	*Measured Repeatability*	*Theoretical Precision*
Al	7.64%	7.68%	5.81%	6.71%
Cr	11.15%	12.66%	14.87%	18.80%
Mn	1.67%	1.83%	2.08%	1.77%
Co	12.09%	6.30%	7.05%	5.86%
Ni	1.22%	0.82%	1.05%	0.85%
Ca	1.67%	1.09%	1.90%	1.04%

fore, it can only reliably be used to estimate the precision of sample measurements if it can be shown that the EPMA errors are dominated by counting uncertainties. Theoretical precisions for each trace element in SC-BK and SC/KA are also reported in Table B.3, and plotted against measured repeatabilities in Figure B.2. As the total counts on peak and background vary between each measurement, average theoretical precisions from all measurements of SC-BK and SC/KA are used.

As can be seen in Table B.3, the theoretical precision matches the measurement repeatability well, except in the case of Co in SC-BK, and trace elements with the highest total counts such as Ni and Ca (though Ca is not as high in concentration as Mn, it was measured for a much longer duration), where the measured repeatability is lower (less precise) than the theoretical precision. The lower repeatability of Ni and Ca can easily be explained by other sources of error (e.g., calibration errors, detector deadtime) becoming comparable to the errors from counting statistics as the number of counts recorded increases. An extreme example of this can be seen from the major element data collected for the two standards, where counting statistics predict that oxides such as MgO in olivine or Cr_2O_3 in chromite can should be repeatable to $\sim$0.1% (1σ relative), when the measured repeatability is in fact $\sim$0.7%. The mismatch between theoretical precision and measurement repeatability in the case of Co in SC-BK cannot be so easily explained, especially as there is no mismatch for Co in SC/KA. It is therefore suggested that the SC-BK olivine standard may be heterogeneous with respect to Co.

These exceptions aside, the match between theoretically predicted precisions and measured repeatability demonstrates:

1. The olivine standards are homogeneous in most trace elements at the level of precision achieved using the EPMA under these measurement conditions.

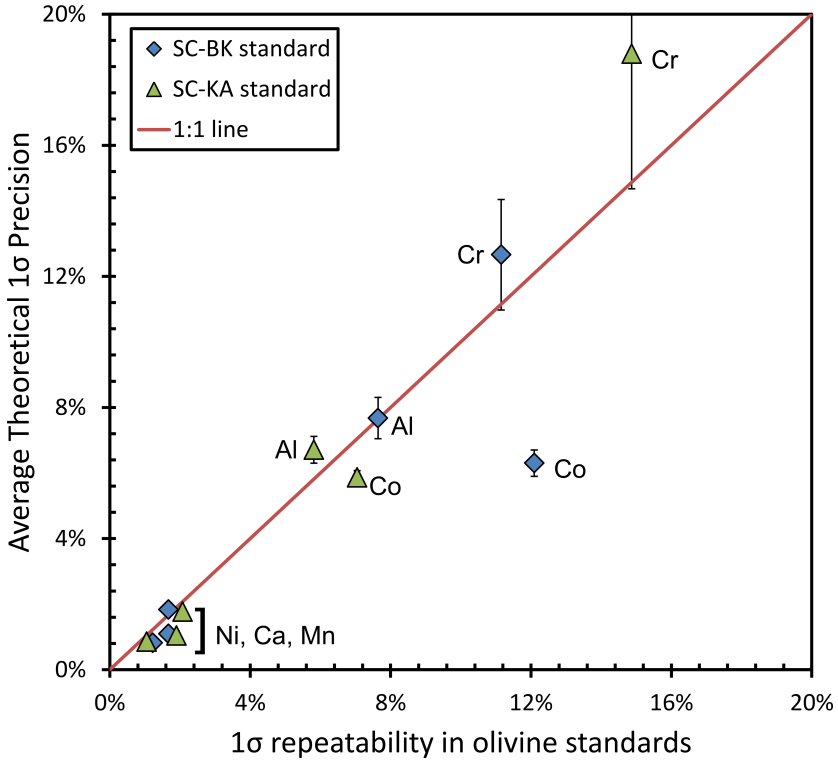

Figure B.2: Average theoretical precisions and associated uncertainties plotted against measured repeatabilities for trace elements measured in SC-BK and SC/KA. Uncertainties plotted are one standard deviation of the theoretical precisions estimated from repeated measurements of the standard. Note data for most minor elements fall to right of 1:1 line; measured repeatability is less precise than predicted from counting statistics alone.

2. Olivine trace element measurement uncertainties are dominated by counting errors at low concentrations.

3. The theoretical precision equation of Cox (1983) can be used to predict the errors associated with measurements of the Winnipegosis Komatiites, providing the concentrations are relatively low.

Using equation B.2 above, the theoretical precision for the Winnipegosis olivine with the highest Al concentration (463 ppm) is 1.46% (1σ relative), and for the olivine with the lowest Al concentration (238 ppm) is 2.63%. As higher concentrations should result in higher net signals and correspondingly better theoretical precisions, all of the olivine measurements should have a theoretical precision within this range. However, as the higher Al-in-olivine concentrations approach precisions where there is a mismatch between theoretical precision and measured repeatability, a conservative estimate of the error is used by taking a theoretical precision close to that of the olivine with the

lowest concentration to be representative. An error of ∼2.5% (1σ relative) is therefore assumed for all Al-in-olivine measurements.

B.4 EPMA Major Element Repeatability

As noted above, in the case of major elements, errors from counting statistics will generally be small relative to other sources of uncertainty. The averages and standard deviations of all analyses of the Mg# of SC-BK and SC/KA are 0.9047 ± 0.0013 (1σ relative = 0.14%), and 0.8946 ± 0.0022 (1σ relative = 0.25%) respectively. However, the results of a single analysis session were far more precise than this, with the Mg# of SC-BK measured as 0.9055 ± 0.0004 (1σ relative = 0.04%) in the first analytical session, and 0.9029 ± 0.0002 (1σ relative = 0.02%) in the second analytical session. Similarly, the Mg# of SC/KA was measured as 0.8968 ± 0.0005 (1σ relative = 0.06%) in session 1, and 0.8926 ± 0.0004 in session 2 (1σ relative = 0.04%). Due to the similarity in magnitude and direction of the shift in measured Mg# between session 1 and session 2 for both olivine standards, this difference is interpreted to result largely from calibration errors. This calibration error therefore results in a difference of about 0.003 Mg# between analytical sessions. As it is impossible to characterise the magnitude of calibration errors based on only two analytical sessions, a blanket error of 1σ absolute = 0.005 (units of Mg#) is assumed for any single measurement of the Mg# of an olivine using the EPMA.

Appendix C

Komatiite and picrite compilation reference list

Table C.1: Reference list for the komatiite and picrite major element and PGE data compilation (Section 3.6.4).

Location	*Age*	*Major elements*	*PGEs*	*Max ol Mg#*
Mauna Kea		Norman & Garcia (1999) Rhodes (1996) Rhodes & Vollinger (2004)	Ireland *et al.* (2009)	Ireland *et al.* (2009)
Hualalai		Ireland *et al.* (2009) Norman & Garcia (1999) Gurriet (1988)	Ireland *et al.* (2009)	Ireland *et al.* (2009)
Loihi		Ireland *et al.* (2009) Norman & Garcia (1999) Garcia *et al.* (1995)	Ireland *et al.* (2009)	Ireland *et al.* (2009)
Kilauea		Ireland *et al.* (2009) Norman & Garcia (1999)	Ireland *et al.* (2009)	Ireland *et al.* (2009)
Mauna Loa		Norman & Garcia (1999) Rhodes (1996) Rhodes & Vollinger (2004)	Ireland *et al.* (2009)	Ireland *et al.* (2009)
Gorgona G1	Sinton *et al.* (1998)	Brügmann *et al.* (1987)	Brügmann *et al.* (1987)	Revillon *et al.* (2000)
Gorgona G2	Sinton *et al.* (1998)	Kerr *et al.* (1996) Walker *et al.* (1999) Kerr (2005)	Brandon *et al.* (2003)	Revillon *et al.* (2000)
W. Greenland	Larsen *et al.* (2016)	Larsen & Pedersen (2000)	Woodland (1999)	Larsen & Pedersen (2000)
Emeishan	Zhou *et al.* (2002)	Li *et al.* (2012)	Li *et al.* (2012)	Li *et al.* (2012)
Schapenburg	Puchtel *et al.* (2016b)	Puchtel *et al.* (2009b)	Puchtel *et al.* (2009b)	
Komati Fm	Puchtel *et al.* (2014)	Puchtel *et al.* (2013)	Puchtel *et al.* (2014)	Puchtel *et al.* (2013)
Kostomuksha	Puchtel *et al.* (2001)	Puchtel *et al.* (2005)	Puchtel *et al.* (2005)	
Coonterunah	Van Kranendonk *et al.* (2007)	Maier *et al.* (2009)	Maier *et al.* (2009)	
Belingwe	Puchtel *et al.* (2009a)	Puchtel *et al.* (2009a)	Puchtel *et al.* (2009a)	Renner *et al.* (1994)
Volotsk	Puchtel *et al.* (2007)	Puchtel *et al.* (2007)	Puchtel *et al.* (2007)	
Alexo	Puchtel *et al.* (2009a)	Puchtel *et al.* (2004)	Puchtel *et al.* (2004)	Sobolev *et al.* (2016)
Regal	Van Kranendonk *et al.* (2007)	Maier *et al.* (2009)	Maier *et al.* (2009)	
Pyke's Hill 1	Puchtel *et al.* (2009a)	Puchtel *et al.* (2004)	Puchtel *et al.* (2004)	Puchtel *et al.* (2004)
Pyke's Hill 2	Puchtel *et al.* (2009a)	Puchtel *et al.* (2004)	Puchtel *et al.* (2009a) Puchtel *et al.* (2004)	Puchtel *et al.* (2004)
Weltevreden	Puchtel *et al.* (2014)	Puchtel *et al.* (2013)	Connolly *et al.* (2011) Puchtel *et al.* (2014)	Puchtel *et al.* (2013)